Solar Influences in the Heliosphere:

Understanding coronal mass ejections and their associated magnetic clouds

Kimberley Steed

Mullard Space Science Laboratory
Department of Space and Climate Physics
University College London

A thesis submitted to University College London
for the degree of Doctor of Philosophy

June 2011

I, Kimberley Steed, confirm that the work presented in this thesis is my own. Where information has been derived from other sources, I confirm that this has been indicated in the thesis.

Much of the work undertaken during study for this Ph.D. can be found in the following articles:

- **Steed, K.**, Owen, C. J., Démoulin, P. and Dasso, S.: Investigating the observational signatures of magnetic cloud substructure. 2011, *J. Geophys. Res.*, 116, A01106.
- Harra, L. K., Mandrini, C. H., Dasso, S., Gulisano, A. M., **Steed, K.**, Imada, S.: Determining the solar source of a magnetic cloud using a velocity difference technique. 2011, *Sol. Phys.*, 268, 213.
- Attrill, G. D. R., van Driel-Gesztelyi, L., Démoulin, P., Zhukov, A. N., **Steed, K.**, Harra, L. K., Mandrini, C. H. and Linker, J.: The recovery of CME-related dimmings and the ICMEs enduring magnetic connection to the Sun. 2008, *Sol. Phys.*, 252, 349.
- **Steed, K.**, Owen, C. J. Harra, L. K., Green, L. M., Dasso, S., Walsh, A. P., Démoulin, P. and van Driel-Gesztelyi, L.: Locating the solar source of 13 April 2006 magnetic cloud. 2008, *Ann. Geophys.*, 26, 3159.

Abstract

Coronal mass ejections (CMEs) are large-scale explosions on the Sun that expel plasma and magnetic field into the heliosphere. The interplanetary counterparts of CMEs, termed interplanetary CMEs (ICMEs), are often directly observed by spacecraft located in the near-Earth environment, and this thesis focuses on understanding the evolution of these structures as the propagate away from the Sun and into the heliosphere. This work contributes to the understanding of space weather in the near-Earth environment, which is known to affect the technological systems at Earth upon which we increasingly rely.

A subset of ICMEs, termed magnetic clouds, in which a flux rope structure can often be identified, form the primary focus of these studies. The process by which a magnetic cloud observed directly in interplanetary space may be linked with its associated CME, through the combined study of remote observations of the Sun and *in situ* observations near-Earth, is discussed. A comparison of the magnetic topology of the erupting structure at both the Sun and in interplanetary space allows us to infer the process by which it erupts, and better understand its evolution as it propagates through the heliosphere.

A subset of magnetic clouds, in which we directly observe unusual internal substructure, is identified. We examine the physical nature of this substructure, characterising the observed behaviour of both the magnetic field and plasma in these regions. To improve our understanding of the external physical processes that influence the evolution of a magnetic cloud in interplanetary space, we investigate, and ultimately evaluate, a number of physical mechanisms that may lead to the formation of unusual magnetic cloud topology.

Acknowledgements

First and foremost, I would like to thank my supervisors Chris Owen and Louise Harra for their support and guidance throughout my PhD studies.

Chris, thank you for providing me with both a knowledgeable and reliable sounding board; you have been invaluable in helping me to develop my understanding of space plasmas.

Louise, thank you for your encouragement and belief in my ability to continue my research in solar physics beyond my PhD studies. It has been a pleasure to work alongside you.

Pascal Démoulin and Sergio Dasso, words cannot express how grateful I am for our many fruitful discussions and your continued encouragement and advice. Thank you for always being there!

I'd like to thank all of the members of solar physics group for welcoming me, even though I was a bit of a curve-ball research-wise, and all of the members of the plasma and planetary groups for accepting me without question, despite my solar tendencies. In particular, I'd like to thank all of my office mates over the last few years; Paul Henderson, for showing me how it should be done, Andrew Walsh, Ilya Alexeev and Colin Forsyth, for their attempts to teach me how it should be done, Gethyn Lewis, for the good times, and the rest of our motley crew; Yasir Soobiah, Segheen Beyene and Roger Duthie.

I'd also like to thank Sheila Kanani and Alison Wallace for their support and encouragement during the final stages of my thesis-writing, provided over Woo woos and wine, respectively, and Jo Bartlett and Deb Baker for providing me with living proof that there is light at the end of the tunnel.

My most heartfelt thanks go to Ian German, my lobster, for celebrating with me during the highs and for simply being there during the lows. Finally, I'd like to thank my wonderful family for their unwavering belief in me.

List of Abbreviations

Abbreviation	Details
2-D/3-D	Two-/Three-dimensional
3DP	Three-dimensional Plasma and Energetic Particle Investigation
ACE	Advanced Composition Explorer
AIA	Atmospheric Imaging Assembly
AR	Active Region
AU	Astronomical Unit (1.5×10^{11} m)
CCD	Charge-Coupled Device
CME	Coronal Mass Ejection
CS1	Current Sheet 1
CS2	Current Sheet 2
CSHKP	Carmichael, Sturrock, Hiroyama, Kopp and Pneuman
EESA - H	(High energy) Electrostatic Analyser
EESA - L	(Low energy) Electrostatic Analyser
EIT	Extreme Ultraviolet Imaging Telescope
ESA	European Space Agency
EUV	Extreme Ultraviolet
FGM	Fluxgate Magnetometer
GGS	Global Geospace Science mission
GOES	Geostationary Operational Environmental Satellite
GSE	Geocentric Solar Ecliptic coordinates
HMI	Helioseismic and Magnetic Imager
HT	deHoffmann-Teller
HXR	Hard X-ray
ICME	Interplanetary Coronal Mass Ejection
IMF	Interplanetary Magnetic Field
ISEE	International Sun-Earth Explorer
$L_\odot$	Solar luminosity (3.85×10^{23} kW)
LASCO	Large Angle Spectroscopic Coronagraph
LCP	Left circularly polarised
$M_\odot$	Solar mass (1.99×10^{30} kg)
MAG	Magnetic Field Experiment
MC	Magnetic Cloud
MCP	Micro Channel Plate
MDI	Michelson Doppler Imager
MFI	Magnetic Field Investigation
MHD	Magnetohydrodynamic(s)
MVA	Minimum Variance Analysis
NASA	National Aeronautics and Space Administration
NOAA	National Oceanic and Atmospheric Administration
PAD	Pitch Angle Distribution
$R_\odot$	Solar radius (6.96×10^8 m)
R_E	Earth radius (6.38×10^6 m)
RCP	Right circularly polarised
SAA	South Atlantic Anomaly
SECCHI	Sun Earth Connection Coronal and Heliospheric Investigation
SDO	Solar Dynamics Observatory

Abbreviation	**Details**
SOHO	Solar and Heliospheric Observatory
SOI	Solar Oscillations Investigation
SMEX	Small Explorer
STEA	Suprathermal Electron Angle scan data mode
STEREO	Solar Terrestrial Relations Observatory
SWEPAM	Solar Wind Electron Proton Alpha Monitor
SWEPAM - E	Solar Wind Electron Proton Alpha Monitor - Electrons
SWEPAM - I	Solar Wind Electron Proton Alpha Monitor - Ions
SXR	Soft X-ray
TRACE	Transition Region and Coronal Explorer
UT	Universal Time
UV	Ultraviolet
UVCS	Ultraviolet Coronagraph Spectrometer

Contents

List of Figures

List of Tables

Chapter 1

Introduction

1.1 The Sun

Our Sun is a fairly unremarkable star when compared to its stellar neighbours. However it is of fundamental importance to the solar system and the life that it supports there. Like other stars, the Sun was formed by the gravitational collapse of an interstellar gas cloud. It is currently located near to the centre of the main sequence when shown on a Hertzsprung-Russell diagram, which plots the evolutionary tracks of stars (Figure 1.1). The Sun is essentially a giant ball of hydrogen and helium gas with trace amounts of some heavier elements, and whilst on the main sequence, energy is supplied via fusion of hydrogen in the core. Once this ceases the Sun will progress to the red giant phase, when it is predicted that it will engulf the Earth. The Sun is currently 4.6×10^9 years old, which means it is about half way through its lifetime. With a mass of 1.99×10^{30} kg, the Sun accounts for more than 99 % of the mass in the solar system. With a luminosity of 3.85×10^{23} kW, it is now believed to be brighter than 85 % of the stars in the Milky Way galaxy, most of which are red dwarfs. The Sun rotates differentially since it is entirely gaseous, which means the rotation period at the equator varies from that at the poles. The Sun's rotation period is therefore latitude dependent, ranging from 25 to 35 days, and this plays an important part in the generation and maintenance of the Sun's magnetic field.

1.1.1 The Solar Interior

The solar interior is often described in terms of the energy generation and transport mechanisms that dominate in different internal regions of the Sun. It comprises

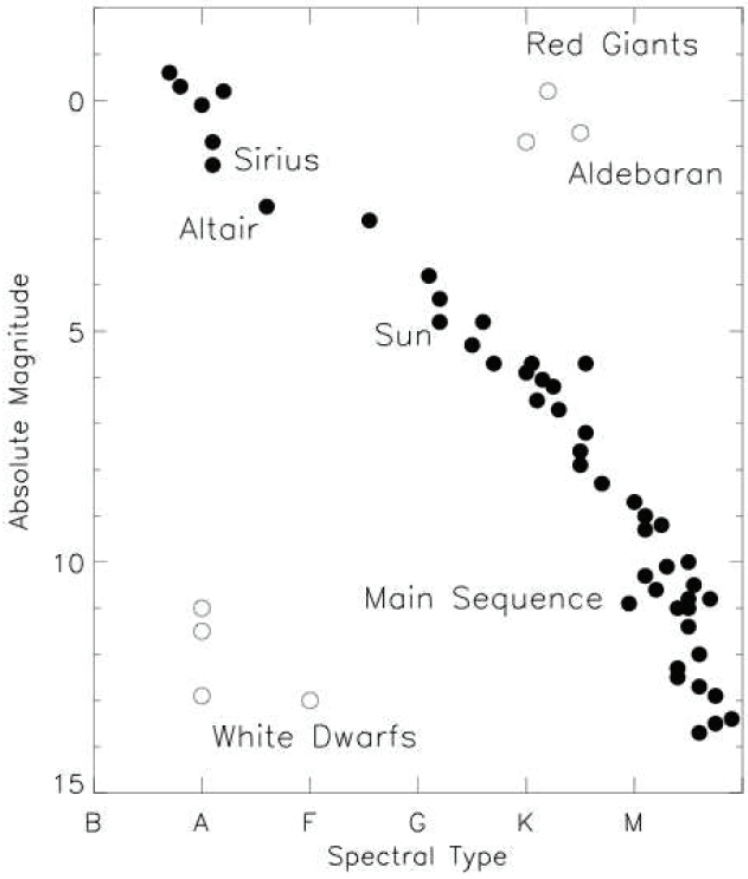

Figure 1.1: A Hertzsprung-Russell diagram showing stars in the solar neighbourhood. The diagram shows the spectral type (related to absolute temperature) versus the absolute magnitude (related to stellar luminosity). The main sequence describes the continuous band of stars stretching from the upper left to the bottom right (solid black circles). Stars that have evolved beyond the main sequence (red giants and white dwarfs) are also plotted (open circles). Figure from Phillips *et al.* (2008). Permission to reproduce this figure has been granted by Cambridge University Press.

the core, radiation and convection zones, as illustrated in the schematic of the solar interior shown in Figure 1.2. The boundaries of these regions can be described in terms of their radial distance from the centre of the Sun, since the respective zones form approximately spherical, concentric shells about the solar centre.

The standard solar model is a spherically symmetric quasi-static model in which the Sun is treated as a spherical ball of gas. It allows the physical conditions in the interior of the Sun to be described and is constrained by a set of well determined boundary conditions, which include luminosity, radius, age and composition of the Sun.

The virial theorem tells us that the Sun cannot have thermal or gravitational energy as its energy source since they are insufficient to account for the observed solar luminosity and age, but that the Sun will heat up as it contracts. In addition, chemical reactions are not capable of releasing enough rest mass energy to account for all of the Sun's energy, leading us to the conclusion that only nuclear reactions

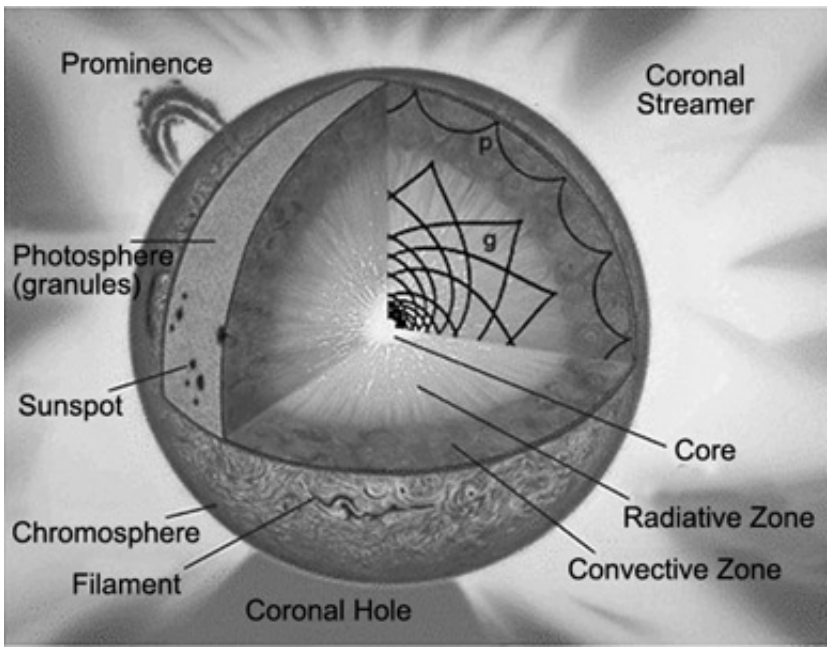

Figure 1.2: A schematic of the solar interior, highlighting the core, radiative and convective zones. Some key features of the solar surface and atmosphere are also detailed. Figure courtesy of NASA.

are capable of providing the required amounts of energy over the Sun's lifetime:

$$t_{nuclear} \simeq \frac{0.1\epsilon M_{\odot} C^2}{L_{\odot}} \simeq 10^{10} years \tag{1.1}$$

where 0.1 is the fraction of mass used up before the star leaves the main sequence, $\epsilon = 0.7$ % is the fraction of the rest mass converted to thermal energy by protons fusing into the nuclei or alpha particles, $M_{\odot}$ is the solar mass, $L_{\odot}$ is the solar luminosity and C is the speed of light.

Fission could provide the required energy, but heavy elements are not abundant on the Sun. However light elements, like hydrogen and helium are abundant and fusion is generally accepted as the source of the Sun's energy.

The internal solar structure can be described by the following set of differential equations, which give relationships for the pressure, opacity and energy generation rate in terms of the density, temperature and composition of the Sun.

Nuclear fusion in the core of the Sun leads to a change in the chemical composition of the solar interior as hydrogen is converted to helium, which should result in a decrease in pressure as the mean molecular mass decreases:

$$\frac{dP}{dr} = -\frac{GM(r)\rho}{r^2} \tag{1.2}$$

where P is pressure, r is radius, G is the gravitational constant, $M(r)$ is mass as a function of radius and ρ is density.

However, this does not happen since the core contracts and consequently increases in temperature. By the ideal gas law, this increase in temperature also increases the pressure and restores the balance of hydrostatic equilibrium:

$$P = \frac{\rho K_B T}{\mu m_H} \tag{1.3}$$

where μ is the molecular weight and hence the number density $n = \rho/\mu m_H$.

The mass of the solar interior as a function of the solar radius is described by:

$$\frac{dM(r)}{dr} = 4\pi r^2 \rho \tag{1.4}$$

Assuming the energy flows across a sphere of radius, r at a rate of $L_r W$, then we can write an equation relating the rate of energy release and the rate of energy transport through the Sun:

$$\frac{dL}{dr} = 4\pi r^2 \rho \epsilon \tag{1.5}$$

where ϵ is the rate of nuclear energy production per unit mass (W kg^{-1}).

Nuclear fusion of light elements, primarily hydrogen into helium provides 99 % of the Sun's energy (the remaining 1 % of the Sun's energy comes from the carbon-nitrogen chain fusion reaction). The solar core region where fusion proceeds extends to R $\approx$ 0.25 R$_\odot$, with temperatures ranging between 8 x 10^6 and 15 x 10^6 K and densities ranging between 2 x 10^4 and 1.6 x 10^5 kg m^{-3}.

The Sun's luminosity, which is a measure of its radiation output, implies a mass loss rate of 4 x 10^9 kg s^{-1}. The study of meteorites indicates that the age of the Sun is 4 x 10^9 years and this means, to date, only 3 x 10^{-4} M$_\odot$ ($\sim$ 0.03 % of the Sun's mass) has been consumed through fusion.

In the Sun, gas pressure is more important than radiation pressure. Thus, since

the thermal energy of the electrons is greater than that of the photons, we might expect thermal conduction to be the most important energy transport mechanism. However, the mean free path of the photons is so much greater than that of the electrons that thermal conduction is negligible in most stars, and energy is therefore transported primarily via radiation between ~ 0.25 $R_\odot$ and ~ 0.71 $R_\odot$. Radiative transport of energy is described by the radiative temperature gradient equation:

$$\frac{dT}{dr} = \frac{3}{16\sigma}\frac{\bar{\kappa}\rho}{T^3}\frac{L_r}{4\pi r^2} \tag{1.6}$$

where σ is the Stefan-Boltzmann constant and $\bar{\kappa}$ is the opacity of the matter.

The transport of energy by conduction and radiation will occur whenever a temperature gradient is maintained within a body. However in the outer layers of the solar interior, increased opacity leads to the steepening of the temperature gradient and the onset of convection above ~ 0.71 $R_\odot$. For convection to become the dominant energy transport mechanism in the Sun, the following criteria must be satisfied:

1. Convection will only occur in liquids and gases when the temperature exceeds some critical value, i.e. it will only begin because the state of the fluids is unstable. The criterion for stability is:

$$\left|\frac{dT}{dr}\right|_{adiabatic} < \frac{T}{P}\frac{\gamma - 1}{\gamma}\left|\frac{dP}{dr}\right| \tag{1.7}$$

   where $\gamma = C_p/C_V$ is the adiabatic index, the ratio of specific heats in the gas. (For a fully ionised ideal gas, $\gamma = 5/3$.)

2. In a gas, convection will occur if the rising element is lighter than its surroundings but this depends on the rate at which the element expands due to decreasing pressure, and the rate at which the surrounding density decreases with height.

In the Sun, as with other stars, the temperature falls with increasing radius as we move from the core outwards, which implies that both the temperature gradient (dT/dr) and pressure gradient (dP/dr) are negative. Initially dT/dr is mostly determined by electron scattering because the gas is fully ionised. However, as T falls, electrons begin to recombine with nuclei. The atoms that are subsequently formed are more effective absorbers of radiation, and as a result the opacity increases and the temperature gradient becomes steeper. A convective cycle is established, the evidence for which can been seen in patterns of granulation and supergranulation in the

surface layers of the Sun. The condition for instability is known as the Schwarzchild criterion and implies that when $|dT/dR|_{rad} > |dT/dr|_{adiabatic}$, rising gas elements will remain hotter than their surroundings, and thus stay buoyant.

1.1.2 The Solar Surface

The "surface" of the Sun lies above the convection zone and can be seen in optical wavelengths with the naked eye. It is known as the photosphere, from the Greek for "light". Here, the solar temperature reaches a minimum (6000 K), before it starts to rise again in the solar atmosphere. The photosphere is the thinnest solar layer ($\sim$ 100 km), and is also the layer of the Sun at which the solar radius is defined, $R_\odot$ = 6.96 x 10^5 km. The photosphere appears as a solid sphere because its opacity is so high. The most significant cause of this high opacity is the continuous absorption between ultraviolet and infrared wavelengths in the solar spectrum, but absorption at other discrete wavelengths also plays a part.

Observed photospheric features include sunspots. A sunspot is initially comprised of a dark core, known as the umbra, but as it increases in size filaments develop, lying approximately radially around the core. These are collectively described as the penumbra. Larger spots tend to form groups, with the leading spot lying closer to the equator than the trailing spot. Photospheric faculae are frequently seen around sunspot groups. These are $\sim$ 300 K hotter than their surroundings and are composed of many small bright points. Sunspots had been seen even before telescopes were invented in the early 1600s, but despite the long history of sunspot observations, the mechanism by which they are formed is still not well understood.

Granulation is also evident in white-light observations of the photosphere and is linked to the structure of the convective cells in the solar interior. The granules are separated by intergranular lanes, which are darker than the granules themselves, indicating that they are cooler. While granules are associated with upward motions of plasma, intergranular lanes show downward motions of plasma. Both large- and small-scale granules have been identified. While typically cells are $\sim$ 1000 km in diameter, there are also mesogranular and supergranular cells with sizes up to $\sim$ 30,000 km in diameter.

1.1.3 The Solar Atmosphere

Above the photosphere lies the solar atmosphere, which comprises only a tiny fraction of the Sun's mass. It is expected that the temperature of the Sun decreases

with increasing distance from its energy source. However, while this is the case in the solar interior, beyond the top of the photosphere the temperature begins to slowly rise in the lowest solar atmospheric layer, known as the chromosphere. This temperature then increases dramatically in the transition region to the very high MK temperatures observed in the uppermost atmospheric layer, known as the corona. Heating by conduction, radiation or convection cannot be responsible for the dramatic rise in temperature in the solar atmosphere, since a transfer of heat from a cool environment to a hot environment would contravene the 2nd law of thermodynamics. The source of coronal heating remains unsolved, in spite of many theoretical possibilities.

Given their high temperatures, the chromosphere, transition region and corona are primarily observed in ultraviolet (UV), extreme ultraviolet (EUV) and soft X-ray (SXR) wavelengths. To properly measure at these wavelengths, the observer must be located above the Earth's atmosphere to avoid atmospheric absorption, and there have been several solar missions launched with this objective. The most recent of these spacecraft is the Solar Dynamics Observatory (SDO), which is currently returning observations of the solar atmosphere in unprecedented detail. Figure 1.3 shows a composite image of the Sun's atmosphere from the Atmospheric Imaging Assembly (AIA) instrument onboard SDO, combining images at the wavelengths 211 Å 193 Å and 171 Å to create this view of the Sun. When viewing images of the Sun, two of the traditional compass points are reversed, such that east is west, and west is east. This convention is used throughout this thesis.

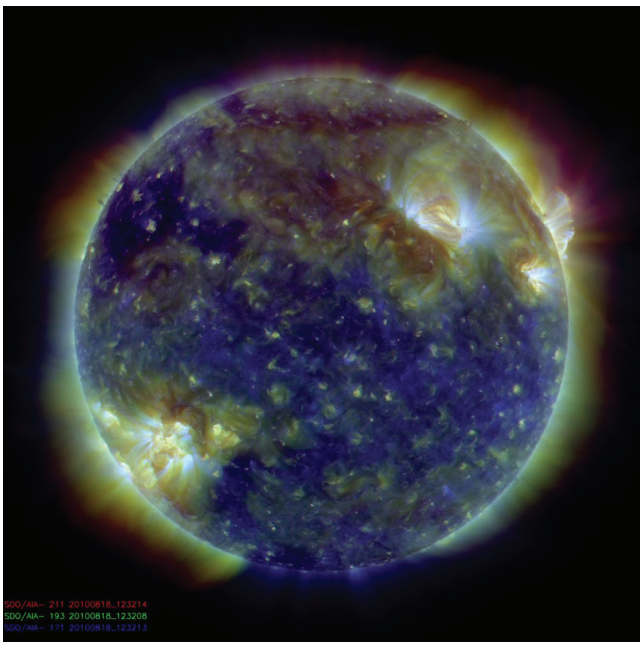

Figure 1.3: A composite image of the Sun's atmosphere from the AIA instrument onboard the Solar Dynamics Observatory (SDO). Images at the wavelengths 211 Å 193 Å and 171 Å which are spectral lines that are formed at coronal temperatures, are combined to create this view of the Sun.

The chromosphere, meaning "colour", owes its name to the red aura seen above the solar limb during an eclipse, which is caused by emission from the Hα line at 6563 Å. The temperature in the chromosphere is higher than the photosphere, at $\sim$ 20,000K and chromospheric structures are best seen using monochromatic imaging in strong chromospheric lines, e.g. Hα and Ca II H and K. Detailed observations have revealed that the chromosphere is much more dynamic than the underlying photosphere, and is made up of small bright cells that form the chromospheric network. Many hundreds of narrow, jet-like features, known as spicules have also been observed, which can exceed 10,000 km in length, but are only around 1000 km wide.

Different chromospheric features are revealed in the observations of spectral lines formed at different heights in the atmosphere. Unlike Ca II H and K lines, which are collisionally controlled, the Hα line is photoelectrically controlled, and while this means it does not provide information on the temperature of the chromosphere, it is ideal for observing long, dark regions, known as filaments, on the solar disk. These structures are termed prominences when observed in emission on the solar limb. Other elongated dark features known as mottles and fibrils may also be readily observed in this line, together with sunspots, surrounded by bright, plage regions. More information on the chromosphere and its links to upper atmospheric solar regions is obtained by observing in the UV wavelength range.

Between the solar chromosphere and the corona lies a very thin interface, known as the transition region. The temperature rises steeply through this region to coronal temperatures $> 1 \times 10^6$ K. The chromospheric network is still evident in the transition region and other observed features include loop structures with temperatures between 10^5 - 10^6 K and many small brightenings, known as blinkers, however the transition region is difficult to identify and is still not well understood.

The corona, from the latin meaning "crown", is the uppermost layer of the solar atmosphere and extends out into the heliosphere. The corona is extremely hot and tenuous and is visible in white-light due to the Thomson scattering of photospheric light by coronal electrons. During a solar eclipse, the corona is observed as an extended white-light halo, as shown in Figure 1.4. Like the chromosphere and transition region, the corona is observed on the solar disk in UV, EUV and SXR wavelengths since the photosphere does not emit at these wavelengths and active regions, diffuse coronal loops and X-ray bright points can all be identified. Other observed coronal features include streamers, identified by enhanced emission, and coronal holes, identified by decreased emission. The strength of the coronal magnetic field varies from B $\approx$ 10 mT (100 G) at the base of the corona to B $\approx$ 7 nT (7×10^{-5} G) in the solar wind at a distance of 1 AU from the Sun.

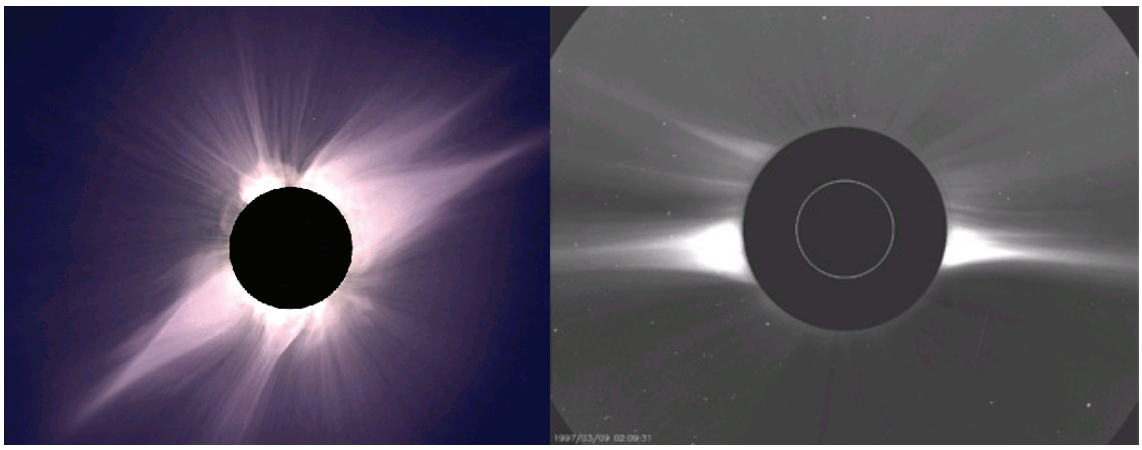

Figure 1.4: The solar corona is visible in white-light due to the Thomson scattering of photospheric light by coronal electrons. This figure shows white-light observations of the corona during a total solar eclipse (the dark disk is the moon occulting the Sun) (*left*) and from the LASCO coronagraph onboard the SOHO spacecraft (*right*).

A coronal emission line (5303 Å) was first observed in 1869 during a total solar eclipse. Later more emission lines were observed, but the presence of these could not be explained by the discovery of new elements, since the periodic table was nearly complete. In 1939 Grotrian showed that the coronal red line (6374 Å) was emitted by Fe X, and in 1942 Edlén identified the remaining coronal lines as forbidden transitions in Fe, Ni and Ca. In the meantime, it was suggested by Bowen that gaseous nebulae are very dilute, hence an atom may stay in a metastable excited state for a long time. These discoveries subsequently led to the conclusions that the solar corona is both hot and tenuous, since high temperatures are required to produce the high degrees of ionisation inferred from the spectra and forbidden transition lines occur when metastable levels become over-populated because collisional de-excitation is rare.

The coronal spectrum consists of a continuum observed as a result of Thomson scattering of photospheric light by coronal electrons, superposed with bright emission lines. The corona can be divided into two main components, known as the K-corona and the F-corona. The K-corona is the electron scattered component and dominates out to ~ 2 $R_\odot$. It is a featureless continuum without any Fraunhofer lines, since the high speeds of the coronal electrons (0.03c) means that these lines are broadened so much that they are no longer visible. The second coronal component is the dust-scattered component, known as the F-corona, that dominates beyond ~ 2.5 $R_\odot$. The spectrum is the same as for the photosphere and includes Fraunhofer lines. Gradual changes are observed in the white-light corona over the duration of the solar cycle. At solar minimum, long symmetrical streamers are observed at the equator, and plumes at the poles. During solar maximum, the corona is visibly less symmetrical and more structures are observed.

1.2 The Magnetic Sun

The Sun's magnetic field is the source of all solar activity. It is believed that the solar dynamo is the physical process that generates the Sun's magnetic field. The solar interior is a highly conducting plasma and the rotation of this plasma generates electric currents which convert plasma motion to magnetic energy. The resulting magnetic field is dipolar, like many other celestial bodies, including the Earth. The magnetic field extends above the solar surface and has different manifestations in different atmospheric layers.

Any dynamo theory must be able to account for all observed solar activity phenomena, including the emergence of sunspots at high latitudes and their subsequent migration to the equator (Spörer's law), which is illustrated by the well-known butterfly diagram shown in Figure 1.5, the variable length of the solar cycle and polarity reversals at the poles.

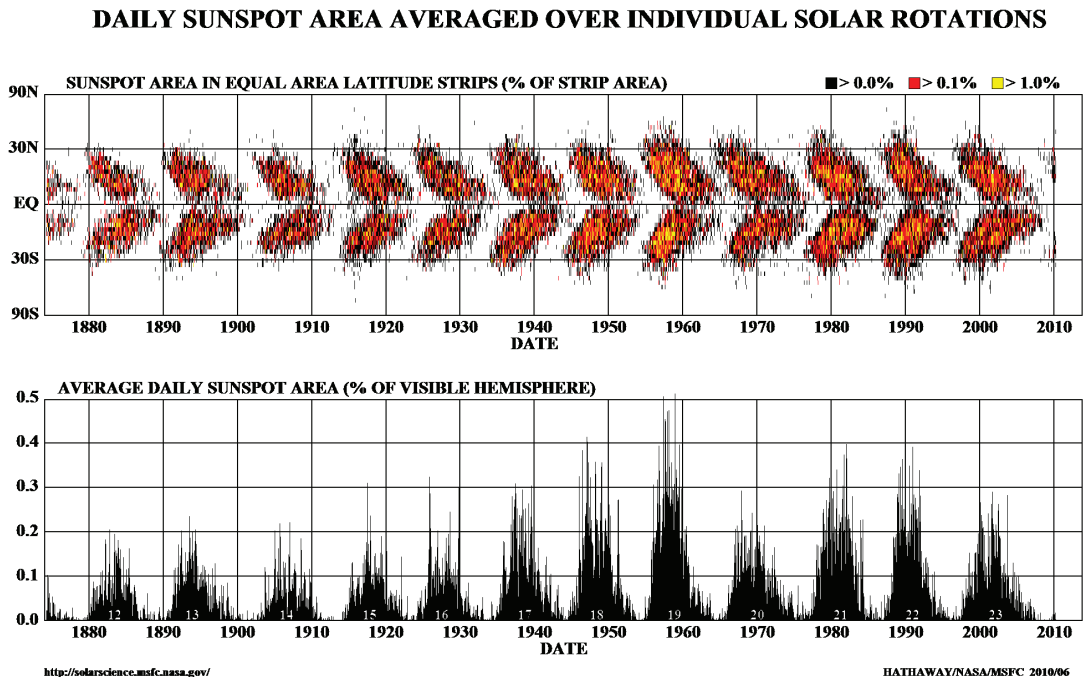

Figure 1.5: This well-known butterfly diagram shows sunspot area as a function of solar latitude over time and illustrates the relationship between sunspot emergence and the solar cycle. Spörer's law shows that at solar minimum sunspots emerge at high latitudes and subsequently migrate to the equator. Figure courtesy of Marshall Space Flight Center, NASA.

1.2.1 Generating the Solar Magnetic Field

Using helioseismology, it has been established that a region of high shear, known as the "tachocline" is the seat of solar magnetic fields (Spiegel and Zahn, 1992;

Charbonneau *et al.*, 1999). The tachocline is located between the radiation and convection zones in the solar interior, forming the boundary between the rigidly rotating core and the differentially rotating regions. The solar dynamo is usually broken down into three components:

1. The generation of strong, large-scale fields of periodically reversing polarity;
2. The rise of these fields in the photosphere;
3. The processing, spreading across and removal from the photosphere of magnetic flux.

A flux tube that is in thermal balance with its surroundings ($T_{internal} = T_{external}$) is buoyant, since the lower internal gas pressure ($p_{internal} < p_{external}$) implies lower mass density, $\rho_{internal} < \rho_{external}$. The arising magnetic buoyancy force will lead to the rise of flux tubes. Flux tubes also experience an opposing drag force due to velocity shear in the ambient medium, and the rate of rise, $v_{\uparrow}$, for flux tubes is determined by the balance of buoyancy and drag:

$$v_{\uparrow} = v_A \left(\frac{\pi}{C_d}\right)^{1/2} \left(\frac{a}{H_p}\right)^{1/2} \tag{1.8}$$

where v_A is the Alfvén speed and H_p is the pressure scale height.

The flux tube will eventually penetrate through the surface of the Sun, and the properties of this emerging flux can then be used to infer details of the dynamo process.

After decades of magnetic measurements on the Sun, including both the weaker, facular fields as well as the stronger fields, Babcock (1961) put forward a conceptual model, which describes the 22-year magnetic cycle of the Sun in 5 stages.

The Sun's magnetic field is approximated by a dipole field symmetric about the rotation axis and the field lines are initially poloidal, connecting the north and south poles. Differential rotation pulls and stretches this poloidal field horizontally around the Sun into a helical spiral, the effect of which is most intense in the activity belts (latitude $\sim 30°$). Magnetic flux then begins to emerge at the surface and the first active regions of the cycle are formed around latitudes $\theta = 30°$. The active region latitudes move towards the equator over time, reaching $\theta = 8°$ after around 8 years following Spörer's law. Moreover, Joy's law (Hale *et al.*, 1919) shows that the leading polarity in bipolar sunspot groups tends to lie closer to the equator than

that of the following polarity (with the extent of the tilt increasing with latitude), whilst Hale-Nicholson's law (Hale, 1924) adds that active regions on opposite sides of the hemisphere have opposite leading polarities, which alternate between successive sunspot cycles. As the leading polarities move toward the equator, flux cancellation occurs, resulting in the neutralisation and subsequent reversal of the general poloidal field. After 11 years, the magnetic field is again poloidal and the dipole field is now oppositely directed to that in the initial stage.

This model was amended by Leighton (1969) to include his interpretation that the mean flux transport, included by Babcock simply as an observed fact, was actually a result of the combined effect of the dispersal of magnetic elements by a random walk process and the asymmetry in the flux emergence.

The original Babcock-Leighton model has a number of limitations and, since its inception, subsequent dynamo models have aimed at fully dynamical solutions of the induction equation together with the coupled mass, momentum and energy relations for the plasma. However, the solar dynamo is still not well understood and many questions remain unanswered.

The Sun's activity ebbs and wanes over an 11 year period referred to as the solar cycle. In 1843, the 11 year cyclic variation in the number of sunspots was discovered by the German astronomer, Heinrich Schwabe. The amplitude of the sunspot number variation can be more than a factor of 4 between cycles. Some variety in the period of the solar cycle has also been observed in records dating back to 1750, with intervals in the range 8 - 15 years, making it difficult to predict when the next peak in solar activity will occur. There have been prolonged periods of time in history when no sunspots have been observed at all, the most notable of which is a period known as the Maunder minimum, after the astronomer Edward Maunder, who noted that during the period from 1645 to 1715 the sunspot cycle virtually disappeared. It is interesting to note that the most recent solar minimum, marking the end of solar cycle 23 and the onset of solar cycle 24 has been unusually long, but, despite the availability of extensive solar observations, it is not clear why this is the case.

Since the discovery of the variation of the number of sunspots over the solar cycle, it has come to light that there are also a number of other solar parameters that are observed to vary over this period, including sunspot area, Ca II plage area and 10.7 cm microwave radio flux emission. Changes in solar irradiance are also observed over the cycle, due to competition between dark sunspots and bright faculae in which the faculae dominate. This results in a change in solar irradiance of 0.2 % from solar cycle maximum to minimum.

The coronal structure at solar minimum is that of two diametrically opposite lobes, but during solar maximum the corona is much more radial. At solar minimum, the X-ray corona is often completely devoid of active regions and is much fainter and weaker than the solar maximum corona. Polar coronal holes are large and prominent at the minimum stage of the cycle and white-light observations show that the streamer belts are concentrated in the equatorial plane. At solar maximum the X-ray corona is bright and highly structured with many active regions present that dominate the emission. The polar coronal holes are somewhat diminished and the white-light corona is also much more highly structured, with streamers present at all latitudes. Figure 1.6 illustrates the change in emission and structure observed in the X-ray corona over the duration of a solar cycle.

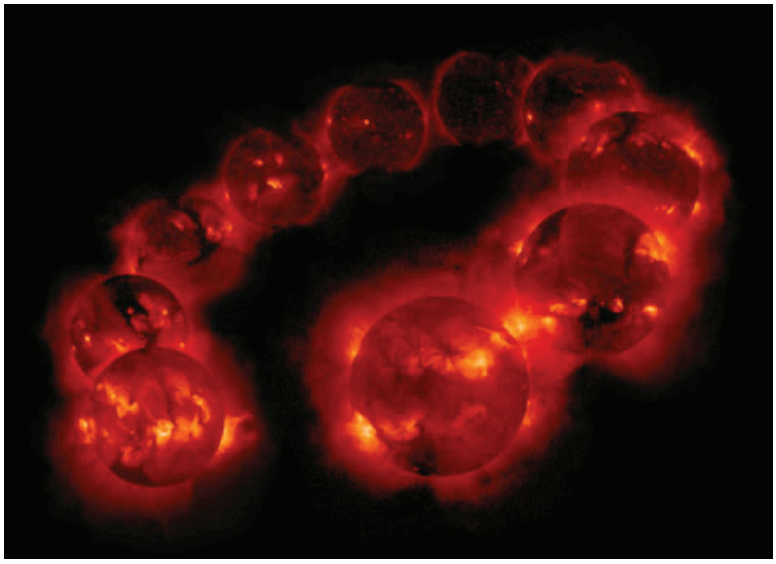

Figure 1.6: The composite image shows the evolution of X-ray emission from the corona over the solar cycle. At solar maximum, the emission is brightest (*front*) and it decreases and becomes more diffuse at solar minimum (*back*). Figure courtesy of ISAS, Japan.

1.2.2 Measuring the Solar Magnetic Field

Magnetic flux, Φ, is a measure of the amount of magnetic field passing through a given surface and is measured in the c.g.s. units of Maxwells (Mx) (1 Mx = 10^{-8} Weber). The magnetic field, B, is measured in the c.g.s. units of Gauss (G) (1 G = 10^{-4} T). In a magnetic field of strength one Gauss, one Maxwell is the total flux across a surface of one square cm perpendicular to the field (1 Mx = 1 G cm^2).

The magnetic field strength on the Sun ranges from 10 - 100 G, but the solar magnetic field extends well beyond the Sun itself and is carried into space by the solar wind, forming the interplanetary magnetic field (IMF). The magnetic field strength of the IMF is significantly smaller than that at the Sun and measures 7 x

10^{-5} G at 1 AU. Comparatively, the magnetic field strength at Earth is 0.3 - 0.6 G.

The magnetic field of the Sun at the photosphere can be deduced from the Zeeman splitting of Fraunhofer spectral lines, but this is only successful if the magnetic field is strong. Under the influence of a magnetic field a spectral line can be split into several spectral lines with slightly different frequencies. The Zeeman triplet is comprised of two shifted σ components and the unshifted π component. An electron orbiting an atom is equivalent to a current which induces a magnetic field. When an external magnetic field is applied, it exerts a torque on the magnetic field of the electron, which depends on the alignment (θ) between the electron's magnetic field and the external magnetic field. The electron acquires an additional potential energy, which may be positive, zero, or negative, depending on the angle θ. The stronger the external magnetic field, the greater the added or subtracted potential energy. As a result, there are two σ components of the spectral line, displaced to either side of the unperturbed central component π.

The shift in the wavelength of the two σ components from the central wavelength is given by

$$\delta\lambda = \frac{\pi e}{M_e}\frac{\lambda^2 gB}{c} = 4.7 \times 10^{-13}\lambda^2 gB \tag{1.9}$$

where the factor ($\pi e/M_e c = 4.7 \times 10^{-13}$) is a standard constant. Magnetic field strengths between 100 - 200 G can be measured by this method.

The Zeeman effect is longitudinal when the magnetic field is parallel to the line-of-sight direction, When this is the case, the undisplaced line disappears and only the σ components are present, which are circularly polarised in the opposite sense. When the magnetic field is perpendicular to the line-of-sight direction then the Zeeman effect is transverse and all three components of the spectral line are seen. The undisplaced component, π is linearly polarised perpendicular to the magnetic field, while the σ components are linearly polarised parallel to the magnetic field. The above is valid for absorption lines, but in the case of emission lines the sense of circular polarisation is reversed, as are "parallel" and "perpendicular". Babcock developed the magnetograph in 1952, which utilises the circular polarisation of the Zeeman components of the spectral lines, and allows the measurement of magnetic fluxes in active regions and also quiet Sun regions. Magnetograms are currently available from both ground-based and space-based observatories.

At present, magnetic measurements made of the Sun using this method are typically of the photospheric magnetic field, due to the limitations of currently available

technology. The Zeeman effect increases as λ^2, meaning that as the temperature increases, spectral lines broaden, and it may be possible to measure the coronal magnetic field using infrared coronal lines. However this has not yet been achieved.

1.2.3 Structure of the Coronal Magnetic Field

There are three major components of the corona that make up its magnetic field; active regions, coronal holes and the quiet Sun.

1.2.3.1 Active regions

Active regions are concentrated regions of solar activity and are located in regions of enhanced magnetic flux density. They are visible as sunspot groups in optical wavelengths, whilst in EUV and X-ray wavelengths they are characterised by bright emission from hot, dense coronal loops structures, as shown in Figure 1.7 (*upper left*). The magnetic field of active regions is often bipolar in nature, which means they are mainly made up of closed magnetic field lines.

Following the initial emergence of flux in an active region, the structure may persist for days, weeks or months, depending on the amount of magnetic flux in the region, during which time further flux emergence, flux cancellation, magnetic reconfigurations and magnetic reconnection processes may take place. The extremely dynamic nature of active regions results in plasma heating, flares and coronal mass ejections. Active regions are typically confined to an activity belt on the Sun, which lies at latitudes of $\pm$ 40°.

1.2.3.2 Coronal holes

Coronal holes are identified on the Sun as large areas of decreased emission evident in X-ray and EUV observations. The magnetic field in a coronal hole is often described as "open" because it appears to an observer that the magnetic field is connected to the Sun only at one end, extending into interplanetary space. In fact, far out in the heliosphere, this "open" field forms the interplanetary magnetic field. Coronal holes appear darker than surrounding regions because heated plasma is readily evacuated along the open field lines and escapes into interplanetary space. Consequently coronal holes are depleted of plasma most of the time and the density in these regions is $\sim 10^7$ - 10^8 cm^{-3}. The continuous outflow of plasma from coronal

holes makes up the fast component of the solar wind, which travels at speeds in excess of 700 km s^{-1}.

At solar minimum, coronal holes are large and prominent features, forming near the solar poles, like that shown in Figure 1.7 (*bottom left*). However during solar maximum not only are they smaller and more complex, but they can form anywhere and often extend down to the equator. Whilst coronal holes are predominantly monopolar magnetic field regions, they are interspersed with diffuse patches of opposite polarity field. Mixed magnetic field, most evidently in the form of small bipoles, also occurs within coronal holes.

1.2.3.3 Quiet sun

The majority of the Sun is not dominated by active regions or coronal holes, but by regions historically referred to as the *quiet* Sun. Today, however, it is known that many small-scale dynamic processes are taking place all over the Sun, and in fact the quiet Sun is comprised of both small-scale phenomena, such as network heating events, nanoflares, explosive events, bright points and soft X-ray jets and large-scale structures, such as trans-equatorial coronal loops and coronal arches. Figure 1.7 (*right*) shows the quiet Sun observed in EUV. Despite their small scale, features like bright points are clearly evident even in full disk images of the Sun.

The quiet Sun is characterised by mixed polarity "salt and pepper" magnetic field. This description derives from magnetogram images, which are essentially magnetic maps of the Sun, in which black regions denote "negative" magnetic flux that is directed into the Sun and white regions denote "positive" magnetic flux that is directed out of the Sun. The quiet Sun is brighter than coronal holes because heated plasma upflowing from the chromosphere remains trapped until it cools down and precipitates back to the chromosphere. A modern definition of the quiet Sun is that it encompasses all closed magnetic field regions, excluding active regions.

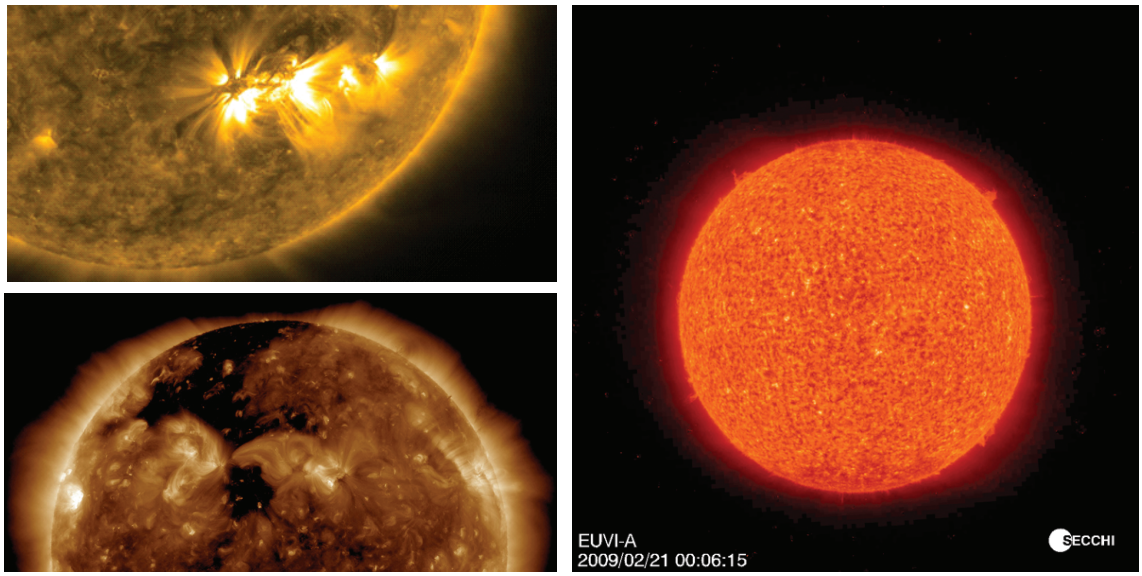

Figure 1.7: Hot, dense loops indicative of the closed magnetic field lines within an active region observed by SDO/AIA in the extreme ultraviolet wavelength 171 Å (*top left*). A dark coronal hole extends from the top of the Sun to almost halfway down observed on 27 May 2010 by SDO/AIA at the extreme ultraviolet wavelength 193 Å (*bottom left*). Coronal holes are magnetically open areas from which high speed solar wind streams into space. The quiet Sun observed at the extreme ultraviolet wavelength 304 Å by STEREO/SECCHI, in which small-scale features like bright points are observed (*right*).

1.3 Magnetohydrodynamics

Magnetohydrodynamics (MHD) is a branch of continuum mechanics, which studies the flow of electrically conducting fluid in the presence of an electromagnetic field. In the simplest case, the plasma is treated as a single conducting fluid. The root of MHD lies in magnetic fields inducing currents in a moving conductive fluid, which creates forces on the fluid, and also changes the magnetic field itself. Mutual interaction of fluid flow, v and magnetic field, B gives rise to the Lorentz force, $j \times B$, which accelerates the fluid, while the electromotive force, $v \times B$, creates a current which modifies the electric field. MHD helps us to understand many aspects of solar-heliospheric physics, since the Sun and interplanetary medium are primarily made up of plasma.

The set of equations which describe MHD are a combination of the Navier-Stokes equations of fluid dynamics, since the average properties of the plasma are governed by the basic conservation laws for mass, momentum and energy, and Maxwell's equations of electromagnetism, since electric and magnetic fields and currents are always important in plasmas, and so their effects must be included. These equations may be manipulated to tell us much about the solar plasma conditions. Combining simplified Maxwell's equations and Ohm's law, Alfvén's Frozen Flux theorem may be derived and an idea of the degree of coupling between the plasma flow in a region and the ambient magnetic field may be obtained from the magnetic Reynold's number, R_M, which is described in § 1.3.5. In § 1.3.6, we obtain expressions for the Alfvén velocity, the pressure scale height and the forces exerted by magnetic pressure and magnetic tension. A quantity known as plasma β is introduced and the conditions for a force-free magnetic field are described.

Ideal MHD assumes that the fluid has so little resistivity that it can be treated as a perfect conductor, and ideal processes can convert magnetic energy to kinetic energy without magnetic dissipation. Non-ideal (resistive) MHD, in which magnetic dissipation is finite leads to the reconnection of colliding magnetic field lines (see magnetic reconnection, § 1.3.7). Non-ideal processes can convert magnetic energy into both kinetic energy and heat.

1.3.1 Description of a Plasma

A plasma is a quasi-neutral gas that is comprised of equal numbers of positively and negatively charged particles, which may be subject to electric, magnetic and other forces. Plasmas exhibit collective behaviour. There are three important criterion

which must be satisfied if an ionised gas is to be considered a plasma:

1. Shielding and Quasi-neutrality

   A plasma can be divided up into a number of volume elements, the dimensions of which are small compared to typical length scales, L, over which variations are observed in the macroscopic properties of the plasma, but are large compared to the size of the particles. Each fluid element must be large enough, so that any charge concentrations that arise will be shielded within the fluid volume element. The Debye length, λ_D, describes the distance over which a balance is obtained between the thermal particle energy and the electrostatic potential energy arising from any charge separation. The quasi-neutrality condition, which a plasma must obey can be expressed as:

$$L \gg \lambda_D \tag{1.10}$$

2. The "Plasma Parameter"

   Another condition that must be satisfied before collective behaviour can occur is that there should be enough charged particles around a specific charge concentration to shield it. A Debye sphere is a spherical volume of radius the Debye length. The number of particles within the sphere is N_D. The criterion that must be met for collective shielding to occur can be expressed as:

$$N_D \gg 1 \tag{1.11}$$

3. Collision criterion

   A plasma can coexist within a neutral gas, but it is necessary that the density of neutral particles is not so high that collisions with neutrals interfere with charged particle motions to an extent that prevents collective behaviour. The plasma frequency, ω_p, describes the oscillations about an equilibrium position if the electrons are displaced relative to the ions and is a useful parameter for characterising the time-scale on which electrons move to correct a charge imbalance in the plasma.

   For a plasma to continue to maintain collective behaviour, the frequency of collisions with neutrals must be much less than that of plasma oscillations. In terms of a period, τ_n, between collisions with neutrals, this condition can be expressed as:

$$\omega_p \cdot \tau_n \gg 1 \tag{1.12}$$

1.3.2 Fluid Equations

1.3.2.1 The equation of mass continuity

The mass continuity equation describes the relationship between the plasma density, ρ and the fluid velocity, $\mathbf{v}$.

$$\frac{\partial \rho}{\partial t} + \nabla \cdot (\rho \mathbf{v}) = 0 \tag{1.13}$$

where ρ is the mass density, $\mathbf{v}$ is the flow velocity, t is time.

The density in a region increases if mass flows into the region with velocity, $\mathbf{v}$ and decreases if the opposite is true and the mass in the region diverges. In both of these cases, mass flux is conserved during the motion of the plasma.

Equation 1.13 can be expanded and written as:

$$\frac{\partial \rho}{\partial t} + (\mathbf{v} \cdot \nabla) n + n (\nabla \cdot \mathbf{v}) = 0 \tag{1.14}$$

1.3.2.2 The equation of motion

The equation of motion describes the conservation of momentum. It relates the fluid velocity, $\mathbf{v}$ to density ρ and to the electromagnetic Lorentz force acting on the fluid element.

$$\rho \frac{\partial \mathbf{v}}{\partial t} + \rho (\mathbf{v} \cdot \nabla) \mathbf{v} = -\nabla p + \mathbf{j} \times \mathbf{B} + q\mathbf{E} + \rho \mathbf{g} + \mathbf{F} \tag{1.15}$$

where - ∇p is the plasma pressure gradient, $\mathbf{j}$ is the current density, $\mathbf{B}$ is the magnetic induction, $\mathbf{j} \times \mathbf{B}$ is the Lorentz force per unit volume, q is the charge density, $\mathbf{E}$ is the electric field strength, $\rho \mathbf{g}$ is the gravitational force and $\mathbf{F}$ indicates additional forces, like the effect of viscosity.

The presence of the Lorentz force in the equation of motion accelerates the fluid and couples the fluid equations to the electromagnetic equations.

1.3.2.3 The energy equation

The energy equation expresses that the heat increases or decreases as the net effect of energy sources and sinks, as the plasma moves in space. It may be expressed as:

$$\frac{\partial p}{\partial t} + \mathbf{v} \cdot \nabla p + \gamma p \nabla \cdot \mathbf{v} = E_l \tag{1.16}$$

where E_l is the total energy loss function and γ is the ratio of specific heat at constant pressure to specific heat at constant volume (normally taken as 5/3). Energy loss can result from e.g. radiative cooling, conduction and energy gain may be the result of e.g. MHD wave dissipation, joule heating, heating due to friction.

The **equation of state** for a plasma that behaves as an ideal gas relates pressure, P and temperature, T.

$$p = R\rho T = nk_B T \tag{1.17}$$

where R is the universal gas constant (8.3×10^3 m^2 s^{-2} deg^{-1}), n is the total number of particles per unit volume, and k_B is Boltzmann's constant (1.381×10^{-23} J deg^{-1}).

To be complete, the fluid equations require an appropriate equation for the pressure tensor components. Assuming that the plasma behaves like an ideal gas, this pressure equation can be the ideal gas equation, relating pressure, p to the plasma temperature, T and density, ρ.

1.3.3 Electromagnetic Equations

1.3.3.1 Maxwell's equations

- Poisson's equation (also known as Gauss' law for E), implying charge conservation:

$$\nabla \cdot \mathbf{E} = \frac{\rho_e}{\epsilon} \tag{1.18}$$

  where ρ_e is the charge density and ϵ is the permittivity of free space.

- Faraday's law:

$$\nabla \times \mathbf{E} = -\frac{\partial \mathbf{B}}{\partial t} \tag{1.19}$$

where **E** is the electric field, **B** is the magnetic field and t is time.

Faraday's law means that time-varying magnetic fields may give rise to electric fields.

- Gauss' law for B:

$$\nabla \cdot \mathbf{B} = 0 \tag{1.20}$$

Equation 1.20 means that there are no magnetic sources or monopoles.

- Ampère's law:

$$\nabla \times \mathbf{B} = \mu_0 \mathbf{j} + \frac{1}{c^2} \frac{\partial \mathbf{E}}{\partial t} \tag{1.21}$$

where c is the speed of light in a vacuum (3×10^8 m s^{-1}) and $\partial \mathbf{E}/\partial t$ is the displacement current. Equation 1.21 means that either currents or time-varying electric fields may produce magnetic fields.

1.3.3.2 Ohm's law

A simplified Ohm's law is assumed in this thesis:

$$\mathbf{j} = \sigma(\mathbf{E} + \mathbf{v} \times \mathbf{B}) \tag{1.22}$$

since plasma moving with a velocity, **v** across a magnetic field is subject to an electric field described by $\mathbf{v} \times \mathbf{B}$. σ is the electrical conductivity, assumed constant. This form of Ohm's law couples the electromagnetic equations to the plasma fluid equations through **v**, the plasma velocity.

1.3.4 The MHD Approximation

The fundamental equations (given below) use the following assumptions (Priest, 1982; Attrill, 2008b):

- Quasi-neutrality of the plasma is assumed, so local electric charge densities are neglected since $\rho_{electrons} = \rho_{ions}$. As a result, the concept of charge conservation is irrelevant. In this case, $qE \rightarrow 0$ under the MHD approximation and Poisson's equation (Equation 1.18) becomes $\nabla \cdot \mathbf{E} = 0$.
- An inertial (not accelerating or rotating) frame of reference is used.
- The plasma is treated as a single fluid system. This assumes that both electrons and ions are collision-dominated so that a given particle remains reasonably close

to its neighbours during timescales of interest. Then, the plasma may be divided into small, identifiable fluid elements. The characteristic length scale is greater than internal plasma lengths (e.g. ion gyroradius and the mean free path length).
- The characteristic timescale is greater than internal plasma timescales (e.g. ion gyrofrequency and mean free path time). The plasma is therefore assumed to be in thermodynamic equilibrium with distribution functions close to Maxwellian.
- In solar physics, the bulk plasma flow speed, sound speed and Alfvén speed are assumed to be much less than c, so relativistic effects can be ignored. As a result, the displacement current in Ampére's law (Equation 1.21) is neglected.
- μ and ϵ are assumed to be constant and (for solar plasmas) have the vacuum values $\mu_0 = 4\pi \times 10^{-7}$ H m^{-1} and $\epsilon_0 = 8.854 \times 10^{-12}$ F m^{-1}.

These assumptions result in the fundamental MHD equations:

$$\frac{\partial \rho}{\partial t} + \nabla \cdot (\rho \mathbf{v}) = 0 \tag{1.23}$$

$$\rho \frac{\partial \mathbf{v}}{\partial t} + \rho \left(\mathbf{v} \cdot \nabla \right) \mathbf{v} = -\nabla p + \mathbf{j} \times \mathbf{B} + q\mathbf{E} + \rho \mathbf{g} + \mathbf{F} \tag{1.24}$$

$$\frac{\partial p}{\partial t} + \mathbf{v} \cdot \nabla p + \gamma p \nabla \cdot \mathbf{v} = E_l \tag{1.25}$$

$$p = R\rho T = nk_B T \tag{1.26}$$

$$\nabla \cdot \mathbf{E} = 0 \tag{1.27}$$

$$\nabla \times \mathbf{E} = -\frac{\partial \mathbf{B}}{\partial t} \tag{1.28}$$

$$\nabla \cdot \mathbf{B} = 0 \tag{1.29}$$

$$\nabla \times \mathbf{B} = \mu_0 j \tag{1.30}$$

$$\mathbf{j} = \sigma(\mathbf{E} + \mathbf{v} \times \mathbf{B}) \tag{1.31}$$

In the *ideal* MHD approximation, the electrical conductivity of the gas σ, is assumed to be extremely high, so that it can be treated as a perfect conductor. Therefore ideal MHD describes the interaction of inviscid fluids of low electrical resistivity with magnetic and gravitational fields.

Further simplifications to the MHD approximation may be made, including:

- The plasma is assumed to be incompressible so that the density does not change with time and Equation 1.23 reduces to $\nabla \cdot \mathbf{v} = 0$.
- The plasma is assumed to be inviscid, so viscous forces can be neglected and the equation of motion (Equation 1.24) is simplified.
- The system is assumed to vary adiabatically, without energy loss, so the energy equation (Equation 1.25) is simplified.

1.3.5 The MHD Induction Equation

A combination of Maxwell's equations and a simplified Ohm's law leads to the induction equation, which eliminates the electric field and relates $\mathbf{v}$ to $\mathbf{B}$. This ultimately leads to the derivation of Alfvén's Frozen Flux theorem.

Combining Ampère's law $\nabla \times \mathbf{B} = \mu_0 \mathbf{j}$ and Ohm's law in the frame moving with the plasma, $\mathbf{j} = \sigma\left(\mathbf{E} + \mathbf{v} \times \mathbf{B}\right)$, we obtain:

$$\nabla \times \mathbf{B} = \mu_0 \sigma(\mathbf{E} + \mathbf{v} \times \mathbf{B}) \tag{1.32}$$

Taking the curl of this, using Faraday's Law and supposing that σ = constant, then:

$$\nabla \times (\nabla \times \mathbf{B}) = \mu_0 \sigma \left(-\frac{\partial \mathbf{B}}{\partial t} + \nabla \times (\mathbf{v} \times \mathbf{B}) \right) \tag{1.33}$$

Introducing the ohmic magnetic diffusivity:

$$\eta = \frac{1}{\mu_0 \sigma} \tag{1.34}$$

and using the vector triple product identity:

$$\nabla \times (\nabla \times \mathbf{B}) = \nabla(\nabla \cdot \mathbf{B}) - \nabla^2 \mathbf{B} = -\nabla^2 \mathbf{B} \tag{1.35}$$

thus, we obtain the MHD induction equation:

$$\frac{\partial \mathbf{B}}{\partial t} = \nabla \times (\mathbf{v} \times \mathbf{B}) + \eta \nabla^2 \mathbf{B} \tag{1.36}$$

The MHD induction equation expresses that changes in the local magnetic field can be due to advection (plasma motion) and/or diffusion.

1.3.5.1 The magnetic Reynolds number

Dividing the magnitude of the advection term by that of the diffusive term of the induction equation yields the magnetic Reynolds number:

$$R_m = \frac{\nabla \times (\mathbf{v} \times \mathbf{B})}{\eta \nabla^2 \mathbf{B}} = \frac{vB/l}{\eta B/l^2} = \frac{vl}{\eta} = \mu_0 \sigma v l \tag{1.37}$$

where v and l are characteristic values for velocity and length, μ_0 is the magnetic permeability and σ is the electric conductivity.

In the solar corona, where $T \sim 10^6$ K, $\eta \sim 1\ m^2 s^1$, $l = 10^5$ m and $v \sim 10^4$ m s^{-1}, the magnetic Reynolds number is $R_m \sim 10^9$. This means that the diffusive term is negligible compared to the advection term.

If $R_m \ll 1$, the temporal evolution of the field is dominated by the diffusion term. The characteristic time-scale for such Ohmic diffusion is:

$$t_d \equiv \frac{l^2}{\eta} = \frac{l}{v} R_m \tag{1.38}$$

The time taken for the magnetic field of the Sun to diffuse is approximately 10^{10} years.

If $\mathrm{R}_m \gg 1$, the induction equation becomes:

$$\frac{\partial \mathbf{B}}{\partial t} = \nabla \times (\mathbf{v} \times \mathbf{B}) + \eta \nabla^2 \mathbf{B} \rightarrow \frac{\partial \mathbf{B}}{\partial t} = \nabla \times (\mathbf{v} \times \mathbf{B}) \tag{1.39}$$

For such an ideal fluid, Ohm's law is $E + \mathbf{v} \times \mathbf{B} = 0$.

In the solar corona, where the advection term dominates, the plasma and magnetic field are constrained to move together. This result is known as Alfvén's Frozen Flux theorem, since he showed that in such cases field lines move as though they are "frozen" into the fluid. When this is the case, plasma is still able to flow parallel to the field along the field lines, but there is virtually no perpendicular motion of the plasma relative to the magnetic field. Magnetic field lines and flux tubes may be pictured as strings and rubber tubes that are transported and may be deformed by plasma flows.

1.3.6 Applications of the MHD Equations

The equations of MHD can be used to investigate many aspects of the solar conditions.

The left hand side of the equation of motion (Equation 1.15) represents the net change of the momentum density of a fluid element. While the terms on the right hand side of equation 1.15 represent the density of the forces acting on the fluid element. The following solar conditions may be derived through manipulation of the equation of motion:

1. Alfvén speed

   The Alfvén speed, v_A, is the speed at which magnetic disturbances travel along the field. v_A is determined by equating the left hand side of the equation of motion with the magnetic force, while neglecting velocity variations with respect to time:

   $$v_A = \frac{B}{(\mu_0 \rho)^{1/2}} \tag{1.40}$$

   where μ_0 is the magnetic permeability.

   The Alfvén velocity, v_A, in the quiet Sun regions of the low corona is typically ~ 700 km s^{-1}.

2. Pressure scale height

Equating the magnitudes of the first and fourth terms on the right hand side of the equation of motion with the ideal gas law gives a length scale:

$$L = \frac{RT}{g} \equiv H \tag{1.41}$$

where H is the scale height for the fall-off of the pressure with height.

In the corona, H is 50,000 km, while the scale height is much smaller in the chromosphere, at only 500 km.

3. Pressure force and magnetic tension force

   In the momentum equation, the $\mathbf{j} \times \mathbf{B}$ term describes the magnetic force (Lorentz force). Using Ampère's law, we find that:

$$\mathbf{j} \times \mathbf{B} = \frac{1}{\mu_0}(\nabla \times \mathbf{B}) \times \mathbf{B} = -\nabla \left(\frac{B^2}{2\mu_0} \right) + \frac{(\mathbf{B} \cdot \nabla)\mathbf{B}}{\mu_0} \tag{1.42}$$

   where the first term on the right hand side describes the gradient of the isotropic magnetic pressure (pressure force) and the second term on the right hand side is the force arising from the magnetic tension (magnetic tension force). If the field lines are not straight, but have a radius of curvature R, their tension B^2/μ_0 exerts a transverse force $B^2/(\mu_0 R)$ per unit volume. A net force is exerted on the plasma if the stress arising from the curvature is not balanced by the magnetic pressure, however there is no net force along the magnetic field $\mathbf{B}$.

4. Plasma β parameter

   The magnitude of the plasma pressure, p and the magnetic pressure, $B^2/2\mu_0$ are compared in the plasma β parameter, which is defined as:

$$\beta = \frac{\text{plasma pressure}}{\text{magnetic pressure}} = \frac{2\mu_0 p}{B^2} \tag{1.43}$$

   Below the photosphere $\beta \geq 1$, thus gas pressure dominates and the magnetic field is moved around by the convective motion of the plasma in this region. Above the photosphere $\beta \ll 1$, thus magnetic pressure is the dominant influence.

   A plasma is described as a low-β plasma when $\beta \ll 1$ and a high-β plasma when $\beta \geq 1$.

5. Force-free magnetic field conditions

   In force-free fields, the current j runs parallel to $\mathbf{B}$, so $\nabla \times \mathbf{B} = \alpha \mathbf{B}$, where α is a scalar function of position. This is a force-free field equation, where α is constant along a given field line.

In the particular case where α is independent on the field line i.e. it is uniform in space, we have linear or constant-α force free fields. The solutions are well understood and widely used in magnetic extrapolations. The particular case $\alpha = 0$ gives potential field, which is current-free. The potential field has the smallest energy of all the fields in a finite volume with a given B_n (the normal component of B) on the boundary.

1.3.7 Magnetic Reconnection

Magnetic reconnection occurs when oppositely directed magnetic field lines approach each other and interact, such that they appear to "break" and merge, resulting in a change in the connectivity of plasma elements in a magnetic field. Reconnection occurs when the conditions for frozen-in flux break down and the diffusion term in the induction equation becomes more important than plasma motion. This results in a change in the topology of the magnetic field and the conversion of magnetic energy into kinetic energy and heat.

The frozen-in flux approximation when the magnetic Reynolds number is high describes how plasma can only mix along flux tubes and not across them. Two distinctly different plasma regimes cannot diffuse into one another, and this leads to the separation of different plasma regimes in space through the formation of thin current sheets, which act as boundaries between these different regions (e.g. the solar wind and a planetary magnetosphere). A current sheet is a thin current-carrying layer across which the magnetic field changes in direction or magnitude, or both. In equilibrium, there is a total pressure balance between the current sheet and its surroundings on both sides.

1.3.7.1 The Sweet-Parker reconnection model

Sweet (1958) and Parker (1957) considered a process in which oppositely directly field lines are convected by a flow towards a thin current sheet, which is assumed to be much longer than it is wide. Within such a small-scale length current sheet, the field is no longer frozen into the plasma since the magnetic Reynolds number within these regions is very small. Here, diffusion of the magnetic field through the plasma becomes important. If oppositely oriented field lines from opposing sides of the current sheet are continually convected into this diffusion region and there is a strong magnetic field gradient across the current sheet, then these field lines can "merge". The resulting "reconnected" field lines are sharply bent through the current sheet. The inflowing plasma and reconnected field lines are accelerated

by magnetic tension forces, acting to straighten these kinked field lines, and are expelled from the ends of the current sheet with outflow speeds of the order of the Alfvén velocity, forming two oppositely directed exhaust jets. This process allows the plasma from either side of the current sheet boundary to "mix" as it flows along the newly formed "merged" field lines. Magnetic energy is released during the process of magnetic reconnection, resulting in accelerated and heated plasma flows.

The speed of the inflowing plasma and magnetic field is related to the Alfvén speed in the outflowing regions and the magnetic diffusivity and length of the current sheet. Assuming that mass flux is conserved and that the speed of the inflow is equal to the diffusion speed, which indicates that reconnection is proceeding in a steady state, then:

$$v_i^2 = \eta \frac{v_A}{L} \tag{1.44}$$

where v_i is the speed of the inflow, η is the magnetic diffusivity, v_A is the Alfvén speed (speed of the outflow) and L is the length of the current sheet.

This may also be expressed in a dimensionless form:

$$M = \frac{1}{R_m^{1/2}} \tag{1.45}$$

where $M = v/v_A$ is the reconnection rate, defined as the Alfvén Mach number and R_m is the magnetic Reynolds number in terms of the Alfvén speed.

For typical coronal conditions, where the magnetic Reynolds number is very large, the Sweet-Parker mechanism yields a reconnection rate of 10^{-4} - 10^{-6}. Considering only 2 dimensions, the rate of reconnection is the rate at which field lines move through the X-type neutral point, so named for the geometry of the region. The length of the current sheet in this model is comparable to the global length scale of a flaring region (10^5 km) and yields a time-scale for magnetic dissipation of $\approx 10^6$ years. However, a solar flare releases stored energies of 10^{28} - 10^{32} ergs into the corona within a typical duration of only $\sim$ 100 s, which implies much larger dissipation rates than obtained with the Sweet-Parker current sheet. So, while the reconnection rate obtained is faster than simple diffusion, it is still far too slow to explain the observed solar eruptive phenomena.

1.3.7.2 The Petschek reconnection model

There are two main approaches applied in the theory to achieve fast reconnection. The first is to find a mechanism to create a high resistivity, which allows rapid dissipation. The other approach is to reduce the size of the diffusion region, effectively reducing the dissipative scale length. It is this second approach that was adopted by Petschek (1964).

Based upon the principle mechanism of the Sweet-Parker reconnection model, Petschek (1964) proposed a much faster model, which involves reducing the size of the diffusion area so that the length of the current sheet, L is comparable with its width, l ($L \equiv l$). In this scenario, a smaller fraction of the plasma flows through the diffusion region and slow-mode shocks arise where the abrupt change in the flow speed occurs. The shock waves represent an obstacle in the flow and are thus the main sites where inflowing magnetic energy is converted to heat and kinetic energy, accelerating the outflow and resulting in very different values of $\mathbf{v}$ and $\mathbf{B}$ at large distances, compared to their values at the input to the reconnection region.

By assuming a magnetic potential field in the inflow region, Petschek (1964) estimated the maximum outflow speed and found that the field strength scales logarithmically with distance:

$$\mathbf{B_0}\,(L_e) = B_0[1 - \frac{4M}{\pi} \ln\left(\frac{L_e}{\Delta}\right)] \tag{1.46}$$

where $\mathbf{B}_0$ is the external magnetic field, L_e is the distance from the diffusion region and M is the maximum reconnection rate.

Petschek (1964) also estimated the maximum reconnection rate, M at a distance, L_e, where the internal magnetic field is half of the external value, as:

$$M = \frac{\pi}{8 log R_m} \tag{1.47}$$

This results in a reconnection rate of $\sim$ 0.01 - 0.02, for solar coronal conditions, where the magnetic Reynolds number is high. This is the fastest reconnection rate possible with the Petschek mechanism, and is about three orders of magnitude faster than the Sweet-Parker rate.

Petschek's model was the first of the "fast reconnection" models. Since then, a new generation of more general almost-uniform and non-uniform models have been

developed, which include the Petschek mechanism as a special case.

The rate at which magnetic reconnection progresses is largely dependent on the following characteristic speeds:

1. The external flow speed at a given distance from the diffusion region;
2. The Alfvén speed in terms of the external magnetic field;
3. The global magnetic diffusion speed.

Comparing the Alfvén Mach number, which compares the external flow speed with the Alfvén velocity, and the magnetic Reynolds number, enables the rate at which reconnection progresses to be classified, as follows:

- Super-slow:
$$M \leq \frac{1}{R_m} \tag{1.48}$$
The advection term in Ohm's law is negligible and diffusion of the magnetic field completely dominates, as it does in a solid conductor. This simple diffusion is slow in space plasmas. Linear reconnection belongs to this category (Priest *et al.*, 1994)

- Slow:
$$\frac{1}{R_m} < M \leq \frac{1}{\sqrt{R_m}} \tag{1.49}$$
When the rate of reconnection exceeds the threshold, $1/R_m$, the advection term in Ohm's law becomes important and diffusion of the magnetic field, less so. The Sweet-Parker reconnection model belongs to this category (Sweet, 1958; Parker, 1957, 1963).

- Fast:
$$M > \frac{1}{\sqrt{R_m}} \tag{1.50}$$
Even when the magnetic Reynolds number is high, as is the case in the solar corona, the reconnection rate is in the range 0.01 - 0.1. Petschek's reconnection model belongs to this category ($M \sim \frac{1}{(logR_m)}$) (Petschek, 1964).

Fast reconnection mechanisms are key to explaining the short time-scales over which energy is released in explosive solar phenomena, where the magnetic Reynolds number is very large (10^6 - 10^{12}). However, even slow reconnection can become applicable when R_m is reduced by kinetic effects or turbulence.

1.3.7.3 3-D magnetic reconnection

Magnetic reconnection models like that of Sweet-Parker and Petschek are purely 2-dimensional and the reality can often be better approximated by magnetic 3-D topologies, of which a wider variety exist, although they are understandably more complex. In the 2-D picture, magnetic reconnection proceeds at an X-type neutral point, so named for the geometry of the visualised magnetic configuration, and the corresponding neutral region in a 3-D volume is termed a magnetic null point. In regions where multiple magnetic dipoles occur, each dipolar domain is separated by separatrix surfaces in 3-D space. Interactions of 2-D separatrix surfaces result in the formation of 1-D separators, and 3D magnetic null points form at locations where separators intersect. Other features of 3-D magnetic configurations include a dome-like separatrix surface, called a fan dome, and a spine curve, which describes the symmetry axis in a unipolar region that is surrounded by opposite polarity magnetic flux.

It is not possible for these 3-D topologies to become infinitely complex, since at some point magnetic stresses will disrupt highly sheared structures and the neighbouring field lines will reconnect to a simpler topology. Magnetic reconnection can occur when field lines are stressed or pushed towards a 3-D separatrix layer, a fan surface, a spine, or a separator. Here, they experience high plasma β near the region where the magnetic field tends to zero, and oppositely directed magnetic field lines approaching each other from either side of a magnetic null point can reconnect.

1.4 The Dynamic Sun

The Sun is extremely dynamic and one of the features of this is the large-scale explosions that blast vast amounts of plasma and magnetic field into space. These explosions, known as coronal mass ejections (CMEs), and their evolution as they propagate into the heliosphere are the focus of this thesis.

There is overwhelming evidence for magnetic reconnection on the Sun, established from the observations made by numerous spacecraft missions over the last few decades (e.g. Forbes, 2001; Schindler and Hornig, 2001; Ugai, 2001; Hood *et al.*, 2002; Biskamp, 2003; Kliem *et al.*, 2003). This process is believed to be the driving force behind the large-scale eruptive activity observed on the Sun in the form of flares and coronal mass ejections (CMEs). In this section, the key observational evidence for such an assumption and the theoretical efforts made to model the initiation of these phenomena are discussed.

1.4.1 Solar Flares

Initiated in the solar corona, solar flares are dynamic events that are triggered by an instability in the underlying magnetic field configuration, which evolves to a more stable state by altering the magnetic topology of the region through magnetic reconnection (e.g. Tsuneta and Lemen, 1993; Tsuneta, 1996; Shibata, 1995, 1996; McKenzie, 2002). This results in the sudden release of kinetic energy and heat, producing enhancements across the electromagnetic spectrum. Heating, particle acceleration and expulsion of mass are all common features of flares (e.g. Kosugi and Somov, 1998; Aschwanden, 2002).

Flares release a significant amount of energy over very small time-scales, ranging from 10^{16} J in nano-flares to 10^{25} J in large events (e.g Kopp *et al.*, 2005). The energy released must lie in stressed magnetic fields, since no other energy source is sufficient. Not all of the energy in the magnetic field can be released and only energy above the ground (potential) state is available. Thus, flares occur in regions of non-potential field, i.e. where currents or shears are present, which means that they often, but not exclusively, originate in active regions. Flares are often classified by the energy they release, and the most common flare classification scheme in use today is the GOES SXR Classification which categorises flares, as follows: B class (10^{-7} W m^2), C class (10^{-6} W m^2), M class (10^{-5} W m^2), and X class (10^{-4} W m^2). Larger flares have been found to occur more often in active regions whose magnetic field is relatively complex (Foukal, 2004).

Flare evolution occurs in three main phases, which are characterised by the observed emission and termed the pre-flare, impulsive, and the main/gradual phase. During the pre-flare phase, a brightening lasting usually just a few minutes can often be detected in EUV and soft X-ray radiations (Neupert, 1968; Silva *et al.*, 1997; Warren *et al.*, 1999). The highest energy flare emissions reach their peak intensity in all wavelengths during the impulsive phase, and short duration spikes of emission lasting just a few seconds are often seen in microwaves, EUV and hard X-rays during this phase (Hoyng *et al.*, 1981; Kane, 1983), while the duration of the entire impulsive phase is of the order of minutes. On rare occasions, the very brightest flares can even be seen in photospheric white light images (Carrington, 1859; Martinez Oliveros *et al.*, 2011). Following the impulsive phase, Hα and soft X-rays may continue to increase for 10 - 20 mins (Tsuneta *et al.*, 1997b; Shibata, 1999; Sui *et al.*, 2006), before the onset of the gradual phase, in which flare emissions decrease over a time period of several hours. Solar flares are broadly classified into impulsive and long duration events. Long duration events can last for many hours and are generally associated with eruptive behaviour. Large and long duration flares are most commonly associated with CMEs (Sheeley *et al.*, 1975).

The standard 2-D flare model is the most widely accepted model for solar flares and, while it cannot explain all flares, it is able to fit most of the observations. This model is often termed the CSHKP model, from the initials of the five scientists, (Carmichael, 1964; Sturrock, 1966; Hirayama, 1974; Kopp and Pneuman, 1976), upon whose concepts it is based. With the advent of observations from the Yohkoh mission, this model was further developed by Tsuneta (1996, 1997a) and Shibata (1995) and is illustrated in Figure 1.8. In this model, a filament is activated, becomes unstable and begins to rise above the neutral line in an active region. The rising filament stretches a current sheet above the neutral line, which is prone to Sweet-Parker or Petschek reconnection (see § 1.3.7). Footpoint shearing leads to the onset of the tearing-mode instability, triggering a flare near the reconnection X-point. This accelerates particles in a downward direction and produces shock waves and plasmoid ejection in an upward direction. When the reconnection exhaust jet collides with the soft X-ray (SXR) magnetic loops below the X-point, resulting in an MHD fast shock, this produces hard X-ray (HXR) emission above the flare loop tops and leads to further acceleration.

Particles also stream down the legs of the loop, heating the chromospheric footpoints of the newly reconnected field lines. The dense, chromospheric material is heated so rapidly that energy cannot be radiated away and plasma expands to fill the SXR loops, in a process known as chromospheric evaporation. As the reconnection proceeds, more and more field lines reconnect producing an arcade of loops seen in SXR. Once the flare loops cool down by thermal conduction and radiative loss, they also become detectable in EUV. Hot ridges (T $\sim$ 15 - 20 MK) are observed along the separatrices with the slow shock, produced by heated plasma in the reconnection outflows, while the flare footpoints, seen in Hα as ribbons, can be seen to move apart (Svestka, 1976; Martin, 1989). Similar motions are also seen at HXR footpoints. While this model fits a lot of the observational features in hard X-rays, soft X-rays, Hα and radio wavelengths and provides a physical mechanism to explain the processes of filament eruption, magnetic reconnection and coronal mass ejection, it does not specify what drives the initial magnetic system to become unstable.

Building on the original ideas of the standard 2-D solar flare model, there are now many other solar flare models, simulating increasingly complex scenarios (e.g. the equilibrium loss model (Forbes and Priest, 1995), 2-D quadrupolar flare models (e.g. Uchida, 1980; Uchida *et al.*, 1998a,b; Hirose *et al.*, 2001). These models can most often be distinguished from one another by their initial magnetic topologies, which are prone to specific instabilities or drivers.

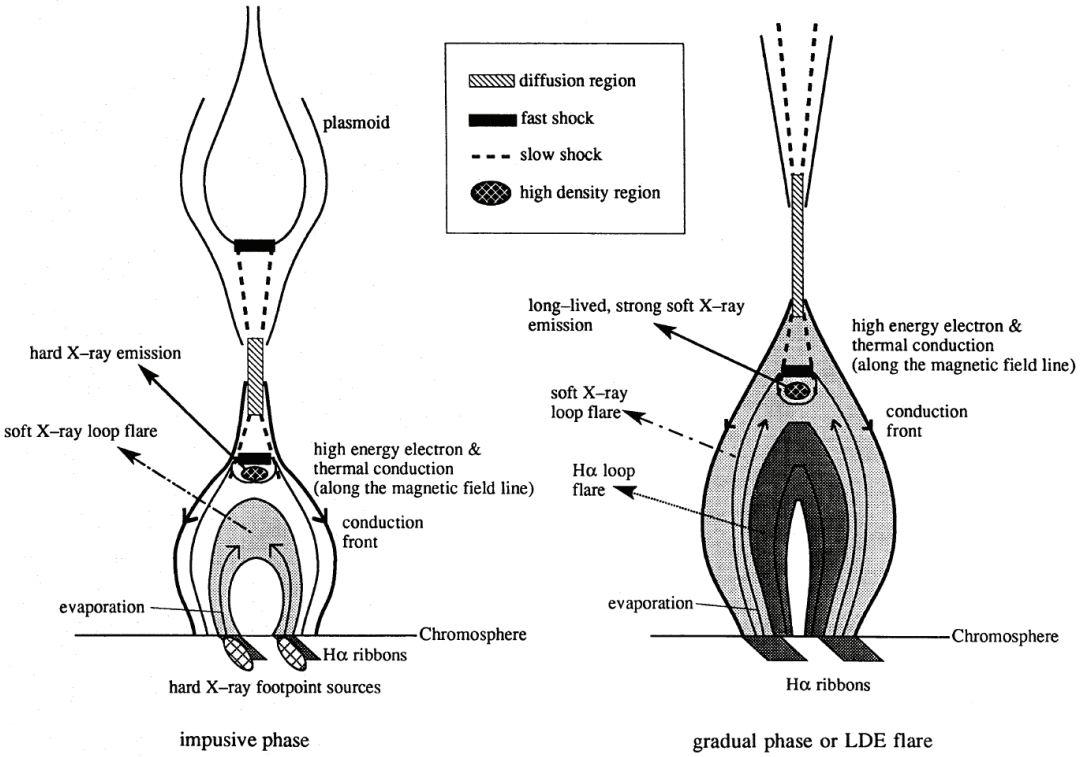

Figure 1.8: The CSHKP model (Carmichael, 1964; Sturrock, 1966; Hirayama, 1974; Kopp and Pneuman, 1976) is a model of solar flares that explains their observable features on the basis of magnetic reconnection. This model explains the features of solar flares observed in Hα, soft X-ray and hard X-ray wavelengths. Figure adapted from Magara *et al.* (1996). Permission to reproduce this figure has been granted by Institute of Physics Publishing.

1.4.2 Coronal Mass Ejections

Like all main sequence stars, the Sun is losing mass through dynamic phenomena in its atmosphere. Aside from the steady solar wind outflow, coronal mass ejections (CMEs) are responsible for the sporadic ejection of plasma and magnetic field into interplanetary space.

Each large-scale CME structure typically expels mass in the region of 10^{14} - 10^{16} kg (1 billion tonnes), with typical speeds ranging from a few km s^{-1} to nearly 3000 km s^{-1} (Gopalswamy *et al.*, 2004), with an average value of 450 km s^{-1}, which is slightly higher than the slow solar wind speed. This corresponds to a mass loss rate of $\sim 2 \times 10^{-14}$ - 2×10^{-12} g cm^{-2} s^{-1}, which is ≤ 1 % of the solar wind mass loss in coronal holes, or ≤ 10 % of the solar wind mass in active regions. Accordingly, the kinetic energy of CMEs with angular width $< 120°$ ranges from $\sim 10^{27}$ erg to $\sim 10^{32}$ erg, with an average value of 5×10^{29} erg. Some very fast and wide CMEs can have kinetic energies exceeding 10^{33} erg, generally originating from large active regions and accompanied by powerful flares (Gopalswamy *et al.*, 2005a). While the energy released in flares is mainly distributed in heating and acceleration of particles, the majority of the energy released in CMEs is kinetic.

The first observed CME was seen with a space-based coronagraph onboard the Seventh Orbiting Solar Observatory (OSO-7) spacecraft in 1971 (Brueckner *et al.*, 1972). Historically, a CME is defined as: "...an observable change in coronal structure that (1) occurs on a time-plasscale of a few minutes up to several hours and (2) involves the appearance and outward motion of a new, discrete, bright, white-light feature in the coronagraph field of view" (Hundhausen *et al.*, 1984; Schwenn, 1996). CMEs are most easily observed remotely in white-light with a coronagraph, in which their enhanced plasma density makes them visible as bright features moving outward from the Sun, and they are characterised by speed, angular width, acceleration, and a central position angle in the sky plane. However, coronagraphs are not the ideal way to determine and study their solar origins since a CME can only be observed from a distance of 0.1 $R_\odot$ above the solar limb and the disk is completely obscured. The solar origins of a CME can be much better identified using on disk measurements in the EUV and X-ray wavelengths, but CMEs are more difficult to identify on disk since their signatures are much more subtle. Following the eruption of a CME, a post-eruption arcade is sometimes observed at the eruption site, with density $\sim 10^{15}$ m^{-3}, temperature $\sim$ 10 MK and magnetic field strength $\sim$ few $\times$ 10^{-4} T. This arcade is observed in X-rays, EUV and Hα. Aside from changes in the active region morphology, on disk signatures of CMEs include loss of material observed as dimmings and waves, but not all of these structures are observed in all CMEs. CMEs can also be observed in radio, allowing their density and speed to be measured.

CMEs occurring close to the disk centre often appear to surround the occulting disk of the coronagraph and are termed "halo" CMEs (Howard *et al.*, 1982). Only 3 % of the CMEs observed by the SOHO spacecraft, located on the Sun-Earth line, are halos, but about 11 % have a width exceeding 120° (e.g. Schwenn *et al.*, 2006). CMEs with apparent widths between 120° and 360° are known as partial halos, while the typical width of a CME is $\sim$ 70°. Halos can be "front-sided" or"back-sided", according to their propagation direction relative to the observer, and for differentiation simultaneous disk observations are required. Some halos are asymmetric, heading predominantly above one limb with weak extensions on the opposite limb. These CMEs generally originate from locations closer to the limb than to disk centre. When front-sided, halo CMEs can directly impact Earth causing geomagnetic storms, provided the magnetic field contained in the CMEs has a southward component (e.g. Gonzalez and Tsurutani, 1987). Figure 1.9 shows white-light coronagraph observations of a CME observed above the solar limb (*left panel*) and a halo CME (*right panel*).

Although there is little observed change in the mass and angular size of CMEs with the solar cycle, the frequency of CMEs appears to be highly cycle dependent,

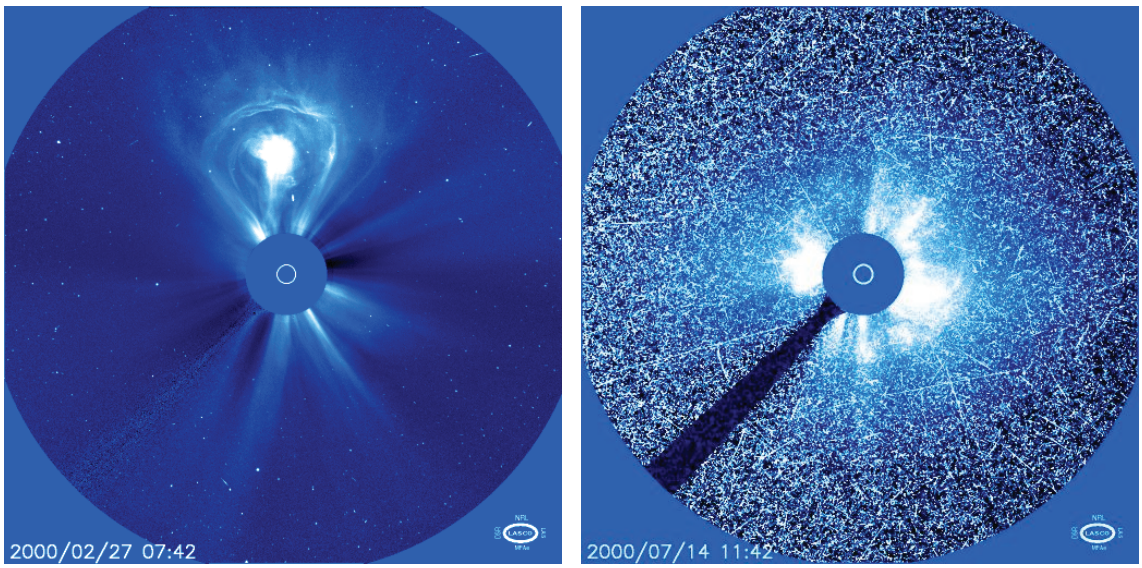

Figure 1.9: A CME erupting near the solar limb (*left*) is observed to have a three-part structure, comprised of a bright front, a lower density cavity and a bright core. When a CME erupts on the solar disk and is directed towards the observer, it is known as a halo CME (*right*). Halo CMEs are more difficult to observe, as they appear to surround the occulting disk. High energy particles directed toward the observing spacecraft may also saturate the detector, creating the "snow" effect seen here. Both of these CMEs are observed in white-light by the C2 coronagraph onboard the SOHO spacecraft. Figure courtesy of NASA.

with the typical CME rate of 0.5/day at solar minimum increasing by an order of magnitude during solar maximum (St. Cyr *et al.*, 2000; Schwenn *et al.*, 2006). There is a weak indication that average speeds are higher at maximum than at minimum, but this is not well established. The central latitude of CMEs also shows some dependence on solar cycle with CMEs mostly centred around the equator at minimum and CMEs observed at all latitudes at maximum. The low-latitude CME rate is generally higher than the high-latitude rate (Howard *et al.*, 1985; St. Cyr *et al.*, 2000), but occasionally they can be very close (Gopalswamy *et al.*, 2003; Schwenn *et al.*, 2006).

The evolution of a CME includes three phases: (1) an initiation phase, (2) an acceleration phase, and (3) a propagation phase (Zhang *et al.*, 2001). The initiation phase is characterised by a slow ascension of certain coronal features (e.g. active region envelopes, filaments) for a period of up to tens of minutes, with a speed typically below tens of km s^{-1}. The major acceleration phase is typically characterised by fast acceleration (e.g. from a few hundred to a few thousand m s^{-2}). The period of continuous acceleration is quite variable: it can last from a few minutes to several hours and the CME, which becomes fully developed during this period, can travel a distance from a fraction of a solar radius to several solar radii. After the completion of the major acceleration phase, a CME travels at a more or less constant speed, a constant angular width and a constant position angle. However, the slowest CMEs have been observed to exhibit minor acceleration, while the fastest CMEs sometimes

exhibit minor deceleration in the outer corona (Gopalswamy *et al.*, 2000a), within only ± 20 m s^{-2} (Moon *et al.*, 2002; Yashiro *et al.*, 2004). This indicates that the major acceleration of a fast CME mainly occurs in the inner corona i.e. below 2 $R_\odot$ and the subsequent evolution is primarily controlled by the interaction between the CME and the medium through which it propagates. This phase is known as the propagation phase, when the ICME is primarily subject to drag forces. The average propagation speed of halo CMEs is 1000 km s^{-1}, more than 2 times the average speed of all CMEs, but this is likely to be an observational effect resulting from the projection of a CME along the line of sight, making it both harder to detect weaker events (Yashiro *et al.*, 2004; Tripathi *et al.*, 2004), and more difficult to accurately determine the radial speed of the ejecta.

Line of sight projection effects make it difficult to infer the geometric shape of CMEs (Burkepile *et al.*, 2004). They are often associated with eruptive prominences at the limb or disappearing filaments on the solar disk, and in these cases CMEs are often commonly observed in white-light as a three-part structure, which is generally attributed to compressed material at the leading edge creating a bright front that surrounds a low-density magnetic bubble, observed as a dark cavity, and an inner bright core formed by dense prominence gas (Hundhausen, 1987). If the CME is super-Alfvénic, it can be expected to drive a shock ahead of it, which is best observed in long wavelength radio emission. The front part of a CME is characterised by elevated electron density ($n_e \sim 10^{14}$ m^{-3}), high coronal temperatures (T $\sim$ 2 MK) and high magnetic field strength (B $\sim 10^{-4}$ T) and is observed in white-light, X-rays and metre wavelengths. While it is sometimes assumed that the leading edge is a compressive wave front, there is little evidence for this except for a few shock wave observations. In many cases the leading edge may just be coronal plasma piled up in front of the CME as is moves outward. The cavity of a CME is a region of lower electron density ($\sim 10^{13}$ m^{-3}), but temperatures are still coronal and the magnetic field increases further to $\sim$ few $\times 10^{-4}$ T. The cavity can be observed in white-light, X-rays and Hα. The prominence core of a CME is the highest density part of a CME (10^{17} m^{-3}), has the lowest temperature (8000 K) and has the highest magnetic field strength (10^{-3} T). It can be observed in microwaves, X-rays, Hα, EUV and at metre wavelengths. Possible interpretations of the observed CME structure include flux ropes, semi-shells, or bubbles.

1.4.2.1 Theoretical models of coronal mass ejections

Theoretical models of CMEs are broadly separated into two categories, those that are directly driven and those based on the concept of the storage and subsequent release of energy (e.g. Klimchuk, 2001). Directly driven models include the *thermal blast*

model (Dryer, 1982; Wu, 1982) which proposes that greatly enhanced gas pressures cannot be contained by the magnetic field, so the corona is literally "blown up" and the *dynamic model* (Klimchuk, 1990; Chen, 1989, 1997; Chen and Shibata, 2000; Krall *et al.*, 2000), in which it is proposed that rapid flux injection as a result of real-time stressing of the magnetic field leads to a sudden increase in magnetic shear, increasing the magnetic pressure and resulting in inflation of the system, resembling a CME. There are significant problems with both of these directly driven models. Hence, the "storage and release" models represent the bulk of the more recent theoretical work on CMEs and are considered the more probable means of CME generation.

Storage and release CME models are characterised by the slow build-up of magnetic stress before an eruption through the shearing/twisting of magnetic footpoints and mass loading in the corona. Three possible storage and release models are summarised, as follows:

1. *Mass Loading Model* (e.g. Low and Smith, 1993; Chou and Charbonneau, 1996; Wolfson and Dlamini, 1997; Guo and Wu, 1998; Low, 1999)

   This scenario is analogous to a spring that is compressed by a heavy weight and explosively uncoils when the weight is shifted to one side.

   During the pre-eruption phase of a CME, a quiescent or eruptive prominence/filament is loaded with coronal material of higher than average density. This extremely dense coronal material is then confined to a small volume to provide adequate compression. Observations of filaments show that they get darker prior to eruption, suggesting that they do increase in density. The concept that prominences play a fundamental role in CME eruption is supported by observations of CMEs occurring co-incident with prominences (Low, 1996, 1999).

   A second concept of mass loading is by a relatively higher electron density distributed over a large volume, which becomes unstable when overlying a volume of lower density. This concept is supported by observations of CMEs from helmet streamers that contain lower density cavities (Hundhausen, 1987, 1999). However, there are also numerous examples in which lower density regions are not observed below a CME.

2. *Tether Release Model* (e.g. Forbes and Isenberg, 1991; Isenberg *et al.*, 1993; Lin *et al.*, 1998; Van Tend and Kuperus, 1978; Van Ballegooijen and Martens, 1989)

This scenario is analogous to tether ropes holding down a compressed spring. As each tether is cut, the tension on the remaining tethers increases until it is so large that they begin to break and the spring uncoils in a catastrophic explosion.

A magnetically dominated configuration involves a force balance between magnetic pressure pushing upward and magnetic tension pulling downwards. A flux rope may be embedded in an arcade field of coronal loops, in which the field lines that provide tension act as tethers and stop the flux rope from rising. As the arcade footpoints are slowly brought together by the converging flow, they meet at the neutral line and reconnect, forming a circular field line disconnected from the photosphere. This process represents the "cutting" of the tethers. So, although the magnetic stress is approximately constant, it becomes distributed over fewer and fewer tethers, and after enough field lines are converted from the arcade to the flux rope, equilibrium is lost and the flux rope rises abruptly; observed as a CME.

A consequence of an eruption occurring like this would be the appearance of an arcade of reconnected loops under the rising flux rope, and this is often observed. However, on many occasions the arcade appears long after the eruption has begun. Also, large-scale CMEs are difficult to explain with this model.

3. *Tether Straining Model* (e.g. Antiochos, 1998; Antiochos *et al.*, 1999; Aulanier *et al.*, 2000; Forbes and Priest, 1995)

The *magnetic breakout model* of Antiochos (1998); Antiochos *et al.* (1999) is one example of a physical model that belongs to the *tether straining* class of CME model.

This scenario is similar to the *tether release model*, except that the number of tethers remains constant while the stress on the tethers gradually increases until they break.

This may be the case in large-scale quadrupolar magnetic configurations, where increasing magnetic stresses due to strong footpoint shearing makes the central arcade inflate. The tethers are unsheared overlying arcade field lines. Above the arcade, a current sheet forms and reconnection starts and the highly stressed core field consequently erupts. This scenario requires reconnection above the erupting filament.

1.4.2.2 The pre-CME corona

Understanding the pre-CME coronal conditions that lead to the magnetic instabilities that drive CME eruptions is key to the physical understanding of these explosive phenomena. In this section, the observational signatures of possible CME drivers during pre-CME conditions are discussed.

Photospheric shear motion

The majority of CMEs originate in active regions, which generally exhibit a roughly bipolar field. The shearing and stressing of the coronal magnetic field is believed to play a significant role in creating the conditions in which both flares and CMEs erupt. The stress of the magnetic field can be observationally determined by calculating the shear angle between potential field and transverse field vectors from a vector magnetogram, which contains information on the magnetic field in 3 dimensions at the photosphere. Evidence for a highly sheared magnetic configuration was found to lead to a filament eruption and flare without the presence of a helmet streamer configuration (Cheng *et al.*, 1984). Conversely, photospheric shear motion, as an indicator of the non-potentiality of an active region, may be a viable proxy for the prediction of the CME productivity of an active region (Falconer *et al.*, 2002).

The kink instability

Sigmoid structures are helical structures that form as a result of shearing and stressing of magnetic field lines above the neutral line. Once the helical twist exceeds some critical angle, the structure becomes susceptible to the kink instability, which may produce a disruption of the magnetic field leading to CME eruption. The sigmoidal shape is observed in projection as "S-shaped", and is regarded as an observational signature of azimuthal currents in twisted coronal structures, such as loops, arcades or filaments. There is now mounting observational evidence that the kink instability is key for many flares and CMEs (e.g. Canfield *et al.*, 1999; Rust, 2001; Yurchyshyn, 2002).

1.4.3 The Relationship Between Large-Scale Eruptive Phenomena

While both CMEs and solar flares are associated with the release of magnetic energy in the solar corona, the relationship between the phenomena remains controversial (Harrison, 1986; Harrison *et al.*, 2003). When a CME occurs it often has a close flare association (Svestka, 2001), but this is not always the case and the question

of causality is much debated. Conversely, flares may occur with or without CMEs, and even big flares (at least GOES M class) have no associated CME in 40 % of cases (Andrews, 2003).

When both flares and CMEs are produced conjointly, it seems that they share at their onset the same energetic processes for CME acceleration and flare energy release (Zhang *et al.*, 2004). However, it is generally accepted that they are quite distinctly different plasma processes, but related to each other by a common magnetic instability that is controlled on a larger scale. While flares are more localised events, CMEs are global phenomena with large angular extents, which probably indicates the involvement of a large fraction of the low corona. Both phenomenon can be related to geomagnetic storms, interplanetary shock waves and solar energetic particle events.

1.5 The Heliosphere

1.5.1 The Solar Wind

The presence above the solar surface of a tenuous gas at $T > 10^6$ K has two major implications. The first is that the very high thermal conductivity, which implies very efficient outward (and inward) heat transport from the inner corona, means that the corona will extend into interplanetary space (Chapman, 1957), rather than being confined near the surface like planetary atmospheres. The second is that in order for the pressure to eventually decrease to interstellar medium values, the corona cannot be in hydrostatic equilibrium and must in fact be expanding (Parker, 1958). The huge pressure difference between the corona and the interstellar medium drives the plasma outwards, despite the countering force of gravity, and there is at all times and all latitudes relative to the ecliptic, an outflow of particles travelling at several hundreds of km s^{-1}. The existence of the solar wind was predicted several years before it was actually observed by *in situ* measurements from the Mariner 2 spacecraft in 1962, primarily through the work of Chapman and Parker in 1957-58. In 1958, Parker concluded that: "...probably it is not possible for the solar corona, or indeed, perhaps the atmosphere of any star, to be in complete hydrostatic equilibrium out to large distances. We expect to always find some continued outward hydrodynamic expansion of gas.". He went on to propose a hydrodynamic model of a continuously expanding corona, or solar wind.

To treat an expanding atmosphere, Parker started with conservation equations (mass, momentum and energy) and derived an equation of motion, using boundary

conditions to eliminate unphysical solutions. Parker made a number of assumptions about the solar wind:

1. it is an ideal gas
2. it flows radially away from the Sun
3. electromagnetic forces in the wind are negligible
4. changes are slow compared to the wind generation time-scale
5. the wind is isothermal
6. mass is conserved in a flow across a spherical surface
7. the system is spherically symmetric

Parker then derived the following equation of motion, that reveals the existence of the solar wind:

$$\frac{1}{v}\frac{d\mathbf{v}}{dr}\left(\mathbf{v}^2 - \frac{2kT}{m}\right) = \frac{4kT}{mr} - \frac{GM_\odot}{r^2} \tag{1.51}$$

where $\mathbf{v}$ is velocity, T is temperature, k is the Boltzmann constant, G is the gravitational constant, $M_\odot$ is the mass of the Sun and r is the radial distance from the Sun.

The right hand side of the equation is negative for T observed in the lower corona. However, since the gravitational force term (second term on the right hand side) decreases as $1/r^2$, it will eventually become smaller than the first term on the right hand side, which decreases only as $1/r$. Thus, there is a critical radius, r_c, at which the right hand side of this equation changes sign:

$$r_c = \frac{GM_\odot m}{4kT} \tag{1.52}$$

The left hand side of equation 1.51 must go through zero at the critical radius and analysis of these conditions show that there exist five classes of solution to the equation of motion, which are illustrated in Figure 1.10.

We are interested in single-valued, continuous solutions that describe plasma motions from near the Sun to large solar distances. Since classes *I* and *II* are double-valued and confined to small and large r, respectively, they may be excluded.

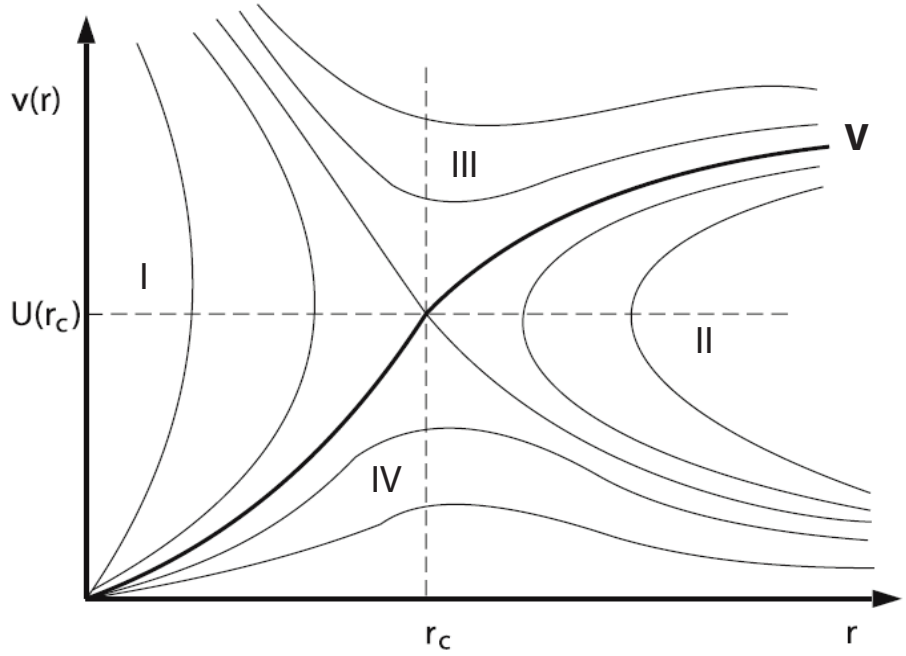

Figure 1.10: Graphical representation of the five classes of solutions resulting from the equation of motion derived for the solar wind. Figure courtesy of Parker (2007). Permission to reproduce this figure has been granted by Springer Science + Business Media.

Solutions of class *III* do not satisfy the observation that general plasma velocities near the Sun are subsonic, while solutions of class *IV* are subsonic everywhere. This class of solutions is known as the "solar breeze solution" and would mean that at large solar distances, the solar wind would only reach speeds of ~ 1 km s^{-1}, which is observed to not be the case. The most likely solution is class *V*, in which the solar wind starts subsonically near the Sun before reaching supersonic speeds at larger solar distances.

While the solar wind at 1 AU is always observed to be supersonic, it is typically divided into two regimes; the fast wind and slow wind. However, these outflowing streams are marked apart by more than just the speed with which they propagate. Table 1.1 summarises the general properties of the solar wind, determined from *in situ* observations at 1 AU.

Table 1.1: Properties of the fast and slow solar wind at 1 AU.

Parameter	Minimum	Average	Maximum
Flux (cm^{-2} s^{-1})	1	3	100
Velocity (km s^{-1})	200	400	900
Density (cm^{-3})	0.4	6.5	100
Magnetic field (nT)	0.2	6	80

Results from the Ulysses mission, which made multiple passes of the Sun at various solar latitudes, including the poles, show that the fast solar wind typically

propagates away from the Sun with speeds in excess of 700 km s^{-1}. It is characterised by its steady flow and is well-correlated with latitudes of polar coronal holes, where the magnetic field lines appear, to all intents and purposes, "open", extending out to large solar distances, whilst maintaining their connection to the Sun. The slow solar wind typically propagates with speeds in the region of $\sim$ 350 km s^{-1}. It is characterised by bursty flows and originates from the equatorial streamer belt. Figure 1.11 shows that the transition from low to high speed wind is abrupt and that the dynamic pressure of the solar wind, which is a function of speed and density, is greater from the poles than around the equator. The presence of equatorial coronal holes at times of increasing solar activity brings these fast streams down into the equatorial plane in the region of the streamer belt at solar maximum.

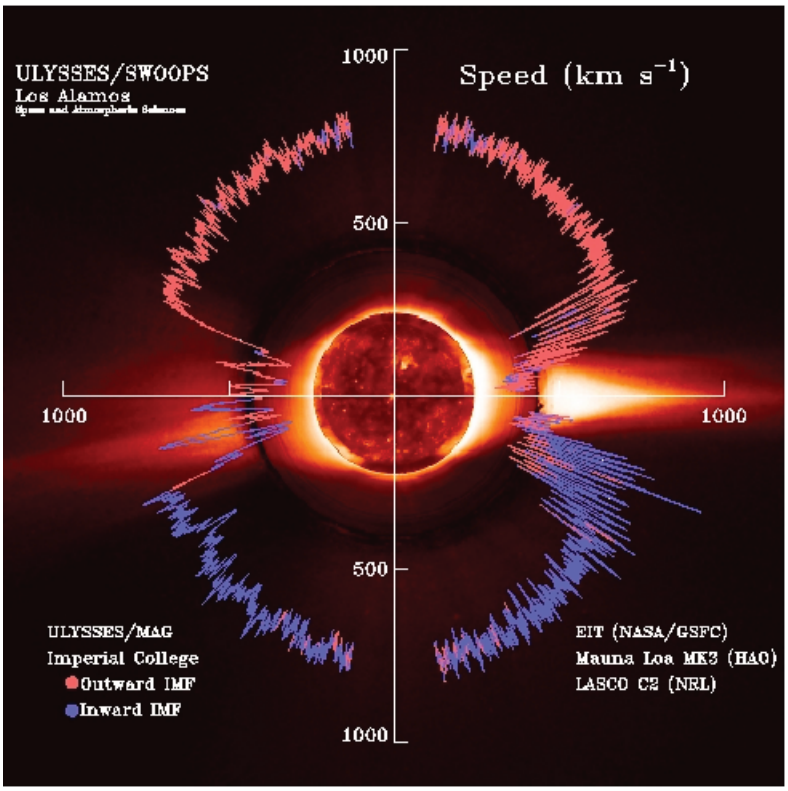

Figure 1.11: Solar wind speed derived from Ulysses observations between March 1992 and March 1997, showing characteristic solar wind speeds around solar minimum. High velocity fluctuations are observed in the slow solar wind in the equatorial regions and we can clearly see the opposite magnetic polarities of the two solar hemispheres. Figure adapted from McComas *et al.* (1998) and courtesy of ESA. Permission to reproduce this figure has been granted by Springer.

Results from the SOHO mission have also shown that the fast component of the solar wind emanates from coronal holes. Plumes seem to emerge from tiny bright spots inside coronal holes, but it has been been shown that these are not the main source of the high speed wind since they occupy only a small part of coronal holes, and the wind seems to originate from all over the coronal hole. Spectroscopic EUV observations in polar coronal holes have shown Doppler shifts ($\sim$ 10 km s^{-1}) outwards from the solar surface (blue-shift). These are concentrated at the network

boundaries and suggest that the fast wind is being accelerated there.

The origin of the slow wind is not at all clear, though it seems to originate from the tips of helmet streamers above active regions, which are at lower latitudes and where the field is predominantly "closed". In order for the slow solar wind to escape, Fisk (1996) proposed that the combination of the Sun's differential rotation and super-radial expansion brings high latitude field lines down to lower latitudes where reconnection occurs with closed field lines, allowing plasma within closed loops to escape into the slow solar wind. Line profiles observed with the UVCS instrument onboard SOHO at a few solar radii have shown a difference in speeds of H^+ and O^{5+} ions in coronal holes, with O^{5+} ions reaching speeds of $v \sim 500$ km s^{-1} above 2 $R_\odot$, while H^+ only has a velocity of $v \sim 250$ km s^{-1} (e.g. Cranmer *et al.*, 1998). In equatorial regions, where the slow solar wind originates, lighter H^+ moves faster than heavier O^{5+}, as expected for a gas in thermal equilibrium. In thermal equilibrium, this implies that the O^{5+} ions would be much hotter than the protons by about two orders of magnitude, and this suggests that the O^{5+} ions are being preferentially accelerated to higher velocities, possibly by Alfvén waves.

The solar wind becomes super-Alfvénic at a radius known as the Alfvén radius, R_A. When $r \ll R_A$ the solar magnetic field enforces the co-rotation of the solar wind with the Sun. Beyond this distance, the magnetic field is frozen in to the coronal plasma, and the field will be carried out into interplanetary space by the solar wind. As a result of the radial expansion of the solar wind and solar rotation, the field lines are drawn out into an Archimedean spiral, known as the Parker spiral, as illustrated in Figure 1.12. The angle between a radial vector and the IMF is $\sim 45^\circ$ at the Earth's orbit. Co-rotating interaction regions (CIRs) (Tsurutani and Gonzalez, 1997) are formed when high speed streams overtake slow streams. At the edges of a CIR, a pair of shocks form which accelerate particles. Prolonged periods of southward IMF within CIRs are likely to be the source of the 27-day recurrent geomagnetic activity observed at the Earth (Kamide and Maltsev, 2007).

Near solar minimum, the Sun's field can be approximated by a simple dipole, and a current sheet at the equator, known as the Heliospheric current sheet (HCS) is formed separating the two opposite magnetic polarities of the northern and southern solar hemispheres. There is a small offset between the solar rotation and magnetic axes and as the magnetic axis precesses around the rotation axis, the neutral current sheet also rotates with the Sun, sweeping regions of opposite polarity across the Earth. This results in the warped structure of the HCS, which is often described as being like a ballerina's skirt, as shown in Figure 1.13. In principle then, a spacecraft in the equatorial plane of the heliosphere should observe outwardly directed field lines for half the time and inwardly directed field lines for the other half. In practice,

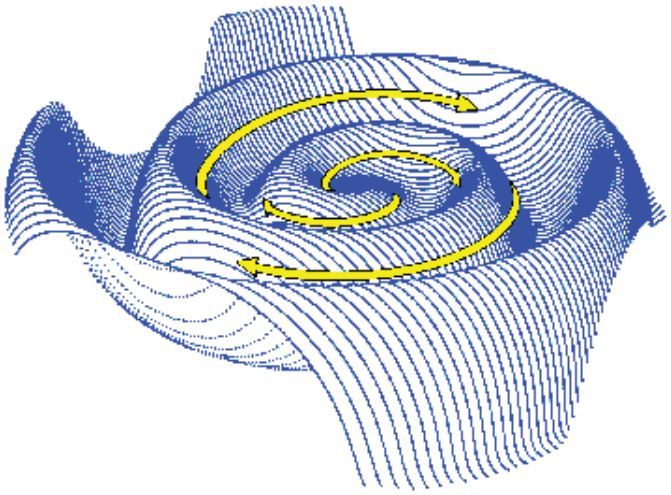

Figure 1.12: The Parker spiral structure of the interplanetary magnetic field (IMF), indicated by the yellow arrows, superposed on a schematic of the Heliospheric Current Sheet (HCS), shown in blue. The IMF is frozen into the radial outflow of the solar wind, and is therefore convected out into interplanetary space. However, the feet of the field lines are also frozen into the solar surface, which rotates with a $\sim$ 27-day period, thus the IMF is wound into an Archimedean spiral, which makes an angle of 45° to the Earth-Sun line. The spiral winds tighter with increasing distance from the Sun. Figure courtesy of J. Jokipii, University of Arizona.

the current sheet has localised warps that complicate the polarity pattern, so the real observations are more complex. As the Sun approaches activity maximum, the magnetic structure of the Sun increasingly deviates from the simple bipolar structure of minimum activity, and the HCS becomes more warped.

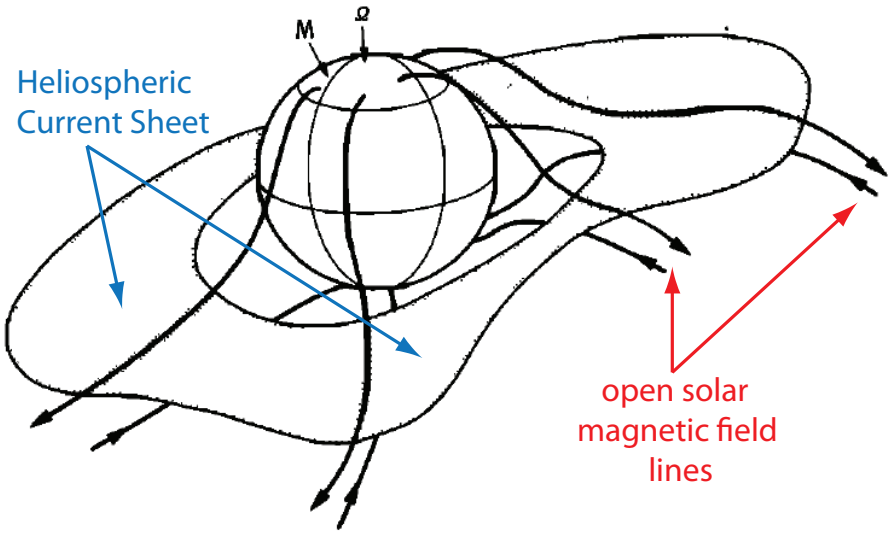

Figure 1.13: A three-dimensional sketch of the Heliospheric Current Sheet (HCS). Along the plane of the Sun's magnetic equator, the oppositely directed open field lines run parallel to each other and are separated by a thin current sheet known as the "heliospheric current sheet". The solar magnetic dipole M is tilted with respect to the Sun's axis of rotation ω, resulting in the wavy, "ballerina skirt"-like structure of the HCS as it extends into interplanetary space. Figure adapted from Smith *et al.* (1978). Permission to reproduce this figure has been granted by the American Geophysical Union.

As the solar wind flows out into interplanetary space, it carves out a region of space called the heliosphere. Approaching the point at which the solar wind pressure can no longer balance the pressure of the interstellar medium, a shock, known as the termination shock, will develop and the solar wind slows to subsonic speeds. The heliopause lies beyond the termination shock and is the theoretical boundary at which the solar wind is stopped by the interstellar medium. The distance to the heliopause can be estimated by determining the point at which the solar wind ram pressure is comparable to the interstellar medium pressure and it is predicted to be a distance greater than 100 AU beyond the known major planets.

1.5.2 Interplanetary Coronal Mass Ejections

The propagation of CMEs into interplanetary space was first identified in the 1970s through regions of plasma with unusual characteristics, and the interplanetary counterparts of CMEs are currently referred to as "Interplanetary Coronal Mass Ejections" (ICMEs). There are now many cases in which CMEs have been identified in the interplanetary medium using *in situ* measurements of magnetic fields and particles. By the 1980s, many of the signatures associated with ICMEs had been identified and a subset of ICMEs with their own distinct features had been identified and termed "magnetic clouds" (MCs).

1.5.2.1 Magnetic clouds

Magnetic clouds are large-scale, helical magnetic structures that were first discovered by Burlaga *et al.* (1981) and Klein and Burlaga (1982) when they noticed that some ICME events showed particularly smooth magnetic profiles that were variable on time-scales of hours and also had low plasma temperatures. ICMEs that do not exhibit the magnetic signatures of magnetic clouds have often been termed "complex ejecta" (Burlaga *et al.*, 2002), since their magnetic configurations are often observed to be more complicated. Magnetic clouds are often, at least preliminarily, identified at 1 AU using three main criteria (Burlaga, 1991):

1. the magnetic field direction rotates smoothly through a large angle during an interval of the order of one day;
2. the magnetic field strength is higher than average;
3. the temperature is lower than average.

While other large-scale solar wind structures, such as interplanetary sector boundaries, corotating interaction regions (CIRs) or post-shock ICME flows can exhibit any of the above features (e.g. Bothmer and Schwenn, 1992), the combination of all three appears to be unique to magnetic clouds (e.g. Bothmer and Schwenn, 1998).

MCs may only be observed when the central part of an ICME passes over the observing spacecraft (Jian *et al.*, 2006), and consequently there is still much disagreement about what proportion of all ICMEs are magnetic clouds, with estimates ranging from ≈ 30 % (Gosling, 1990) to as high as 80 % (Marubashi, 2000). There is also evidence of a solar cycle effect, ranging from roughly 100 % magnetic clouds for

the few ICMEs near solar minimum to ≈ 15 % around solar maximum (Richardson and Cane, 2004b). Recent cloud studies by Huttunen *et al.* (2005) and Wu *et al.* (2003) agree that the overall frequency of magnetic clouds varies over the course of the solar cycle but found that this is not in phase with either the sunspot cycle nor the total CME rate during 1996-2002.

Magnetic clouds are largely interpreted as magnetic flux ropes, connected at both ends to the Sun, as illustrated in Figure 1.14, and may in fact be prominence cavities associated with those CMEs with a three-part structure (Chen, 1996). Relating shocks, ICMEs and solar events can be particularly complicated at times when several ejections are moving away from the Sun, and it is when studying structures like this that observations from multiple, well-separated spacecraft are of immense value.

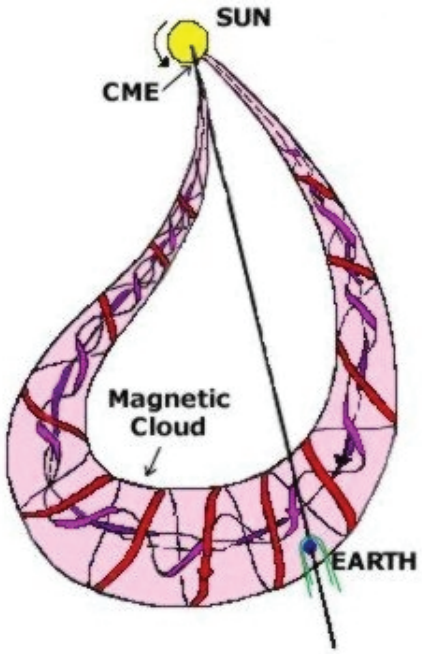

Figure 1.14: A schematic of a magnetic cloud, illustrating its flux rope structure and its connectivity to the Sun. Figure adapted from Marubashi (1997). Permission to reproduce this figure has been granted by the American Geophysical Union.

1.5.2.2 Theoretical models of magnetic clouds

The global magnetic structure of transient features in the solar wind has been the subject of much debate for a long time (e.g. Morrison, 1954; Cocconi *et al.*, 1958; Gold, 1959). For the structure of magnetic clouds, Goldstein (1983) introduced the now widely used force-free, large-scale, cylindrical magnetic flux rope model,

given by the equation $\nabla \times \mathbf{B} = \alpha \mathbf{B}$, where α is a function of position, and there is an infinite number of configurations corresponding to the possible choices of α to explain the magnetic field variations in magnetic clouds. "Force-free" means that the Lorentz force vanishes (see § 1.3.6); however, the force-free configuration can be regarded as one in which the magnetic pressure is balanced by the tension of the curved magnetic field lines (Ferraro and Plumpton, 1966).

A simple solution for a cylindrically symmetric force-free field with constant α was found by Lundquist (1950):

$$B_A = B_0 J_0 (\alpha R) \tag{1.53}$$

$$B_T = B_0 H J_1 (\alpha R) \tag{1.54}$$

$$B_R = 0 \tag{1.55}$$

where B_A is the component of the magnetic field along the axis of the magnetic cloud, B_T is the component of the magnetic field in the azimuthal direction, B_R is the radial component of the magnetic field, J_0 and J_1 are Bessel functions, R is the distance from the axis, $H = \pm 1$ determines the handedness of the magnetic field, and B_0 and α are constants.

The lines of force of the magnetic field given by this solution are a family of helices with pitch angle increasing from the axis of the magnetic cloud (where the magnetic field is a straight line) to the boundary (where the lines of force are circles). With this solution, magnetic clouds are described as magnetic flux ropes, that is, cylindrical configurations with a two-component magnetic field, one along the axis of symmetry and another in the azimuthal direction. Although a magnetic cloud may be locally cylindrically symmetric, it cannot extend to infinity; hence it must be curved.

Later studies have shown that not every cloud fits a force-free, cylindrically symmetric model (Forbes *et al.*, 2006). Other configurations have been proposed, including spheromak solutions of the force-free equation (Ivanov and Kharshiladze, 1985; Vandas *et al.*, 1991; Vandas *et al.*, 1993) and toroidal solutions (Ivanov *et al.*, 1989; Romashets and Ivanov, 1991). In other models, the static assumption has also been removed, and the effects of expansion and interaction with the ambient solar wind have been included (Osherovich *et al.*, 1993; Farrugia *et al.*, 1995; Marubashi, 1997). Pressure gradients have also been observed inside magnetic clouds, indicating that they are not force-free structures, and some non-force-free methods have also been introduced to address this (Mulligan and Russell, 2001; Hidalgo *et al.*, 2000).

The propagation, structure and evolution of magnetic clouds form the primary interests of this thesis and are discussed further in Chapters 3, 4, and 5.

1.6 Space Weather

Space weather describes the conditions in space that affect the Earth and the interplanetary environment, and is driven by the behaviour of the Sun. It is associated with many types of physical phenomena; including geomagnetic storms, ionospheric disturbances and aurora. Important drivers of space weather include coronal mass ejections and solar flares, but disturbances may also be created by the "normal" solar wind.

Geomagnetic activity and the arrival of ICMEs at Earth are intrinsically linked (Gosling *et al.*, 1991). The derivation of the properties of an ICME from its associated CME is essential for any prediction of the ICME geoeffectiveness, and therefore for space weather forecasting. The intensity of geomagnetic activity is governed by the southward interplanetary magnetic field component (Tsurutani and Gonzalez, 1997), since magnetic reconnection between the solar magnetic field and the magnetosphere is more effective when the solar field is directed southwards, and because this is strongly enhanced within some ICMEs or the associated sheaths, the majority of major geomagnetic storms are ICME-related (Richardson *et al.*, 2001).

Space weather can influence the performance and reliability of space-borne and ground-based technological systems, and can have harmful effects on human health. Adverse conditions in the space environment can cause disruption of satellite operations, communications, navigation, and electric power distribution grids, leading to a variety of socio-economic losses. The causes of very intense storms that can lead to power outages and satellite losses are still not clear, but may be linked to high velocity CMEs, multiple ICMEs or multiple magnetic storms.

The work undertaken within this thesis builds on the current understanding of the structure and evolution of CMEs as they propagate into interplanetary space. Research of this nature can not only provide insights into why some CMEs are more geoeffective than others, but improve the accuracy of the process of identifying the eruption of Earth-directed CMEs on the Sun. Ultimately, we will be better able to predict both the time of arrival of a CME at Earth and its geoeffectiveness at a much earlier stage of propagation, allowing appropriate action to be taken to mitigate its effects on Earth.

1.7 Aim of Thesis

Understanding how and why CMEs erupt, and the subsequent evolution of the associated ICMEs during their expansion into interplanetary space is of great interest, given their potential geoeffectiveness and the socio-economic impacts of space weather at Earth. The research presented in this thesis combines remote observations of the Sun and *in situ* plasma and magnetic field measurements in interplanetary space. This work takes important steps towards improving our understanding of how and why CMEs evolve as they propagate through the heliosphere, and demonstrates the importance of a "cradle to grave" analysis in understanding the complex evolution of such an event, from its initiation at the Sun to its detection at 1 AU. This thesis aims to contribute new and original scientific research on the subjects of interplanetary coronal mass ejections and solar-heliospheric connections.

1.8 Outline of Following Chapters

Chapter 2 comprises a description of the various solar telescopes and *in situ* instruments that provided data used in this work. Chapter 3 comprehensively reviews the observational signatures of interplanetary coronal mass ejections, both at the Sun and in interplanetary space. Here, we also describe work on the process of locating the solar source of a magnetic cloud, demonstrating the complexities of tying together the Earth-end and Sun-end of an eruptive event. Chapter 4 presents our new results on the physical nature of the regions exhibiting unusual magnetic topology, indicative of internal substructure, observed within some magnetic clouds. Chapter 5 tackles the question of what causes magnetic cloud substructure, focusing on the quantitative evaluation of several possible explanations, including magnetic reconnection, multiple flux ropes, flux rope perturbation and MHD waves. Chapter 6 discusses the collective contribution of this work to the fields of study of interplanetary coronal mass ejections and solar-heliospheric connections. Possibilities for future work are also considered.

Chapter 2

Instrumentation and Mathematical Techniques

2.1 Instrumentation

Remote sensing observations of the Sun and *in situ* observations in interplanetary space are required to study solar influences in the heliosphere, allowing us to investigate many aspects of a coronal mass ejection prior to, during and post-eruption. The data used in the work presented in this thesis comes from solar instrumentation, which includes a magnetograph, extreme ultraviolet imagers and white-light coronagraphs and *in situ* instrumentation which includes fluxgate magnetometers and electrostatic plasma analysers. The wide range of data available from these instruments helps us to understand the connection between the low-coronal signatures of CMEs and their associated interplanetary counterparts, including their structure and evolution as they propagate into the heliosphere.

2.2 Remote Sensing Measurements

2.2.1 The Solar and Heliospheric Observatory (SOHO)

The Solar and Heliospheric Observatory (SOHO, Domingo *et al.*, 1995) was launched in 1995 as a joint mission between the European Space Agency (ESA) and the U.S. National Aeronautics and Space Administration (NASA). From its orbit about the L1 libration point upstream of Earth, it has a continuous view of the Sun and is able to send back a near constant stream of data on the Sun and its environment,

uninhibited by Earth occultations and the moon's shadow, which affect spacecraft observing from low Earth orbit.

SOHO has a suite of 12 instruments onboard, of which a number are used to observe the solar corona, and the data from these instruments is used extensively in this thesis.

2.2.1.1 SOHO/Michelson Doppler Imager (MDI)

The primary scientific goal of the Michelson Doppler Imager (MDI, Scherrer *et al.*, 1995) is to investigate the internal structure of the Sun through helioseismology, as part of the Solar Oscillations Investigation (SOI). MDI also makes associated non-helioseismology measurements and several times a day polarisers are inserted into the instrument to measure the full disk line-of-sight magnetic field at the photosphere. The resulting magnetograms are available every 96 minutes.

Figure 2.1 shows a schematic of MDI's light path and primary optical components. To make magnetic measurements, the polarisation analyser wheel moves between right circularly polarised (RCP) and left circularly polarised (LCP) positions between filtergrams. A longitudinal magnetogram is constructed by measuring the Doppler shift separately in RCP and LCP light, since the difference between these two is a measure of the Zeeman splitting. This is approximately proportional to the magnetic flux density, which corresponds to the line-of-sight component of the magnetic field averaged over the resolution element. In full disk mode, MDI has a field of view of 34' × 34' using an array of 1024 × 1024 pixels and a spatial resolution of 4". However, when the high-resolution path is selected, these measurements are magnified by a factor of 3.2 to provide 1.25" resolution over an 11' × 11' field of view.

2.2.1.2 SOHO/Extreme Ultraviolet Imaging Telescope (EIT)

The Extreme Ultraviolet (EUV) Imaging Telescope (EIT, Delaboudinière *et al.*, 1995) provides wide-field EUV images of the corona and the transition region on the solar disk and up to 1.5 $R_{\odot}$ above the solar limb, enabling the dynamics and evolution of coronal structures to be studied over a wide range of scales, sizes and temperatures. EIT is a normal incidence telescope with a 45' × 45' field of view, allowing it to obtain full disk solar images. A back-illuminated charge-coupled device (CCD) is used to record the images and is a 1024 × 1024 array of 2.6" square pixels, resulting in a spatial resolution of approximately 5". Generally EIT observes with a

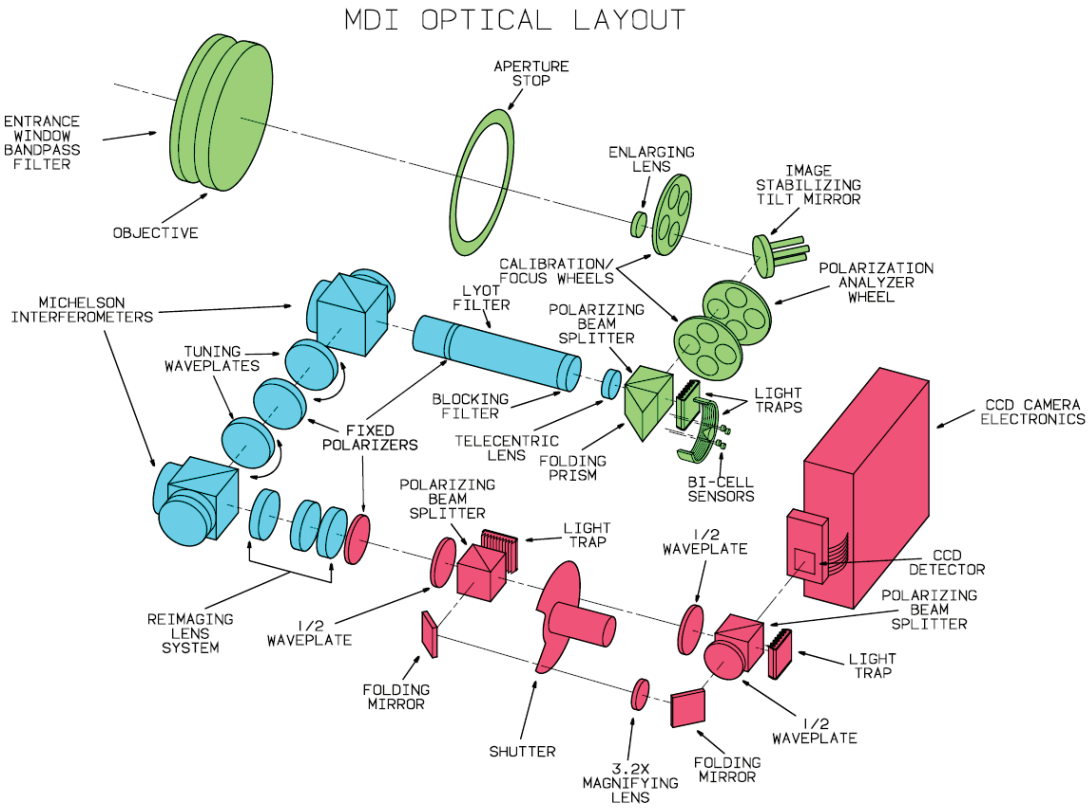

Figure 2.1: A schematic of MDI's optical layout. The optical systems are highlighted in green, the filter arrangement in blue and the camera system in pink. Figure adapted from Scherrer *et al.* (1995). Permission to reproduce this figure has been granted by Springer.

temporal cadence of several minutes between observations, limited by the telemetry allocated to the instrument. It is possible for a sub-array of pixels, each 32 × 32 in size, to be read out while the rest of the CCD field is discarded, allowing the limited EIT telemetry to be used for detailed study of small areas of the Sun with higher time resolution.

EIT is capable of imaging solar plasma over a temperature range of 6×10^4 K to 3×10^6 K using four spectral emission line bandpasses centred on the intense emission lines at: Fe IX (171 Å), Fe XII (195 Å), Fe XV (284 Å), He II (304 Å). Figure 2.2 shows that the main body of the telescope is comprised of two mirrors mounted at either end of an aluminium cylinder and makes use of multi-layer optics. By dividing the telescope mirrors into quadrants, the emissions from narrow temperature ranges can be isolated by "tuning" the coatings of each quadrant to the desired wavelength.

2.2.1.3 SOHO/Large Angle Spectroscopic Coronagraph (LASCO)

Historically, observations of the tenuous white-light corona could only be made during a solar eclipse when the intense photospheric light from the disk of the Sun

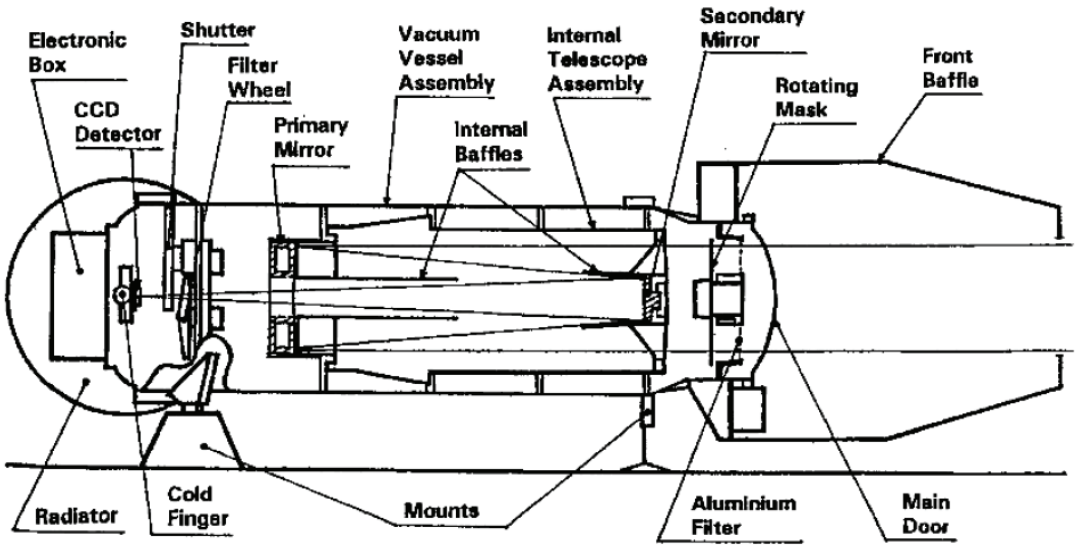

Figure 2.2: A schematic of EIT indicating its major subsystems. Figure adapted from Delaboudinière *et al.* (1995). Permission to reproduce this figure has been granted by Springer Science + Business Media.

was occulted by the moon lying along the Sun-Earth line. In 1930, Bernhard Lyot invented the coronagraph, a telescopic attachment that acts as an occulting disk, allowing the solar atmosphere to be observed without the need to wait for a solar eclipse, revolutionising scientists' understanding of the solar corona.

The Large Angle Spectroscopic Coronagraph (LASCO, Brueckner *et al.*, 1995) is a wide-field, white-light and spectrometric coronagraph consisting of three optical systems, C1, C2 and C3. These have nested fields of view that together observe the solar corona using very narrow visible wavelength bands from just above the limb at 1.1 $R_\odot$ out to very great elongations. The C1 coronagraph is a mirrored version of an internally occulted coronagraph observing the corona between 1.1 and 3 $R_\odot$, however due to technical problems following the temporary loss of contact with the SOHO spacecraft in June 1998, there is no data from C1 after this date. Data from C1 is not used in the work in this thesis. The C2 and C3 coronagraphs are externally occulted instruments, observing between 1.5 to 6 $R_\odot$ and 3.7 to 30 $R_\odot$, respectively.

Three coronagraphs with overlapping fields of view were required to overcome two limitations of an externally occulted coronagraph. The first is that for a given distance from the occulting disk to the first imaging element, the instrument can only provide images of the corona for distances >1.5 $R_\odot$, consequently the spatial resolution in the inner corona is small. Secondly, because of size limitations, the aperture cannot usually exceed a few centimetres. The design of the C2 coronagraph is shown in Figure 2.3. The suppression of scattered light within the instrument plays a key part in improving the image quality.

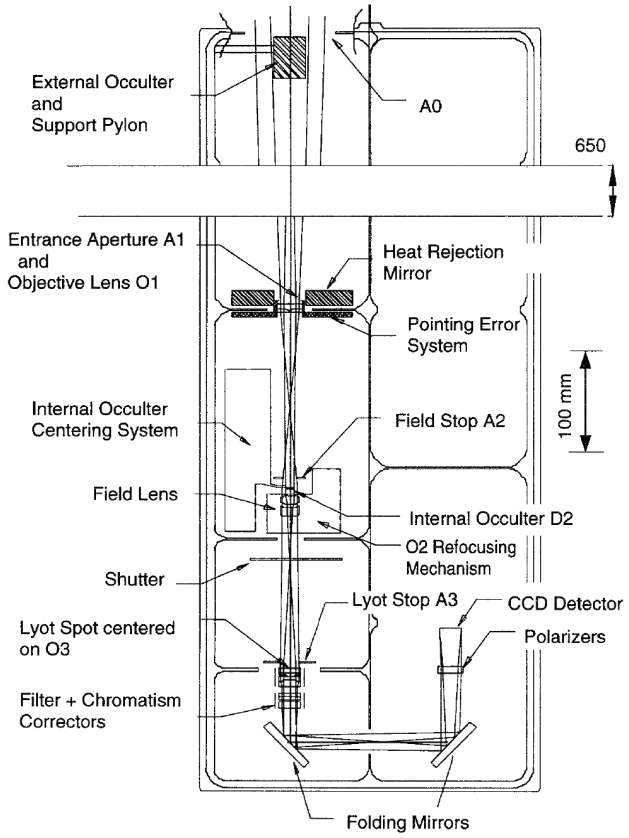

Figure 2.3: The optical layout of the C2 coronagraph. Figure courtesy of Brueckner *et al.* (1995). Permission to reproduce this figure has been granted by Springer Science + Business Media.

The spatial resolution of C2 and C3 are poor at small solar distances due to vignetting at the inner edge of the field of view, but this improves significantly for greater solar distances, as shown in Figure 2.4 for C2. C2 and C3 mostly operate in synoptic mode at a cadence of about 24 min. (C2) and 45 min. (C3).

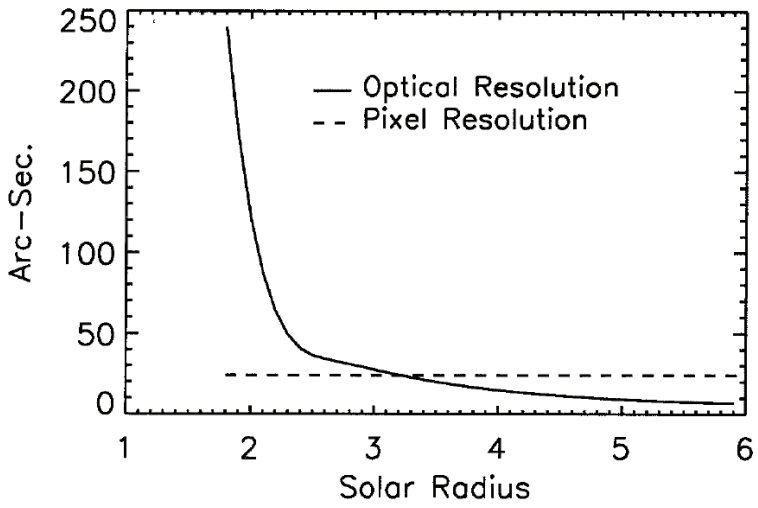

Figure 2.4: Optical and pixel resolution of C2. Pixel resolution is the size of two pixels. Figure adapted from Brueckner *et al.* (1995). Permission to reproduce this figure has been granted by Springer Science + Business Media.

2.2.2 Transition Region and Coronal Explorer (TRACE)

The Transition Region and Coronal Explorer (TRACE, Handy *et al.*, 1999) is a single instrument NASA Small Explorer (SMEX), launched on 2 April 1998 to provide high temporal and spatial resolution images of the solar photosphere, transition region and corona. TRACE is located in a Sun-synchronous polar orbit allowing it to continuously observe the Sun. The TRACE orbit is such that it passes through the South Atlantic Anomaly (SAA) and observations are paused during the predicted times of the SAA.

The TRACE telescope is of a 30 cm Cassegrain design and makes use of multi-layer optics and a lumogen-coated CCD detector with 0.5" pixels, to measure 3 EUV wavelengths and several UV wavelengths, corresponding to a temperature range of 6000 K to 1×10^7 K. At 8.5' × 8.5', TRACE's field of view is significantly smaller than that of the full-disk field of view of SOHO/EIT, imaging approximately one-tenth of the solar disk, but this allows the instrument to image the Sun at the higher temporal resolution of typically < 1 min. and results in improved spatial resolution of 1". This makes the TRACE instrument a useful tool for the detailed study of coronal dynamics and the evolution of coronal structures.

The designs of TRACE and EIT share many similarities, in particular the quadrant design of the TRACE telescope is much like that on EIT, with the use of similar EUV multi-layer coatings on the telescope mirrors, as shown in Figure 2.5. These optics are sensitive to the EUV wavelengths Fe IX (171 Å) (this line is actually centred slightly above 173 Å, but is referred to as 171 Å to be consistent with EIT), Fe XII (195 Å) and Fe XV (284 Å) and the UV wavelength range 1200 - 7000 Å. Four filters in a filter wheel are used in various combinations to image a variety of specific wavelengths, as detailed in Table 2.1.

Table 2.1: TRACE temperature response.

Wavelength ($\AA$)	Emission	Bandwidth ($\AA$)	Temperature (K)
171	Fe IX/X	6.4	1.6 - 20 x 10^5
195	Fe XII/XXIV	6.5	5.0 - 20 x 10^5
			1.1 - 2.6 x 10^7
284	Fe XV	10.7	1.25 - 4.0 x 10^6
1216	H I Lα	84	1.0 - 3.0 x 10^4
1550	C IV	30	6.0 - 25 x 10^4
1600	UV cont. C I Fe II	275	4.0 - 10 x 10^3
1700	Continuum	200	4.0 - 10 x 10^3
5000	White light	broad	4.0 - 6.4 x 10^3

Table adapted from Handy *et al.* (1999). Permission to reproduce this table has been granted by Springer Science + Business Media.

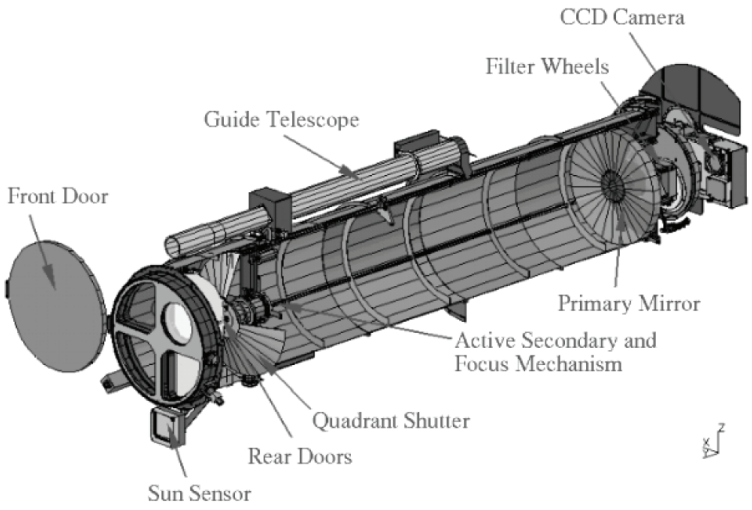

Figure 2.5: An isometric diagram of the TRACE telescope. Wavelength selection is determined by a quadrant selector located just behind the entrance filter chamber. The bandpass is determined by multi-layer coatings on the primary and secondary mirrors. Filters are mounted at the entrance of the telescope to reduce visible and stray light inside the telescope, and a pair of filter wheels are mounted behind the primary mirror to further filter the beam and provide wavelength selection in the UV channel. Figure adapted from Handy *et al.* (1999). Permission to reproduce this figure has been granted by Springer Science + Business Media.

The CCD detector is an MDI flight spare and is a front-illuminated 1024 × 1024 array of 0.5" pixels. To make the CCD sensitive to the EUV and UV wavelengths detected by TRACE, the front surface was coated with lumogen, a coating that fluoresces at visible wavelengths when hit by UV and EUV photons. The decrease in sensitivity of the lumogen in orbit has been substantially less than expected, at the level of 5 - 10 % in the centre of the EUV channel fields of view.

After 12 years of successful operation, TRACE completed its final observing sequence on 21 June 2010 following the launch of the next generation of EUV imaging instrument, the Atmospheric Imaging Assembly (AIA) onboard the Solar Dynamics Observatory (SDO) on 11 February 2010. TRACE will be permanently switched off by the end of 2010 when cross-calibration with AIA is complete.

2.3 *In Situ* Instruments

2.3.1 The WIND spacecraft

The WIND spacecraft (Harten and Clark, 1995) is part of NASA's Global Geospace Science (GGS) mission and carries a suite of 8 instruments designed to study the regions near the magnetospheric bow shock and magnetopause and to study the properties of the solar wind. WIND was launched on 1 November 1994 and, over a

period of 2 years, was placed in a halo orbit about the L1 libration point, located 1.5 $\times$ 10^6 km upstream of Earth. It is a spinning spacecraft with its spin axis aligned with the ecliptic plane, pointing towards the Sun. WIND's present orbit is a much more complex "petal" orbit that brings it as close as 10 R_E and as far as 80 R_E from the Earth, taking the spacecraft up to an angle of 60° from the ecliptic plane with respect to Earth. However, this orbit means that WIND does not continuously observe the solar wind, sometimes moving through the different plasma regimes of the magnetosheath and magnetosphere. In this thesis, we use measurements of field and particle distributions in the solar wind environment from the magnetic field and plasma instruments onboard WIND.

2.3.1.1 WIND/Magnetic Field Investigation (MFI)

The Magnetic Field Investigation (MFI, Lepping *et al.*, 1995) instrument provides high temporal resolution three-dimensional measurements of the interplanetary magnetic field (IMF) at up to 92 ms intervals for standard analysis. This occasionally increases to 44 vectors s^{-1} (one vector every 22 ms) to allow the instrument to measure very rapid fluctuations in the IMF when a pre-programmed "trigger" is observed. MFI enables large-scale structure and fluctuation characteristics of the IMF to be investigated through the use of a twin triaxial flux-gate magnetometer, which is mounted on a 12 m boom on the Wind spacecraft, so as to reduce the field of the spacecraft at the instrument to $\pm$0.1 nT or less. The dual configuration of the magnetometer has two advantages, firstly it provides redundancy in case of hardware failure and secondly, it improves the accuracy of the calibration of the instruments by permitting accurate removal of the dipolar portion of the spacecraft magnetic field during data processing.

In the absence of an external magnetic field, the sensors are "balanced" and no signal is recorded. When an external field is applied, the sensor balance is disturbed and a signal appears at the output of the sensors. After amplification and filtering, this signal is applied to a synchronous detector and high gain integrating amplifier which is used to generate a current proportional to the magnitude of the applied field, this is then fed back to the sensor to "null" the effective magnetic field seen by it. The output of a single axis magnetometer is then a voltage proportional to the magnitude, direction and polarity of the ambient magnetic field, with respect to the sensor axis orientation. A triaxial magnetometer is created when three single axis magnetometers are positioned orthogonal to one another.

To ensure that MFI is able to measure the full range of magnetic field strengths it encounters in interplanetary space, it has 8 dynamic ranges spanning a wide range

of measurements, from ±4 nT to ±65536 nT per axis, with the high upper range chosen to allow comprehensive pre-flight testing of the instrument within the Earth's magnetic field. The appropriate range for magnetic field measurement is selected automatically, using the following criteria: when the output of any magnetometer axis exceeds 7/8's of the full scale, the microprocessor generates a command to increase the magnetometer to the next, less sensitive range. When the output of all axes drops to below 1/8th, then the magnetometer is commanded to step down to the next most sensitive range. The noise levels experienced by MFI are low ($\leq$ 0.006 nT), with values several orders of magnitude lower than the lowest recorded levels of IMF fluctuations at 1 AU, allowing magnetic phenomena in the solar wind to be easily identified and studied.

2.3.1.2 WIND/3-D Plasma Analyser (3DP)

The three-dimensional plasma and energetic particle investigation (3DP, Lin *et al.*, 1995) makes measurements of the full three-dimensional distribution of suprathermal electrons and ions from solar wind plasma down to low energy cosmic rays. The primary scientific goals of the instrument are to explore the suprathermal electron population in the solar wind and study particle acceleration and transport and wave-particle interactions, but it is its role as a solar wind monitor that we exploit in this thesis.

Although, 3DP is capable of measuring electrons and ions with energies up to the MeV range using detectors mounted on double-ended semi-conductor telescopes, the ions and electrons studied in this thesis have much lower energies and are measured by top-hat symmetrical spherical section electrostatic analysers with microchannel plate detectors (see Figure 2.6).

Figure 2.7 shows the proton energy flux in the interplanetary medium, highlighting some common features present in the solar wind and outer magnetosphere. The 3DP electrostatic analysers are sensitive to ions and electrons with $\approx$ 3 eV to 30 keV energies. All of these analysers have either 180° or 360° fields of view in a plane, an energy resolution of $\Delta E/E \approx 0.2$, and angular resolution varying from 5.6° (near the ecliptic) to 22.5°. Full 4π steradian coverage can be obtained in one-half or one spin. Four analysers are required to comprehensively measure the solar wind plasma at these energies, measuring high and low energy ions (PESA - H and PESA - L) and high and low electron fluxes (EESA - H and EESA - L), and these are mounted on booms to minimise the effects of spacecraft potential. PESA and EESA analysers are swept over their energy range 32 or 64 times per spin. Moments of the electrons and ion distributions are computed onboard and include density, velocity, and the

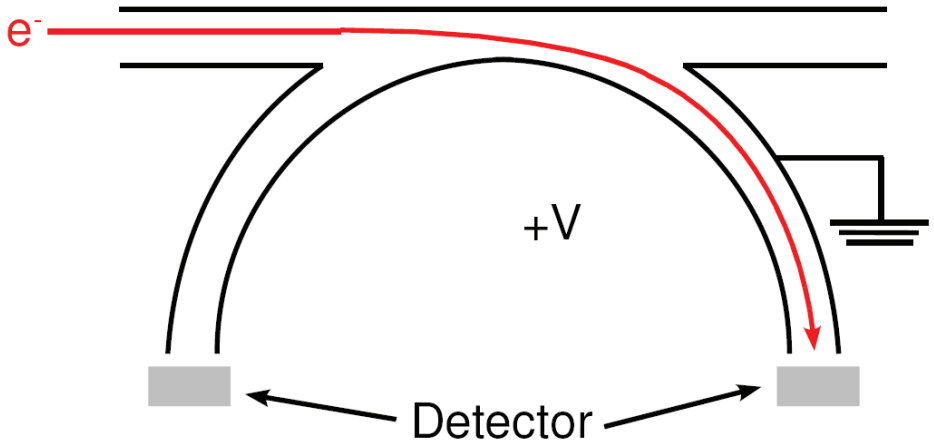

Figure 2.6: A schematic of a hemispherical electrostatic plasma analyser. Figure courtesy of Walsh (2009).

pressure tensor, from which temperature is extracted. Full three-dimensional distributions with various angular and energy resolutions are also produced and pitch angle distributions (PADs) can also be calculated from the EESA data.

2.3.2 The Advanced Composition Explorer (ACE)

The Advanced Composition Explorer (ACE, Stone *et al.*, 1998) was launched on 25 August 1995 and carries a suite of instruments designed to measure and compare the elemental and isotopic composition of the solar corona, the nearby interstellar medium and the galaxy. It is also able to investigate particle acceleration processes that occur in these environments. To provide context for these ion composition studies, ACE also carries three instruments that provide information on the heliospheric conditions and it is observations from these instruments which we use extensively to investigate the plasma and magnetic field conditions in the near-Earth environment in this thesis. ACE orbits in a halo about the L1 libration point, 1.5 x 10^6 km upstream of Earth and is a spinning spacecraft, with its spin axis directed towards the Sun. It is continuously exposed to the solar wind and other solar transients and provides real-time solar wind measurements.

2.3.2.1 ACE/Magnetometer (MAG)

The magnetic field experiment (MAG, Smith *et al.*, 1998) measures the interplanetary magnetic field in three dimensions using the flight spare from the magnetometer instrument flown on WIND. Twin, triaxial flux-gate magnetometers are mounted on booms 4.19 m from the centre of the spacecraft and and provide standard and

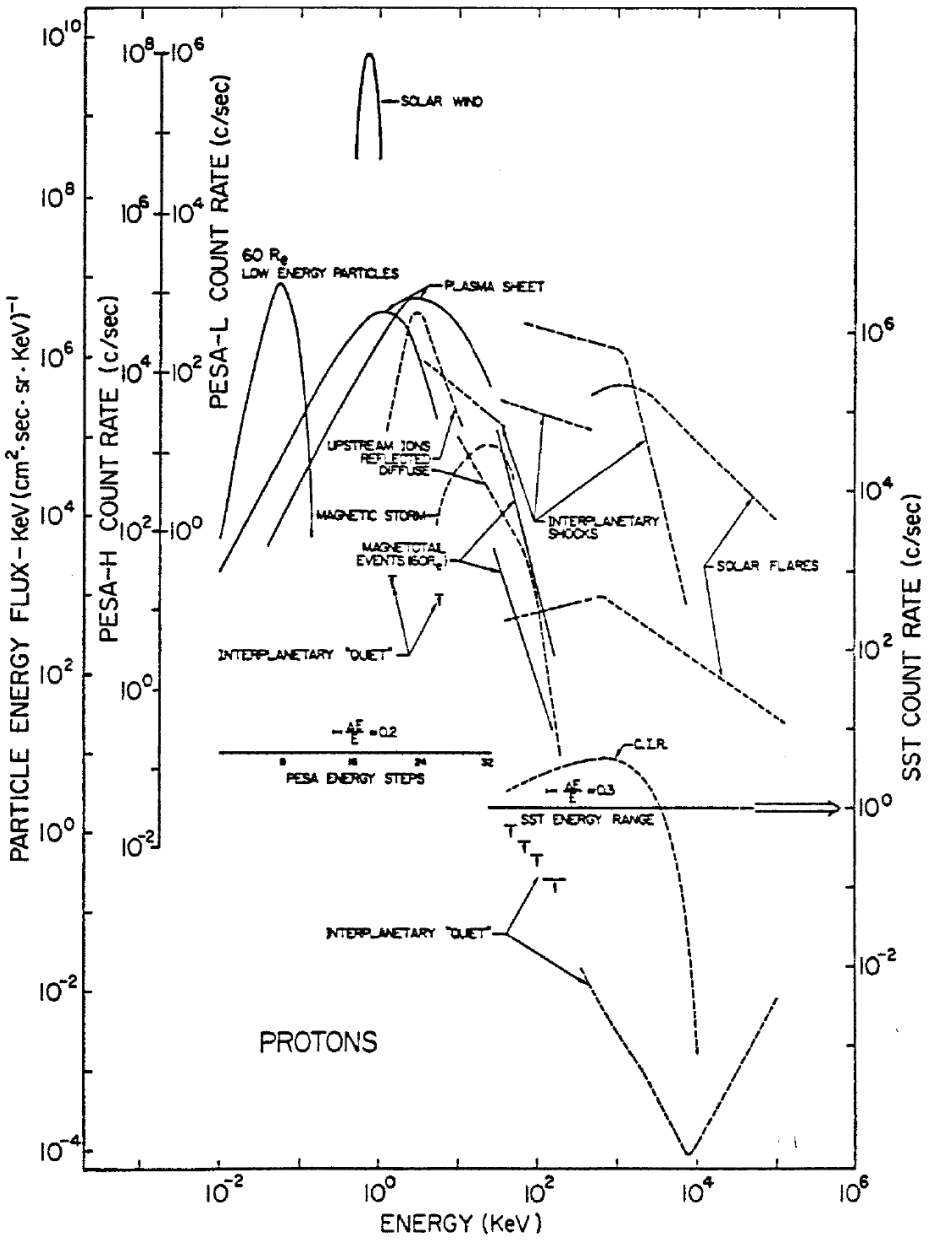

Figure 2.7: Proton energy flux (E(dJ/DE)) in the interplanetary medium and outer magnetosphere, determined by the ISEE-3 mission. Counting rates per channel for the proton electrostatic analyser (PESA) and semi-conductor detector telescopes (SST) are indicated on the left and right axes, respectively. Figure adapted from Lin *et al.* (1995). Permission to reproduce this figure has been granted by Springer Science + Business Media.

high resolution magnetic field measurements with between 3 and 6 vector s^{-1} resolution, corresponding to measurements at 33 s and 16 s intervals, and providing continuous coverage of the IMF. The sampling rate was decreased from that used on WIND/MFI to better meet the telemetry requirements of the ACE spacecraft. The only other modification made to the unit was to incorporate the ACE data bus. As a result, the instrument is very similar to WIND/MFI, described previously in § 2.3.1.1.

2.3.2.2 ACE/Solar Wind Electron Proton Alpha Monitor (SWEPAM)

The Solar Wind Electron Proton Alpha Monitor (SWEPAM, McComas *et al.*, 1998) is designed to measure the three-dimensional characteristics of solar wind and suprathermal electrons from $\approx$ 1 - 900 eV and ions from 0.26 - 35 keV, and makes use of modified spare solar wind electron and ion sensors from the *Ulysses* mission. The SWEPAM instruments are electrostatic analysers, which operate very similarly to the WIND/3DP instrument described in § 2.3.1.2, with separate analysers required for ions and electrons. SWEPAM-I makes full 3-D plasma measurements of protons and alpha particles every 64 s and has an energy resolution ΔE/E $\approx$ 5 % with an angular resolution of 5° in the polar direction and 3° to 4.5° in the azimuthal direction. SWEPAM-E makes full 3-D plasma measurements of electrons every 64 s and has an energy resolution ΔE/E $\approx$ 12 % with an angular resolution of 21° in the polar direction and 9° to 28° in the azimuthal direction.

Suprathermal electron pitch angle distribution (PAD) functions in are available from SWEPAM, operating in the suprathermal electron angle scan (STEA) data mode. This mode utilises the 10 highest voltage levels, corresponding to electron energies centred at 84 through to 1377 eV. The energy channel is $\approx$ 12 % wide and each of the pitch angle bins is 9°, and spans from 0 to 180 °. In STEA mode, a decrease in the number of energy levels measured (from 20 to 10) makes an increased angular resolution in the azimuthal direction possible (from 30 to 60 ϕ-angles), allowing narrow electron beams to be resolved. Suprathermal electrons PADs are useful for understanding the connectivity of an interplanetary coronal mass ejection to the Sun, and we make much use of these measurements in this thesis.

2.4 Mathematical Techniques

2.4.1 Physical coordinates Systems

Many measured quantities in space physics are vectors e.g. position, velocity, magnetic field. They are usually represented numerically by three cartesian components x, y and z which depend on the coordinates system used. There are a number of coordinates systems that may be used in the study of the solar-heliospheric environment, in order to best interpret and understand the observations of various physical processes. One commonly used coordinates systems is the geocentric solar ecliptic system.

2.4.1.1 Geocentric Solar Ecliptic System

The geocentric solar ecliptic (GSE) system is typically used in interplanetary space when considering the Sun-Earth system and is a right-handed system, centred at the Earth. The x component of this system points along the Earth-Sun line, the z component of this system is directed parallel to the ecliptic pole and points northwards and the y component of this system is directed towards dusk (opposing planetary motion), such that it forms an orthogonal, right-handed set.

2.4.2 Minimum Variance Analysis

In situ observations of the magnetic field of a magnetic cloud in interplanetary space are often readily available in geocentric solar ecliptic coordinates. However, it is often useful to transform these magnetic field measurements to the local coordinates system of the flux rope, and minimum variance analysis (MVA) is a useful mathematical technique with which to do this.

Minimum variance analysis finds, from single spacecraft time-series data, an estimate for the normal to a boundary in space. It allows the direction, $\mathbf{n}$ in which the projection of a series of N vectors has a minimum quadratic deviation to be determined, and also provides the directions of intermediate and maximum variance (e.g Sonnerup and Scheible, 1998). In the ideal, one-dimensional case, it is assumed that the boundary to be investigated evolves more slowly than the time-scale of a spacecraft crossing the structure and that the magnetic field component in the normal direction is independent of the distance from the boundary. Then, by considering measured magnetic field vectors either side of the boundary and near to its centre,

the direction in which the magnetic field variance is minimised is determined, and this approximates the normal to the boundary.

This method is useful to determine the orientation of structures that present three clearly distinguished variance directions. The output of this analysis, derived in Gulisano *et al.* (2007), is a matrix with real eigenvalues λ_1, λ_2, λ_3, which represent the degree of variance in each of those three orthogonal directions, and orthogonal eigenvectors ($\hat{X}_{MV}$, $\hat{Y}_{MV}$, $\hat{Z}_{MV}$), which represent the directions of minimum, maximum and intermediate variation of the magnetic field.

The eigenvalues provide the corresponding variance associated with each direction and the separation between these values indicates how well-defined the minimum variance analysis direction is. Siscoe and Suey (1972) proposed a significance criterion to determine if a set of 100 vectors presents significantly distinct spatial directions. They found that when the ratio between the minimum and intermediate eigenvalues ($\lambda_{min}/\lambda_{int}$) is < 0.72 and the ratio between the maximum and intermediate eigenvalues ($\lambda_{max}/\lambda_{int}$) is > 1.37, the information obtained about the direction of the normal to the boundary and the normal to the surface is sufficiently valid. If the eigenvalues corresponding to the minimum and intermediate directions are approximately equal, no information about the direction of the normal to the boundary can be obtained. If the separation between the eigenvalues corresponding to the intermediate and maximum variance directions is very small, then the normal to the surface can still be determined, but it is not possible to obtain any meaningful information on the components tangential to the surface.

From the eigenvectors it is possible to construct the rotation matrix, $\mathbf{T}$ such that the components of the field in the minimum variance frame of reference can be written as:

$$\mathbf{B_{MV}} = \mathbf{T}.\mathbf{B} \tag{2.1}$$

where $B_{X_{MV}}$ is the field component that corresponds to $\hat{X}_{MV}$ (minimum variance direction), $B_{Y_{MV}}$ corresponds the maximum variance direction and $B_{Z_{MV}}$ corresponds to the intermediate variance.

In this thesis, MVA is used to determine the axis orientation of magnetic clouds observed in interplanetary space at 1 AU (Chapters 3 and 4). More on MVA and its application in the context of magnetic flux ropes is discussed in Chapter 3.

2.4.3 Cross-correlation

Cross-correlation is a measure of the similarity of two time-series as a function of a time-lag applied to one of them.

The correlation coefficient is calculated by firstly computing the covariance of two data series, which is a measure of how two variables, x and y change together,

$$Cxy(r) = [sum(x(i) - \bar{x})(y(i + r) - \bar{y}]/(n - r) \tag{2.2}$$

The value obtained for the covariance is divided by the standard deviations of x and y to produce a correlation coefficient in the range -1 to +1.

By considering the time delay corresponding to the maximum value of the cross-correlation function, cross-correlation can be used to determine the time delay of the observations made on one spacecraft with respect to those made on another spacecraft.

2.4.4 DeHoffmann-Teller Analysis

DeHoffmann-Teller Analysis is a means of identifying the frame of reference (HT frame) in which the electric field associated with an observed structure in a magnetised plasma is as small as possible (ideally zero), and in which the structure therefore appears as close as possible to being stationary. This concept was first used to analyse jump conditions across MHD shock waves (De Hoffmann and Teller, 1950), and is often employed now to identify the passage of a moving quasi-static structure, facilitating further analysis and interpretation of the data. This is possible since the existence of an HT frame indicates that a coherent quasi-stationary pattern of magnetic field and plasma velocity, such as a wave or current layer, is present.

The method of finding the HT frame, as derived in Khrabrov and Sonnerup (1998), fits the experimental data with a model in which the observed temporal variations and electric fields are caused entirely by the motion of the sampled structure with a velocity $V = V_{HT}$ relative to the instruments. The HT velocity vector, V_{HT} that best agrees with the set of measured values of $\mathbf{B}$ and electric field $\mathbf{E}$ is determined, making use of a least squares fit technique to minimise the residual electric field. Alternatively, $\mathbf{E}$ may be replaced with the convection electric field $-v \times \mathbf{B}$ when appropriate, and measured values of the plasma bulk velocity, v may be

used instead.

The existence of the HT frame implies that the magnetic field structure sampled is stationary when viewed in that frame. Most one-dimensional, time-independent current layers, including shocks, rotational and tangential discontinuities, can be transformed to a frame of reference where the electric fields either side of the layer disappear. However, there are some exceptions in which an intrinsic electric field component along the normal to the layer may remain in its interior. Figure 2.8 shows a simple illustration, in the form of a tangential discontinuity, for each of these cases. When the electric field in the layer does not tend to zero, then a "true" HT frame is not obtained. However, the measurements acquired inside these layers comprise only a small proportion of the total data set and so should not strongly influence the result. The resulting HT frame is usually unique and is useful for observational and theoretical studies of the layer.

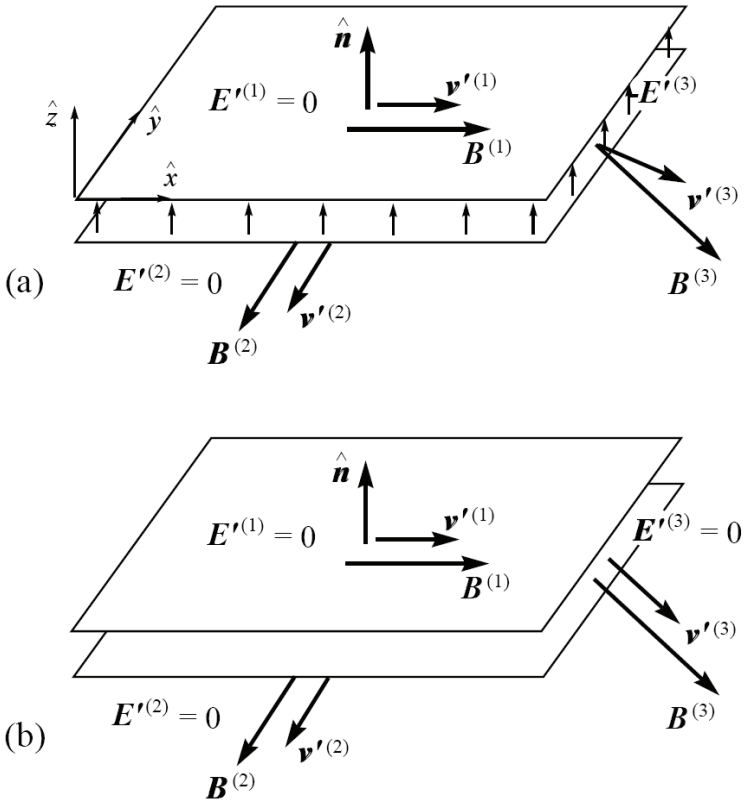

Figure 2.8: Magnetic field and velocity in the "proper" frame of a time-independent tangential discontinuity structure (a)when an intrinsic electric field $E'^{(3)}$ exists in the interior of the layer; (b)when $E'^{(3)} = 0$ so that the proper frame is also a true HT frame. Figure courtesy of Khrabrov and Sonnerup (1998). Permission to reproduce this figure has been granted by the International Space Science Institute.

To practically determine V_{HT} from experimental data, the residual electric field must be minimised, leading to the following linear equation for V_{HT}:

$$V_{HT} = K_0^{-1}\langle K^{(m)} v^{(m)} \rangle \tag{2.3}$$

where m is the number of measurements (m = 1, 2...M). In these expressions, each K^m is the matrix of projection, $P^{(m)}$, into a plane perpendicular to $B^{(m)}$, multiplied by $B^{(m)^2}$:

$$K_{\mu\nu}^{(m)} = B^{(m)^2}\left(\partial_{\mu\nu} - \frac{B_\mu^{(m)} B_\nu^{(m)}}{B^{(m)^2}}\right) \equiv B^{(m)^2} P_{\mu\nu}^{(m)} \tag{2.4}$$

The angle brackets $\langle ... \rangle$ denote an average of an enclosed quantity over the set of M measurements, and $K_0 \equiv \langle K^{(m)} \rangle$. Equation 2.3 gives V_{HT} in terms of the measured quantities, $v^{(m)}$ and $B^{(m)}$.

In this thesis, deHoffmann-Teller analysis is employed in Chapter 5 in the investigation of thin current sheets present within magnetic clouds in interplanetary space at 1 AU.

2.4.4.1 The Walén Relation

The Walén relation can be used to determine the normal component of the flow velocity and makes use of the determination of the deHoffmann-Teller frame, as described in § 2.4.4. It is used to examine the extent to which the plasma flow speed in the HT frame agrees with the Alfvén speed in a current layer.

A component-by-component scatter plot of these two velocities is referred to as a Walén plot. It is usual to expect that the plasma velocities remaining in the HT frame are very small relative to the calculated HT velocity and the Alfvén speed. When the flow velocity in the HT frame, $v'^{(m)}$ is observed to be proportional to the Alfvén velocity, $V_A^{(m)}$, it is interpreted as an indication that the region studied has the structure of an Alfvén wave, for which $\langle B^{(m)} \rangle \cdot \hat{n} \neq 0$ and $v'^{(m)} = \pm V_A^{(m)}$, where the sign on the right-hand side is the same as the sign of the product $\left(\langle v'^{(m)} \rangle \cdot \hat{n}\right)\left(\langle B^{(m)} \rangle \cdot \hat{n}\right)$. The comparison of measured data to this predicted behaviour is known as the Walén test and this provides a useful indication of whether magnetic reconnection is taking place in the region that is under examination, since the outflowing plasma and magnetic field in reconnection exhaust jets typically propagates with speeds of the order of the Alfvén speed.

Additionally, this relation can be used to determine the velocity of motion of the layer along the normal, from which the thickness of the layer may be determined.

In this thesis, the Walén test is used to investigate the presence of magnetic reconnection in and around magnetic clouds in interplanetary space at 1 AU (Chapter 5).

Chapter 3

Magnetic Clouds and their Solar Origins

In this Chapter, we address the issue of associating magnetic clouds with their solar origins. Locating the solar source of a magnetic cloud allows to compare observations of a CME near the Sun and in interplanetary space, so we can better understand the evolution of the structure as it propagates into the heliosphere. In § 3.1.1, we describe the current understanding of the topology of magnetic clouds. The range of observational signatures that are now understood to be associated with magnetic clouds is vast, and in § 3.1.2, we describe many of the typical magnetic field and plasma parameters observed *in situ*. Similarly, there are a number of signatures of CME eruption evident in the low corona and these are described in § 3.1.4. In § 3.1.5, we examine the associations that can be made between observations of a magnetic cloud in interplanetary space and coronal observations of its associated CME.

A magnetic cloud was observed *in situ* at 1 AU on 13 April 2006, and in § 3.2 we describe the process of locating its solar origins. We determine that the magnetic cloud originates from an unusually small solar source. The associated CME eruption was observed to occur in a small, northern hemisphere active region on 11 April 2006 (see § 3.2.3). Its link with the magnetic cloud observed *in situ* is discussed in § 3.2.3.1 and was established by considering the location of the CME eruption on the Sun, transit time, its helicity sign, the magnetic flux contained within the magnetic structure and its orientation.

3.1 Introduction

Understanding CMEs is a complex process. The observations currently available allow us to sample ICMEs in interplanetary space with *in situ* spacecraft, directly measuring the properties of the plasma and magnetic field within the structure. However, CMEs have often significantly evolved over the duration of their journey to a solar distance of 1 AU (e.g. Klein and Burlaga, 1982; Bothmer and Schwenn, 1994, 1998; Crooker and Horbury, 2006), and while coronagraph observations allow us to probe CMEs at an earlier stage of their outward propagation, and therefore nearer to their solar sources, they are unable to provide us with quantitative measurements of plasma and magnetic field parameters.

Combining remote observations from coronagraphs and *in situ* observations of CMEs allows us to associate an ICME observed in interplanetary space with its near-Sun counterpart, but this process is far from simple. Since CMEs propagate away from the Sun approximately radially, those ICMEs which are readily observed near Earth are typically halo CMEs which, as discussed in § 1.4.2, means that they surround the occulting disk in the coronagraph field of view, making their structure and radial velocity difficult to distinguish.

While coronagraph observations and *in situ* measurements provide much information on a CME's propagation and evolution from the Sun to 1 AU and beyond, there is a gap in the observations in the inner heliosphere between ~ 30 $R_\odot$ and 0.3 AU, and less is known about the structure and evolution of CMEs in this region. Although in recent years, observations from the Heliospheric Imager (HI) instruments onboard the STEREO spacecraft have begun to fill this gap, building on the work done to probe this region using Interplanetary Scintillation (IPS).

3.1.1 Magnetic Cloud Topology

The observed large-scale rotation of the magnetic field of magnetic clouds has led to the conclusion that they have a magnetic flux rope structure. The first ideas for the magnetic field configuration of magnetic clouds were proposed in the early 1980's when Burlaga *et al.* (1981) and Klein and Burlaga (1982) suggested that the magnetic field lines could be a family of helices, centred about the magnetic cloud axis.

As discussed in § 1.5.2.2, the force-free configuration of magnetic clouds, in which the electric current is parallel to the magnetic field, was considered by Goldstein (1983) and the equation $\nabla \times \mathbf{B} = \alpha \mathbf{B}$ obtained. Burlaga (1988) considered $\alpha =$

1 and obtained the cylindrically symmetric solution proposed by Lundquist (1950). With this solution, magnetic clouds are described as magnetic flux ropes. These are cylindrical configurations in which the magnetic field is directed along the axis of the flux rope towards the centre of the cloud and azimuthally towards the boundaries of the flux rope (Forbes *et al.*, 2006).

Flux rope fitting techniques can be an invaluable tool for describing *in situ* observations of magnetic clouds. However, it has proven difficult to assess their accuracy from single spacecraft data. The Lundquist (1950) magnetic cloud model often provides a fairly good fit to the experimental data and in many cases is more than sufficient to allow further analysis of the cloud. However, there are discrepancies, and in recent years other magnetic configurations have been proposed, such as spheromak solutions of the force-free equations (Ivanov and Kharshiladze, 1985; Vandas *et al.*, 1991; Vandas *et al.*, 1993) or toroidal solutions (Ivanov *et al.*, 1989; Romashets and Ivanov, 1991).

The effects of expansion of magnetic clouds and their interactions with the surrounding solar wind have also been considered (Osherovich *et al.*, 1993; Farrugia *et al.*, 1995; Marubashi, 1997). Coronagraph observations of CMEs have revealed that near to the Sun their cross-section is approximately circular, and so it might be expected that an ICME at 1 AU might also be roughly circular. However, an ICME's shape can become distorted as it propagates into the heliosphere, with the forces acting on the ICME in the direction of its motion different to those acting perpendicular to its motion (Forbes *et al.*, 2006). It is therefore possible that the cross-section of an ICME may become elliptical as it propagates into the heliosphere, and several non-force-free models have been developed to fit clouds with elliptical cross-sections and expanding clouds (Hidalgo, 2003). These scenarios are supported by observations of pressure gradients inside magnetic clouds.

As discussed in § 1.4.2, CMEs are frequently observed by coronagraphs to have a three-part structure as they leave the Sun, but this structure is often less clear when the associated ICME is observed *in situ*. The compressed material observed ahead of an ICME and the ICME ejecta itself are interpreted as corresponding to the bright, dense leading edge and the low density cavity of the CME. The third part of the structure; the dense core, which is believed to be comprised of cool, dense prominence material, is only occasionally encountered, identified *in situ* as dense plasma with unusually low ion charge states. There appears to be considerable variation in the distribution of apparent prominence material between the events studied and this may be due to either its 3-D distribution inside the ICME or to true ICME variability (Schwenn *et al.*, 1980; Burlaga *et al.*, 1998; Wurz *et al.*, 1998; Gloeckler *et al.*, 1999).

Magnetic clouds can become disconnected from the Sun at one or both footpoints as the cloud propagates to large solar distances. A conceptual model of how the field lines of the magnetic cloud could become disconnected from the Sun was developed by Gosling *et al.* (1995a) based upon an MHD simulation of flux rope release in Earth's magnetosphere (Hesse and Birn, 1991), in which reconnection between open and closed field lines progressively disconnects closed field lines. Observations of disconnected field lines in ICMEs are rare, and only the following two steps of the model are important for CMEs. The first step toward disconnection of a flux rope is partial disconnection, in which closed loops with sheared footpoints reconnect to form a flux rope that is still connected to the Sun at both ends. This is followed by the reconnection of an open field line with a field line in one of the legs of the flux rope to form an open coil in a process known as "interchange reconnection" (Crooker *et al.*, 2002), as illustrated in Figure 3.1.

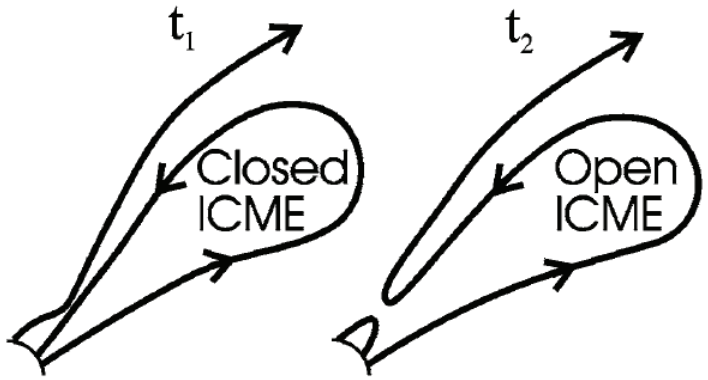

Figure 3.1: Before (t_1) and after (t_2) interchange reconnection acts to partially disconnect an ICME from the Sun. Figure adapted from Crooker *et al.* (2002). Permission to reproduce this figure has been granted by the American Geophysical Union.

There are still many unanswered questions about the large-scale structure of magnetic clouds. Although observations have shown that they take the form of a magnetic flux rope, the distribution of the current density within the flux rope, and the overall structure along the axial magnetic field are not well known. Multi-spacecraft, *in situ* observations are needed to resolve these issues (Forbes *et al.*, 2006).

3.1.2 *In situ* Signatures Associated with ICMEs

It is now well-established that ICMEs are the heliospheric counterparts of CMEs, with signatures that are clearly linked to the CME process. However, the event to event variability of ICME signatures is vast, making the association of a given magnetic cloud with its associated CME a complex and intricate process.

Identifying ICMEs *in situ* is far from straightforward and requires the study of a combination of different signatures to ensure correct identification of the ejecta. It is not yet clear why different identification methods yield different results, but possibilities include inhomogeneity of ICMEs, the variability of individual ICMEs depending on the solar source conditions, or the consequences of their evolution and propagation (Wimmer-Schweingruber *et al.*, 2006).

There exists a vast resource of *in situ* solar wind data, within which there are a great many observations of magnetic clouds. ICMEs have been studied at a number of locations in interplanetary space at a range of heliocentric distances. The Helios spacecraft have provided us with the closest measurements to the Sun to date, at distances of $\sim$ 0.3 AU (e.g. Burlaga *et al.*, 1982; Webb and Jackson, 1990; Webb *et al.*, 1993), while large number of clouds have been identified near 1 AU in the last 15 years with the WIND and ACE missions (e.g. Cane and Richardson, 2003a; Huttunen *et al.*, 2005; Wu and Lepping, 2007). There is also a plethora of data available at larger heliocentric distances up to 5 AU from the Ulysses spacecraft,, which continued to make measurements until June 2009, when it ceased operations after 18 years of monitoring the solar wind (Phillips *et al.*, 1992; Gosling *et al.*, 1995b; Riley *et al.*, 2000). Observations of ICMEs are also occasionally available from other spacecraft, such as Cluster and Geotail (e.g. Foullon *et al.*, 2005), whose primary objectives are not the study of the solar environment.

Before encountering the main body of an ejection, spacecraft located in the solar wind will often first observe a shock, followed by a region of shocked, compressed plasma and magnetic field known as the sheath (e.g. Tsurutani *et al.*, 1988), provided an ICME is travelling sufficiently quickly relative to the ambient solar wind. The nature of CME-driven shocks and the associated sheath regions are discussed in § 3.1.2.1. Magnetic clouds are typically preliminarily identified by three main criteria: the magnetic field rotates smoothly over a large angle during an interval of the order of one day, the magnetic field strength is higher than in the typical solar wind, and the proton temperature is lower than in the typical solar wind (Burlaga *et al.*, 1981; Klein and Burlaga, 1982; Burlaga, 1995). However, there are also many other observational signatures associated with this kind of ejecta, and in § 3.1.2.2 to § 3.1.2.4 the magnetic field, plasma and particle signatures that are most commonly associated with the *in situ* observations of ICMEs, and particularly magnetic clouds, are addressed. Although technically remote observations rather than *in situ* measurements, radio emissions can also be used to probe ICMEs in interplanetary space, as described in § 3.1.2.5.

3.1.2.1 Shocks and the associated sheath regions

Shock waves play an important role in both the solar corona and interplanetary space, since they are able to accelerate particles up to high energies (Forbes *et al.*, 2006). Interplanetary shocks can occur ahead of CMEs when the material ejected from the Sun propagates through interplanetary space with a speed in excess of the fast-mode magnetosonic speed in the solar wind; a shock must form to allow the accommodation of these two flow regimes. The propagation of ICME-driven shocks in the heliosphere is observed *in situ* in interplanetary space. It is also evident in coronagraph observations, type II radio emissions and Doppler scintillation measurements of spacecraft radio signals along lines of sight passing close to the Sun.

In the inner heliosphere, most shocks are ICME-related (Lindsay *et al.*, 1994) since most co-rotating interaction region shocks only form beyond 1 AU (Gosling *et al.*, 1976). Spacecraft in the solar wind will first see the fast forward shock, then the region of shocked, compressed plasma and magnetic field called the sheath, and finally the ICME plasma itself. Thus, ICME-driven shocks, while not a true signature of the ICME proper, are useful indicators of the possible presence of a following ICME and can be used as such successfully. Roughly 50 % of ICMEs are associated with interplanetary shocks (Marsden *et al.*, 1987) and fast CMEs with velocities in excess of 10^3 km s^{-1} certainly drive a shock wave ahead of them. The strength of the shock may initially decrease before increasing beyond 4 $R_\odot$ as the Alfvén speed decreases, then weakening as it expands out into the heliosphere. The shock is also generally stronger on the nose and weaker on the flanks (Forbes *et al.*, 2006). Slower shocks have been found to originate from those CMEs that are associated with filament eruptions (Cane *et al.*, 1986), and while all shocks generally decelerate in the inner heliosphere (Wu, 1988; Wu and Hada, 1991), slower shocks exhibit smaller variations in speed as they propagate to large solar distances than faster shocks. *In situ* data provides us with information on the shock normal and the shock speed that can help to determine which part of the ICME is observed. At the nose of the ICME, shock normals are expected to be radial, while they become less so towards the flanks (Szabo *et al.*, 2001).

The spatial extent of an ICME-driven shock is often much greater than its associated ICME, with studies suggesting that shocks are typically quasi-spherical over at least $\sim 100^\circ$ around the event longitude (Cane, 1988). Depending upon the location of the CME eruption on the solar disk relative to the *in situ* observing spacecraft, only the shock may be observed in some instances. When the CME source region is beyond $\sim 50^\circ$ east relative to the observing spacecraft, only the western flank of the shock is detected. As the source region moves closer to, then crosses the longitude

of the spacecraft, the shock is detected followed by the ICME. Finally, the source region moves beyond ∼50° west of the spacecraft and the eastern flank of the shock is detected, but not the ICME (Borrini *et al.*, 1982b; Cane, 1988; Richardson and Cane, 1993). ICMEs from less energetic events may be narrower.

The internal pressure of high-latitude ICMEs is sometimes higher than that of the ambient solar wind, resulting in their "over-expansion" (Gosling *et al.*, 1994) and the formation of forward-reverse shock pairs located on the leading and trailing edges of the ICME. Alternatively, Manchester and Zurbuchen (2006) propose that these shock pairs may form near solar minimum as a result of interactions between fast and slow solar wind streams deflected by the ICME. It is not typical for ICMEs bounded by forward and reverse shocks to be observed near Earth at 1 AU, since they are primarily observed in association with high latitude ICMEs.

The sheath is a region of shocked, compressed plasma sandwiched between the preceding shock and the body of the ejecta, which can last for many hours. Draping around the ICME may cause the magnetic field to be deflected out of the ecliptic (McComas *et al.*, 1989). This can result in the formation of a "planar magnetic structure" (PMS), which are extended regions where magnetic field vectors lie within a common plane, despite their variable direction (Nakagawa *et al.*, 1989) (see Figure 3.2). Draping of the magnetic field, together with the high density, compressed plasma in this region means these regions are often highly geoeffective (e.g. Huttunen *et al.*, 2005). If the preceding shock is perpendicular, then the compression is particularly strong and there is an increased probability of the occurrence of an intense geomagnetic storm (e.g. Tsurutani *et al.*, 1999; Jurac *et al.*, 2002; Siscoe and Schwenn, 2006).

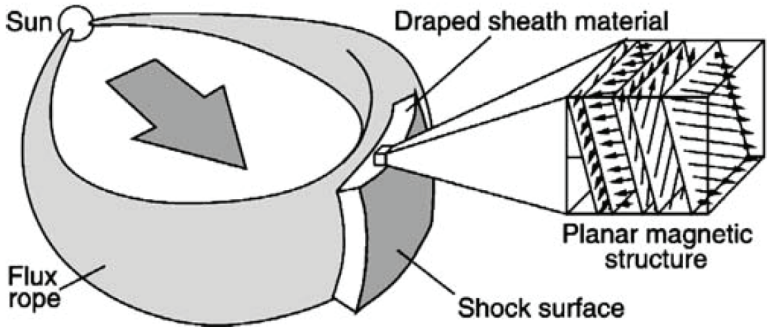

Figure 3.2: A fast-moving ICME compresses the solar wind ahead of it, leading to magnetic fields draped along this surface. This is termed a planar magnetic structure (PMS). Figure courtesy of Jones *et al.* (2002). Permission to reproduce this figure has been granted by the American Geophysical Union.

It is sometimes difficult to identify the boundary between the trailing edge of the sheath and the ICME, which is partly due to the dynamic nature of ICME

propagation, but may also be due in part to the evolution of the structure with time by processes like reconnection. This can result in a flux rope that is peeled away at the front, but has an extended "back" part (e.g. Cargill and Schmidt, 2002; Gosling *et al.*, 2005a).

3.1.2.2 Magnetic field of ICMEs

The magnetic field signatures of magnetic clouds have been extensively studied, since single spacecraft measurements through an ICME yield much information about the magnetic field structure. The magnetic field within ICMEs is significantly smoother than the highly variable "sheath" region which travels ahead of a fast ICME, and in which a great deal of turbulence is observed. Magnetic clouds characteristically show enhanced magnetic fields (>10 nT) that rotate slowly through a large angle over a time-scale of the order of 1 day. However, the magnetic field configurations of non-cloud-like ICMEs may be more complicated. The mean magnetic field intensity decreases with radial distance from the Sun as $R^{1.3}$ to $R^{1.5}$. This rate of decrease is slower than for the interplanetary magnetic field, whose orientation is subject to the Parker spiral (Forsyth *et al.*, 2006).

Large-scale, force-free, cylindrical models of magnetic flux ropes, like that of Lundquist (1950), suggest that the magnetic field in the axial direction is strongest towards the centre of the flux rope, whilst the azimuthal magnetic field direction displays a large-scale rotation. Observationally, it is usual to see a peak in the axial magnetic field near the centre of a magnetic cloud and it is expected that this component will tend to zero towards the boundaries of the magnetic cloud. A bipolar signature is often observed due to the reversal of the azimuthal magnetic field component of the flux rope, passing through zero towards the centre of the magnetic cloud. All these characteristics are guidelines to define the flux rope boundaries from the measured field components in, say, the GSE coordinate system. Boundaries need to be confirmed after rotating the magnetic data in the local MC coordinate system in order to fully separate the azimuthal and axial components. The process of identifying the boundaries of magnetic clouds is further discussed in § 3.1.3.

The direction of the magnetic field rotation within magnetic clouds has been found to be related to the solar cycle. A study by Bothmer and Schwenn (1998) of magnetic clouds observed by the Helios spacecraft between 1974 and 1980 revealed that 74 % of the clouds exhibited south to north rotations of the magnetic field vector. They later showed that the dominance of magnetic clouds with south to north rotation in odd cycles and north to south rotation in even cycles was likely a consequence of the magnetic configuration of their solar source regions, which has a

hemispheric dependence (Bothmer and Rust, 1997), as shown in Fig 3.3.

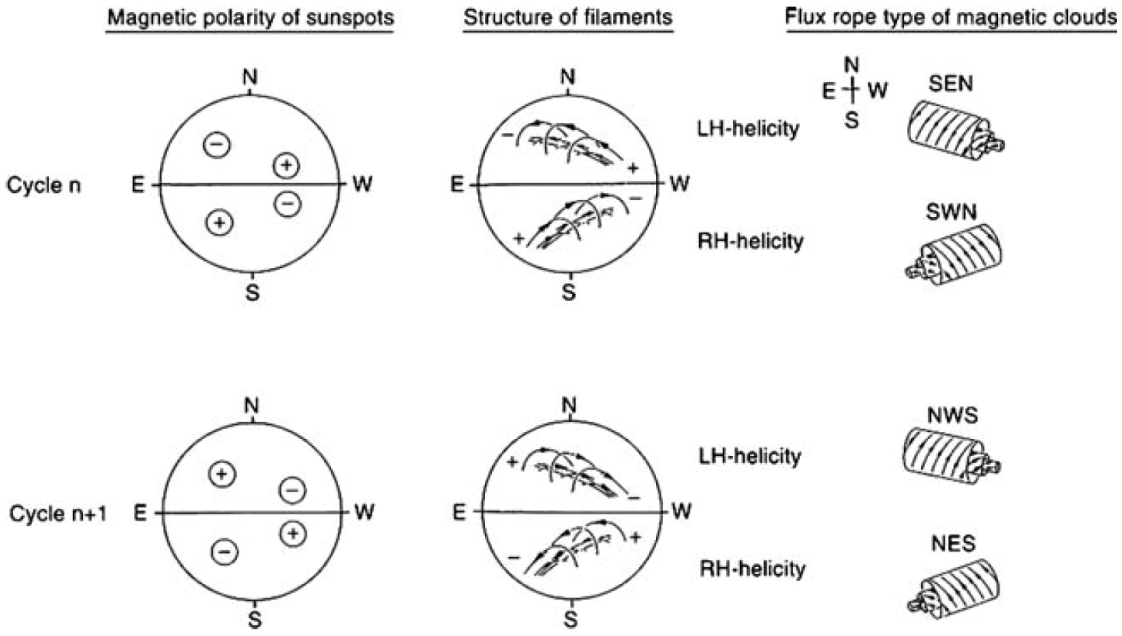

Figure 3.3: Solar cycle dependence of the magnetic structure of filaments at the Sun and of the corresponding magnetic clouds in interplanetary space. Figure courtesy of Wimmer-Schweingruber *et al.* (2006) and adapted from Bothmer and Schwenn (1998). Permission to reproduce this figure has been granted by Springer Science + Business Media.

3.1.2.3 Plasma dynamics of ICMEs

Studies of the behaviour of plasma within ICMEs has revealed an array of signatures from which not only are ICMEs in the solar wind identified, but the nature and evolution of these ejecta may be better understood.

The evolution of ICMEs in the solar wind is of great interest, and heavily dependent on the velocity of the ejecta. The velocity profile of the plasma within ICMEs is often observed to steadily decrease over the duration of the ejecta, and this is widely interpreted as a signature of expansion of the ICME in the rest frame of the solar wind, the details of which are discussed more fully in § 4.1.1.2. However, not all ICMEs exhibit expansion signatures and similar signatures may be associated with fast solar wind streams originating from coronal holes, so one must be wary of false ICME identification.

As discussed in § 1.3.6, plasma β describes the ratio of plasma pressure to magnetic pressure. In ICMEs, plasma pressure is typically low and magnetic pressure dominates, leading to low values of plasma β. Consequently, the measurements of plasma β in ICMEs are typically distinctly different to those in the ambient solar wind, where plasma β is relatively high, with values approaching 1. Figure 3.4 shows

how plasma β varies with solar distance, illustrating the transition from low beta values in the corona to high beta values in the solar wind.

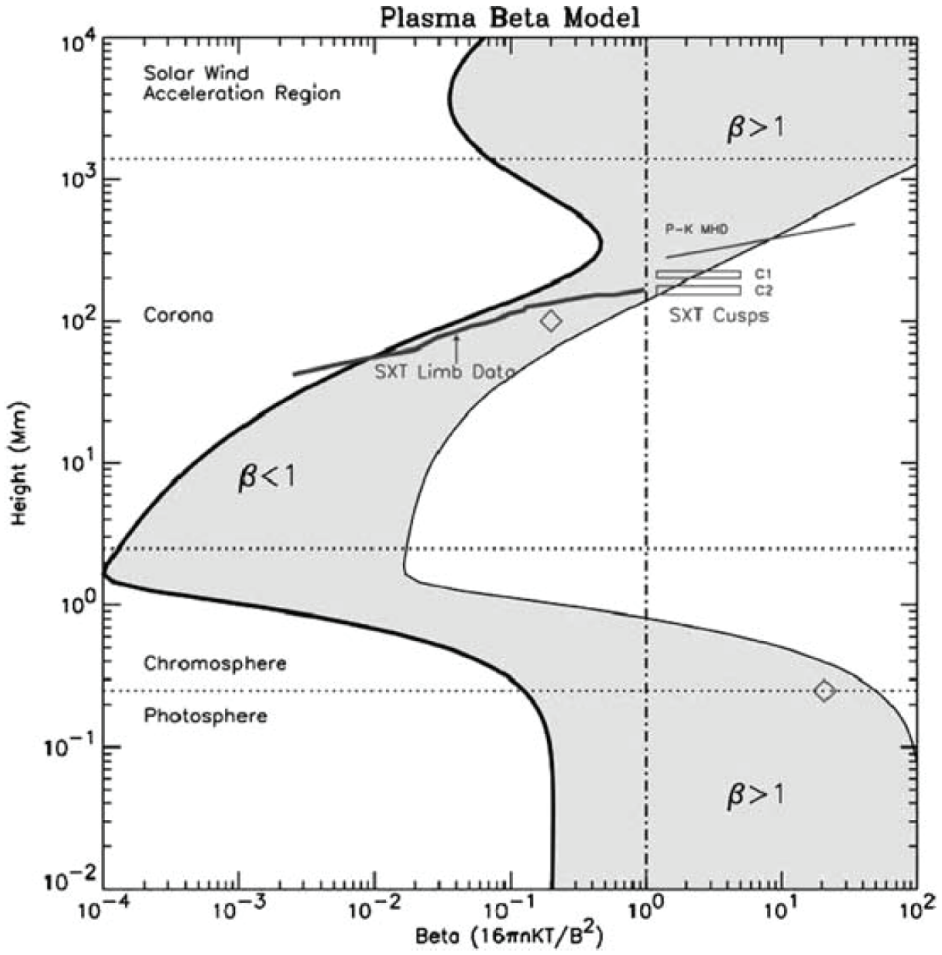

Figure 3.4: A survey of coronal plasma β as a function of height above the photosphere. Figure courtesy of Allen Gary (2001). Permission to reproduce this figure has been granted by Springer Science + Business Media.

Extreme density decreases (to < 1 cm^{-3}) are typically observed in ICMEs (Richardson *et al.*, 2000). Following the study of 46 magnetic clouds observed by Helios between 0.3 and 1 AU, Bothmer and Schwenn (1998) concluded that the mean density within these clouds decreases with heliocentric distance slightly faster than in the solar wind, where $n = 6.1R^{-2.1}$ cm^{-3} (R is in AU) (Schwenn, 1990). It has been shown that the radial size of a magnetic cloud increases as it propagates into the heliosphere, indicating expansion of the flux rope structure. Calculations of the density of a cloud depending on its distance from the Sun, based on observations of magnetic cloud expansion rates, suggest that density decreases as $R^{-2.56}$, and this value is found to agree reasonably well with observations (Bothmer and Schwenn, 1998), assuming that clouds are cylindrical in shape, the length of the flux rope is proportional to R, and mass is conserved within the flux rope. Further discussion of magnetic cloud expansion can be found in § 4.1.1.2.

Similarly, low proton temperatures relative to the ambient solar wind are expected (Gosling, 1990; Richardson and Cane, 1995; Mulligan *et al.*, 1999) as a result of expansion of an ICME in the solar wind. In the ambient solar wind there is an empirical correlation between the solar wind speed (V_{SW}) and plasma proton temperature (T_p) (Lopez, 1987). It was first noted by Gosling *et al.* (1973) that there are anomalous intervals of unusually low T_p in the solar wind, which were later shown to be linked to ICMEs, and Richardson and Cane (1995) found that $T_p < T_{ex}/2$ can be used as a criterion for identifying ICME ejecta in interplanetary space, where T_{ex} is the "expected T_p" determined from the empirical V_{SW} - T_p correlation and the simultaneously observed solar wind speed. T_p also shows a dependence on solar cycle; the fraction of the solar wind that has $T_p < T_{ex}/2$ increases from ≈ 4 % at solar minimum to ≈ 12 % around solar maximum.

Depressions of T_p are one of the most reliable signatures of ICMEs, and are present in most cases of ejecta (Richardson and Cane, 1995; Mulligan *et al.*, 1999). As with many of the signatures of ICMEs though, T_p depressions are not exclusive to ICMEs and other solar wind structures such as the heliospheric current sheet, may also exhibit this signature, so it is important to consider the solar wind context. It might be expected that adiabatic cooling due to ICME expansion will lead to faster cooling of ICME plasma, but this is not the case and the rate at which the proton temperature decreases is found to be similar in the solar wind data at Helios and data from spacecraft located at 1 AU (Totten *et al.*, 1995; Wang *et al.*, 2005).

Enhancements in the plasma electron temperature, T_e, relative to T_p are observed in some magnetic clouds (Osherovich *et al.*, 1993; Fainberg *et al.*, 1996; Sittler Jr. and Burlaga, 1998) and non-cloud ICMEs (Richardson, 1997), suggesting efficient transport of electron thermal energy along field lines connected to the corona (Zurbuchen and Richardson, 2006). Richardson (1997) suggested that $T_e/T_p > 2$ can be used as a more reliable indicator of an ICME, than considering T_e alone. As previously mentioned, magnetic clouds characteristically have low proton temperatures and low plasma β. When the threshold set by Richardson (1997) is exceeded, the plasma pressure becomes dominated by the electron component (Zurbuchen and Richardson, 2006).

One of the most utilised and reliable ICME composition signatures is the enhanced ratio of the relative abundances of α- particles (ionised helium) to hydrogen, N_α/N_p (Hirshberg *et al.*, 1970, 1972). This ratio is typically ~ 8 % in ICMEs, but it can reach ~ 25 % or more (Neugebauer, 1981; Borrini *et al.*, 1982b), compared to a value nearer to 3 - 5 % in the ambient solar wind (e.g. Neugebauer, 1981; Schwenn, 1990). The elevated value found in ICMEs compares well with the solar value of around 10 %. The values observed in ICMEs are a result of fractionation of the

solar wind helium content, which appears to act in the chromosphere and/or low corona (Laming and Feldman, 2001). One possible mechanism is inefficient Coulomb drag (Geiss *et al.*, 1970), in which helium experiences a smaller proton drag than other heavy ions and is fractionated against the bulk solar wind protons, leading to an enrichment in helium that cannot be lost to the photosphere and is ultimately cleared out by CMEs. This unusual composition is only observed in $\sim$ 30 % of ICMEs (Zwickl *et al.*, 1983; Mulligan *et al.*, 1999; Richardson and Cane, 2004), and magnetic clouds are more likely to exhibit a helium enhancement than non-flux rope ICMEs.

Detailed analysis of the composition of ICMEs, aside from enhanced N_α/N_p signatures, has only be possible since the 1990's with the launch of the Ulysses and, later, the ACE missions, but the charge-state composition of particles observed within ICMEs can provide a useful way to relate *in situ* plasma and magnetic field observations to their solar source (e.g. Hundhausen *et al.*, 1968; Geiss *et al.*, 1995). ICMEs may include enhancements in heavy ion abundances (Mitchell *et al.*, 1983; Ipavich *et al.*, 1986) and enhanced ion charge states (Bame *et al.*, 1979; Fenimore, 1980; Ipavich *et al.*, 1986). The thermal environment of ICMEs and their associated CMEs can be better understood by considering the ionic charge state of heavy ions (Hundhausen *et al.*, 1968; Buergi and Geiss, 1986), and the elevated ionic charge states observed in many ICMEs are indicative of high temperature origins and may well be a signature of magnetic fields reconnecting during CME eruption (e.g. Galvin, 1997; Wimmer-Schweingruber *et al.*; Henke *et al.*, 2001; Lepri *et al.*, 2001; Zurbuchen *et al.*, 2003; Richardson and Cane, 2004; Rodriguez *et al.*, 2004; Lepri and Zurbuchen, 2004). Enhanced iron (Fe) charge states have been identified in roughly 50 % to 70 % of all ICMEs, while in a smaller fraction of ejecta and preferentially associated with magnetic clouds, enhancements in oxygen charge states, where $O^{7+}/O^{6+} > 1$ are observed, though a relative enhancement of O^{7+}/O^{6+} might be a more reliable ICME indicator (Richardson and Cane, 2004). The charge states of these ions are frozen in to the plasma near the Sun at the very high temperatures found in the corona; the exact temperatures are determined by the balance between ionisation and recombination times and the expansion time for the solar wind (Hundhausen *et al.*, 1968). Unusually low charge states, like He^{+}/He^{2+}, are also occasionally observed in ICMEs and imply low coronal temperatures and the presence of prominence material of chromospheric origin, although observations of low charge states in ICMEs is very rare (e.g. Schwenn *et al.*, 1980; Gosling *et al.*, 1980).

Observations of elemental composition in ICMEs can be used to probe the conditions in the solar corona prior to a CME eruption, and may prove useful in distinguishing between CME initiation models. However, the range of variability of

elemental abundances in ICMEs is large, both from event to event as well as within an individual event. It ranges from no compositional signature at all relative to the ambient solar wind, to unusual events with compositions never seen in other contexts (Wimmer-Schweingruber *et al.*, 2006).

3.1.2.4 Suprathermal electron signatures

Particles with energies higher than those that constitute the core of solar wind distributions serve as tracers of magnetic field lines. They gyrate about field lines, like core particles, but their considerably higher velocity components result not only in larger gyroradii but in high field-aligned speeds that create particle beams (Crooker and Horbury, 2006). At 1 AU, the contribution from the core population begins to significantly decrease and the electrons become suprathermal at around 70 eV. Electrons > 250 eV are well within the suprathermal range, and the distribution at this energy typically includes very little of the core electron population and the count rates are high; resulting in very few artefacts being introduced to the data at this energy.

Counterstreaming beams of suprathermal electrons, which normally focus into a single field-aligned "strahl" directed away from the Sun (Pilipp *et al.*, 1987), are typically associated with ICMEs (Zwickl *et al.*, 1983; Gosling *et al.*, 1987) and tell us about the connectivity of magnetic field lines to the Sun. As tracers of magnetic field lines, suprathermal particles can help us to distinguish between the possible topologies of the magnetic structure. When a counterstreaming beam of suprathermal electrons is observed, it indicates the presence of closed field lines that are still connected to the Sun at both ends. These beams are physically interpreted as electrons flowing in opposite directions along magnetic field loops within ICMEs that are connected to the Sun. It is common for unidirectional beams to also be observed within an ICME, indicating that one of the footpoints is no longer connected to its solar source, while a lack of beams, termed a "heat flux dropout" in the observations of these electrons implies a mix of open and closed fields (e.g. Gosling *et al.*, 1995a; Shodhan *et al.*, 2000; Crooker *et al.*, 2004; Crooker and Horbury, 2006) and suggests that some field lines are disconnected from the Sun at both ends, but this signature is not sufficient for an observer to be certain that this is the case (Crooker *et al.*, 2002, 2003). Counterstreaming suprathermal electron beams are now one of the most widely-used signatures in ICME identification. Nearly all ICMEs observed within 5 AU of the Sun contain some closed field lines, and on average appear to contain more closed than open fields (~ 60 % in magnetic clouds at 1 AU) (Shodhan *et al.*, 2000).

Counterstreaming electron flows have also been used to explore magnetic cloud field polarities. Electron flows are usually stronger in one direction. If the dominant electron flow is assumed to be from the footpoint closer to the spacecraft, the relative directions of the field and electron flow indicate the field polarity, which should be constant during the magnetic cloud encounter assuming a single flux rope configuration. However, Kahler *et al.* (1999) found changes in polarity which cannot be explained by a single flux rope.

When using suprathermal electron fluxes to investigate ICMEs, care must be taken to avoid confusing the bidirectional electron flows expected in association with ICMEs with similar signatures that can be exhibited by other solar wind events. Shocks may also exhibit counterstreaming electron signatures (Gosling *et al.*, 1993), usually observed as a beam of electrons flowing opposite to the electron outflow from the Sun (Wimmer-Schweingruber *et al.*, 2006). However, the short duration ($<$ 1 hr) of shock-related beams allows them to be distinguished from ICME-associated beams, which are typically longer duration events. Mirroring on field lines connected to regions of elevated magnetic field magnitude can also result in counterstreaming on open field lines (Gosling *et al.*, 2001), but electron fluxes on open fields can be distinguished from those on closed fields by careful examination of the shape of the pitch angle distribution.

Other particle signatures of ICMEs include short-term depressions in the cosmic ray intensity on the time-scale of a few days, bidirectional energetic particle flows, and unusual flow directions during solar energetic particle onsets (Zurbuchen and Richardson, 2006).

Table 3.1 provides a summary of the known *in situ* signatures of ICMEs at $\sim$ 1 AU.

3.1.2.5 Radio observations

Although technically remote observations rather than *in situ* measurements, radio emissions are also used to probe ICMEs in interplanetary space.

Type II radio emissions are a signature of shocks generated both in the corona, where metric type II bursts are produced, and ahead of ICMEs (Cane *et al.*, 1987), which produce hectometric-kilometric type II bursts during their propagation in the interplanetary medium. They are generated at the plasma frequency and its harmonic by electrons accelerated at the shock front (Lengyel-Frey *et al.*, 1985), and while the observed frequency is directly related to the plasma density near

Table 3.1: *In situ* signatures of ICMEs (description applies to ∼1 AU heliospheric distance) in the magnetic field (B), plasma dynamics (P), plasma composition (C), plasma waves (W), and suprathermal particles (S).

Signature	Description	Selected references
B1: B Rotation	$\gg 30^{\circ}$, smooth	Klein and Burlaga (1982)
B2: B enhancement	> 10 nT	Hirshberg and Colburn (1969); Klein and Burlaga (1982)
B3: B variance decrease		Pudovkin *et al.* (1979); Klein and Burlaga (1982)
B4: Discontinuity at ICME boundaries		Janoo *et al.* (1998)
B5: Field line draping around ICME		Gosling *et al.* (1987); McComas *et al.* (1989)
B6: Magnetic clouds	(B1, B2 and $\beta = \frac{\sum nkT}{B^2/(2\mu_0)} < 1$)	Klein and Burlaga (1982); Lepping *et al.* (1990)
P1: Declining velocity profile/expansion	Monotonic decrease	Klein and Burlaga (1982); Russell and Shinde (2003)
P2: Extreme density decrease	≤ 1 cm^{-3}	Lepping *et al.* (1990)
P3: Proton temperature decrease	$T_p < 0.5 T_{exp}$	Gosling *et al.* (1973); Richardson and Cane (1995)
P4: Electron temperature decrease	$T_e < 6 \times 10^4 K$	Montgomery *et al.* (1974)
P5: Electron temperature increase	$T_e \gg T_p$	Sittler Jr. and Burlaga (1998); Richardson (1997)
P6: Upstream forward shock/"Bow Wave"	Rankine-Hugoniot relations	Parker (1961)
C1: Enhanced α/proton ratio	$He^{2+}/H^{+} > 8$ %	Hirshberg *et al.* (1972); Borrini *et al.* (1982a)
C2: Elevated oxygen charge states	$O^{7+}/O^{6+} > 1$	Henke *et al.* (2001); Zurbuchen *et al.* (2003)
C3: Unusually high Fe charge states	$\langle Q \rangle_{Fe} > 12$; $Q_{Fe}^{>15+} > 0.01$	Bame *et al.* (1979); Lepri *et al.* (2001); Lepri and Zurbuchen (2004)
C4: Occurrence of He^{+}	$He^{+}/He^{2+} > 0.01$	Schwenn *et al.* (1980); Gosling *et al.* (1980); Gloeckler *et al.* (1999)
C5: Enhancements of Fe/O	$\frac{(Fe/O)_{CME}}{(Fe/O)_{photosphere}} > 5$	Ipavich *et al.* (1986)
C6: Unusually high $^3He/^4He$	$\frac{(^3He/^4He)_{CME}}{(^3He/^4He)_{photosphere}} > 2$	Ho *et al.* (2000)
W1: Ion acoustic waves		Fainberg *et al.* (1996); Lin *et al.* (1999)
S1: Bidirectional strahl electrons		Gosling *et al.* (1987)
S2: Bidirectional ∼ MeV ions	2nd harmonic > 1st harmonic	Palmer *et al.* (1978); Marsden *et al.* (1987)
S3: Cosmic ray depletions	Few % at ∼ 1 GeV	Forbush (1937); Cane (2000)
S4: Bidirectional cosmic rays	2nd harmonic > 1st harmonic	Richardson *et al.* (2000)

Table adapted from Zurbuchen and Richardson (2006). Permission to reproduce this table has been granted by Springer Science + Business Media.

the shock, the drift rate provides a rough estimate of the shock speed. The first clear detection of type II bursts, at kilometric wavelengths, was made by the radio receivers onboard the IMP-6 spacecraft (Malitson *et al.*, 1973), and observations of this type are now routinely made with radio instruments like WAVES onboard the WIND spacecraft, and the instrument of the same name onboard the STEREO spacecraft (e.g. Gopalswamy *et al.*, 2008, 2009).

The density in the heliosphere falls off with distance. This information allows the location of the source of kilometric type II radio bursts to be determined from the measured frequency of these emissions. Frequencies as low as 20 or 30 kHz are often detected, which correspond with the densities typically measured at 1 AU, of 5 to 10 cm^{-3}. This suggests that the CME-driven shocks producing these radio signals extend well into interplanetary space and that the frequency drift rate of the associated type II emissions can therefore be used to track CMEs and shocks through the heliosphere, beyond the limit of the white-light coronagraph observations (Schwenn *et al.*, 2006). Figure 3.5 illustrates the frequency drift of type II radio bursts for an ICME on January 14 2002, observed by the WAVES instrument onboard the WIND spacecraft.

As discussed in § 3.1.2.1, only when the discrepancy between the speed of a CME and the ambient solar wind is sufficiently high will a shock be generated, and this

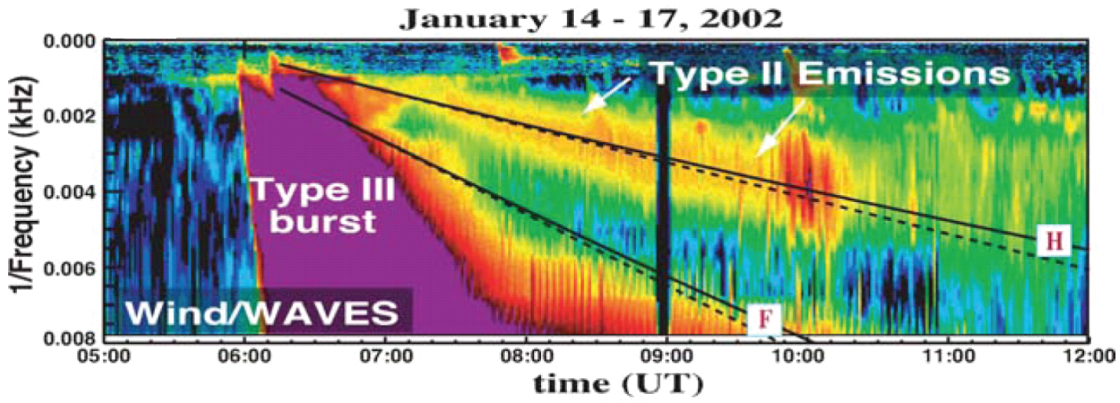

Figure 3.5: A plot of intensity as a function of 1/frequency and time showing frequency drifting type II radio emissions for an ICME on 14 January 2002. Figure from Forsyth *et al.* (2006) and adapted from (Reiner *et al.*, 2003). Permission to reproduce this figure has been granted by Springer.

typically means that only fast CMEs drive a shock ahead of them. Whilst tracking the radio emissions from CME-driven shocks is considered a relatively accurate means of determining the velocity profile of ICMEs during their propagation in interplanetary space, this is only feasible when a strong shock is generated. There are many instances of ICMEs with no associated shock or only a weak shock and these events do not typically exhibit signatures that can be detected in radio observations.

3.1.3 Identifying Magnetic Cloud Boundaries

The exact locations of ICME boundaries are often difficult to ascertain with absolute certainty (Goldstein *et al.*, 1998; Wei *et al.*, 2003), since the various ICME signatures evident in the magnetic field, plasma and particle observations do not define precisely the same regions of the solar wind (Zwickl *et al.*, 1983; Crooker *et al.*, 1990; Richardson and Cane, 1995; Neugebauer *et al.*, 1997; Mulligan *et al.*, 1999). This is not unexpected given that the various signatures all arise from different physical phenomenon. The internal structure of ICMEs is also sometimes highly inhomogenous, increasing the difficulty of locating the boundaries with different ICME signatures. It is not unusual for a number of possible boundaries to be identified in the data, however rather than clarifying the situation, the inclusion of additional observations, like those of ion and electron beams and solar wind composition data, often results in the identification of more possible boundaries (e.g. Zwickl *et al.*, 1983; Crooker *et al.*, 1990; Neugebauer *et al.*, 1997; Richardson *et al.*, 2003).

At the boundary of a magnetic flux rope, a current sheet is generally expected since there is a change of connectivity of magnetic field lines (from twisted field

lines inside the flux rope to solar wind-like field lines outside). Then, the in- and out-bound boundaries in *in situ* data are typically expected where magnetic discontinuities are present (e.g. Dasso *et al.*, 2006). While in some cases such discontinuities can be identified with little ambiguity, in other cases the boundaries are less distinct and may include complex structures, perhaps indicative of waves or field line reconnection (Vasquez *et al.*, 2001).

Dasso *et al.* (2006) report that reconnection can be forced in front of an MC when a flux rope is overtaking the magnetic field ahead of it. The consequence of this reconnection is a flux tube that is peeled away at the front, but has an extended back part. This "back" region is expected to exhibit different behaviour to both the main body of the ejecta and the solar wind, but its presence increases the complexity of accurately identifying the rear boundary of a magnetic cloud.

Minimum variance analysis (see § 2.4.2) can also prove useful in determining the location of magnetic cloud boundaries. When the magnetic field data are transformed to the local cooordinates of the magnetic cloud, using MVA, the interval exhibiting the clearest rotation defines the region of the magnetic cloud. In addition, the eigenvalue separation is largest when the minimum variance direction is well-defined and the flux rope boundaries may be further refined by considering this criterion.

3.1.3.1 Limitations of single spacecraft observations

Several theoretical models have been proposed for the topology of magnetic clouds, but a comparison of theoretical predictions with physical observations is complicated. Although magnetic clouds are three-dimensional objects, the experimental data are limited to observations along a line that traces the trajectory of a spacecraft through the cloud as it propagates into interplanetary space (Forbes *et al.*, 2006). This means that while models must include the magnetic field topology, consideration should also be given to the position inside the cloud where experimental data are obtained.

Minimum variance analysis (see § 2.4.2) can be utilised to estimate the trajectory of a spacecraft through a magnetic cloud. The magnetic field components obtained from MVA are used to provide an approximation of the impact parameter, p, defined as the minimum distance from spacecraft to the cloud axis. A small impact parameter indicates that the spacecraft passes close to the magnetic cloud axis and near to the "nose" of the flux rope, while larger impact parameters suggest that the spacecraft is more likely to be passing through a "leg" of the flux rope.

The technique employed to estimate the impact parameter from MVA used in this thesis was developed by Gulisano *et al.* (2007) and is valid for the force-free Lundquist (1950) model. The deviation from zero of the mean value of the $B_{x,cloud}$ component of the magnetic field (in the direction of minimum variance) can be used to obtain an estimation of p:

$$p \approx R\sqrt{\frac{< B_{x,cloud} >}{1.6B_0}} \tag{3.1}$$

where R is the radius of the MC and B_0 is the magnetic field strength at the centre of the magnetic cloud determined from the results of the minimum variance analysis.

Multi-spacecraft observations of individual ICMEs provide unique information on their structure and boundaries. The vast spatial extent of CMEs means that it is possible for multiple, widely-separated spacecraft to sample an ICME at different points. It also provides the potential for ICMEs to be observed at multiple locations simultaneously. Such observations are rare, but the availability of *in situ* measurements over a significant period of time means that there are now a number of events for which multi-spacecraft observations from missions like Helios 1 and 2, WIND, ACE and Cluster are available. Observations at different spacecraft may vary depending upon the event under study and the spacecraft separation. When considering observations of ICMEs at different spacecraft, it is important to establish if the ICMEs at different locations are related and not just assume that they are part of the same event (e.g. Cane *et al.*, 1991).

3.1.4 On Disk Solar Signatures Associated with CMEs

Morphological changes in the corona often provide evidence of a CME eruption. The development in the low corona of large CMEs is often fast and is accompanied by an opening of the magnetic field over a large region. In this section, we discuss disappearing filaments (§ 3.1.4.1), large-scale dimmings observed in EUV and soft X-rays (§ 3.1.4.2), coronal waves (§ 3.1.4.3) and coronal loop structures (§ 3.1.4.4), which are all signatures of the opening of the magnetic field.

3.1.4.1 Disappearing filaments

Ground-based emission line observations can be used to look at the conditions on the Sun prior to eruption, allowing the chain of events leading up to the eruption of a CME to be studied. Features associated with solar activity such as flares and filaments are best observed in the Hα line. Filaments, or eruptive prominences, frequently accompany CMEs (Hundhausen, 1993; Hanaoka *et al.*, 1994; Gopalswamy *et al.*, 1996). When a filament begins to rise in the course of a CME, the Hα emission is Doppler shifted and may no longer be visible in narrow band images. These are termed "Disappearing Filaments". Figure 3.6 shows Hα observations of a disappearing filament associated with a halo CME on 5 January 2005.

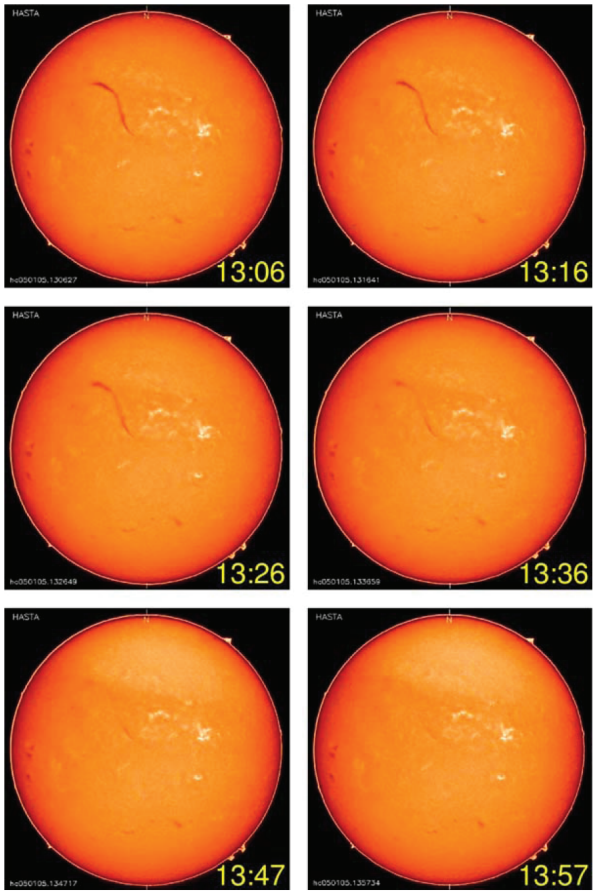

Figure 3.6: A disappearing filament associated with a halo CME was observed in Hα by the HASTA-telescope on 5 January 2005. Figure courtesy of Schwenn *et al.* (2006). Permission to reproduce this figure has been granted by Springer Science + Business Media.

Yang and Wang (2002) showed that the connection between filament disappearances observed in the Hα spectral line and CMEs is weak, ranging from 10 % to 30 %, but a study by Jing *et al.* (2004) has suggested that this figure might be nearer to 56 %, since they distinguished between filament disappearances and eruptions, excluding those that did not erupt and filaments < 2000 arcsec^2 in size. Filament disappearance does not alway imply filament eruptions. Depending on their physi-

cal nature, disappearing filaments can re-appear. Mouradian *et al.* (1995) proposed two possible processes by which filaments could "disappear", the first is by dynamic sudden disappearance (DSD), due to the restructuring of the magnetic field, ultimately leading to the disappearance of a filament through eruption and the second possibility is thermal disappearance (THD), due to heating of the plasma in the filament so that it is no longer visible in the Hα spectral line. The filament may then re-appear as it cools. It can be difficult to distinguish between these two processes, but looking for ascending motion using EUV observations and evolution of its geometrical shape help to establish if a filament is erupting.

3.1.4.2 Coronal dimmings

Following a CME eruption, large-scale transient dimming features, known as "coronal dimmings" (Hudson *et al.*, 2003), are often observed in the vicinity of the eruption and are most conspicuously observed by EUV imaging instruments such as SDO/AIA, its predecessor TRACE and SOHO/EIT. Dimming regions are also visible at soft X-ray wavelengths (Sterling and Hudson, 1997); most recently observed by Hinode/XRT, which is now building on the observations made in the past by Yohkoh/SXT. Dimmings are often detected as a relative deficit of coronal emission, compared with pre-CME conditions and appear suddenly like transient coronal holes on the Sun's disk (Rust, 1983), persisting for many hours. In the conventional 2-D picture of field-line opening followed by magnetic reconnection, the transient coronal holes represent the opened field; in 3-D they would represent the footpoints of a large-scale flux rope, and coronal dimmings generally map out the apparent footpoints of CMEs observed in white-light (Thompson *et al.*, 2000).

Coronal dimmings have been interpreted as the opening of the closed field lines during the initial phase of a CME, resulting in the rapid evacuation of coronal material and indicating mass loss of the order of 10^{14} g (Hudson *et al.*, 1996). This is an order of magnitude smaller than the mass loss in a typical CME, inferred from coronagraph observations, but it suggests that at least part of the mass loss can be detected by observing dimmings. Spectroscopic measurements in dimming regions have indicated significant outflow velocities, confirming that plasma is indeed being expelled (Harra and Sterling, 2001).

Dimmings can be most clearly depicted in coronal images by taking difference images. In the case of "running difference" images, each image has the previous frame subtracted, while "base difference" images involve the subtraction of a pre-event "base" image from all subsequent images. This technique allows changes in the intensity in the corona to be more clearly observed, allowing the boundaries of

the dimming regions to be defined. Figure 3.7 is a base difference image showing the dimmings (darker regions of lower intensity) associated with a CME eruption on 12 May 1997 (brighter region of increased intensity). Observations of dimmings often demonstrate that plasma removal is on a global scale. In many cases the dimmings are trans-equatorial, and are observed to spread to large distances from the initial erupting site (Cargill and Harra, 2007). By progressive stepping reconnection with the surrounding bipoles, the erupting configuration becomes large-scale even in the low corona (Attrill *et al.*, 2007).

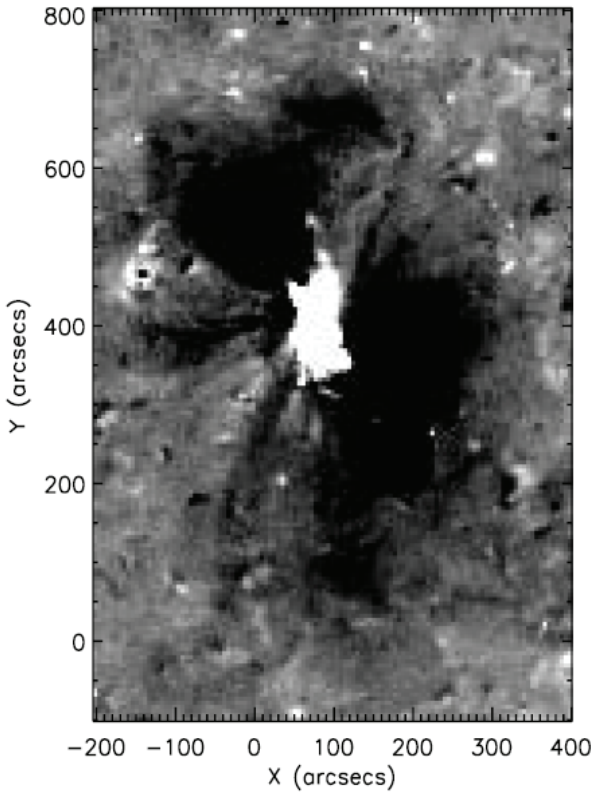

Figure 3.7: A base difference image showing the maximum spatial extent of the coronal dimming regions (darker regions of lower intensity) associated with a CME eruption on 12 May 1997 (brighter region of increased intensity). Figure adapted from Attrill (2008b). Permission to reproduce this figure has been granted by Springer Science + Business Media.

The post-CME recovery appears in the low corona as the disappearance of the newly-formed dimmings. It seems reasonable to believe that magnetic reconnection, either on a large-scale or by reconnection interchange on smaller spatial scales, could contribute to the replenishment of the lost coronal mass by providing closed flux tubes capable of trapping charged particles (Attrill *et al.*, 2007). Reconnection with closed loops will "step" the "open" magnetic field out of the dimming (dispersing the "open" flux), whilst reconnection with "open" magnetic field will physically disconnect the magnetic field line from the Sun.

It was believed that when the intensity of the dimming recovers to pre-event levels, this indicates that the CME is disconnected from the Sun, however it has re-

cently been shown by Attrill *et al.* (2008a) that this is not necessarily the case. Unidirectional/bidirectional suprathermal electron flows observed at 1 AU provide an indication of an ICME's connectivity to the Sun. Given the detection of suprathermal electron flows at 1 AU after the associated dimmings are expected to recover, reconnection with closed magnetic field appears to be dominant and acts to disperse the "open" magnetic field out into regions of quiet Sun, thus recovering the intensity of the dimmings whilst maintaining the magnetic connectivity to the Sun.

3.1.4.3 Coronal waves

Coronal waves are large disturbances that travel across the disk of the Sun (Moses *et al.*, 1997; Thompson *et al.*, 1998), and are often colloquially referred to as "EIT waves", since this phenomenon was first observed by the EUV Imaging Telescope (EIT) onboard the SOHO spacecraft. These waves appear as a bright front of enhanced EUV emission, propagating quasi-radially away from a source region over a hemisphere of the Sun at speeds of 200 to 300 km s^{-1}. Processed images are used to study coronal waves because they are too subtle to easily detect in raw data. "Running difference" images may be used to show the extent of a disturbance, whilst "base difference" images must be used to show real enhancements (brightenings) and depletions (dimmings) in intensity (Attrill, 2008b). Figure 3.8 shows running difference images of an EIT wave propagating across the solar disk on 24 September 1997.

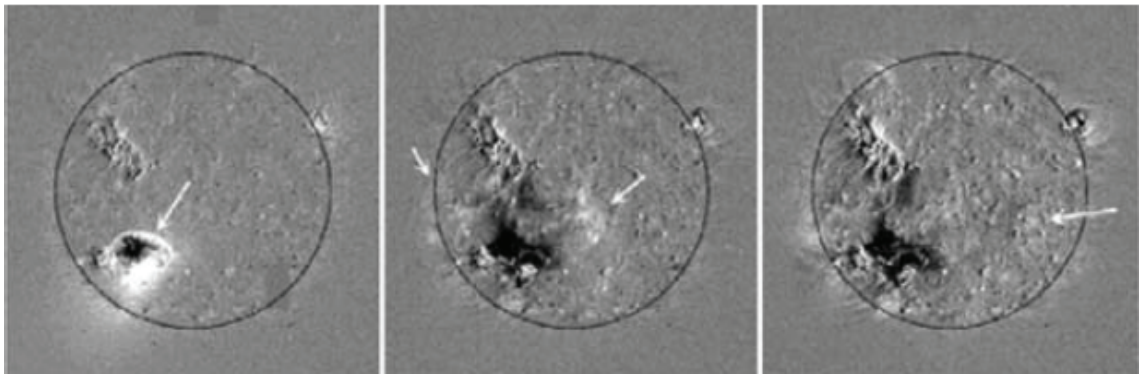

Figure 3.8: Running difference images of an EIT wave that propagated across the solar disk on 24 September 1997. The arrows indicate the EIT wave-front. Figure adapted from Biesecker *et al.* (2002). Permission to reproduce this figure has been granted by Institute of Physics Publishing.

The exact nature of these waves is not fully understood, and it is not yet clear if they are a coronal manifestation of the well known Moreton waves seen in Hα. These waves have been identified as the chromospheric trace of a shock wave emanating from a flare site and typically propagate more quickly than EIT waves at speeds ranging from 440 to 1125 km s^{-1}, with a mean value of 650 km s^{-1} (Smith and

Harvey, 1971). Alternatively, it has been suggested by Delannée (2000) that the coronal wave is actually a CME lifting off the disk, with the wave being the stretching or opening of closed magnetic field lines in response to an erupting filament. EIT waves have a strong association with CMEs (Biesecker *et al.*, 2002) and often with EUV dimmings, which are usually restricted to the region traced by the transit of Moreton waves and trail the bright front.

3.1.4.4 Post-eruption coronal loop structures

Long duration flares observed at soft X-ray wavelengths are closely associated with CMEs (Sheeley *et al.*, 1983; Webb and Hundhausen, 1987). These are observed as the appearance of large-scale loop systems, also called eruptive arcades or post-eruptive arcades, which often form and evolve in the aftermath of coronal eruptions and are observed to occur in the lower corona close to the onset site of the eruption. Their detection depends on their temperature, therefore on the wavelength in which the observations are made. Post-eruptive arcades observed at 195 Å by SOHO/EIT have almost one-to-one correlation with CMEs (Tripathi *et al.*, 2004). Figure 3.9 shows an example of EUV observations of a post-eruption arcade.

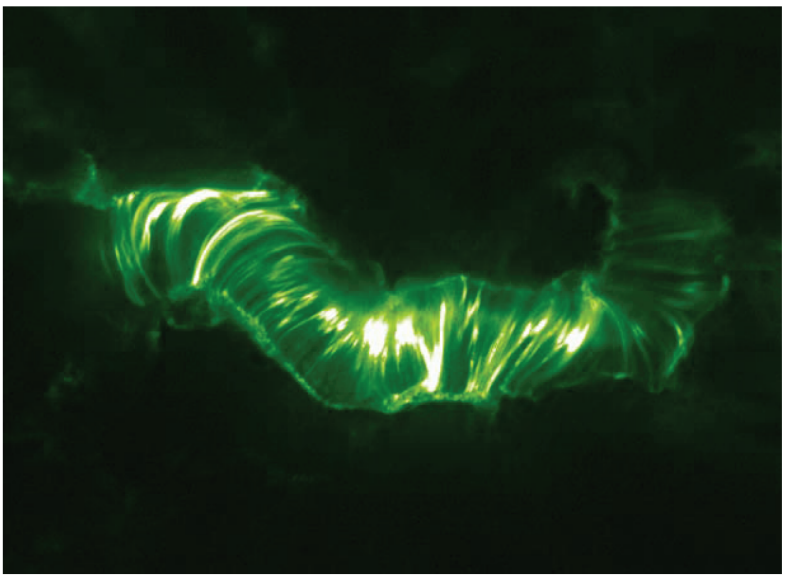

Figure 3.9: EUV observations from TRACE at 195 Å of a post-eruption arcade associated with flare activity during the Bastille day event on 14 July 2000. The field of view is 2.3 $\times$ 10^5 by 1.7 $\times$ 10^5 km. Figure courtesy of Schwenn *et al.* (2006). Permission to reproduce this figure has been granted by Springer Science + Business Media.

The global response of the corona to a CME eruption is evident in large-scale loop structures. Trans-equatorial loops are present in a significant fraction of all active regions. The overall structure of the large trans-equatorial loop changes as a result of reconnection between two active regions (Tsuneta, 1996b), and a trans-

equatorial loop has been observed to disappear, forming part of a CME (Khan and Hudson, 2000). In fact, front-side halo events may start with the disappearance of trans-equatorial loops, observed in X-rays (Pohjolainen *et al.*, 2001). Further evidence of reconnection in coronal loop structures include observations of rising loops, a cusp-shaped loop structure and cool loops lying underneath hot loops.

Cusp-shaped features are evident in soft X-ray images during the late phase of a CME-related flare. The cusp may have an elevated temperature (Tsuneta *et al.*, 1992) and this morphology points to an energy source in the solar corona, which many models suggest indicates large-scale reconnection (Pick *et al.*, 2006).

3.1.5 Linking Magnetic Clouds and their Solar Sources

Linking magnetic clouds with their associated coronal eruptions can be far from simple and requires consideration of a number of physical characteristics that can provide quantitative links between a CME observed near the Sun and subsequently in the interplanetary environment. There are a number of constraints that must be placed on the association between CMEs and their associated MCs: the relative location of the solar source and the spacecraft detecting the ICME *in situ*, the transit time for the ejecta to travel from the Sun to where it is observed *in situ* in interplanetary space, and the measure of physical parameters, such as orientation, magnetic flux and helicity. It is important to note that it is the combination of physical characteristics and signatures that is the key to successfully tying together the interplanetary-end and the Sun-end of an eruptive event. Combining observations of the same event at both the Sun and *in situ* near Earth helps us to investigate the magnetic topology of the erupting structure directly, which in turn is crucial to the understanding of how and why an eruption occurred.

3.1.5.1 Location on the Sun

As discussed in § 1.4.2, CMEs typically propagate away from the Sun in a radial direction, as confirmed by both coronagraph and *in situ* observations. This means that we expect that a CME that is observed from the vicinity of Earth is a halo, or at least a partial halo, CME and its source region is expected to be close to disk centre (typically within a distance of $R_{\odot}/2$ of disk centre).

When the source region of a CME lies far from disk centre, then it is likely that the ICME will not be detected by *in situ* spacecraft located at 1 AU. However, the spatial extent of CME-driven shocks significantly exceeds the size of the following

ICME, as discussed in § 3.1.2.1, and a shock may still be detected at its flanks (Borrini *et al.*, 1982b; Cane, 1988; Richardson and Cane, 1993).

On rare occasions, some Earth-directed CMEs originate at the limb or even behind it. These extreme cases have proved themselves to be particularly geoeffective, resulting in major geomagnetic storms (Zhang *et al.*, 2003). Very large-scale CMEs (some involve half of the corona) may also originate far from disk centre (Zhukov and Veselovsky, 2007). CMEs may also be deflected away from their radial path by streamers (e.g. Gopalswamy *et al.*, 2000a). So, while our search for a CME source region often begins near disk centre, it is not limited to it.

3.1.5.2 Estimating CME transit speeds

The accuracy with which the speed of a CME may be determined near to the Sun is heavily dependent on the location of the eruption on the Sun, with respect to the observer. CMEs are most easily observed using white-light coronagraph observations, but the structure of a CME erupting on the limb can be much more easily resolved than a halo CME erupting on the disk and propagating towards an observer, since it is observed in the plane of the sky. As discussed in § 2.2.1.3, the limitations of coronagraph observations mean it is not possible to track every step of a CME eruption from the low corona, where EUV observations are employed, out into the heliosphere, since the occulting disk of the coronagraph makes white-light observations below 1.4 $R_\odot$ impossible. CME onset time is often determined by measuring the height of a feature as it propagates through the field of view of the white-light observations and then extrapolating back to the solar surface to determine the launch time, but this is not a very accurate process, particularly in the case of halo and partial halo CMEs, for which radial speeds are often vastly overestimated. Schwenn *et al.* (2005) have shown that the leading edge expansion velocity of a CME (the speed at the position angle of the fastest moving front, measured in the direction orthogonal to the main expansion direction) gives a better proxy to the radial velocity, as well as to the transit time for a CME to reach 1 AU, than the velocity measured in the direction of the largest expansion. Often the velocity measured in the direction of the largest expansion is a combination of the expansion and radial velocity with a projection on the plane of sky. As discussed in § 3.1.2.5, the speed of a CME can also be determined from the change in frequency of the associated type II radio burst, but the use of this signature is limited since interplanetary type II radio bursts are usually only observed for particularly fast CMEs.

CME cone models have been developed to provide a way of determining the

angular width, central position angle and the radial speed and acceleration for halo CMEs (Zhao *et al.*, 2002). Cone models are so named, since the boundary of emission observed by LASCO for halo CMEs should form a cone of constant angular spread and the apex (the point the cone narrows to from a round cross-section) of the cone is located at the centre of the Sun. As such, cone models make the following assumptions: (1) the central positions of halo CMEs observed by LASCO is located near to both the CME source region and the centre of the solar disk, (2) their bulk velocities are directed radially and (3) the angular width of a CME remains constant as it propagates into interplanetary space, which was shown to be the case in observations (Webb and Jackson, 1990; Webb *et al.*, 1997). Not all CMEs can be reproduced with the cone model, and the success of this technique is limited by the assumptions made.

Determining the transit time of a CME from the Sun to its *in situ* observation at $\sim$ 1 AU is not straightforward, since a CME may accelerate or decelerate as it propagates into interplanetary space. CMEs observed below the average solar wind speed are typically accelerated, while those above this velocity are decelerated (Lindsay *et al.*, 1999; Schwenn *et al.*, 2005). Typical CME acceleration speeds of 200 m s^{-2} have been estimated from statistical analysis by Zhang (2005), with the duration of the acceleration in the region of 40 minutes. These values yield an acceleration distance of 0.82 $R_{\odot}$, by which a CME has reached a speed of around 480 km s^{-1}. However, the acceleration experienced by a CME is extremely variable between events, ranging from a few m s^{-2} to $>$ 1000 m s^{-2} (Gopalswamy *et al.*, 2000a). However, these values are obtained from measuring the plane-of-sky speeds, which may vary significantly from the radial CME speed.

In some cases, an eruption may be observed on the Sun and its interplanetary counterpart subsequently identified near Earth. Alternatively, following the *in situ* detection of an ICME near Earth, it may be extrapolated back to the Sun to locate its solar source. One major advantage of *in situ* observations of ICMEs is the ability to directly measure the velocity of the propagating structure, making estimates of CME transit times starting from the interplanetary observations usually more precise than when starting from the solar observations. Although it is possible to produce reasonable estimations of CME transit time from solar observations, for example correlation has been found between the transit time and the CME velocity measured close to the outward edge of the coronagraph field of view (Gopalswamy *et al.*, 2000a, 2001b; Zhang *et al.*, 2003), these are less reliable since this leading velocity is a combination of the global and expansion motion. This is not the case *in situ* where the global motion of the ICME and the expansion velocity of the ICME may be determined separately. The *in situ* velocity measurements are also considered more representative of the mean speed of the ejecta since the acceleration

or deceleration of a CME predominantly takes place close to the Sun (< 1 $R_\odot$).

A probable "launch window" for a CME can be estimated from the measured bulk proton speed of the magnetic cloud at its centre and by anticipating that the CME may have accelerated or decelerated as it propagated away from the Sun. Selecting the time of arrival of the centre of the cloud, rather than that of the shock front, reduces the likelihood of mixing up the expansion of the structure and its global motion in the solar wind. Considering a typical magnetic cloud, travelling at 450 ± 50 km s^{-1}, an estimate for the time of its eruption is 3.6 ± 0.4 days earlier than it is observed at 1 AU (Bothmer and Schwenn, 1998).

3.1.5.3 Orientation of the magnetic structure

The orientation of a CME is directly observable in the corona. Filaments are aligned with polarity inversion lines and provide a good indication of the orientation of the erupting magnetic structure, allowing predictions to be made about the magnetic topology of the CME. In interplanetary space, the orientation of the flux rope can be deduced from the vector observations of the magnetic field using a minimum variance analysis (see § 2.4.2). The intermediate variance direction determined from this method corresponds with the axial direction of the cloud, z_{cloud}. Improvements on the orientation can be realised by fitting flux rope models to the data. The comparison between various models gives an estimation of the uncertainty of the orientation (typically $\pm 10°$, see Dasso *et al.* (2005) for a review).

When comparing the direction of the MC axis with the orientation of the erupting structure, rough alignment between the MC axis and disappearing filaments (Bothmer and Schwenn, 1994, 1998; Marubashi, 1997; Zhao and Hoeksema, 1998; Yurchyshyn *et al.*, 2001, 2005; Ruzmaikin *et al.*, 2003), and X-ray sigmoids (Watari *et al.*, 2001) is often observed. However, the orientation of the axis of some MCs does undergo significant rotation compared to its pre-eruption magnetic configuration. Rotations larger than 30° are not unusual, with some rare cases exhibiting rotation up to 160° (Dasso *et al.*, 2007; Harra *et al.*, 2007). This rotation is interpreted as the consequence of the writhing of the magnetic flux tube. Nevertheless, a comparison of the orientation of the magnetic structure observed *in situ* with the orientation of the erupting structure can be a useful tool in the process of associating a magnetic cloud with its solar source.

Given the large scale of many ICMEs it is not unusual for the passage of the *in situ* spacecraft to be through one of the "legs" of the flux rope rather than the apex of an ICME loop. In this case, the "polarity" of the ICME leg can be determined

from local magnetic fields, but these can turn back on themselves. A more reliable indicator is the direction of the strongest counterstreaming suprathermal electron beam relative to the magnetic field direction (Kahler *et al.*, 1999). The fact that one beam is usually stronger supports the assumption that passage is through one leg, since the stronger beam is presumed to come from the nearest solar connection point (Pilipp *et al.*, 1987). A comparison of the *in situ* observations of suprathermal electron beams provides an indication of the probable magnetic configuration of the solar source region of the magnetic cloud, as well as a clue to its location during the eruption, i.e. whether the CME originates from in either the western or eastern solar hemispheres.

3.1.5.4 Magnetic flux

Since the magnetic field is only measured along the trajectory of the spacecraft as it passes through the observed magnetic cloud, it is only possible to directly derive the axial and azimuthal magnetic fluxes of the magnetic cloud if it is assumed that the flux rope has symmetrical, cylindrical geometry and the spacecraft passes only a small radial distance from the flux rope axis (i.e. the impact parameter is small) (Dasso *et al.*, 2006). However, when this cannot be assumed to be the case, it is usually still possible to obtain estimates of the magnetic flux in a magnetic cloud by fitting a model to the data (see Dasso *et al.*, 2005, for a review). Precise determination of the magnetic flux is dependent upon assumptions of the shape of the flux rope cross-section, particularly in the case of the axial magnetic flux, and the location of the MC boundaries, the length of the flux rope and the invariance of the orientation of the MC axis. It is expected that the magnetic flux estimations may vary by 10 % between those obtained from a model and those obtained directly from the data (Démoulin, 2008).

Dasso *et al.* (2006) report that reconnection can be forced in front of an MC when a flux rope is overtaking the magnetic field ahead of it. The consequence of this reconnection is a flux tube that is peeled away at the front, but has an extended back part, comprised of magnetic field that was originally part of the flux rope. In this way, the magnetic cloud's flux may be diminished as it propagates through the heliosphere, with reports suggesting that up to $\sim$ 60 % of a magnetic cloud's flux may be lost (Dasso *et al.*, 2006), although this value is typically much smaller ($<$ 25 %) (Dasso *et al.*, 2007; Mandrini *et al.*, 2007).

Measurements of magnetic flux in the photosphere may be obtained from line-of-sight magnetograms, but when linking a magnetic cloud with its solar source it is specifically the flux involved in a CME that is important. CMEs originating on the

disk are often associated with observations of coronal dimmings; regions of intensity decreases observed in association with CMEs (Thompson *et al.*, 2000) (see § 3.1.4.2). Double dimmings are present on either side of the magnetic configuration and are believed to mark the position of the ejected flux rope footpoints, since the magnetic flux found in the dimming regions corresponds approximately to the axial magnetic flux of the associated MC (Lepping *et al.*, 1997; Webb *et al.*, 2000; Qiu *et al.*, 2007). Dimmings are not always observed following a CME eruption, however this does not necessarily mean that they are not present, simply that they cannot be easily resolved. This may be the case when considering CME eruptions from very small source regions, or if the emission from an associated flare "masks" the underlying dimming regions. Partly due to the difficulties in defining the maximum extension of dimmings, the relationship between the magnetic flux present in dimmings and in the related MC is not entirely clear.

The presence of dimmings does not imply that a CME is simply launched from the corona, since *in situ* observations of MCs show that they are highly twisted flux tubes (typically with more than 10 turns (Gulisano *et al.*, 2005)), while evidence of such a high twist has never been found in the corona. It is more probable that most of the flux rope is rapidly formed by reconnection of a sheared arcade (before the arcade height becomes larger than the plasma scale height, $\approx$ 100 Mm). Alternatively, the ejected flux rope may be formed by successive reconnections in a sheared arcade during the eruption process (e.g. Amari *et al.*, 2003; Gosling, 1990). Evidence supporting the latter interpretation has been found by Mandrini *et al.* (2005) and Attrill *et al.* (2006), who computed the magnetic flux in the dimming regions associated with eruptions occurring in two isolated bipolar ARs and found that this was comparable with the azimuthal flux of the associated MCs (when assuming a length compatible with both solar and interplanetary observations).

For those CME eruptions in which associated dimmings are difficult to observe, comparisons may still be made between the amount of flux available in a prospective source region and the axial flux in an observed magnetic cloud, to strengthen the identification of the solar origins of an event. Following the *in situ* observation of an MC, there may be a number of candidate regions on the Sun from which the associated CME may have erupted and since the amount of flux in a MC cannot exceed the amount of flux in its source region prior to eruption, measurements of the active region magnetic flux can be used to further deduce the most likely source region.

3.1.5.5 Magnetic helicity

Magnetic helicity, H is a measure of the topological structure of the magnetic field, and is particularly suited to characterising twisted and sheared field lines. Magnetic helicity is an approximately conserved quantity in resistive MHD with low resistivity (Berger, 1984) because it is almost preserved on a time-scale less than the global diffusion time-scale. Therefore this provides a quantitative link between eruptions from the corona and corresponding CMEs observed *in situ* at 1 AU. Thus, the erupting structure in the solar corona is expected to have the same helicity sign as the ICME (Bothmer and Rust, 1997). Magnetic helicity quantifies how the magnetic field is sheared and twisted, compared to a potential field in which it would be in its lowest energy state. For a magnetic flux rope, the helicity is given by

$$H = \Phi^2 \left(T_w + W_r\right) \tag{3.2}$$

where Φ is the axial magnetic flux within the rope, T_w is the twist or number of windings of the field lines around the axis, and W_r is the writhe; which is a measure of the distortion of the flux rope axis.

Even when a flux rope is in a stable configuration, magnetohydrodynamic simulations have shown that there is moderate writhe of the twisted flux rope (Toeroek and Kliem, 2003; Aulanier *et al.*, 2005). However, when the flux rope becomes kink unstable (see § 1.4.2.2), the writhe becomes large (Gibson *et al.*, 2004; Toeroek and Kliem, 2005). For a cylindrical flux rope with little or no writhe, the sign of helicity of the rope equals the sign of twist. Positive helicity corresponds to positive (right-handed) twist and negative helicity to negative (left-handed) twist. It is possible to determine the sign of helicity of the coronal source region of a cloud by examining the chirality (handedness) of the magnetic structure prior to, during and post-eruption (Martin, 2003).There are several ways to determine chirality in the coronal field (Démoulin, 2008).

The most direct way to determine the dominant chirality of an active region is by investigating the sign of magnetic shear (angle between the observed and computed magnetic field) using vector magnetograms (Démoulin, 2008). Vector magnetograms allow both the longitudinal and transverse components of the magnetic field to be measured, using the circular and linear polarisation of magnetically sensitive spectral lines in the solar photosphere and chromosphere. Knowledge of the full magnetic vector allows one to determine the size and nature of any currents in the system, as well as obtain measures of twist and helicity. The "α_{best}" method (Pevtsov *et al.*, 1997) involves the fitting of the vector magnetic field with a linear force-free field,

$j = \alpha \mathbf{B}$, yielding a single value, α_{best}, which represents the global shear of the region.

Magnetic tongues of newly emerged flux provide another way of directly determining the helicity of the coronal field. When the apex of a flux rope emerges across the photosphere, the presence of twist produces a contribution of the azimuthal field projected onto the line-of-sight component. This is observed in longitudinal magnetogram data as two elongated "tongues" of opposite polarities in the active region field (López Fuentes *et al.*, 2000)(*lower left panel*, Figure 3.10). For a positive twist, the leading polarity appears elongated and extends southward of the following polarity. The situation is the mirror image for a negative sign of twist. Even with a lack of magnetic data, it is possible to infer the sign of helicity from the sheared orientation of chromospheric fibrils or coronal loops, relative to the direction given by a potential field.

The chirality of prominences/filaments is most easily determined from the fine structure, known as "barbs", observed along both sides of a prominence. In a prominence, the "spine" is the long axis running along the length of the top of the structure and it is from here that the barbs originate. The direction of the barbs provides an indication of the chirality of the region in which it is formed. When barbs curve from the spine to the right and downward to the chromosphere, this indicates that a filament is formed in a region of negative (left-handed) chirality, while the opposite is true for filaments formed in a region of positive (right-handed) chirality (Martin, 2003) (*upper right panel*, Figure 3.10).

Overlying a filament are coronal loops and this coronal arcade also has a chirality, such that if a filament is dextral, the overlying arcade is skewed to the left. Again, the opposite is true for sinistral filaments. Between the top of the filament structure and the coronal arcade, X-ray features known as sigmoids are often found, which take the shape of a "S" or "reverse S" (*upper left panel*, Figure 3.10). Sigmoids are associated with enhanced dissipation in a layer of steepened current density, which forms under a dynamic flux rope, and is threaded by sigmoidal field lines (Titov and Démoulin, 1999). These X-ray features have the same chirality as the overlying coronal field with S-shaped (reverse S-shaped) ones associated with right skewed (left skewed) coronal arcades and sinistral (dextral) filaments.

The signs of chirality of sigmoids and coronal arcades are unambiguously interpreted as having a direct relationship with their sign of helicity. S (reverse-S) shaped sigmoids and right-skewed (left-skewed) coronal arcades have a positive (negative) sign of helicity (Figure 3.10). However, a clear relationship between the chirality of a filament and its sign of helicity has not been established, and Martin (2003) raise the open question of whether a filament does have a net sign of helicity or whether

there is a balance of opposing signs of helicity within filaments.

Although the chirality of a stable filament is not a reliable indication of the sign of helicity of the magnetic structure, this is not necessarily the case during the eruption of a filament. During eruption, the apex of a filament may rotate and Green *et al.* (2007) show that the direction of rotation of the filament is consistent with the conversion of twist into writhe under the ideal MHD constraint of helicity conservation, providing an indication of the sign of helicity of the erupting structure. They found that for a positive (negative) sign of helicity the filament apex rotates clockwise (counter-clockwise), consistent with the flux rope taking on a reverse (forward) S-shape, which is opposite to that observed for the associated sigmoid. This may be simply expressed as:

$$\text{sign(rotation)} \cdot \text{sign(helicity)} > 0 \tag{3.3}$$

where the rotation is considered positive (negative) in the clockwise (counter-clockwise) direction.

Flare ribbons observed following an eruption may also be used to infer the sign of helicity in the erupting region. In a sheared field, the flare ribbon locations are separated along the magnetic polarity inversion line (PIL). In some cases, they also have a characteristic J-shape if the twist is of the order or above one turn (Moore *et al.*, 1995; Démoulin *et al.*, 1996) that can be identified in Hα and UV wavelengths. A forward J-shape implies the region has a positive sign of helicity, while a reverse J-shape implies the region has a negative sign of helicity (*lower right panel*, Figure 3.10).

The curvature of the fibrils that make up the penumbral region surrounding a sunspot may also be used as an indicator of the sign of helicity of the region, since the direction of the fibrils is related to the twist of the sunspot magnetic field (Nakagawa *et al.*, 1971; Rust and Martin, 1994; Chae, 2001). A sunspot in which the fibrils are curved in a counter-clockwise direction implies that a region has a negative sign of helicity, since it results from the clockwise rotation of the sunspot during its formation. The opposite is true of sunspots in which the fibrils are curved in the clockwise direction.

The sign of helicity of a magnetic cloud can be investigated directly, using *in situ* observations. As with magnetic structures on the Sun, the chirality of a magnetic cloud can be used to infer its sign of helicity. As discussed in § 3.1.1, the magnetic topology of a magnetic cloud is characterised by large scale rotation of the azimuthal

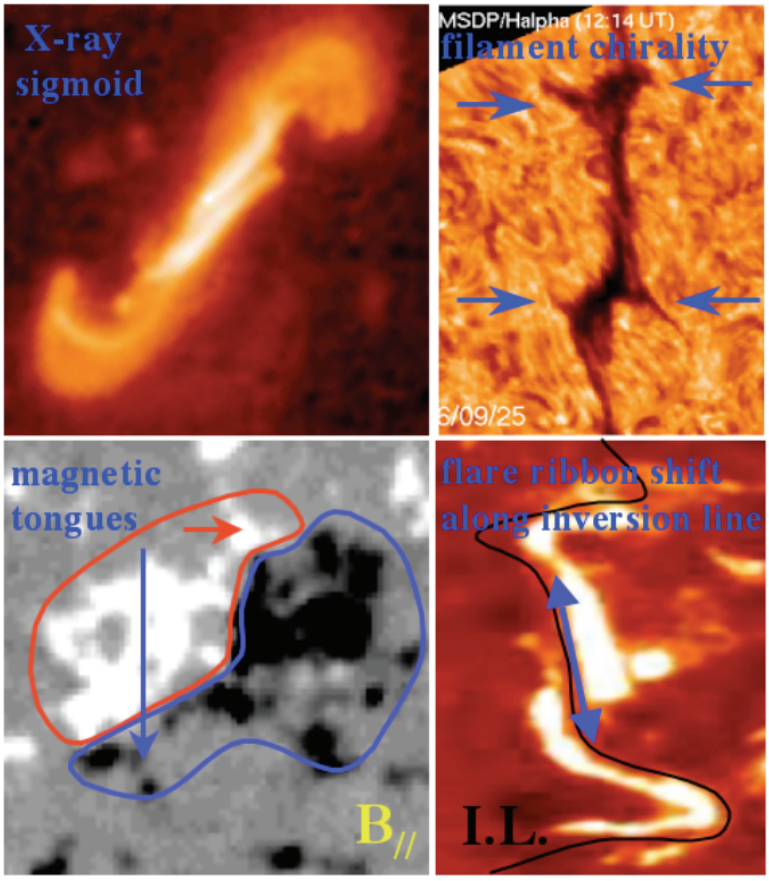

Figure 3.10: Observational signatures of magnetic helicity sign in the solar corona. Figure courtesy of Démoulin (2008). Permission to reproduce this figure has been granted by the European Geosciences Union.

component of the magnetic field. The direction of rotation of the azimuthal component of the MC's magnetic field relative to the direction of the axial magnetic field is directly related to the sign of helicity of an MC (Bothmer and Schwenn, 1994, 1998). Figure 3.11 illustrates that when the rotation of a magnetic cloud indicates that it is left-handed (right-handed), this implies that its sign of helicity is negative (positive).

Rust and Martin (1994) and (Bothmer and Schwenn, 1994, 1998) found that most MCs have the same sign of helicity as the associated CME eruption. The sign of helicity of the magnetic structure also exhibits some dependence on the solar hemisphere from which it originates. In the northern hemisphere, the sign of helicity is preferentially negative, while a positive sign of helicity is expected in the southern hemisphere. $\sim$ 70 % of the observed ejecta conform to these hemispheric chirality rules (Pevtsov and Balasubramaniam, 2003).

Theoretical work undertaken by Berger (1984) to determine the magnitude of magnetic helicity at the Sun significantly preceded developments in techniques to estimate helicity from the data, and it is only in recent years that this has been

MC Type / Magnetic helicity / Number of MCs during 1974–1981	Variation of magnetic field vector	Direction of magnetic field on flux tube axis	Rotation of magnetic field vector in *Bz*-*By*-plane (*Bx**-*By**-plane)
SEN — Left-handed 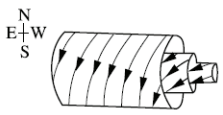 17	South (–*Bz*)→north (+*Bz*)	East (+*By*)	
SWN — Right-handed  17	South (–*Bz*)→north (+*Bz*)	West (–*By*)	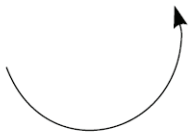
NES — Right-handed 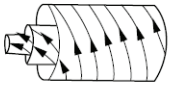 6	North (+*Bz*)→south (–*Bz*)	East (+*By*)	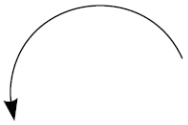
NWS — Left-handed  6	North (+*Bz*)→south (–*Bz*)	West (–*By*)	
Orientations for high inclinations to the ecliptic SEN, NWS, SWN, NES	East (+*By*)→west (–*By*) West(–*By*)→east(+*By*)	North (+*Bz*)→south (–*Bz*) South (–*Bz*)→north (+*Bz*)	Rotations in *By*-*Bz*-(*By**-*Bx**-) plane

Figure 3.11: Sketch showing the different magnetic configurations of MCs and their magnetic helicity sign based on the concept of the magnetic flux rope geometry for magnetic clouds and the field rotation that a spacecraft would observed during a cloud's passage. Figure courtesy of Bothmer and Schwenn (1998). Permission to reproduce this figure has been granted by the European Geosciences Union.

employed when linking a magnetic cloud with its associated CME. The magnitude of the magnetic helicity can be determined in magnetic clouds in interplanetary space just as for the estimation of magnetic fluxes; both directly from the data if it can be assumed that the impact parameter is small and has cylindrical, symmetrical geometry (Dasso *et al.*, 2006) or by fitting a model to the magnetic cloud data (Dasso *et al.*, 2003).

In the solar corona, the evolution of longitudinal magnetograms tells us about the flux of magnetic helicity. By considering magnetograms prior to and after the eruptive event, the decrease in the coronal helicity during a CME can be estimated. The value obtained in the corona is expected to be approximately comparable with

the value estimated in the magnetic cloud, with results from the few events that have been studied in this way indicating that a difference of a factor of 2 is reasonable (Mandrini *et al.*, 2005).

3.2 Locating the Solar Source of the 13 April 2006 Magnetic Cloud

The work described in this section of the thesis can be found in the following published article:

Steed, K., Owen, C. J. Harra, L. K., Green, L. M., Dasso, S., Walsh, A. P., Démoulin, P. and van Driel-Gesztelyi, L.: Locating the solar source of 13 April 2006 magnetic cloud. 2008, *Ann. Geophys.*, 26, 3159.

3.2.1 Event Context

Using *in situ* data from the ACE spacecraft, we identify and describe an interplanetary magnetic cloud observed near Earth on 13 April 2006. Combining these observations with multi-instrument and multi-wavelength observations from SOHO, TRACE and ground-based solar observatories, the solar source of this magnetic cloud is determined.

During the estimated "launch window" of the CME, a number of large active regions were present on the Sun, which were initially considered to be the most likely candidate source regions of the observed magnetic cloud. However, this is shown to not be the case and the CME associated with the 13 April 2006 magnetic cloud is now believed to originate from a small, spotless active region that emerged in the northern hemisphere. Evidence of an eruption in this region is observed on 11 April 2006, 59 hours before the associated magnetic cloud is observed at 1 AU.

The link between this eruption and the interplanetary magnetic cloud is supported by a number of pieces of evidence. During the eruption the solar source region is located near to the centre of the solar disk, while its position slightly to the east of the central meridian from the perspective of the observing spacecraft is in approximate agreement with the trajectory of the *in situ* spacecraft through the western leg of the magnetic cloud. The transit time of the ejecta is in agreement with estimations made from the observed radial velocity of the magnetic cloud at 1 AU and estimates of the axial flux within the magnetic cloud do not exceed the

amount of available flux in the associated active region. The sign of helicity of the magnetic cloud is in agreement with the sign of helicity in the erupting active region, which differs from the sign of helicity of all of the other candidate source regions on the Sun at this time. In addition, the active region is located on the boundary of a coronal hole, and a high-speed solar wind stream originating from this region is observed near Earth shortly after the passage of the magnetic cloud. This study is the first to use this kind of signature to associate a magnetic cloud with its solar source.

3.2.2 Overview of the 13 April 2006 Magnetic Cloud

3.2.2.1 Identifying the 13 April 2006 magnetic cloud

We analysed 16 second resolution data from the Magnetometer Instrument (MAG, Smith *et al.*, 1998) and 64 second resolution data from the Solar Wind Electron Proton and Alpha Monitor (SWEPAM, McComas *et al.*, 1998), both onboard the ACE spacecraft located in the vicinity of the Lagrangian point, L1, over the 3 day interval 12:00 UT on 12 April 2006 to 12:00 UT on 15 April 2006. The magnetic field intensity and its components in geocentric solar ecliptic (GSE) coordinates, proton number density, the plasma, magnetic and total pressures, solar wind speed and proton temperature as a function of time are shown in Figure 3.12, and are used to describe and characterise the magnetic cloud arriving at $\sim$1 AU on 13 April 2006.

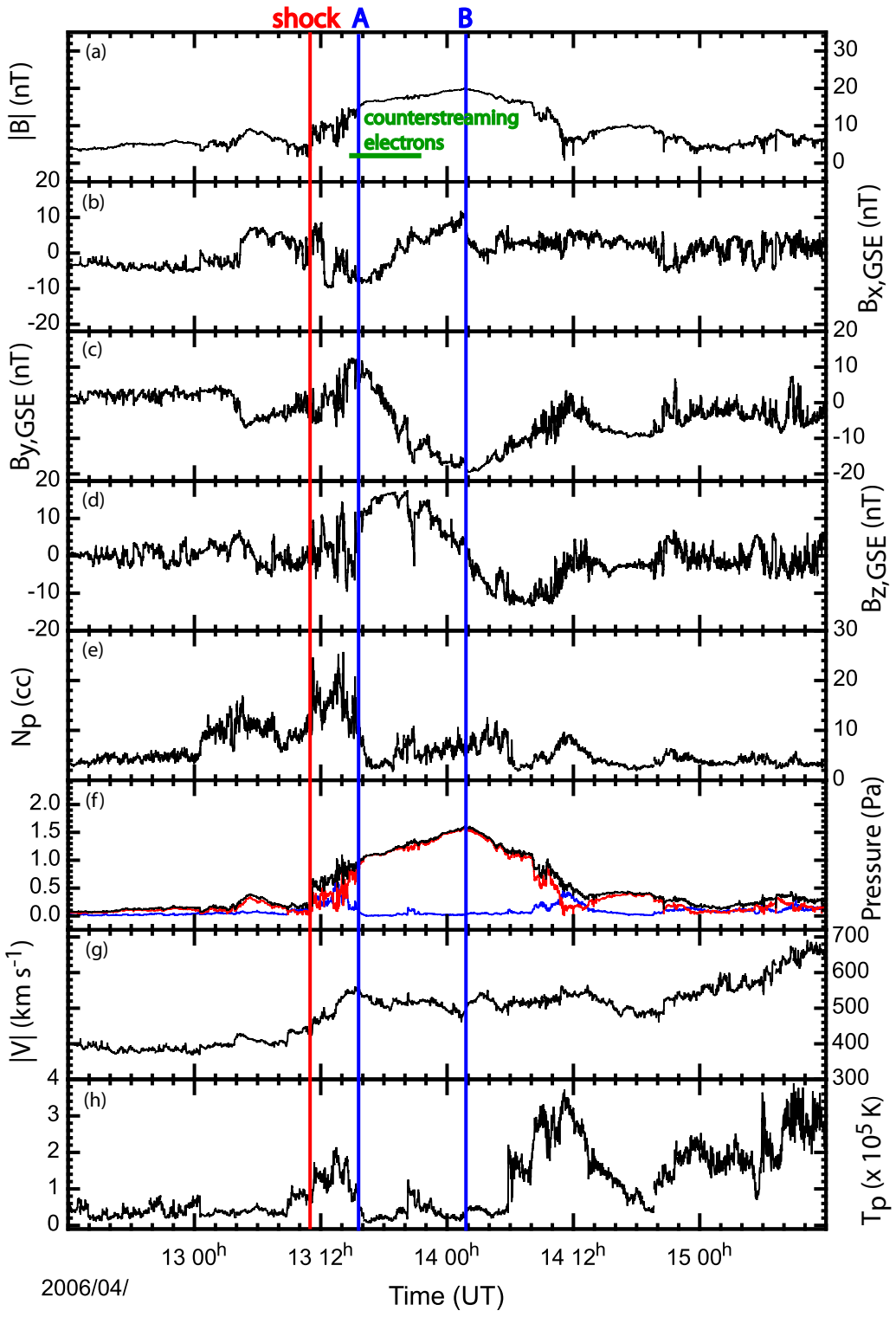

Figure 3.12: Interplanetary magnetic field and plasma data obtained from the ACE spacecraft during the passage of the ICME ejecta. This plot shows (a) the magnetic field intensity, (b), (c) and (d) the B_x, B_y and B_z components of the magnetic field in Geocentric Solar Ecliptic (GSE) coordinates, respectively, (e) proton number density, (f) plasma (blue trace), magnetic (red trace) and total (black trace) pressures, (g) solar wind bulk speed and (h) proton temperature as a function of time. Vertical lines indicate the arrival of a shock (red) at ∼11:00 UT 13 April 2006 and the boundaries, A and B, (blue) of the magnetic cloud at ∼16:00 UT 13 April 2006 and ∼01:15 UT 14 April 2006, respectively. The duration over which counterstreaming, suprathermal electrons are observed is indicated by the horizontal green line between ∼14:30 UT and ∼22:00 UT 13 April 2006.

Travelling ahead of the magnetic cloud is a weak, forward fast shock and this was the first component of the ejection to be observed *in situ*, at ∼11:00 UT on 13 April 2006. This was identified in the data by simultaneous observations of discontinuities in the magnetic field intensity, proton density, solar wind bulk speed, and proton temperature, all of which increased. This CME-driven shock was produced because the speed of the leading edge boundary of the cloud relative to the solar wind was greater than the magneto-acoustic speed (Lepping *et al.*, 1997). The time of the shock is highlighted in Figure 3.12 by a vertical red line. Following the shock is a region of compressed, high density plasma. Between ∼11:00 UT and ∼16:00 UT on 13 April 2006, the magnetic field exhibits increased variability, during which it fluctuates over very small time-scales. Peaks are also observed in observations of both the proton density and temperature. The combination of these signatures indicates the passage of the hot, dense pile-up of the shocked "sheath" plasma, which immediately precedes the arrival of the body of the magnetic cloud.

A number of magnetic field and plasma signatures that are considered to be typical of a magnetic flux rope were used to identify the 13 April magnetic cloud. Magnetic clouds are widely modelled as large-scale, force-free, cylindrical magnetic flux ropes (e.g. Lepping *et al.*, 1990; Marubashi, 1997; Lynch *et al.*, 2003; Dasso *et al.*, 2005). In this scenario, the magnetic field is helical, such that it is in the axial direction towards the centre of the flux rope and in the azimuthal direction at the flux rope boundary. As a magnetic cloud passes over a spacecraft located in the solar wind, a bipolar signature, observed in the azimuthal magnetic field component, is anticipated. This is indicative of the large-scale rotation of the magnetic field within the structure. A smooth, coherent rotation of the $B_{x,GSE}$, $B_{y,GSE}$, and $B_{z,GSE}$ components of the interplanetary magnetic field is observed, with a clear bipolar signature evident in the $B_{y,GSE}$ component. The magnitude of the magnetic field in magnetic clouds is also typically elevated relative to values in the surrounding solar wind, exhibiting little variability. The magnetic field strength of the 13 April 2006 cloud is observed to increase from a pre-event value of $\sim$ 5 nT to a maximum value of $\sim$ 20 nT toward the trailing edge of the cloud. Within the ejecta, the proton temperature remains predominantly low and the combination of these magnetic field and plasma signatures suggests that the leading boundary of the magnetic cloud passed the spacecraft at $\sim$ 16:00 UT on 13 April 2006 and the trailing boundary at $\sim$ 01:15 UT on 14 April 2006. This implies that the duration of this magnetic cloud is $\sim$ 9 hrs, which is significantly shorter than the typical duration of $\sim$ 1 day.

Counterstreaming beams of suprathermal electrons are typically associated with ICMEs (Zwickl *et al.*, 1983; Gosling *et al.*, 1987) and tell us about the connectivity of magnetic field lines to the Sun. When a counterstreaming beam of suprathermal electrons is observed, it indicates the presence of closed field lines that are

still connected to the Sun at both ends. It is common for unidirectional beams to also be observed within an ICME, indicating that one of the footpoints is no longer connected to its solar source, while complete drop-outs in the observations of these electrons can indicate that the magnetic structure has become completely disconnected from the Sun. Counterstreaming beams of electrons at suprathermal energies are observed within the 13 April 2006 magnetic cloud between ∼14:30 UT and ∼22:00 UT on 13 April 2006, and this interval is highlighted in Figure 3.12 by a horizontal green line in panel (a) (For pitch angle distribution data for suprathermal electrons at 272 eV within the 13 April 2006 magnetic cloud, see Figure 4.3).

3.2.2.2 Geometry of the 13 April 2006 magnetic cloud

As mentioned previously, magnetic clouds are widely modelled as force-free, large-scale, cylindrical magnetic flux ropes (e.g., Lepping *et al.*, 1990; Lynch *et al.*, 2003; Marubashi, 1997). The lines of force of the magnetic field given by the solution for a cylindrically symmetric force-free field with constant α are a family of helices with pitch angle increasing from the axis of the magnetic cloud (where the magnetic field is a straight line), to the boundary (where the lines of force are circles) (Burlaga, 1988). The orientation of the observed magnetic structure can be determined using a minimum variance analysis (MVA) of the magnetic observations (Sonnerup and Cahill, 1967). This method can be used to find the natural coordinate system of a flux rope, allowing us to better see the nature of the fluctuations in the azimuthal and axial magnetic fields of the flux rope, and is discussed further in § 2.4.2. Figure 3.13 shows the magnetic field components of the magnetic cloud in local magnetic coordinates obtained from the minimum variance analysis.

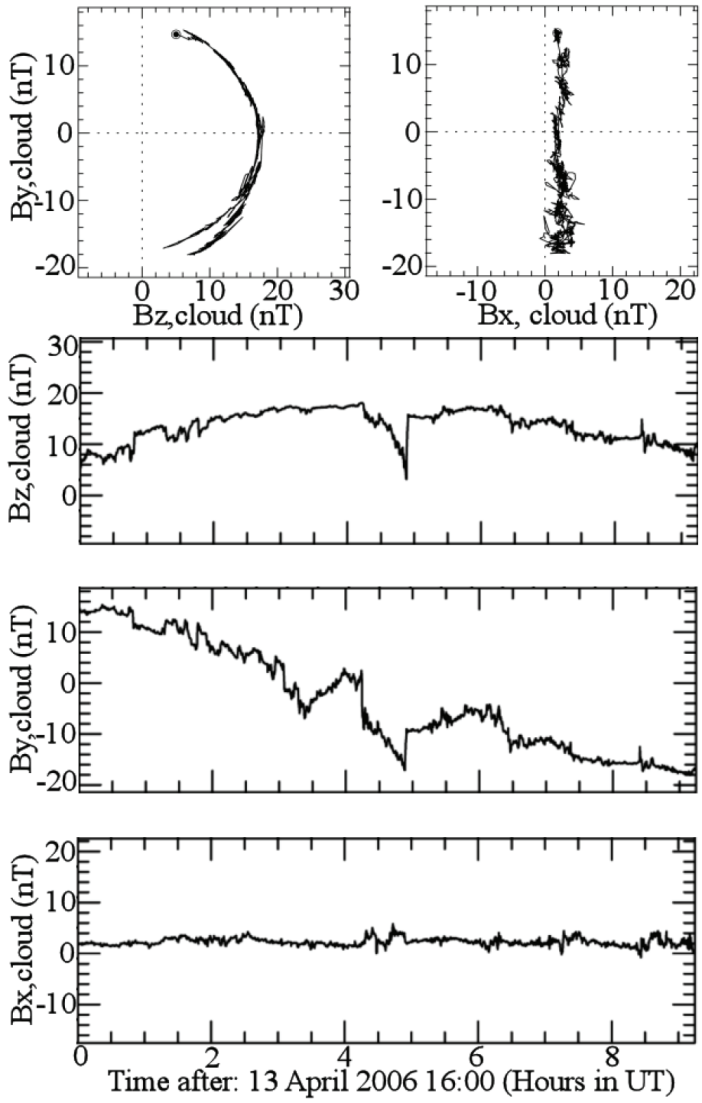

Figure 3.13: Magnetic field components in local magnetic coordinates from the minimum variance analysis performed over the duration of the magnetic cloud (16:00 UT 13 April 2006 - 01:15 UT 14 April 2006). The two upper panels show the hodograms for the MC. The upper left panel shows the coherent rotation, while the upper right panel shows the noise in the $x, cloud$ direction. The lower three panels show the evolution of the magnetic field components (with the orientation of the cloud given by the minimum variance method, see § 2.4.2). Permission to reproduce this figure has been granted by the European Geosciences Union.

Minimum variance analysis can be used to confirm the boundaries of the magnetic cloud by considering the interval over which the maximum rotation is observed. In the case of the 13 April 2006 magnetic cloud, the results of the minimum variance analysis confirm the boundaries determined by visual inspection of data in GSE coordinates. The MV analysis gives a ratio between the intermediate and the minimum eigen-values of ~ 17 (which implies that the minimum variance direction is well-defined (Siscoe and Suey, 1972)) and a low mean value and no large-scale trend for the $B_{x,cloud}$ series inside the MC, which are arguments in favour of having

a well-defined MC axis (Gulisano *et al.*, 2007).

The trajectory of the ACE spacecraft through the 13 April 2006 magnetic cloud can be estimated using a technique developed by Gulisano *et al.* (2007), which is valid for the force-free Lundquist (1950) model, and in which the magnetic field components obtained from MVA are used to provide an approximation of the impact parameter, p, defined as the minimum radial distance from the spacecraft to the cloud axis. The deviation from zero of the mean value of the $B_{x,cloud}$ component of the magnetic field (in the direction of the minimum variance) can be used to obtain an estimation of p (see Figure 5, upper panel in Gulisano *et al.* (2007)), as:

$$p \approx R\sqrt{\left(\frac{< B_{x,cloud} >}{1.6B_0}\right)} \tag{3.4}$$

where R is the radius of the magnetic cloud and B_0 is the central magnetic field strength.

The magnetic field in the $x, cloud$ direction is expected to be zero when the spacecraft passes through the centre of a magnetic cloud, i.e. when $p = 0$. The mean value of $B_{x,cloud}$ in the 13 April 2006 magnetic cloud is $\sim$ 3 nT and the magnetic field at the cloud axis, B_0, can be estimated as the maximum observed field because at this position the magnetic field is practically axial ($B_{z,cloud}$ is the largest field component by a factor ≈ 6); thus $B_0 \sim 18$ nT. A value for p/R of ~ 30 % was obtained.

From the measured velocity of the cloud at 1 AU, the spacecraft trajectory through the cloud and the time period over which ACE observes the cloud, we estimate a radius, $R \sim 5.7$ x 10^{-2} AU, which implies a small magnetic cloud ($\sim$ 3 times smaller than average (Lepping *et al.*, 1990)).

Once the magnetic field has been transformed to the local coordinate system of the magnetic cloud using MVA, the orientation of the axis of the magnetic cloud can be determined. The maximum variance direction is in the $y, cloud$ direction and represents the rotation of the azimuthal magnetic field, whilst the intermediate direction is in the $z, cloud$ direction and represents the magnetic field at the axis of the cloud (when the impact parameter is small).

The MV analysis suggests that in GSE coordinates, the axial magnetic field of the 13 April 2006 magnetic cloud lies predominantly in the z_{GSE} direction, while the rotation of its magnetic field is mostly contained within the y_{GSE} direction, rotating from positive to negative. Figure 3.14 illustrates the orientation of the magnetic

cloud in the y-z plane of the geocentric solar ecliptic co-ordinate system.

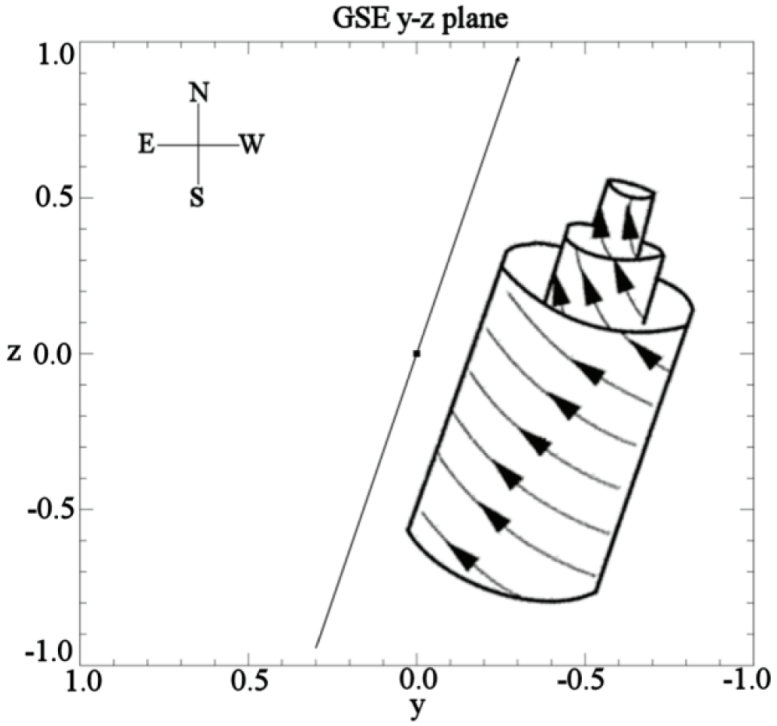

Figure 3.14: The orientation of the magnetic cloud obtained from performing a minimum variance analysis over the cloud duration is illustrated in the y-z GSE plane. The axial field is mainly in the positive z_{GSE} (northward) direction, whilst the rotation of the MC is mainly in the y_{GSE} direction, rotating positive to negative (east to west). This indicates that the MC is left-handed and the sign of helicity of the MC is negative. Adapted from Bothmer and Schwenn (1998). Permission to reproduce this figure has been granted by the European Geosciences Union.

The MC axis orientation is described by θ and ϕ, where θ is the angle between the ecliptic plane and the MC axis, and ϕ is the angle between the direction of x_{GSE} and the projection of the MC axis onto the ecliptic plane (measured positive when anticlockwise). We find that $\theta \sim 68°$ and $\phi \sim 294°$, so the projection of the axis of the cloud on the ecliptic plane points predominantly towards the solar west (negative y_{GSE} direction) with a positive x_{GSE} component. The chirality of the magnetic flux rope can be determined directly from the observations by considering the rotation of the magnetic field. In the case of this magnetic cloud, the field rotation implies that the chirality of the magnetic cloud is left-handed, which corresponds with a negative sign of helicity.

The rear boundary of the 13 April 2006 magnetic cloud is not clearly defined in the magnetic field and plasma data. To further confirm the location of the rear boundary, we consider that the magnetic flux in closed structures, such as flux ropes, is expected to be conserved (Dasso *et al.*, 2006). By fixing the start time of the magnetic cloud in the ACE observations at 16:00 UT on 13 April, it can be

seen that in order for the flux within the magnetic cloud to be conserved, the rear boundary must lie in the vicinity of 01:15 UT on 14 April 2006. At the boundary of a magnetic flux rope, a current sheet is generally expected since there is a change of connectivity of magnetic field lines (from twisted field lines inside the flux rope to solar wind-like field lines outside). Then, the in- and out-bound boundaries in *in situ* data are typically expected where magnetic discontinuities are present (e.g. Dasso *et al.*, 2006). As expected, a discontinuity is observed in the $B_{x,GSE}$ component of the magnetic field at 01:15 UT on 14 April 2006.

A number of locations for the rear boundary were explored before the boundary at $\sim$ 01:15 UT on 14 April 2006 was selected. For each of the preliminarily identified boundaries we performed an MV analysis over the MC duration and found that changes in the rear boundary location of the magnetic cloud between $\sim$ 01:15 UT and $\sim$ 11:00 UT 14 April 2006 do not result in major changes in the orientation of the magnetic cloud axis.

A physical interpretation of the magnetic field and plasma observations towards the rear of this magnetic cloud is far from simple. It is noted that beyond the rear boundary at 01:15 UT on 14 April 2006, the magnetic field strength remains elevated and the magnetic field continues to rotate. Low proton temperatures also persist until 05:47 UT, and it is at this latter point in time that the observations deviate sufficiently from those expected within a magnetic cloud, that we can be fairly confident that we are no longer observing this particular flux rope structure. However, continued study of the behaviour of the magnetic field and plasma beyond this point reveals the possible presence of a second structure, observed between 13:24 and 19:37 UT on 14 April 2006. Here, we again observe a decrease in the variability of the magnetic field, while measurements of the magnetic and plasma pressures show a region where magnetic pressure dominates. However, we cannot conclude that this is a second flux rope, since the characteristic rotation of the magnetic field is absent, and so too are low proton temperatures. It is possible that we are observing a region associated with the 13 April 2006 magnetic cloud that results from its interaction with the solar wind as it propagates through interplanetary space, and this scenario is discussed further in § 4.2.2.

3.2.3 Solar Observations of the Associated CME

Estimates of the transit time of the CME from the Sun to 1 AU allow us to identify a "launch window"; a period of time within which the CME is likely to have erupted. This information provides us with a starting point when searching solar observations for evidence of the CME associated with the magnetic cloud observed *in situ*. The

radial speed of a magnetic cloud can be directly measured in interplanetary space, and is believed to representative of the average propagation speed of the ejecta, since acceleration and deceleration of CMEs has been shown to only take place near to the Sun. The mean speed of the 13 April 2006 magnetic cloud at 1 AU is $\sim$ 520 km s^{-1}. Assuming that the speed remains relatively constant as the magnetic cloud propagates into interplanetary space, this corresponds to a transit time from the corona to 1 AU of 80 hrs, calculated from the arrival time of the centre of the magnetic cloud. Selecting the time of arrival of the centre of the cloud, rather than that of the shock front, reduces the likelihood of mixing up the expansion of the structure and its global motion in the solar wind. This suggests that the CME is likely to have originated at the Sun at $\sim$ 12:00 UT on 10 April 2006. To allow for possible changes in the CME speed during its propagation into interplanetary space, a suitable launch window for the magnetic cloud is determined to be between 9 April 2006 and 11 April 2006.

As discussed in § 3.1.4, the coronal response to a CME eruption is associated with a range of signatures evident in solar observations. These range from coronal waves and dimmings to disappearing filaments and coronal loop structures. An initial survey of the entire solar disk during the identified launch window revealed none of the more obvious CME signatures that might be expected. During this period no large, eruptive flares and no dimmings or coronal waves were observed. The lack of obvious evidence of a CME eruption makes the source region of the magnetic cloud difficult to determine.

The majority of CMEs originate from active regions, where the magnetic field configuration is more complex than in the quiet Sun. At $\sim$ 12:00 UT on 10 April 2006, the middle of the estimated launch window, four active regions were observed on the Sun at EUV wavelengths. AR10871 was located on the east limb, AR10866 and AR10867 were located on the west limb, and AR10869 was located slightly south-west of the centre of the disk. There was also a region of emerging flux east of disk centre, which later developed into AR10870. A small active region north-east of disk centre emerged on 10 April 2006, but did not become sufficiently large to develop sunspots or be allocated a NOAA active region number. The active regions on the limbs were much larger than those on the disk, but any CMEs erupting from these regions were considered unlikely to be directed towards the Earth, since a CME is expected to propagate away from the Sun approximately radially (Hundhausen *et al.*, 1994; St. Cyr *et al.*, 1999, 2000).

The Extreme-Ultraviolet Imaging Telescope (EIT, Delaboudinière *et al.*, 1995) onboard the SOHO spacecraft, which observes the full Sun regularly with four different filters and with a pixel size of 2.6 arcsec, was initially used to look for any

evidence of eruptive activity in the active regions present on and around 10 April 2006, focusing on the region close to the centre of the solar disk. At 05:47 UT on 10 April 2006, an EUV brightening was observed at 195 Å, corresponding to a GOES B4.4 class X-ray flare in active region 10869 with an onset time of 05:42 UT (peaking at 05:48 UT), indicating possible reconnection following an eruption in this region. The EIT observations of the ejecta, combined with the location of the active region near to the disk centre and the good agreement of the time of the eruption with the estimated CME transit time suggest that this CME might be the solar source of the magnetic cloud observed near Earth on 13 April 2006. However, it is necessary to check other association criteria and investigate other solar regions for evidence of a CME eruption before concluding.

As discussed in § 3.1.5.5, magnetic helicity is an approximately conserved quantity in resistive MHD with low resistivity (Berger, 1984) and provides a quantitative link between CMEs and their interplanetary counterparts. The erupting structure in the solar corona is expected to have the same helicity sign as the associated ICME (Bothmer and Rust, 1997). There are a range of signatures from which the sign of helicity of a magnetic structure can be determined. However, in the case of active region 10869, there is only one way to determine the sign of helicity from the available data.

Magnetic tongues of newly-emerged flux provide a way of directly determining the helicity of the coronal field. When the apex of a flux rope emerges across the photosphere, the presence of twist produces a contribution of the azimuthal field projected onto the line-of-sight component. This is observed in longitudinal magnetogram data as two elongated "tongues" of opposite polarities in the active region field (López Fuentes *et al.*, 2000). For a positive twist, the leading polarity appears elongated and extends southward of the following polarity. The situation is the mirror image for a negative sign of twist. A positive twist is expected in southern hemisphere active regions, whilst the opposite is true in the northern hemisphere, according to the hemispheric chirality rules (Pevtsov and Balasubramaniam, 2003). Observations of the longitudinal magnetic field of AR10869 from the Michelson Doppler Imager (MDI, Scherrer *et al.*, 1995) onboard the SOHO spacecraft allow us to study the evolution of the magnetic configuration of this region. This active region emerges only days before the eruptive activity is observed and observations of "magnetic tongues" during the emergence of flux in this region allows us to infer its sign of helicity. These observations indicate that the sign of helicity in AR10869 is positive, as expected given its southern hemisphere location, and is not in agreement with the negative sign of helicity of the magnetic cloud. We conclude that it is highly improbable that AR10869 is the solar source of the 13 April 2006 magnetic cloud.

Next, we turn to the active regions located on the solar limbs during the CME launch window, AR10866, AR10867 and AR10871. Despite the decreased likelihood of a CME observed near Earth originating from a source region far from the centre of the solar disk, cases of such a scenario have been reported. We first consider whether these active regions could be the source of the CME associated with the magnetic cloud observed *in situ* by investigating their helicity signs, using "magnetic tongues" as in the case of AR10869. These active regions are well-established and despite the east limb location of AR10871, it is possible to observe flux emergence in this region during a previous solar rotation. Inspection of the helicity signs of all of these active regions on the Sun indicates that they all have a positive sign of helicity, the opposite sign to that of the cloud. We are thus able to rule out these regions as possible source regions of the associated CME with some confidence.

The same process was also employed in the investigation of the areas of emerging flux observed on the solar disk within the estimated launch window. We found that while the southern hemisphere active region, AR10870 also appears to have a positive sign of helicity, it seems that the small, northern hemisphere active region has a negative sign of helicity; in agreement with the helicity sign of the magnetic cloud. The schematic included in Figure 3.15 illustrates the relative positions of the elongated "tongues" of opposite polarity emerging flux in the small, northern hemisphere active region. The leading polarity positive flux extends to the north of the following polarity negative flux, and this chirality indicates that the region has a negative sign of helicity.

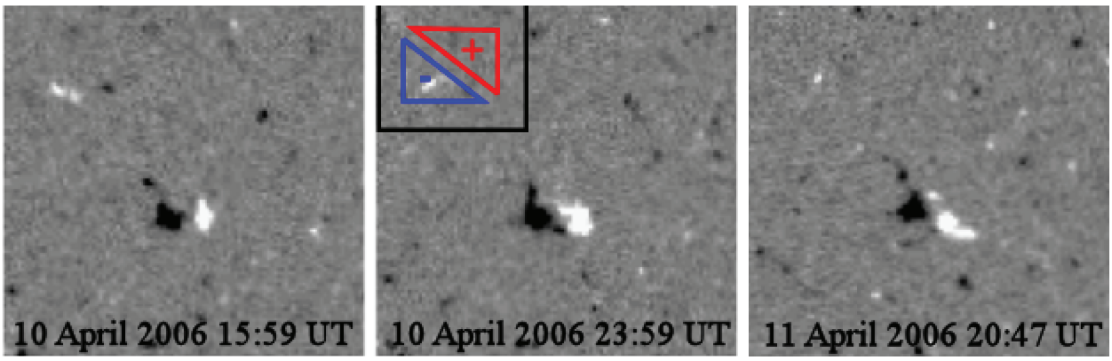

Figure 3.15: Longitudinal magnetogram observations from SOHO/MDI of flux emerging in the small, northern hemisphere active region. White corresponds to positive polarity magnetic field, whilst black corresponds to negative polarity magnetic field. The first magnetogram (*left*) shows magnetic flux in the active region soon after it begins to emerge. In the second magnetogram (*centre*) the leading (positive) polarity field extends to the north of the following (negative) polarity field. Included on this magnetogram is a schematic illustrating the relative positions of two elongated "tongues" of opposite polarities when the emerging active region has a negative sign of helicity, as in the case of this active region. The last magnetogram (*right*) shows the well-separated footpoints of the developed active region. Permission to reproduce this figure has been granted by the European Geosciences Union.

At 09:24 UT on 11 April 2006, a cusp-shaped feature was observed in this active region by EIT at 195 Å. This feature is accompanied by the formation of post-eruption loops observed by the Transition Region and Coronal Explorer (TRACE, Handy *et al.*, 1999) at 171 Å. Figure 3.16 highlights the location of this active region during the eruption, together with the locations of all of the other active regions on the visible disk at this time, while Figure 3.17 shows the coronal evolution of the erupting active region in EUV with EIT and TRACE. Highlighted are cusp-shaped coronal loops that are thought to be produced as a result of the reconnection of field lines previously opened by an eruption, so provide a signature of eruption (Sturrock, 1968). While the presence of a solar eruption in this active region suggests that the source region of the 13 April 2006 magnetic cloud has been identified, the evidence is not conclusive and we must eliminate all other possible sources.

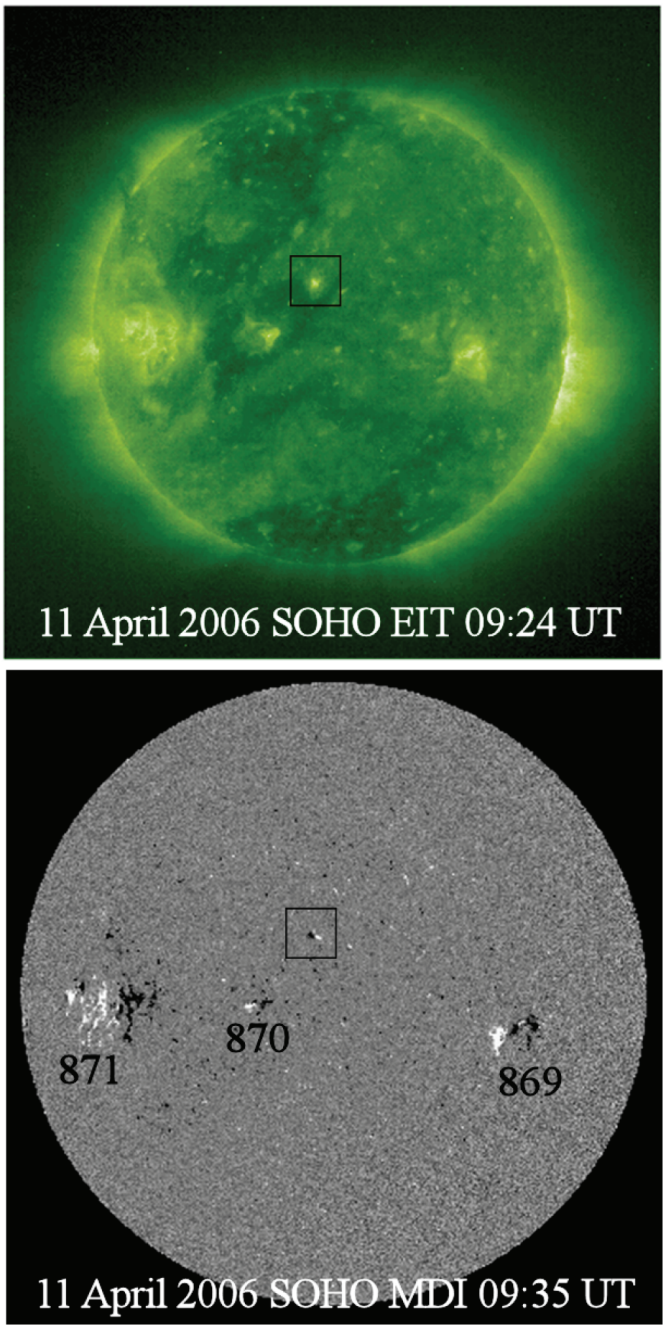

Figure 3.16: The locations of all of the active regions on the visible disk of the Sun at the time at which the CME associated with the magnetic cloud erupted. At 09:24 UT on 11 April 2006, there are four active regions on the Sun observed by SOHO/EIT at 195 Å and observed a short time later by SOHO/MDI. The eruption originates from a small, spotless active region located slightly north east of disk centre (shown within the boxes). AR10869 is located towards the west limb, and AR10870 and AR10871 are both located east of the central meridian. All of the active regions that have been allocated NOAA active region numbers are situated in the southern solar hemisphere. Permission to reproduce this figure has been granted by the European Geosciences Union.

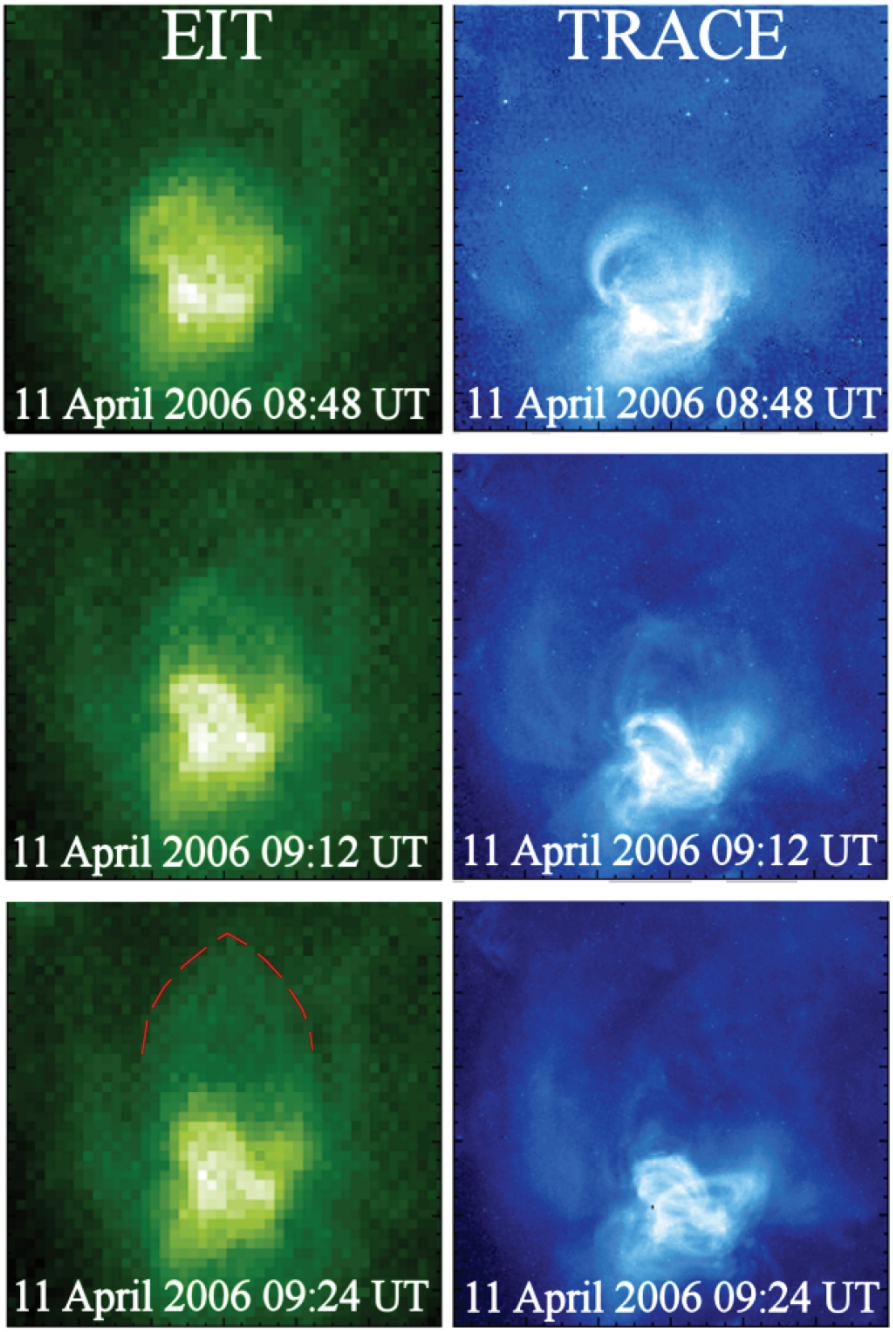

Figure 3.17: Coronal evolution of the small, northern hemisphere active region prior to and following the eruption that occurred in this region at ∼ 09:24 UT on 11 April 2006. The left column shows data from SOHO/EIT at 195 Å. A cusp-shaped coronal loop is observed at 09:24 UT (red dashed line) providing evidence of an eruption in this region. The right column shows data from TRACE at 171 Å, in which post-eruption loops are observed coinciding with the time of the eruption estimated from the SOHO/EIT observations. The field of view of these images is 120 x 120 arcsec (2.62 arcsec per pixel). Permission to reproduce this figure has been granted by the European Geosciences Union.

We consider that the source of the CME may be located in the quiet Sun. Filaments, or eruptive prominences frequently accompany CMEs (e.g., Hundhausen, 1993; Hanaoka *et al.*, 1994; Gopalswamy *et al.*, 1996). When a filament begins to rise during the eruption of a CME, the Hα emission is Doppler shifted and may no longer be visible in narrow band images. These are known as "disappearing filaments" (Pick *et al.*, 2006). Hα observations, obtained from a number of solar observatories, show several quiescent filaments present on the solar disk during the launch window of the magnetic cloud, located in both the northern and southern hemispheres. Observations of the evolution of the only quiescent filament clearly visible in the northern hemisphere (which is expected to have a negative sign of helicity) reveal that it shows no evidence of erupting within the CME launch window. We also studied the small, northern hemisphere active region for evidence of a filament eruption, which might further suggest that the CME originated from this region. However, given the small size of the region, the spatial resolution of the available Hα data was not sufficient to resolve any filaments or filament eruptions in the observations.

Earth-directed, halo CMEs appear to surround the occulting disk in white-light coronagraph observations. In the case of a partial halo CME, which does not originate exactly at the centre of the solar disk, the location of the CME in the coronagraph field of view can tell us about the location of its solar source. A very faint, partial halo CME was observed at $\sim$ 06:00 UT on 10 April 2006 by the Large Angle Spectroscopic Coronagraph (LASCO, Brueckner *et al.*, 1995) onboard the SOHO spacecraft. This is the only partial halo CME recorded in the LASCO CME catalog during the launch window of the magnetic cloud, and this was verified by a visual inspection of the LASCO data. The first observation of this CME was by the C2 coronagraph at 06:06 UT, and at 11:18 UT the CME became visible in the C3 coronagraph. The linear speed and the estimated onset time of this CME recorded in the LASCO CME catalog are 183 km s^{-1} and $\sim$ 04:00 UT respectively. However, projection effects mean that the plane of sky speed may not be representative of the actual radial speed of the ejecta. The CME extends into the south west quadrant of the coronagraph field of view, and it is expected that the source region of the ejecta should be located south west of the disk centre. However, a lack of eruption signatures on the solar disk corresponding to this CME have led us to conclude that this was a back-sided event; a conclusion that was also reached by the scientists who compile the LASCO CME catalog.

Detailed study of the Sun indicates that the small, northern hemisphere active region is the most likely source of the CME associated with the 13 April 2006 magnetic cloud. Next, the evidence that links the eruption of a CME in this active region with the *in situ* observations of the magnetic cloud observed at 1 AU is

presented.

3.2.3.1 Linking the magnetic cloud with its solar source

CMEs predominantly propagate away from the Sun in a radial direction. When a CME originates within $R_{\odot}/2$ of the centre of the solar disk, it is expected that its interplanetary counterpart will be observed *in situ* near Earth. When evidence of an eruption was observed at 09:24 UT on 11 April 2006 in the small, northern hemisphere active region, this active region was located slightly north-east of disk centre. Its location implies that this CME is likely to be classified as a halo or partial halo and would be observed by the ACE spacecraft at 1 AU.

This active region is situated on the boundary of a coronal hole. While active regions contain mainly closed magnetic field lines, coronal holes are regions of low emission dominated by "open" magnetic field lines (Kopp and Holzer, 1976a). Despite the small size of this active region, its location means that it might be expected to erupt more readily than if it were situated in the quiet Sun (Bravo *et al.*, 1999). Reconnection between the active region field and the coronal hole field leads to closed active region fields being opened. This removes field overlying the core of the AR and leads to the rapid decrease of the field strength with respect to height, and increases the ease of the escape of the ejecta (Baker *et al.*, 2007; Toeroek and Kliem, 1997).

Liu (2007) showed observationally that CME source regions in coronal holes produce fast ejecta (with speeds of up to 2000 km s^{-1}). This suggests that the speed of this eruption may be faster than might be expected for a region of this size. Measurements of the velocity of the magnetic cloud near Earth show that it was propagating at a mean velocity of 520 km s^{-1}. However, for this CME to travel to 1 AU in only 59 hrs, it must have had a substantially faster initial velocity, which decreased as it propagated away from the Sun. These observations suggest that the mean velocity of this ejecta, during its transit from the Sun to 1 AU, should have been nearer to 710 km s^{-1}.

Moreover, an association can be made between the fast solar wind stream observed following the cloud, and its solar origins. The location of the source region near to the central meridian at the time of the eruption, together with its close proximity to a coronal hole that is situated to the east of this active region explains the presence of the high speed stream following the cloud. Prior to the arrival of the magnetic cloud, the solar wind speed is representative of the average speed of the slow solar wind, propagating at $\sim$ 400 km s^{-1}. The propagation speed of the

magnetic cloud is faster than this solar wind flow, consequently resulting in the formation of a forward fast shock. Shortly after the eruption in the small northern hemisphere active region, the coronal hole crosses the central meridian of the Sun. Following the passage of the magnetic cloud at 1 AU, a high speed solar wind stream originating from this region is observed near Earth with speeds reaching up to $\sim$ 700 km s^{-1}. These observations provide further evidence of the correct association between the source region identified and the observed magnetic cloud.

The conserved nature of magnetic helicity means that a magnetic cloud and its associated CME must share the same sign of helicity. Observations of the chirality of the 13 April 2006 cloud directly from *in situ* measurements indicated that it is left-handed, corresponding to a negative sign of helicity. By considering "magnetic tongues" of emerging flux in the active regions present on the Sun during the CME launch window, we found that only one, the small, northern hemisphere active region, has a negative helicity sign, in agreement with the cloud.

The magnitude of the magnetic flux within the magnetic cloud cannot exceed the amount of magnetic flux available in the source region of the associated CME. From the value obtained for the radius of the cloud and an estimate of the magnetic field at the cloud axis, B_0, the classical, linear, force-free model of Lundquist (1950), $\nabla \times \mathbf{B} = \alpha \mathbf{B}$, with constant α (e.g., Burlaga *et al.*, 1981; Burlaga, 1988; Lepping *et al.*, 1990) can be used to estimate the flux within the 13 April 2006 magnetic cloud. The axial flux, F_z, is $\sim 2.0 \times 10^{20}$ Mx and the azimuthal flux, F_ϕ per unit length, is $\sim 1.1 \times 10^{21}$ Mx/AU. The azimuthal flux within the magnetic cloud is greater than the axial flux, as is expected for a highly twisted flux rope.

In the corona, the flux involved in a CME eruption is often estimated by considering the spatial extent of the associated coronal dimmings. In the case of the eruption on the 11 April 2006, studies of difference images constructed from EIT data have not revealed any evidence of coronal dimmings in the CME source region. However, this does not necessarily mean that they are not present. Given the small size of this active region it is likely that the spatial resolution of the EUV observations is not sufficient for us to resolve these dimmings.

In these circumstances, we instead compare the amount of flux in the entire active region with estimates of the flux in the magnetic cloud. MDI returns the longitudinal flux density, averaged over the pixel field of view. Multiplying the flux density by a given area then gives the total flux contained within this area. To measure the magnetic flux within an active region a polygonal contour, defined by visual inspection, is fitted around the region and the flux is summed within it. The MDI instrument requires some corrections, and for this we follow the method of

Berger and Lites (2003). In our data, the flux values must be corrected by a factor of 1.45 which gives the magnetic flux of the active region (the average between values obtained for the positive and negative fluxes) to be $7(\pm 0.4) \times 10^{20}$ Mx. We can show therefore that the flux in the magnetic cloud does not exceed the amount of flux in the northern hemisphere active region, despite its small size.

Comparisons can often be made between the orientation of the magnetic structure in interplanetary space and its magnetic configuration in the corona. In this particular case, the lack of clear observations of the erupting structure in the corona means the association with its interplanetary counterpart is not straightforward. The orientation of the magnetic cloud can be determined directly from the *in situ* data. Using a minimum variance analysis, we determined that the orientation of the cloud axis is described by $\theta \sim 68°$ and $\phi \sim 294°$. The orientation of the cloud implies that the ACE spacecraft crossed the western "leg" of the magnetic cloud and this is in agreement with the eastern position of the source region, with respect to the central meridian.

3.2.4 Discussion and Conclusions

A magnetic cloud was identified on 13 April 2006 in *in situ* observations of the solar wind at 1 AU. The reasons for selecting this event for further study were twofold. Firstly, at the time that this study was commenced the *in situ* magnetic field and plasma observations from April 2006 were some of the most current data available. Secondly, the event exhibited a significant number of the known magnetic cloud signatures, and the relative lack of complexity of this event meant it was particularly well-suited for further study of its solar origins. Detailed analysis of this magnetic structure revealed that the magnetic field undergoes smooth rotation, the magnetic field strength is elevated and the proton temperature is low, and these signatures were observed over a period of $\sim$ 9 hours, implying a small magnetic cloud. The geometry of the cloud, inferred directly from observations, implies that the axis is predominantly in the $z_{,GSE}$ direction and the rotation is predominantly contained in the $y_{,GSE}$ direction. It exhibits left-handed chirality, corresponding with a negative sign of helicity.

The associated CME is believed to originate from a small, northern hemisphere active region, in which evidence of eruptive activity is observed on 11 April 2006. There are a number of pieces of evidence that link this eruption with the observed magnetic cloud, including the location of the active region close to disk centre, the transit time of the CME, and unique agreement between the helicity signs of the active region and the cloud. Estimates of the flux in the magnetic cloud do not

exceed the flux in the active region, the orientation of the cloud is in agreement with the eastern hemisphere location of the active region during eruption and the fast solar wind stream observed following the cloud has been associated with the coronal hole bordering this active region.

Here, we consider several possible eruption scenarios for this event:

1. Simple expansion of coronal loops or pre-existing flux rope.

   In this scenario, the axial flux of the magnetic cloud should match the longitudinal flux in the coronal dimmings, which are thought to reveal the footpoints of the expanding and erupting magnetic structure. However, the eruption studied in this event showed no dimming signature. In this case, the longitudinal flux contained within the active region sets an upper limit for what is expected to be detected in the MC. In our case this holds, as we find that the active region flux is a factor of 3.5 larger than the axial flux of the MC.

2. Flux rope formation during the eruption.

   In this scenario, the flux rope was not present before the eruption, but instead was formed through successive reconnection as the eruption proceeded. This means that the azimuthal field of the magnetic cloud comes purely from reconnection, which not only produces the ejected flux rope, but also produces the flare loops below. As a result of this Qiu *et al.* (2007) propose that in this case the azimuthal flux is approximately equal to the reconnection flux observed in the flare ribbons. In our case no flare ribbons were produced so we cannot further investigate this scenario.

3. Eruption of a flux rope with reconnection proceeding underneath.

   In this scenario (also known as the CSHKP scenario (Carmichael, 1964; Sturrock, 1966; Hirayama, 1974; Kopp and Pneuman, 1976), see § 1.4.1), as the flux rope rises reconnection proceeds below it. This reconnected flux closes down to form flare loops and up to add azimuthal flux to the pre-existing flux rope. In this case, Qiu *et al.* (2007) propose that the azimuthal flux is greater than the reconnected flux. Again, the absence of flare ribbons means that this scenario cannot be tested.

Unfortunately, the observational evidence available is not sufficient for us to conclude with any certainty which of these eruption scenarios is most like to have

occurred for this event. This is likely due, in part, to the small size of the CME source region and the limited spatial resolution of the observations available when this event occurred. However, EUV observations of cusp-shaped coronal loops are an indication of the presence of magnetic reconnection in this region, even though it is not energetic enough to produce a solar flare. The presence of reconnection, together with the measurements of the magnetic flux in the active region and magnetic cloud leads us to favour the second or third scenarios.

The Atmospheric Imaging Assembly (AIA) onboard the Solar Dynamics Observatory (SDO) provides full disk observations of the Sun at 10 different wavelengths, 6 of which are in the EUV, at a vastly improved spatial resolution and with a cadence of only 10 seconds. These observations will, no doubt, revolutionise the study of CMEs from small solar sources, like those from very small active regions and X-ray bright points, allowing the nature of these regions to be probed in unprecedented detail.

This study does not present the first example of a well-defined magnetic cloud observed *in situ* originating from an unusually small solar source. Mandrini *et al.* (2005) studied an eruption from an X-ray bright point situated within a coronal hole; which formed the smallest magnetic cloud observed to that point in time. Although there are similarities between our event and that studied by Mandrini *et al.* (2005), there are also some interesting differences. The eruption in Mandrini *et al.* (2005) produces a transition from sigmoid to cusp in the structure of the X-ray bright point, and twin dimmings. These can be used to investigate the erupting field, and Mandrini *et al.* (2005) propose that the longitudinal flux in the dimmings (60 % of the X-ray bright point's flux) is well correlated with the azimuthal flux in the magnetic cloud. In our case, the observational signatures of the eruption are far more subtle and we are unable to investigate this aspect. Also, there is a factor of 2 difference between the source region flux in these two case studies, yet a factor of 10 difference in the axial field and the azimuthal field per unit length between the studied magnetic clouds, with the MC cloud in this work being the larger in all cases.

This study highlights the complexities associated with locating the solar source of a magnetic cloud observed *in situ* near Earth, and serves to emphasise that it is the combination of physical signatures evident in the magnetic field and plasma observations, both in interplanetary space and at the Sun, that is important for successfully tying together the Earth-end and the Sun-end of an event.

Chapter 4

On the Structure and Evolution of Magnetic Clouds

The magnetic topology of ICMEs arriving at Earth is an important factor in determining how geoeffective they are, but the structure observed *in situ* at 1 AU can be very different to the corresponding erupting structure observed on the Sun. In this chapter, we investigate the evolution of the structure of magnetic clouds as they propagate into the heliosphere, furthering our study of the 13 April 2006 magnetic cloud discussed in Chapter 3.

In § 4.1.1, we discuss the current understanding of the nature of CME propagation and in § 4.1.2 we consider the evidence that suggests that the topology of a magnetic cloud does not always conform to the expected flux rope geometry. The magnetic cloud observed near Earth on 13 April 2006 exhibits substructure towards its centre, and in § 4.2.2 we describe the behaviours of the magnetic field and plasma within this ejecta, comparing observations from multiple spacecraft (§ 4.2.2.3). Several other cases of substructure within magnetic clouds have also been identified, and we discuss the similarities and differences between these events in § 4.2.3, before briefly evaluating the possible causes of such topological anomalies in their magnetic structure in § 4.3. Further consideration is given to the processes that give rise to internal structure in magnetic clouds in Chapter 5.

4.1 Introduction

4.1.1 The Propagation of ICMEs

Both simulations of ICME propagation and *in situ* observations of their complex signatures indicate that they evolve substantially as they move out into the heliosphere (e.g. Crooker *et al.*, 1990; Gosling, 1996). Since many ICMEs do not travel at the same speed as the surrounding solar wind, compressions and rarefactions develop at the edges of the events (Crooker and Horbury, 2006). Possible consequences of ICME-solar wind interactions include shocks, acceleration or deceleration of ICMEs and distortion of the ICME shape (e.g. Gosling and Riley, 1996).

Numerical simulations of ICME interactions with the ambient solar wind have shown that CMEs evolve very differently, depending on the speed of the ambient solar wind flow (Riley *et al.*, 1997). Results also suggest that a single interplanetary disturbance can have radically different appearances at various locations, with their appearance also depending heavily on the launch location of the CME with respect to the streamer belt flow (Odstrcil and Pizzo, 1999a,b). Odstrcil *et al.* (2004) found that even relatively small-scale structures in the background solar wind may play an important role in the interplanetary evolution of transient disturbances.

4.1.1.1 CME speed

Following the eruption of a CME, minor acceleration or deceleration ($\pm$ 20 m s^{-2}) (Moon *et al.*, 2002; Yashiro *et al.*, 2004) of the magnetic structure takes place in the inner heliosphere below 2 $R_{\odot}$ (Schwenn *et al.*, 2006), with faster CMEs exhibiting a tendency to decelerate, while slower CMEs accelerate (Gopalswamy *et al.*, 2000a; Schwenn *et al.*, 2005). This change in speed is apparent in discrepancies between the transit speeds of CMEs measured using white-light observations from coronagraphs and their measured *in situ* speeds (e.g. Schwenn, 1986; Cliver *et al.*, 1990; Lindsay *et al.*, 1999). However, beyond solar distances of 0.3 AU, average ICME speeds show little radial variation out to 1 AU. Here, the ICME is primarily subject to drag forces (Forbes *et al.*, 2006).

There are several factors that could influence the transit times of CMEs. As discussed in § 1.4.2, due to projection effects the plane of sky speed of a CME measured using remote observations is not a direct measure of its radial speed. This effect becomes more pronounced the closer to the Sun-Earth line a CME propagates; hence it is most difficult to accurately determine the radial speeds of halo CMEs,

which are propagating towards the observing spacecraft. Burkepile *et al.* (2004) studied the role of projection effects in CMEs observed by the Solar Maximum Mission (SMM). They found that the speeds of around 50 % of CMEs originating at the limb, where projection effects are minimal, are lower than 400 km s^{-1}, the nominal solar wind speed. Remote observations suggest that average halo CME speeds are in the region of 1000 km s^{-1}, more than twice the average speed of all CMEs. There is no indication that CMEs originating on the solar disk are physically any different from those originating on the limb, and these elevated speeds are most likely the result of both projection effects and the increased difficulty in detecting CMEs directed towards the observing spacecraft, of which only the strongest events are easily seen (Yashiro *et al.*, 2004; Tripathi *et al.*, 2004).

Correlations between the plane of sky speeds of CMEs and their radial speeds have been established, for example it is estimated that the radial expansion speeds of CMEs are typically $\sim$ 88 % of the lateral expansion speeds (Dal Lago *et al.*, 2003; Schwenn *et al.*, 2005). This relation is independent of both the speed and angular extent of the CME. While Gopalswamy *et al.* (2001b) concluded that in the case of halo CMEs, the plane of sky speed seems a reasonable representation of the CME initial speed. Transit times also depend upon which feature of the CME is used to time its arrival at the *in situ* spacecraft. Selecting the time of arrival of the centre of the cloud, rather than that of the shock front (Schwenn *et al.*, 2005) or the first detection of ICME material (Gopalswamy *et al.*, 2000a, 2001b), reduces the likelihood of mixing up the expansion of the structure and its global motion in the solar wind.

It is generally agreed that CMEs take, on average, $\sim$ 4 days to propagate from the corona to 1 AU, with the fastest CMEs traversing this distance in $<$ 1 day. Figure 4.1 shows the apparent speeds of all the CMEs observed by SOHO/LASCO from 1996 to the end of 2004. The variability of individual CME speeds, together with the variability in transit speeds for similar CME speeds (e.g. Cane and Richardson, 2003b; Schwenn *et al.*, 2005) is highlighted by the range of transit times reported in the literature. CME transit time is also influenced by the limitations of the methods used to determine the arrival time of ICMEs from remote observations of halo CME speeds. Estimations of transit time by Cane and Richardson (2003a), measured from observations of the first ICME-related disturbance, lie in the range $\sim$ 1.1 to 2.9 days for CMEs travelling at 1500 km s^{-1}, while the assumption that CME speed is constant leads to an estimated transit time of 1.16 days (Schwenn *et al.*, 2005) and the Gopalswamy *et al.* (2000a) model suggests a value of $\sim$ 1.4 days. For ICMEs associated with geomagnetic storms, Zhang *et al.* (2003) estimate that transit time = 96 - V_{CME}/21 hours, though in the case of exceptionally fast CMEs, $\geq$ 2016 km s^{-1}, the transit time tends to zero and this relation cannot hold.

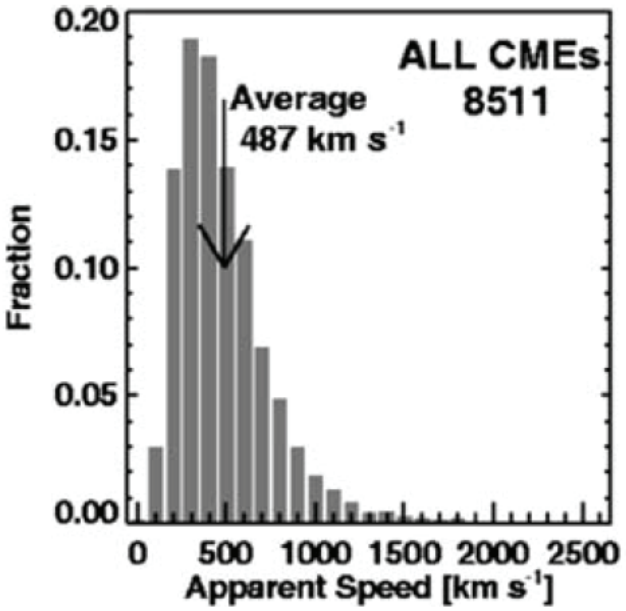

Figure 4.1: Speeds of all CMEs observed by SOHO/LASCO from 1996 to the end of 2004. The speed could not be measured for all the detected CMEs. The average of the distribution is shown on the plot. Figure adapted from Gopalswamy *et al.* (2005b). Permission to reproduce this figure has been granted by N. Gopalswamy.

4.1.1.2 Magnetic cloud expansion

In situ observations of the velocity profiles of magnetic clouds and the increase in their size with solar distance show that they typically expand as they propagate through the heliosphere, with the decrease in total solar wind pressure with solar distance playing a significant role in driving this expansion (Démoulin and Dasso, 2009).

The change in the translational velocity over the duration of a magnetic cloud can be used to calculate its expansion rate. However, the difference, ΔV_x between the leading and trailing edges is not a direct indicator of the expansion rate of a plasma element, since in particular, ΔV_x depends on the size of the magnetic cloud, so that larger magnetic clouds have typically larger ΔV_x values. A better measure of the expansion rate of the magnetic cloud is given by the non-dimensional expansion rate, ζ defined from theoretical considerations by Démoulin *et al.* (2008) and from data analysis by Gulisano *et al.* (2010), which allows an expansion speed with respect to the cloud centre to be computed,

$$\zeta = \frac{\Delta V_x}{\Delta t} \frac{D}{V_c^2} \tag{4.1}$$

where Δt is the time difference between the observations of the in- and out-bound boundaries, V_c is the velocity of the magnetic cloud centre and D is the distance

to the Sun. A simple interpretation of ζ is obtained when it is independent of the distance, D to the Sun. Then the size, S of the magnetic cloud is simply evolving with distance, D as:

$$S = S_0(D/D_0)^{\zeta} \tag{4.2}$$

where S_0 is the reference size at the distance D_0. More generally, ζ measures the proportion by which the magnetic cloud is changing its size with solar distance during the spacecraft crossing (independently of its size, S_0).

Gulisano *et al.* (2010) showed that those magnetic clouds that exhibit the expected linear velocity profile expand with almost the same non-dimensional expansion rate, $\zeta = 0.91 \pm 0.23$. Departures from this general rule occur when the magnetic cloud is significantly perturbed from the linear profile. This is likely a consequence of local and strong perturbation by fast solar wind streams affecting the internal structure of the magnetic cloud, in addition to the direct interaction region between the solar wind and the magnetic cloud. For perturbed magnetic clouds, $\zeta = 0.48 \pm 0.79$.

CMEs usually undergo "self-similar" expansion as they propagate into the heliosphere, which means that the ratio between lateral expansion and radial propagation appears to be constant for most CMEs (Plunkett *et al.*, 1998). The shape of the cross-section of the vast majority of CMEs appears to be nearly perfectly circular (Cremades and Bothmer, 2005), in keeping with the concept of magnetic clouds as cylindrical magnetic flux ropes, and this shape appears to be maintained in halo CMEs propagating along the Sun-Earth line. This observation is rather surprising in that CMEs are usually associated with the eruption of 2-D elongated filament structures (Schwenn *et al.*, 2006).

4.1.2 Unusual Magnetic Cloud Topology

Magnetic clouds have been widely modelled as large-scale, force-free, cylindrical magnetic flux ropes (e.g. Lepping *et al.*, 1990; Marubashi, 1997; Lynch *et al.*, 2003; Dasso *et al.*, 2005). In this scenario, the magnetic field is helical, such that it is in the axial direction towards the centre of the flux rope and in the azimuthal direction at the flux rope boundary. As a magnetic cloud passes over a spacecraft located in the solar wind, a bipolar signature, observed in the azimuthal magnetic field component, is anticipated. This is indicative of the large-scale rotation of the magnetic field within the structure. However, this rotation is not always smooth, and often exhibits both small- and large-scale fluctuations of the magnetic field within the cloud (Crooker *et al.*, 1990). Various physical processes have been proposed that may

influence the topology of a magnetic cloud, both near to the Sun and further out in the heliosphere, including magnetic reconnection (Gosling *et al.*, 2007a), interaction between multiple magnetic flux ropes (e.g. Fainberg *et al.*, 1996; Lepping *et al.*, 1997; Osherovich *et al.*, 1999; Farrugia, 2001), spontaneous formation of current sheets (Owens, 2009), or interaction with dust trails originating from comets (Russell *et al.*, 2009). The possible causes of internal structure in magnetic clouds is the subject of further investigation in Chapter 5.

In a case study by Crooker *et al.* (1990), they identified 11 magnetic field discontinuities within a magnetic cloud previously identified by Zhang and Burlaga (1988), leading to ambiguity over which discontinuities represent the ICME boundaries. Figure 4.2 highlights the identified discontinuities in that cloud. Discontinuities 5 and 8 were the first reported boundaries of this magnetic cloud, but following the determination of discontinuity 1 as the ICME-driven shock, this still leaves several discontinuities that may provide a better approximation of the boundaries of this ICME. Discontinuities 2, 4, 5 and 7 were determined to be tangential discontinuities, aligned nearly parallel to one another. A temperature decrease occurs at discontinuity 2, near the leading edge of the ICME and this may, in fact, represent the true ICME boundary and discontinuity 5 may be interpreted as an unusual boundary structure within the flux rope, rather than the ICME leading edge. It appears that discontinuities 3 and 4 bound a "magnetic hole"; these are complex, pressure-balanced structures that are sometimes found near the leading edges of ICMEs (Burlaga, 1995; Farrugia, 2001). Crooker *et al.* (1990) interpreted discontinuities 6 and 7 as defining the core of the magnetic cloud, since there is minimal twisting of magnetic field lines, while the proton temperature recovers at discontinuity 9, perhaps indicating that this is the true rear boundary of the ICME, rather than discontinuity 8, where the magnetic field observations suggest the magnetic cloud signatures end.

It has previously been suggested that boundaries within ICMEs may be associated with substructures of the ICME. For example, Osherovich *et al.* (1999) discuss a magnetic cloud, observed by Ulysses, which may be modelled as two intertwined helical flux tubes separated by a region of enhanced plasma pressure. Other case studies of the plasma and magnetic field structures within ICMEs show similar complications. These studies include analysis of the magnetic clouds of 18-20 October 1995 (e.g. Lepping *et al.*, 1997; Janoo *et al.*, 1998), and within this Chapter we investigate the internal structure of this, and other similar events, further.

In those events where multiple flux ropes are identified, Vasquez *et al.* (2001) showed that the boundaries between the ejecta can contain many tangential discontinuities, which raise interesting questions about the resulting large-scale structure

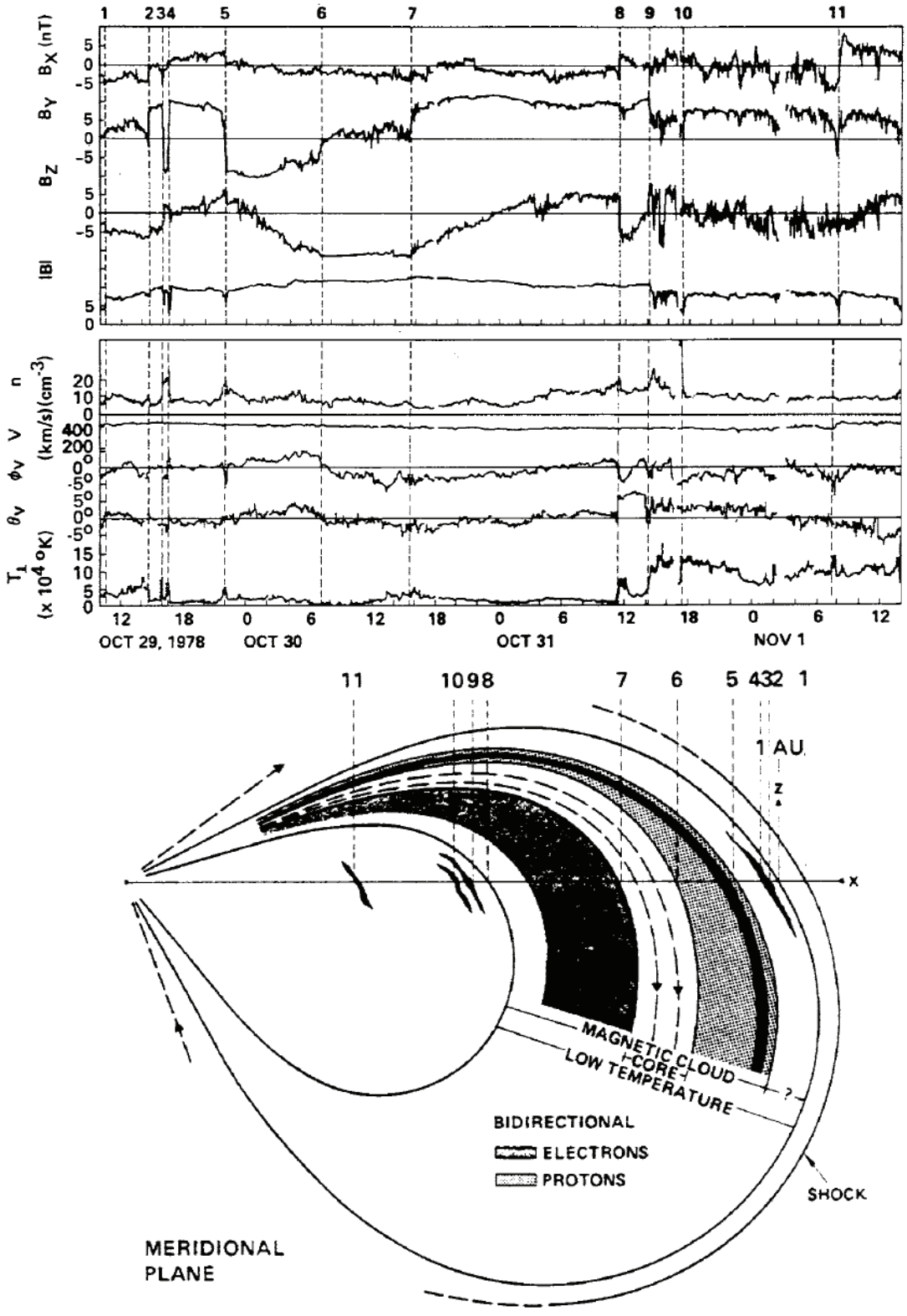

Figure 4.2: Discontinuities, identified by Crooker *et al.* (1990), within the magnetic field observations in the vicinity of a magnetic cloud in October 1978 (*top*). Interpretation in the meridional plane of the structures identified in the magnetic field data and their relationship to intervals of counterstreaming ions (dotted region) and electrons (black) (*bottom*). Figure adapted from Crooker *et al.* (1990). Permission to reproduce this figure has been granted by the American Geophysical Union.

of these ICMEs, since they form boundaries between different plasma regimes within the ejecta. In a small handful of magnetic clouds, multiple reversals of the main gradient of the azimuthal magnetic field component are observed towards the centre of the cloud (Dasso *et al.*, 2007). These authors suggest that in a magnetic flux rope structure, the magnetic flux surfaces of a magnetic cloud could become "warped" as a result of its fast evolution and interaction with the ambient solar wind, giving rise to the observed magnetic field fluctuations. This scenario, together with other possible causes of this kind of substructure, are investigated further in Chapter 5.

These events illustrate the complexities associated with the structure of some magnetic clouds. Discontinuities are increasingly being noted within the larger-scale magnetic flux rope structure of magnetic clouds, but the implications for the topology of these clouds is not always clear.

4.2 Investigating the Observational Signatures of Magnetic Cloud Substructure

The work described in this section of the thesis can be found in the following published article:

Steed, K., Owen, C. J., Démoulin, P. and Dasso, S.: Investigating the observational signatures of magnetic cloud substructure. 2011, *J. Geophys. Res.*, 116, A01106.

4.2.1 Event Context

Magnetic clouds represent a subset of ICMEs that exhibit a magnetic flux rope structure. They are primarily identified by smooth, large-scale rotations of the magnetic field. However, both small- and large-scale fluctuations of the magnetic field are observed within some magnetic clouds. We analysed the magnetic field in the frame of the flux rope, approximated using a minimum variance analysis, and have identified a small number of magnetic clouds within which multiple reversals of the gradient of the azimuthal magnetic field are observed. We herein use the term "substructure" to refer to regions that exhibit this signature.

We examine, in detail, one such magnetic cloud observed on 13 April 2006 by the ACE and WIND spacecraft at 1 AU (see Chapter 3) and show that substructure has distinct signatures in both the *in situ* magnetic field and plasma observations. We

identify two thin current sheets within the substructure region of this event and find that they bound the region in which the observations deviate most significantly from those typically expected in MCs. A comparison of the properties of this magnetic cloud with 5 similar events exhibiting substructure reveals that these clouds have lower non-dimensional expansion rates than non-overtaken magnetic clouds, and that the majority of these clouds are followed by fast solar wind streams.

4.2.2 *In situ* Observations of Substructure in the 13 April 2006 Magnetic Cloud

Figure 4.3 shows data taken of the magnetic cloud encountered by the ACE and WIND spacecraft on 13 April 2006. This MC displays many of the typical characteristics used to identify a magnetic cloud (Steed *et al.*, 2008), and also exhibits the clearest example of substructure towards its centre that we have found. Magnetic field data from the Magnetic Field Investigation (MFI, Lepping *et al.*, 1995) and plasma data from the 3-D Plasma and Energetic Particle Experiment (3DP, Lin *et al.*, 1995) on the WIND spacecraft, located upstream of Earth, are shown at 3 second resolution. Panels (a) and (b) show the total and B_x, B_y and B_z components of the magnetic field in Geocentric Solar Ecliptic (GSE) coordinates, respectively. Panel (c) shows the bulk flow speed of the protons, panel (d) shows the proton number density and panel (e) shows the radial proton temperature. Panel (f) shows the pitch angle velocity distributions of suprathermal electrons at 272 eV observed by the Solar Wind Electron Proton Alpha Monitor/STEA (SWEPAM, McComas *et al.*, 1998) on the ACE spacecraft, which has been temporally aligned with observations of the substructure region at WIND (see § 4.2.2.3). Counterstreaming beams of suprathermal electrons are typically associated with ICMEs (Zwickl *et al.*, 1983; Gosling *et al.*, 1987) and tell us about the connectivity of magnetic field lines to the Sun (see § 3.1.2.4). Figure 4.3(f) shows that counterstreaming suprathermal electron beams at $\sim$ 272 eV are observed throughout much of this magnetic cloud, indicating that it is still connected to the Sun when it is observed at ACE. However, the onset of these bidirectional beams is $\sim$ 1 hr prior to the onset of the magnetic cloud, as determined from the magnetic field observations, suggesting the presence of closed magnetic field lines propagating ahead of the magnetic cloud. We suggest that this may indicate that overlying coronal loops were also pushed out and ejected when this magnetic cloud erupted. We also note that the observations show that the beam is unidirectional as the spacecraft emerges from the substructure region and moves into the back part of the magnetic cloud, indicating that the magnetic structure is partially disconnected from the Sun at one of its footpoints in this region.

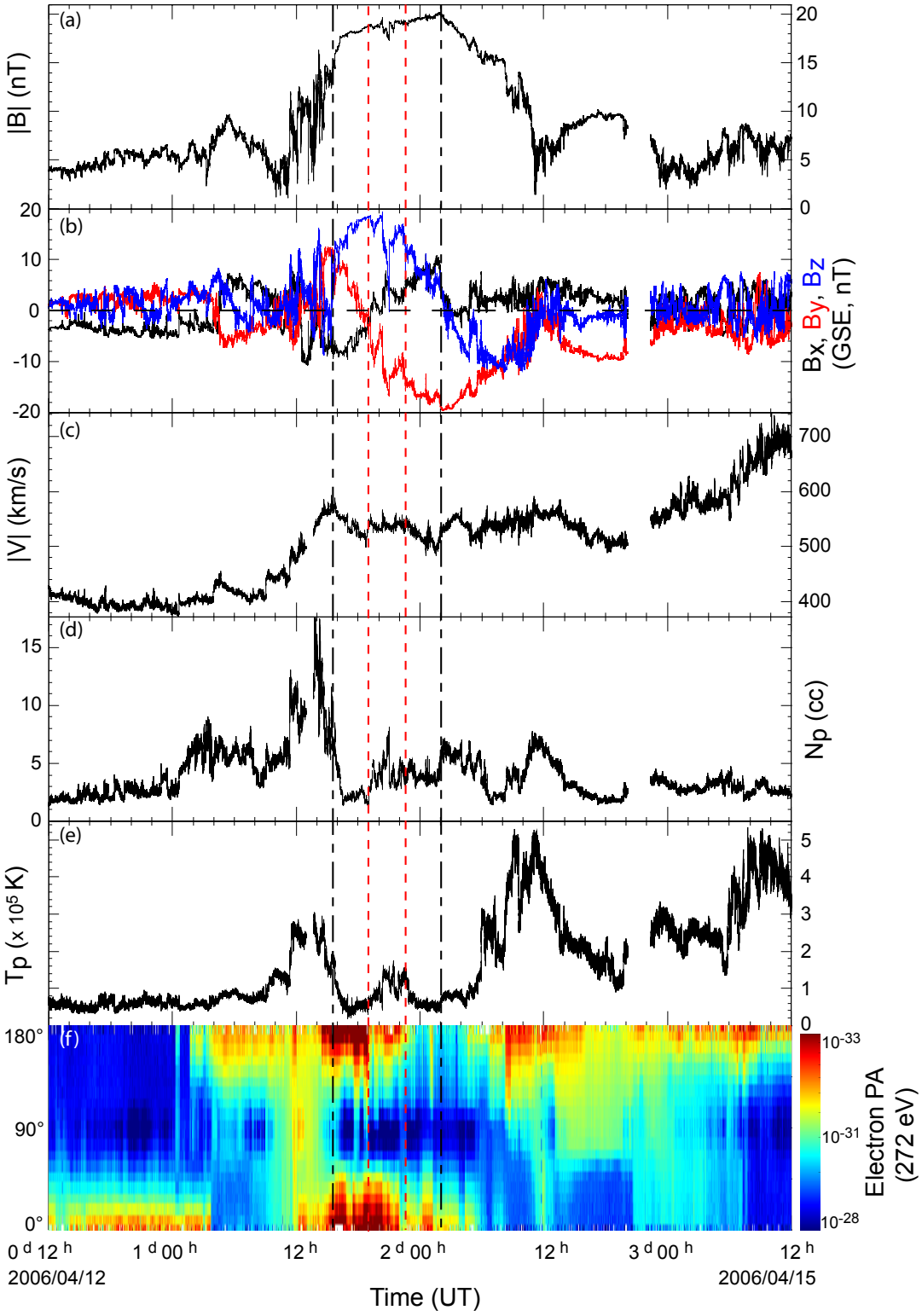

Figure 4.3: Interplanetary magnetic field and plasma data from the WIND spacecraft during the passage of the ICME ejecta in GSE coordinates. Vertical dot-dashed black lines indicate the boundaries of the magnetic cloud and vertical dashed red lines indicate the boundaries of the substructure region. This plot shows (a) the total and (b) the Bx, By and Bz components of the magnetic field, (c) proton bulk flow speed, (d) proton number density, (e) radial proton temperature and (f) the pitch angle velocity distributions $f(v)$ of the suprathermal electrons at 272 eV, in units of s^3 cm^{-6} (observed by ACE and temporally aligned with observations of the substructure region observed by WIND, see Fig. 4.6). Permission to reproduce this figure has been granted by the American Geophysical Union.

In the 13 April 2006 MC, B_z is dominated by the axial field component, while B_x and B_y have a dominant contribution from the azimuthal component (Figure 4.3(b)). However, these boundaries need to be confirmed after rotating the magnetic data in the local MC coordinate system in order to fully separate the azimuthal and axial components. We confirm the boundaries shown in Figure 4.3 by using a minimum variance analysis (MVA) (see § 2.4.2 and § 4.2.2.1) to rotate the data to the MC frame, selecting the interval that shows the clearest rotation (Figure 4.4). The MV analysis gives a ratio between the intermediate and the minimum eigenvalues of $\sim$ 12, which implies that the minimum variance direction is well defined (Siscoe and Suey, 1972). The MC axis orientation was also determined using MVA by Steed *et al.* (2008) (see § 3.2.2.2), and is described by θ and ϕ, where θ is the angle between the ecliptic plane and the MC axis and ϕ is the angle between x_{GSE} and the projection of the MC axis on the ecliptic plane (measured positive when anti-clockwise). They found that $\theta \sim 68°$ and $\phi \sim 294°$.

Vertical dot-dashed black lines in Figure 4.3 indicate the boundaries of the magnetic cloud at WIND, which are found to be very similar to those determined by Steed *et al.* (2008) and described in Chapter 3, using data from the ACE spacecraft. Unusual magnetic field and plasma observations persist beyond the identified rear boundary of this magnetic cloud and we suggest that this may be the result of interaction between the magnetic cloud flux rope and the solar wind (see also Chapter 5). Dasso *et al.* (2006) reported that magnetic reconnection can be forced in front of an MC when a flux rope is overtaking the magnetic field ahead of it. The consequence of this reconnection is a flux tube that is peeled away at the front, but has an extended back part. This "back" region is expected to exhibit different behaviour to both the main body of the ejecta and the solar wind. Steed *et al.* (2008) investigated several locations for the rear boundary of this MC and, despite the complexity of the observations towards the rear of the ejecta, they found that changes in the rear boundary location over a time interval spanning almost 10 hours did not result in major changes in the orientation of the MC axis. Within this magnetic cloud the rotation of the magnetic field evident in B_y is not smooth, and vertical dashed red lines bound the region where the B_y magnetic field observations deviate from the larger scale trend bipolar signature, exhibiting multiple reversals of the gradient of this magnetic field component towards the centre of the cloud. Associated changes in the other magnetic field directions and the plasma measurements are also observed in this region.

4.2.2.1 Magnetic field observations

Figure 4.4 shows 3 second resolution data from the MFI instrument on the WIND spacecraft over the interval of the magnetic cloud, rotated to a local co-ordinate system defined using a minimum variance analysis (MVA) (Sonnerup and Cahill, 1967) on the magnetic field. The maximum variance ($B_{y,cloud}$) direction contains the effects of the rotation of the azimuthal magnetic field, and shows that the large-scale rotation over the duration of the 13 April 2006 magnetic cloud is positive to negative. However, a number of reversals of the gradient of this magnetic field component are observed between 19:03 UT and 22:38 UT on 13 April 2006. We have identified these signatures as substructure within the magnetic cloud. The boundaries of this substructure are again highlighted by vertical short-dashed red lines. Within the substructure region, relatively sharp discontinuities are observed at 20:23 UT and 21:02 UT, indicating the presence of thin current sheets, labelled CS1 and CS2 respectively, and highlighted by vertical long-dashed green lines. Detailed analysis of the nature of these current sheets is undertaken in Chapter 5. The unusual substructure signatures observed in the $B_{y,cloud}$ magnetic field component of this magnetic cloud persisted for approximately 3.5 hours.

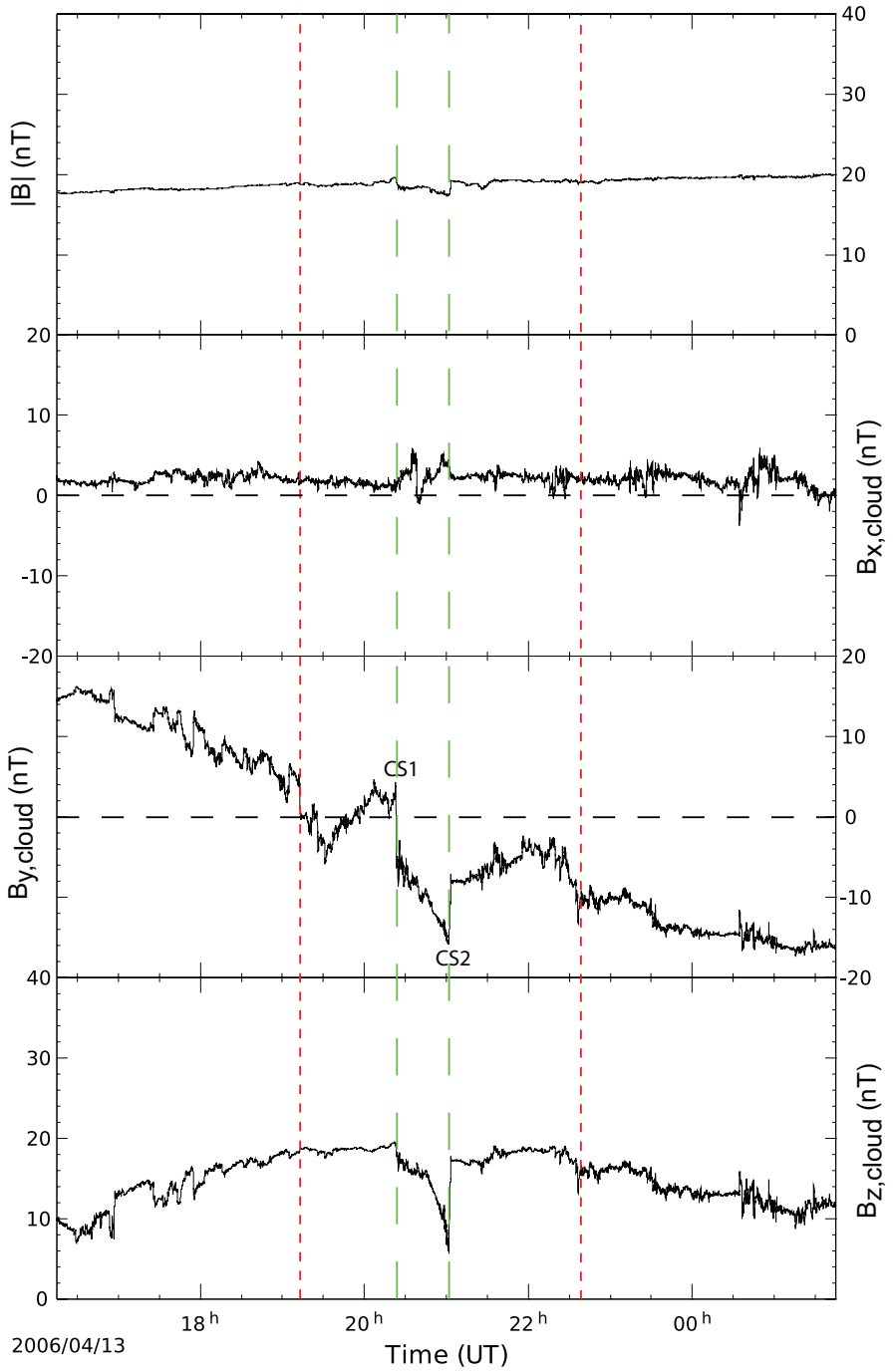

Figure 4.4: Magnetic field components in local magnetic coordinates obtained from a minimum variance analysis performed over the duration of the 13 April 2006 magnetic cloud. The panels show the magnitude of the magnetic field and the evolution of the magnetic field components in the minimum ($B_{x,cloud}$), maximum ($B_{y,cloud}$) and intermediate ($B_{z,cloud}$) variance directions. Vertical short-dashed red lines indicate the boundaries of the substructure region, within which reversals of the azimuthal magnetic field ($B_{y,cloud}$) gradient are observed. Discontinuities consistent with the presence of thin current sheets are also observed at 20:23 UT (CS1) and 21:02 UT (CS2), indicated by the vertical long-dashed green lines, coincident with an observed decrease in the axial magnetic field ($B_{z,cloud}$) component and its subsequent recovery. Permission to reproduce this figure has been granted by the American Geophysical Union.

The axial magnetic field is contained in the intermediate direction ($B_{z,cloud}$) in our local co-ordinate system. It also departs from what is expected from a force-free, cylindrical flux rope model. Observations of $B_{z,cloud}$ show that towards the centre of the MC, where it is expected that the magnetic field is strongest, the magnetic field begins to decrease where $B_{z,cloud}$ has a discontinuity at 20:23 UT, coinciding with the time at which we observe CS1. The decrease of $B_{z,cloud}$ is large, since it changes from 19 nT to 6 nT between 20:23 UT and 21:02 UT. At 21:02 UT when CS2 is observed, a sharp discontinuity is also observed in $B_{z,cloud}$, resulting in the rapid recovery of this magnetic field component to pre-disturbance levels. It is interesting to note that the onset of the substructure signatures in the azimuthal magnetic field occurs approximately 70 minutes before there are any notable changes observed in the axial magnetic field, and that the observed reduction in the $B_{z,cloud}$ component of the magnetic field is mostly confined between CS1 and CS2. The observed large fluctuations in the axial and azimuthal components of the magnetic field are weakly reflected in the magnetic field magnitude, since there are only some small changes observed during this period of time when the surrounding magnetic field is very smooth.

4.2.2.2 Corresponding plasma observations

The changes in the magnetic cloud, evident in the magnetic field observations, are accompanied by associated changes in the physical properties of the plasma in this region. Figure 4.5 shows 3 second resolution plasma measurements from the 3dp instrument on the WIND spacecraft, in GSE coordinates. Panels (a) and (b) show translational proton velocity, V_x and proton density, N_p, respectively. The expected temperature, T_{ex} is typical of the plasma proton temperature found in the ambient solar wind, and is determined by an empirical correlation with the observed solar wind speed, V_{sw} (Lopez, 1987, and references therein). Figure 4.5(c) shows the observed proton temperature, T_p (black trace) and the expected temperature, T_{ex} (red trace) calculated using the relation from Neugebauer *et al.* (2003), based on 3 years of measurements from ACE. We also show $T_{ex}/2$ (blue trace). Panel (d) shows the proton beta, panel (e) shows the ratio of the relative abundances of helium to hydrogen, N_α/N_p and panel (f) shows the magnitude, B_x, B_y and B_z components of the magnetic field in GSE coordinates, for ease of comparison with the plasma observations. The boundaries of the substructure region and the locations of the current sheets, as determined from the magnetic field observations, are highlighted by vertical short-dashed red lines, and vertical long-dashed green lines, respectively.

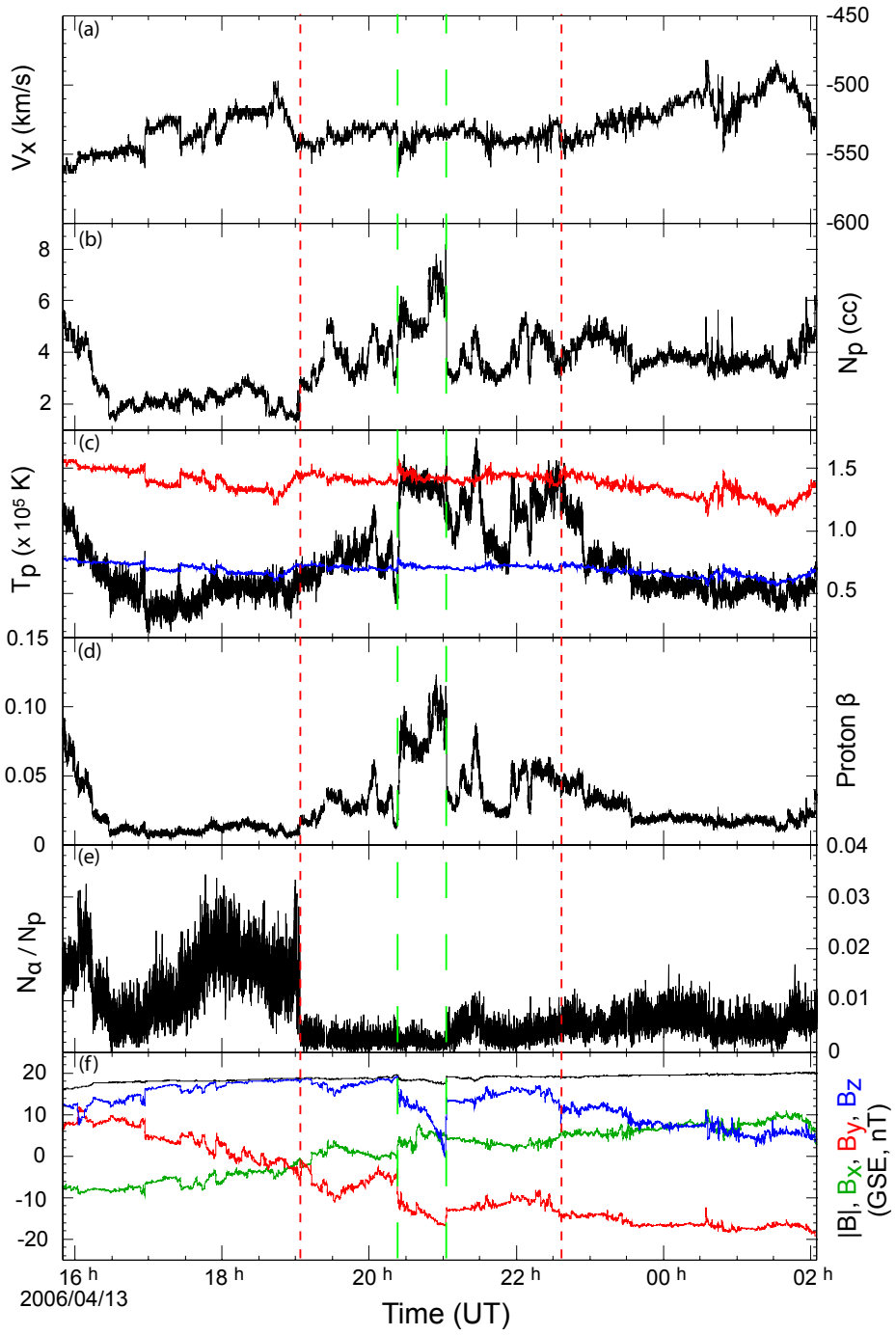

Figure 4.5: Plasma observations from WIND over the duration of the 13 April 2006 magnetic cloud. The plot shows (a) the translational proton velocity, V_x in GSE coordinates, (b) the proton number density, (c) the radial proton temperature (black trace), the expected temperature, T_{ex} (red trace) calculated from the observed solar wind speed and $T_{ex}/2$ (blue trace), (d) the proton beta, (e) the ratio of the relative abundances of helium to hydrogen and (f) the magnetic field observations in GSE, provided for context. Vertical short-dashed red lines indicate the boundaries of the substructure region and vertical long-dashed green lines indicate the locations of the current sheets (CS1 and CS2). Permission to reproduce this figure has been granted by the American Geophysical Union.

Observations of the translational proton velocity, V_x in GSE coordinates, within the magnetic cloud (Figure 4.5(a)), show that the change in speed of the cloud as it passes over the WIND spacecraft, determined from observations of the translational velocity at its leading and trailing edges, is small ($\sim$ 40 km s^{-1}). The non-dimensional expansion rate ζ, provides a measure of the expansion rate of a magnetic cloud, independent of its size, as discussed in § 4.1.1.2. We find that ζ = 0.57 for the 13 April 2006 magnetic cloud.

Increases in both the proton density and temperature are observed within the substructure region. Extreme density decreases (to ≤ 1 cm^{-3}) are typically observed in ICMEs (Richardson *et al.*, 2000) and similarly, for the same bulk flow speed, low proton temperatures relative to the ambient solar wind are expected (Gosling, 1990; Richardson and Cane, 1995; Mulligan *et al.*, 1999), as a result of expansion of the ICME in the solar wind. Richardson and Cane (1995) showed that $T_p < T_{ex}/2$ can be used as a criterion for identifying ICME ejecta in interplanetary space and Figure 4.5(c) shows that while much of the 13 April 2006 magnetic cloud meets this criterion, T_p significantly exceeds the threshold set by $T_{ex}/2$ within the substructure region and here tends towards temperatures expected in the ambient solar wind at this V_{sw}.

Magnetic pressure usually dominates within magnetic cloud structures, resulting in low values of plasma beta. Figure 4.5(d) shows that this is also the case for this magnetic cloud, with a value of 0.01 calculated for proton beta in the main body of the cloud. However, between CS1 and CS2 the magnetic pressure undergoes a small decrease while the plasma pressure undergoes a small increase, leading to slightly elevated proton beta values of 0.08 in this region, higher than the value of 0.03 calculated in the surrounding substructure region. Despite this, these values are still very low relative to the value of 0.2 obtained in the surrounding solar wind. The observed changes in the plasma and magnetic pressure are not reflected in calculations of the total pressure, in which no notable changes are observed throughout the substructure region.

Elevated α (doubly ionised helium) abundances are often observed in solar ejecta (Hirshberg *et al.*, 1972; Zwickl *et al.*, 1983; Mulligan *et al.*, 1999; Richardson and Cane, 2004). N_α/N_p, the ratio of the relative abundances of He^{2+} to hydrogen, is typically $\sim$ 8 % in ICMEs, compared to a value nearer to 3 - 5 % in the ambient solar wind. Figure 4.5(e) shows that the abundance of helium within the pre-substructure part of the cloud is lower than is typically observed within an ICME, approaching 3 %, but this is still slightly higher than the value of 2 % observed in the surrounding solar wind. We show that at 19:03 UT, corresponding with the onset of the substructure region, the abundance of helium decreases rapidly to a mean value of 0.3

% and is sustained at this level throughout the substructure region. Notably, as the spacecraft moves through the substructure region and back into the main structure of the magnetic cloud the helium abundance remains very low.

4.2.2.3 A comparison of multiple spacecraft observations

The 13 April 2006 magnetic cloud is observed by both the ACE and WIND spacecraft, allowing us to compare observations of this event, in particular its substructure, from two spacecraft. In GSE coordinates, the position of the ACE spacecraft is x = 240 R_E, y = 25 R_E, z = -25 R_E. At this time, the position of the WIND spacecraft is x = 200 R_E, y = 30 R_E, z = -15 R_E. Both ACE and WIND were located close to the Sun-Earth line, with ACE observing the magnetic cloud first.

Figure 4.6 shows magnetic field observations from ACE and WIND over the duration of the magnetic cloud. Cross-correlation (see § 2.4.3) is used to compare these datasets within the substructure region and returns a maximum correlation coefficient $>$ 0.9 when the WIND observations lag the ACE observations by approximately 528 s ($\sim$ 9 mins). Therefore, in order to obtain a direct comparison of the magnetic cloud observations from each spacecraft, the ACE data has been time-shifted by 528 s. The boundaries of the substructure region are highlighted by vertical dashed red lines, as before. We find that the ACE and WIND observations of the magnetic field are very similar.

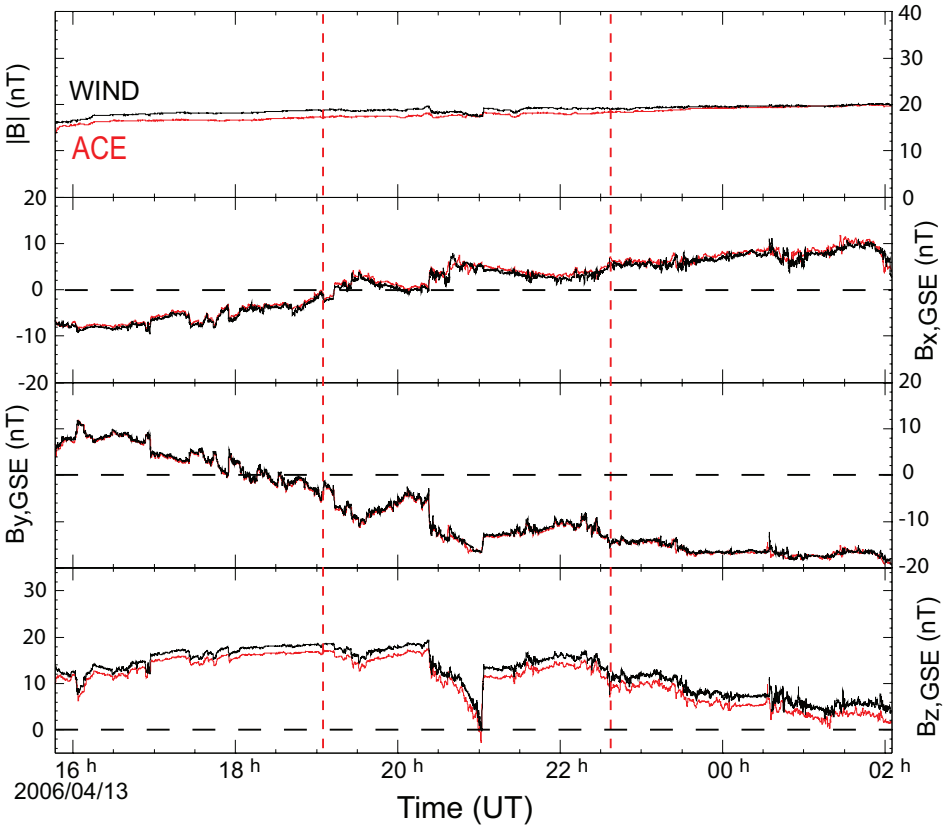

Figure 4.6: Magnetic field observations in GSE coordinates over the duration of the 13 April 2006 magnetic cloud by WIND (black trace) and ACE (red trace). Vertical dashed red lines indicate the boundaries of the substructure region. The ACE data has been time-shifted by 528 seconds ($\sim$ 9 mins.) so that the WIND and ACE observations may be directly compared. This shows that the observations of the magnetic structure from both spacecraft are very similar. Permission to reproduce this figure has been granted by the American Geophysical Union.

4.2.3 The Prevalence of Substructure Within Magnetic Clouds

We have surveyed all 48 of the magnetic clouds observed between March 2001 and November 2007 recorded in the WIND magnetic cloud catalog (`http://lepmfi.gsfc.nasa.gov/mfi/mag_cloud_pub1.html`). To ascertain what proportion of the magnetic clouds observed near-Earth exhibit substructure, magnetic field observations of each MC from the MFI instrument onboard the WIND spacecraft were visually inspected for evidence of substructure, and a subset of magnetic clouds containing these features was identified. A minimum variance analysis was then performed on the magnetic field measurements of each of the clouds in this subset to further enhance the observational signatures of substructure, by rotating the magnetic field vector to the eigen-vector frame given by the minimum variance (an approximation of the magnetic cloud frame).

We have found that in around 60 % of these magnetic clouds, the magnetic field does not rotate entirely smoothly, often exhibiting both small- and large-scale fluctuations. However, we have identified only 5 magnetic clouds, in addition to the 13 April 2006 cloud, that exhibit the multiple reversals in the gradient of the azimuthal magnetic field in which we are interested. For those magnetic clouds that have already been the subject of study by other researchers, we use the most recently discussed boundaries, whilst the remainder of the magnetic cloud boundaries are as stated in the WIND magnetic cloud catalog (estimated using the Lepping *et al.* (1990) magnetic field model). Figure 4.7 shows the evolution of the $B_{y,cloud}$ component of the magnetic field, corresponding to the maximum variance direction obtained from the minimum variance analysis, over the duration of all 6 of the substructure magnetic clouds identified. Vertical dashed red lines indicate the approximate boundaries of the substructure regions, within which reversals of the azimuthal magnetic field ($B_{y,cloud}$) gradient are observed.

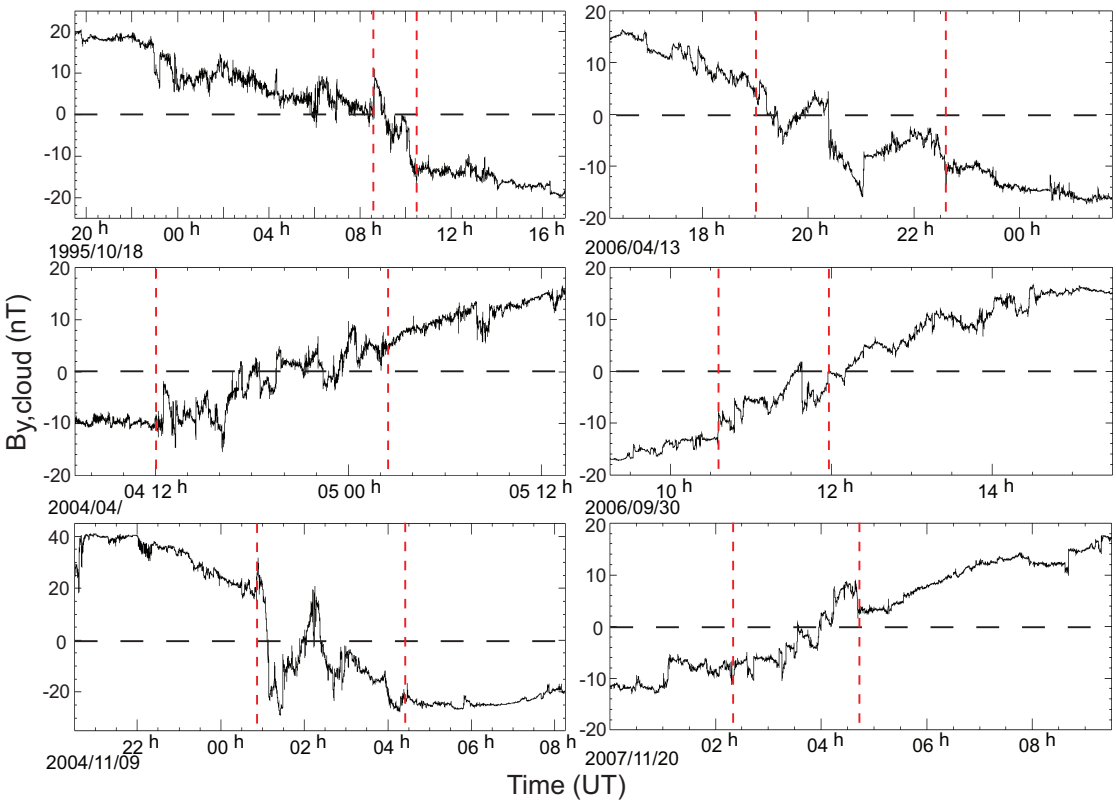

Figure 4.7: The evolution of the $B_{y,cloud}$ magnetic field component (maximum variance direction) is shown over the duration of all 6 of the magnetic clouds exhibiting substructure. Vertical dashed red lines indicate the boundaries of the substructure regions, within which reversals of the azimuthal magnetic field ($B_{y,cloud}$) gradient are observed. Permission to reproduce this figure has been granted by the American Geophysical Union.

Here, we compare some of the properties of these magnetic clouds, allowing us to build a general picture of the characteristics of these types of solar ejecta. We estimate the trajectories of the WIND spacecraft through this subset of magnetic clouds using a technique developed by Gulisano *et al.* (2007), which is valid for the force-free (Lundquist, 1950) model, and in which the magnetic field components obtained from MVA are used to provide an approximation of the impact parameter, p, defined as the minimum distance from the spacecraft to the cloud axis. The deviation from zero of the mean value of the $B_{x,cloud}$ component of the magnetic field (in the direction of the minimum variance) can be used to obtain an estimation of p (see Figure 5, *upper panel* in Gulisano *et al.* (2007)), as:

$$\frac{< B_{x,cloud} >}{B_0} \approx 1.6 \left(\frac{p}{r}\right)^2 + 0.077 \left(\frac{p}{r}\right) + 0.053 \tag{4.3}$$

Including the higher order terms in this relation increases the precision with which we are able to estimate the impact parameter within these perturbed clouds. The resulting impact parameter of the ACE spacecraft for the 13 April 2006 magnetic cloud is 15 %, which is smaller than the estimate provided in (Steed *et al.*, 2008), and reported in § 3.2.2.2.

In addition, we compare the spatial extent of each substructure region relative to the size of its parent magnetic cloud and look for similarities between the overall sizes and durations of the magnetic clouds. We also calculate the average magnetic field strength over the duration of each magnetic cloud and compare the values obtained for each event.

Magnetic clouds often exhibit a linear velocity profile. By considering ΔV_x over the duration of each cloud, we calculate the non-dimensional expansion rate, ζ with respect to the cloud centre, for each of these clouds. By observing the solar wind behind each magnetic cloud, we also determine whether the cloud was being followed, and ultimately overtaken, by a solar wind stream propagating faster than the ejecta. This was shown to be the case for the 13 April 2006 magnetic cloud in Chapter 3.

Table 4.1 shows that the size and duration of each magnetic cloud varies significantly between events, and that the same can be said of the size and duration of the substructure regions, both between the events and relative to the size of their parent magnetic clouds. We also find that there are no clear similarities between the trajectories of the WIND spacecraft through each of these magnetic clouds, determined from the estimated impact parameter of the spacecraft in each case, with some clouds observed closer to their axes than others. Despite the lack of similarities between many of the cloud parameters, we show in Figure 4.7 that the regions in

which substructure are observed all lie towards the centre of their respective parent clouds. In this context, the centre of a magnetic cloud is defined as the point at which the $B_{y,cloud}$ component of the magnetic field tends to zero. Calculations of the average magnetic field strength over the duration of each cloud reveal that it is comparable ($\sim$ 17 nT) in all but one of these events ($\sim$ 32 nT), and the values obtained are within the range expected for a typical magnetic cloud (Lepping *et al.*, 2003). We find that ζ is smaller than the mean value obtained for the non-perturbed (not overtaken) magnetic clouds analysed by Démoulin *et al.* (2008) at 1 AU ($\zeta = 0.8 \pm 0.2$), and those analysed by Gulisano *et al.* (2010) between 0.3 and 1 AU ($\zeta = 0.9 \pm 0.2$). This is coherent with the presence of an overtaking solar wind stream behind these magnetic clouds, as the lowest values of ζ are found for overtaken clouds. There is also one case where the value obtained for ζ is negative, implying that when this cloud is observed by WIND it is actually compressing, rather than expanding.

4.3 Discussion

In this chapter, we have investigated the properties of a subset of magnetic clouds within which substructure, in the form of multiple reversals of the gradient of the azimuthal magnetic field, is observed towards the centre of the magnetic flux rope structure. A particularly clear example of substructure in a magnetic cloud was observed *in situ* by the WIND spacecraft on 13 April 2006, and we show that substructure is evident in both the magnetic field observations and the corresponding plasma observations. In addition to the reversals of the azimuthal magnetic field gradient and the depression of the axial magnetic field, several thin current sheets are identified within the substructure region.

One of the most recent explanations for the presence of current sheets within magnetic clouds is a scenario proposed by Owens (2009), who demonstrated how current sheets can form simply as a result of a magnetic cloud's kinematic propagation from the Sun to the Earth. This model of a kinematically distorted flux rope was able to reproduce an observed discontinuity present in the magnetic structure of some magnetic clouds, and demonstrate that these current sheets thin, and thus increase in intensity, as the angular width of the flux rope increases and the radial expansion speed decreases. We have shown that the rate of radial expansion of the 13 April 2006 magnetic cloud is small at 1 AU. However, unlike the examples studied by Owens (2009), the angular width of this magnetic cloud is believed to be quite small, because despite originating close to disk centre, this CME is not observed by the Large Angle Spectroscopic Coronagraph (LASCO, Brueckner *et al.*, 1995)

onboard the SoHO spacecraft (Steed *et al.*, 2008) (as discussed in § 3.2.3). Owens (2009) also hypothesise that magnetic reconnection occurring across such current sheets in magnetic clouds may result in a single flux rope being fragmented into multiple, smaller flux ropes.

The idea of multiple flux ropes giving rise to observations of unusual ICME signatures is not a new one (e.g. Osherovich *et al.*, 1999). Wang *et al.* (2002), and many of the scenarios proposed in recent years, do not require magnetic reconnection as a driving force. For example, it has been suggested that some events observed near Earth are a result of CME-CME interaction, and Gopalswamy *et al.* (2001a) described a scenario where a faster CME ploughs into a slower CME travelling ahead of it. In some cases, both MCs even travel consecutively and the flux rope signatures are preserved (Dasso *et al.*, 2009). On the other hand, Dasso *et al.* (2007) also considered whether the substructure could be explained by a small twisted flux tube with opposite helicity sign in the centre of the flux rope, and concluded that the formation of such a structure is not possible in the corona. It is, however, possible for two flux ropes with the same sign of helicity to interact in interplanetary space, but the symmetrical nature of the 13 April 2006 flux rope signature in $B_{y,cloud}$ implies that the flux ropes would have to be very similar to reproduce the observed substructure signatures, and it is very improbable that this is the case.

Dasso *et al.* (2007) also suggested the simplest interpretation of the observed substructure may be spatial oscillations of the magnetic field, introduced as a result of interactions between a magnetic cloud and the ambient solar wind as the cloud propagates into interplanetary space. They proposed that close to the minimum approach of the magnetic cloud centre, the spacecraft trajectory would be nearly tangential to the magnetic flux surfaces of the flux rope. Here, the azimuthal magnetic field tends to zero and any warping of the flux surfaces would give a clear signal in the $B_{y,cloud}$ component. This could potentially give rise to a signature within the magnetic field of a flux rope that resembles the observations of substructure in $B_{y,cloud}$ identified in this study, but does not explain the observed decrease in $B_{z,cloud}$ towards the centre of the flux rope. However, there are several events in this study for which "warping" is a possible explanation for the observed signatures, since a depression of $B_{z,cloud}$ is not common to all of these events, unlike the multiple reversals of the gradient of $B_{y,cloud}$.

It is also possible that MHD waves may be perturbing the magnetic field on the flanks of the flux rope. For example, the Kelvin-Helmholtz instability (Dungey, 1955; Drazin and Reid, 1985) may be invoked when two fluids are in motion with respect to one another. In this case, the stability of the interface between the magnetic cloud and the solar wind is dependent on the magnitude of the velocity

shear. The fast flowing plasma in the magnetic cloud moving past slower solar wind plasma may create the necessary velocity shear across the boundary between them to invoke the instability. However, if this were the case it is not obvious how these boundary waves would result in the internal substructure signatures we observe. We consider the processes that might explain how substructure arises in magnetic clouds in more detail in Chapter 5.

Similar observations of the magnetic field from the ACE and WIND spacecraft suggest that the 13 April 2006 magnetic structure does not undergo significant temporal or spatial evolution as the magnetic cloud propagates from ACE to WIND. This may be because the magnetic cloud is evolving more slowly than we are able to detect. The close proximity of the ACE and WIND spacecraft to one another results in a time-scale of only a few minutes between the respective observations, which is very small compared to typical time-scales of magnetic cloud evolution, usually of the order of hours. We estimate the trajectories of the ACE and WIND spacecraft through this magnetic cloud by considering the impact parameters of the spacecraft determined from flux rope modelling, as before. We find that the values obtained for the impact parameter are very similar, as expected given the relative spacecraft positions, with a value of p/R of approximately 15 % for both ACE and WIND, where R is the radius of the magnetic cloud.

We are unable to determine from the available observations of this event when the substructure develops, but it is possible that substructure is present, or introduced, as the CME erupts. However, it is also plausible that substructure forms within an ICME as it propagates through the heliosphere. Further study of the solar sources of these types of ejecta would assist with narrowing down the point at which substructure begins to develop within an ICME.

In addition to the 13 April 2006 magnetic cloud, we have identified and studied 5 other magnetic cloud events within which substructure is observed. We initially surveyed 48 magnetic clouds and have found that around 60 % of the clouds in the WIND magnetic cloud catalog do not rotate entirely smoothly, exhibiting varying degrees of internal fluctuations of the magnetic field. However, only a very small proportion of these exhibit clear substructure signatures. These findings suggest that substructure events are rare, but we must also consider that the boundaries of the magnetic clouds included in this study, particularly those determined from the WIND magnetic cloud catalog, may not be entirely accurate. Much progress has been made in recent years in identifying the boundaries of solar ejecta by applying new methods and techniques, in making quantitative comparisons with their solar sources (e.g. Démoulin, 2008) and in using MHD invariants in space (e.g. Dasso, 2009). Accurate identification of magnetic cloud boundaries is particularly difficult

for complex events, like those in which we identify substructure. There has been much discussion and speculation about whether all ICMEs in fact contain flux ropes. However, the presence of a flux rope may not be evident in the *in situ* observations of many events due to the limitations of single spacecraft measurements, and particularly the trajectory of the spacecraft through the ejecta (e.g. Marubashi, 2000; Jian *et al.*, 2006). Similarly, we suggest that the same observational constraints, in particular the lack of availability of multi-spacecraft measurements for each event, mean that we cannot rule out the possibility that substructure may be present in more magnetic clouds than we are able to identify with the available *in situ* observations. All of the magnetic clouds associated with substructure identified in this study were observed during the late declining phase of the solar activity cycle, but given the small sample size of magnetic clouds, there is not yet sufficient evidence to determine if there is any dependence of the formation of substructure within MCs on the phase of the solar cycle.

A comparison of the physical parameters of these magnetic clouds has revealed that they have little in common. Since the solar wind pressure decreases with increasing heliocentric distance, MCs typically expand as they propagate into interplanetary space. A signature of this expansion is observed in the plasma bulk flow velocity in the Sun-Earth direction, which is expected to decrease approximately linearly between the leading and trailing boundaries of the cloud. Conversely, magnetic clouds may become perturbed as a result of their interaction with the solar wind. In a perturbed cloud, the majority of the velocity profile of a cloud is non-linear. Nearly all of the clouds in this study are followed by fast solar wind streams. We have found that the non-dimensional expansion rates of these MCs are low, with values of $\zeta < 0.8$, indicating that these magnetic clouds are perturbed (Gulisano *et al.*, 2010). As a fast stream overtakes a magnetic cloud, it is expected to compress the flux rope and so decrease its expansion rate, as shown in MHD simulations (Xiong *et al.*, 2006) and in *in situ* observations (Gulisano *et al.*, 2010).

4.4 Summary and Conclusions

Substructure is observed within some magnetic clouds, identified by multiple reversals of the gradient of the azimuthal magnetic field of the magnetic flux rope structure. One such event was observed by the ACE and WIND spacecraft, located upstream of Earth, on 13 April 2006. We have shown that substructure is evident in both the azimuthal and axial magnetic field components and the associated plasma observations. In total, we have identified 6 magnetic clouds clearly exhibiting such substructure signatures and a comparison of the properties of these clouds has re-

vealed that they vary significantly from event to event. However, these clouds all exhibit low non-dimensional expansion rates, suggesting that they are perturbed by the surrounding solar wind conditions, and fast solar wind streams are observed overtaking 4 of the 6 events studied.

It is not yet understood when and where substructure develops within magnetic clouds. Further study is necessary to investigate whether substructure is present during CME initiation and/or eruption, or if it develops as a result of the evolution of the magnetic structure as it propagates into the heliosphere. Understanding the driving forces behind the topological changes in a magnetic flux rope that give rise to substructure is the subject of Chapter 5, where we will explore possible scenarios that might lead to the formation of substructure within a magnetic cloud.

Table 4.1: Properties of magnetic clouds exhibiting substructure.

MC Start, UT[a]	MC End, UT	MC Duration, hrs	MC Size, AU	Substructure Duration, hrs	Substructure Size, AU	Spatial extent[b]	Impact Parameter, p/R (WIND)	$< \|B\| >$, nT	$< V_{x,GSE} >$ km s^{-1}	Expansion Rate, ζ	Fast stream behind MC?
18 Oct 95 18:58(D06)	19 Oct 95 17:37	22.7	0.23	1.8	0.019	8 %	15 %	20	-420	0.25	Yes
04 Apr 04 02:48	05 Apr 04 14:48	36.0	0.38	14.3	0.150	40 %	55 %	16	-441	0.77	No
09 Nov 04 20:30(D07)	10 Nov 04 09:00	12.5	0.24	3.6	0.070	30 %	25 %	32	-796	0.64	No
13 Apr 06 15:50(S08)	14 Apr 06 02:05	10.3	0.13	3.6	0.046	35 %	15 %	19	-530	0.57	Yes
30 Sept 06 08:36	30 Sept 06 21:36	13.0	0.13	1.4	0.014	10 %	25 %	16	-404	0.61	Yes
19 Nov 07 23:24	20 Nov 07 12:54	13.5	0.15	2.4	0.023	20 %	0 %	17	-474	-0.26	Yes

[a](D06), (D07) and (S08) denote magnetic cloud boundaries identified by Dasso et al., 2006, Dasso et al., 2007 and Steed et al., 2008, respectively. All other MC boundaries are as recorded in the WIND MC catalog.

[b]Spatial extent of the substructure region as a percentage of total MC size.

Chapter 5

Investigating the Causes of Magnetic Cloud Substructure

The external and internal processes that influence the evolution of ICMEs and magnetic clouds as they propagate into interplanetary space is not currently well understood. Following the identification of internal structure within magnetic clouds in Chapter 4, in this chapter we investigate possible explanations for how this substructure may arise.

In § 5.2 we discuss some of the external processes that may influence the magnetic structure of ICMEs and magnetic clouds as they propagate into interplanetary space, before investigating some of these processes in detail in § 5.2. In § 5.2.1 we discuss whether there is any evidence of magnetic reconnection proceeding within the 13 April 2006 magnetic cloud substructure region in the *in situ* magnetic cloud and plasma observations. A different approach to investigating the causes of substructure is employed in § 5.2.2 and § 5.2.3. Here, numerical simulations are used to consider whether multiple flux ropes could explain the observed substructure magnetic field signatures, and also the consequences of introducing spatial oscillations to the magnetic field of a flux rope, allowing us to consider the effects of "warping". Finally, we determine whether the Kelvin-Helmholtz instability may be invoked at the magnetic cloud boundaries in § 5.2.4, before evaluating our findings in § 5.3.

5.1 Introduction

5.1.1 Possible Causes of Magnetic Cloud Substructure: An Overview

5.1.1.1 Magnetic reconnection in interplanetary space

As discussed in § 1.3.7, magnetic reconnection describes a process in which the frozen-in field condition of ideal magnetohydrodynamics is violated such that pairs of magnetic field lines merge to produce topological changes in the field. One characteristic feature of the reconnection process is the acceleration of plasma away from the reconnection site in a pair of oppositely directed exhaust regions. Observations of such exhausts within the Earth's magnetopause current layer has provided the strongest direct evidence for the reconnection process in space plasmas (e.g. Paschmann *et al.*, 1979, 1986; Sonnerup *et al.*, 1981; Gosling *et al.*, 1982, 1990a, 1991a; Phan *et al.*, 1996, 2000).

Magnetic reconnection also occurs at tangential discontinuities in the solar wind, such as extensive interfaces separating ICMEs and the ambient solar wind plasma, at interfaces between open and closed field lines within ICMEs and, very occasionally, near the Heliospheric Current Sheet (HCS); which separates regions of opposite magnetic polarity. When the Alfvén mach number of the solar wind flow is > 2, as is usually the case in the solar wind near 1 AU, the reconnection site and the field and plasma in both exhausts are carried away from the Sun by the solar wind flow.

The presence of magnetic reconnection in ICMEs was predicted by simulations, in which it was shown that reconnection can occur on the flanks of ICMEs (Cargill and Schmidt, 2002). Schmidt and Cargill (2001) suggested that reconnection within ICMEs might occur as a result of shearing of the ICME by the surrounding solar wind. If the orientations are favourable, the large compression observed ahead of some ICMEs may also trigger reconnection between ICME and sheath magnetic fields.

Early studies suggested that magnetic reconnection in the solar wind was quite rare near 1 AU, with only 6 events identified in nearly 7 years of ACE data (Gosling *et al.*, 2005a). Since then, better techniques for recognising the exhausts and the use of instruments with a higher temporal resolution mean that current estimates of the frequency of reconnection in the solar wind are significantly higher. Using 3 second resolution WIND data, it is estimated that an average of ~ 2 reconnection exhausts per day can be identified in slow wind and ~ 0.6 exhausts per day can

be identified in high speed wind Gosling *et al.* (2007a). These authors conclude that reconnection is almost certainly more prevalent in the solar wind than can be detected by instruments with a ≥ 3 second cadence.

Prior to the identification of any reconnection exhausts in the interplanetary medium, it was suggested that turbulence should drive reconnection in the solar wind, but while turbulence is most pronounced in high speed streams, all of the reconnection exhausts identified prior to 2007 were found to arise in slow solar wind conditions. Magnetic reconnection in the solar wind has since been shown to occur in plasma with low proton β (0.01 - 0.15) and high Alfvén speed (50 - 200 km s^{-1}). The average values of β external to exhausts in the fast wind are considerably higher than β in the slow wind and in association with ICMEs. However, improvements in the techniques used to identify exhausts have since led to the identification of a limited number of exhausts in high speed solar wind data also. The majority of events observed in both the fast and slow solar wind occur at times of decreasing or nearly constant solar wind speed.

Some of the earliest reconnection exhausts identified in interplanetary space, and a significant proportion of the exhausts identified more recently, have been found to be associated with ICMEs. No correlation has been found between exhaust occurrence and magnetic field strength, so while the magnetic field within ICMEs is characteristically elevated relative to the ambient solar wind, this does not appear to be a contributing factor to the relatively high occurrence rates in and around interplanetary ejecta. Multi-spacecraft observations of reconnection exhausts in the solar wind have revealed evidence of prolonged reconnection along a continuous X-line, indicating that reconnection in interplanetary space is not patchy in both space and time.

Observations have shown that field lines need not be anti-parallel for reconnection to occur in the solar wind. Sonnerup (1974) concluded that: "When the field strengths on opposite sides of a thin current sheet are comparable (as is usually the case in the solar wind), reconnection is geometrically possible for a wide range of field shear angles, including very small field shear angles." Some of the early studies reported that field shear angles were typically found to range from 70° to 180°, with a median close to 135° (Gosling *et al.*, 2005a). Since many more exhausts have been identified, it has been found that reconnection in the solar wind occurs most frequently at field shear angles less than 90°. The rate of reconnection is dependent on the shear angle between the reconnecting fields, decreasing as the shear angles get smaller. Assuming a uniform solar wind, a dimensionless reconnection rate of 0.033 has been estimated by Phan *et al.* (2006) and Davis *et al.* (2006).

A weak correlation between field shear angle and the exhaust width has also been found, with wider exhausts, which are largely associated with local magnetic shears $>> 90°$, typically associated with ICMEs. Early identification of reconnection exhausts in the solar wind indicated that typical exhaust widths were in the region of $\sim 2 \times 10^5$ km (Gosling *et al.*, 2006). It has since been found that most reconnection exhausts in the solar wind are $< 4 \times 10^4$ km, which corresponds to a crossing duration of < 100 seconds (Gosling *et al.*, 2007b).

In situ observational signatures of magnetic reconnection

Reconnection exhausts that can be identified by a number of signatures evident in the *in situ* observations of the plasma and magnetic field (Gosling *et al.*, 2005a,b,c). Key signatures include:

- Changes in the magnetic field orientation occurring in two distinct steps; one at the leading edge of an exhaust and one at the trailing edge. Observations show that within an exhaust the field orientation is intermediate between values observed at each of the exhaust boundaries. This field reversal is associated with a bifurcated current sheet.

  This type of magnetic field signature is a common characteristic of reconnection exhausts in the solar wind, but by itself it is insufficient to identify an exhaust.

- One of the most distinguishing features of an exhaust is accelerated or decelerated plasma flow within a bifurcated current sheet.

  An increase (decrease) in bulk flow speed should be observed when a spacecraft encounters an anti-sunward (sunward) directed exhaust, and both anti-sunward and sunward directed exhausts are commonly observed.

- Alfvén waves propagating parallel (anti-parallel) to the magnetic field at exhaust boundaries produce anti-correlated (correlated) variations in the magnetic field, B, and plasma velocity, V, at the leading and trailing edges of the exhaust region.

- When exhausts are bounded by slow-mode-like shocks, then associated increases in density and temperature and a decrease in magnetic field strength are expected.

- The observed change in velocity, $|V|$, across the exhaust boundaries is comparable to, but usually less than, the external Alfvén speed (see § 1.3.6 for an explanation of Alfvén speed), and is dependent upon the shear angle of the reconnecting field lines. For shear of 180°, ΔV is expected to be comparable

to the Alfvén speed. As shear angle decreases, ΔV decreases relative to the Alfvén speed.

Local field shear angles and proton β values do not depend on heliocentric distance, but as heliocentric distance increases, ΔV gets smaller due to weaker magnetic fields and lower Alfvén speeds

- Magnetic field strength decreases within the exhausts are also roughly correlated with the magnitude of the local shears.
- The Alfvén speed within the exhaust is typically very high, ranging from 50 to 200 km s^{-1}.
- Electron temperatures within an exhaust region are often intermediate between those observed either side of the exhaust boundaries, indicating that although the transitions from outside to inside an exhaust are often slow-mode-like for protons, this is not the case for electrons.
- Counterstreaming ion beams are sometimes observed resulting from solar wind plasma entering the exhaust region from opposite directions along the reconnected magnetic field lines.

5.1.1.2 ICME-ICME interaction

Remote observations of the Sun have shown that CMEs can occur in close spatial and temporal proximity (Svestka, 2001). It is possible for an active region to produce more than one CME over the course of its lifetime, sometimes in relatively quick succession. The variable velocities and large angular extent of CMEs makes it inevitable that ICMEs will sometimes interact, and this is most probable at times of high solar activity. There is evidence to suggest that the resultant complex ICME structures may result in strong heliospheric and geomagnetic disturbances (Burlaga *et al.*, 1987; Bothmer and Schwenn, 1995).

Some of the consequences of interactions between ICMEs have been explored through simulations, and include shocks propagating through ejecta (Odstrcil *et al.*, 2003) and, in cases where the two flux ropes exhibit the same sign of helicity, the merging and reconnection of ICMEs (Schmidt and Cargill, 2004).

There are several instances of the detection of multiple flux rope events reported in the literature. Kahler *et al.* (1999) used bidirectional electron fluxes to argue that some magnetic clouds are multiple events, while the reconstruction technique of Hu and Sonnerup (2002) was employed by Hu *et al.* (2003) to infer a magnetic cloud at 1 AU was comprised of two flux ropes. Similarly, Osherovich *et al.* (1999) discuss

a magnetic cloud observed by Ulysses, which may be modelled as two intertwined helical flux tubes separated by a region of enhanced plasma pressure. In a process referred to as "CME cannibalism", a fast CME can overtake a slow CME from the same solar source or a neighbouring solar source resulting in single CME, which may be detected by enhanced radio emission (Gopalswamy *et al.*, 2001a). Burlaga *et al.* (2002) also attempted to understand complex ejecta from several interacting halo CME events, focusing on the substructure evident in the composition and density signatures and emphasising the challenges in quantitatively describing such events.

There is currently no consensus on the expected *in situ* signatures of interacting ICMEs, most likely due to both the complexity and individual nature of these events. However, the presence of boundaries within the ejecta often provides a first indication that an event might be comprised of multiple flux ropes. That said, caution must be exercised as discontinuities contained within the internal structure of ICMEs are not unusual, and further analysis may not lead to the conclusion that the event is the result of ICME-ICME interaction.

5.1.1.3 Solar wind-ICME interaction

The effects of the ambient solar wind on the structure and evolution of ICMEs in interplanetary space is still not well understood, and is currently a very active field of research.

ICMEs observed near 1 AU are most often embedded in slow wind streams, indicative of their solar origins in complex magnetic regions. In cases where ICMEs propagate through high speed streams increased travel speeds can occur, since ICMEs tend to converge to the ambient solar wind speed. In some instances, a fast solar wind stream might travel behind a slower-travelling ICME and plasma at the trailing edge of the ICME may be compressed. If the embedded magnetic field is directed southward, these ICMEs can become more geoeffective as compression results in enhancement of the southward field (e.g. Zhao, 1992; Cane and Richardson, 1997; Fenrich and Luhmann, 1998; Crooker, 2000).

The topology of a magnetic cloud may also be altered by interaction with the preceding solar wind. Magnetic reconnection can occur at the leading edge of magnetic clouds as they overtake the slower solar wind, often containing differently oriented magnetic field, ahead of them. This results in a flux rope that is peeled away at the front, but with an extended trailing region; a region of low but coherent field that exhibits different behaviour to both the magnetic cloud and the ambient solar wind and is comprised of reconnected flux that has been swept behind the flux rope.

Evidence of this configuration was found by Dasso *et al.* (2006) in the 9 November 2004 magnetic cloud, and a schematic interpretation of the observed MC is shown in Figure 5.1. The reconnected magnetic flux in this event was estimated to be ~ 60 % of the total magnetic flux contained in the flux rope. However, in other magnetic clouds this value is typically lower (Dasso *et al.*, 2007; Mandrini *et al.*, 2007).

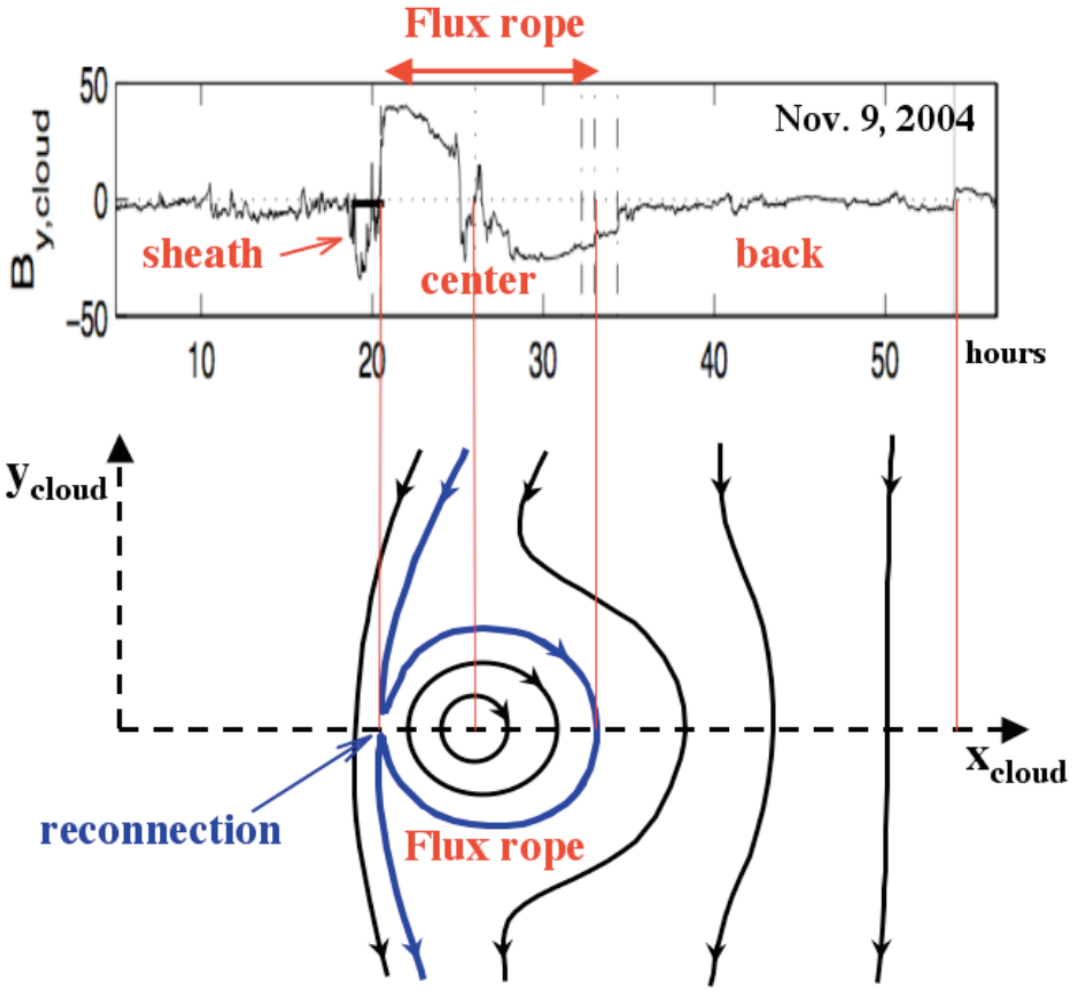

Figure 5.1: Evidence of partial magnetic reconnection of a flux rope during its transit from the Sun to the spacecraft. The $B_{y,cloud}$ component of the magnetic field for the 9 November 2004 magnetic cloud (Dasso *et al.*, 2007) is shown in the top panel. This flux rope partially reconnects with the preceding solar wind as it propagates from the Sun to the Earth and the flux rope is peeled away at the front. In the back of the flux rope an extended region of low but coherent field is present that exhibits different behaviour to both the magnetic cloud and the ambient solar wind. This "back" region comprises reconnected flux that has been swept behind the flux rope. Figure adapted from Démoulin (2008). Permission to reproduce this figure has been granted by the European Geosciences Union.

Spatial oscillation of the magnetic field was suggested by Dasso *et al.* (2007) as the simplest interpretation of substructure within a magnetic cloud. They proposed that close to the minimum approach of the spacecraft to the flux rope axis, the spacecraft trajectory would be nearly tangential to the magnetic flux surfaces of the flux rope, where the azimuthal magnetic field component, $B_{y,cloud}$, ~ 0. Any warping in the flux surfaces would give a clear signal in the $B_{y,cloud}$ component. For

geometrical reasons, warping is difficult to detect away from the cloud centre since the $B_{y,cloud}$ component becomes important, and any fluctuations due to warping can no longer be so easily identified. Dasso *et al.* (2007) propose that the reason the flux rope structure is undulated is probably due to its fast evolution and interaction with the surrounding medium.

5.1.1.4 Kelvin-Helmholtz instability

A wide variety of instabilities can occur in plasma systems and consequently the solar-terrestrial environment is typically not in a state of equilibrium. Instabilities in space plasmas are driven by a range of sources of free energy, such as velocity shear, gravity, temperature anisotropy, electron and ion beams, and currents (Uberoi, 2007).

Plasma instabilities that occur on scales comparable to the bulk scales of the plasma are termed macroinstabilities and can be studied using fluid and magnetohydrodynamic equations. The remaining class of instabilities are microinstabilities and these are kinetic in nature. The Kelvin-Helmholtz instability falls into the former category and is produced by velocity shear flows in fluids and plasmas. Current sheets with tangential discontinuity are prone to such instabilities. The uniform magnetic field either side of a current sheet acts to stabilise it, but it can become unstable when the kinetic energy of the tangential velocity difference exceeds the total magnetic energy density, resulting in the distortion of magnetic field lines.

One of the most well-known instances of the onset of the Kelvin-Helmholtz instability is at the boundary between the Earth's magnetosheath and magnetosphere. Here, the coupling between the relative magnetosheath and magnetospheric flows causes ripples to grow at the interface between these two plasma regimes and facilitates the transport of plasma and momentum from the magnetosheath across the magnetopause to the magnetosphere by mixing the two regions. The conditions for the onset of the Kelvin-Helmholtz instability may also be satisfied in other regions where velocity shear occurs, like the boundaries between an ICME and the ambient solar wind. A critical velocity shear is required to produce the Kelvin-Helmholtz instability, but the shear between the velocity and magnetic field across the boundaries of a magnetic cloud also plays a part in determining if wave growth will occur. The tension in the magnetic field will resist any force acting on it to stretch it, therefore the instability is not likely to be invoked if the shear angle between the velocity and magnetic field across the leading or trailing boundaries of a magnetic cloud is small.

5.2 Investigating the Causes of Substructure in the 13 April 2006 Magnetic Cloud

5.2.1 Magnetic Reconnection Within the Magnetic Cloud?

In Chapter 4, we described the *in situ* magnetic field and plasma observations of the internal structure of the 13 April 2006 magnetic cloud. Within the substructure region of the cloud two clear discontinuities are observed at 20:23 UT and 21:02 UT in the 3 s resolution magnetic field observations from the WIND spacecraft (see Figure 4.4).

These discontinuities are likely the locations of thin current sheets, separating different plasma regimes within the cloud. It is within such regions that it is possible for magnetic reconnection to proceed in, and around, the cloud. The detection of reconnection exhaust jets in *in situ* magnetic field and plasma observations is commonly used to provide evidence of magnetic reconnection in the solar wind and interplanetary space. As discussed in § 5.1.1.1, there are a number of signatures of reconnection exhausts that may be found in *in situ* observations. Key signatures include accelerated or decelerated plasma flow within a current sheet and changes in magnetic field orientation occurring in two distinct steps (one at the leading edge and one at the trailing edge of the exhaust). We investigate the characteristics of the current sheets observed within the substructure region of the cloud to ascertain if such signatures are present, and thus if magnetic reconnection is proceeding in these regions.

The first of the current sheets analysed is observed in the magnetic field observations from the WIND spacecraft between 20:23:01 UT and 20:23:38 UT, and is herein referred to as Current Sheet 1 (CS1) (this notation is consistent with Chapter 4). The short duration over which this feature is observed (37 s) implies that this structure is very thin, and from the concurrent speed of the local plasma, we estimate its width along the WIND spacecraft trajectory is $\sim 2 \times 10^4$ km.

To better understand the geometry of the current sheet, the magnetic field and velocity observations are transformed to the local frame of the structure, determined by calculating the normal to the plane of the current sheet by considering the magnetic field either side of the current sheet. The results of this transformation are shown in Figure 5.2, in which the boundaries of the current sheet are highlighted by vertical, dashed lines. This shows that the majority of the solar wind flow is contained in the x-direction, and there is little variation in the flow and field in this direction. The variations in plasma flow and the magnetic field structure are mostly

perpendicular to the solar wind flow direction. Two-step changes in the orientation of the B_y magnetic field component are observed at the two boundaries of the current sheet, indicating that it is bifurcated, and accelerated plasma flow is observed within this region. Between the boundaries, the magnetic field has a roughly constant orientation, intermediate between that prevailing before and after the current sheet. The combination of these signatures implies that the event observed may be the result of quasi-stationary magnetic reconnection.

An exhaust region is expected to be bounded on either side by kinks in the magnetic field that propagate as Alfvén waves in opposite directions along the reconnected field lines. Plasma enters the exhaust region from both sides and is accelerated away from the reconnection site as it encounters the field line kinks. Figure 5.3 shows a two-dimensional schematic of the geometry of CS1 in the local y-z plane, illustrating that a kinked magnetic field line is observed across CS1. The shear in the magnetic field across this region is 31°, which is small compared to the ideal geometry for the onset of magnetic reconnection, in which the shear angle approaches 180°.

We now make the assumption that the net outflow of plasma in the reconnection exhaust is perpendicular to the magnetic field within the current sheet. Therefore, we assume that the field-aligned component of the plasma flow velocity in this region is associated with $y - z$ translation of the current sheet in the solar wind. Figure 5.4 shows the plasma flow velocities in the rest frame of CS1, approximated by considering only the plasma velocity flowing perpendicular to the magnetic field within the current sheet. At the boundaries of a reconnection exhaust, inflowing plasma is expected, but this is not observed in the case of CS1. The velocity of the outflowing plasma in the current sheet ($\sim$ 235 km s^{-1}) is comparable with the Alfvén velocity ($\sim$ 200 km s^{-1}) in this region.

The Alfvén Mach number, M_A, of the surrounding flow was 2.3, meaning that the reconnection site and the field and plasma in both exhausts were carried away from the Sun by the super-Alfvénic solar wind flow. The orientation of the magnetic field and direction of the outflowing plasma implies that the reconnection site was located south (- z) and east (+ y) of the observed current sheet when it traversed the WIND spacecraft.

The Walén relation relates the changes in flow velocity to density-weighted changes in the magnetic field vector and can be used to determine if the difference between the velocity of the field line, V_f and the velocity of the plasma, V_p is Alfvénic (see § 2.4.4.1 for further details).

Prior to conducting the Walén test, the *in situ* data must be transformed to

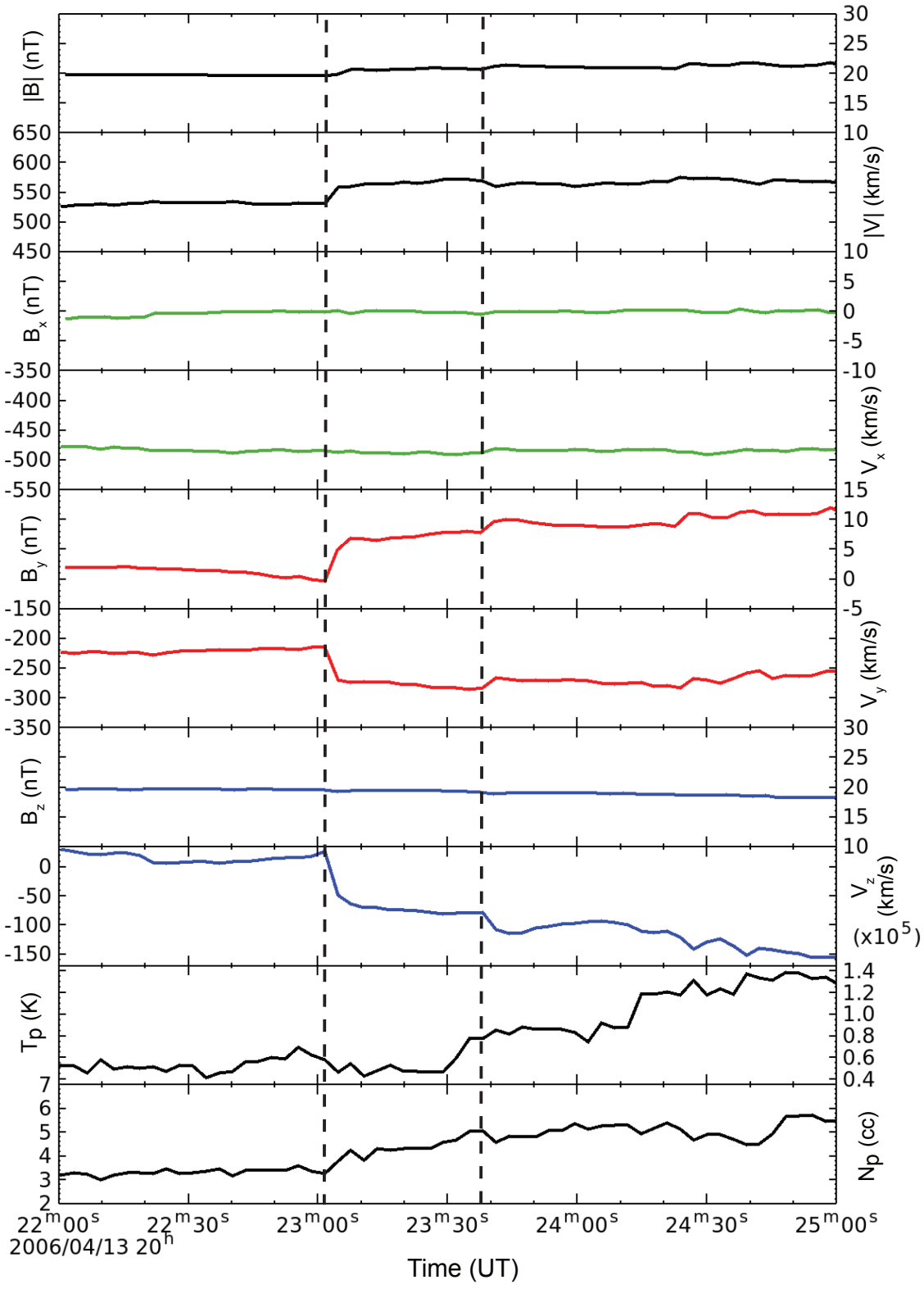

Figure 5.2: Plasma and magnetic field observations in the local frame of CS1 from the WIND spacecraft. The leading and trailing boundaries of the current sheet lie at 20:23:01 UT and 20:23:38 UT, respectively and are highlighted by vertical, dashed lines. Accelerated plasma flow within a bifurcated current sheet and a magnetic field orientation, intermediate between that prevailing before and after the current sheet imply that this event may be the result of magnetic reconnection. No notable changes are observed in the magnetic field strength, proton temperature or proton density with the current sheet.

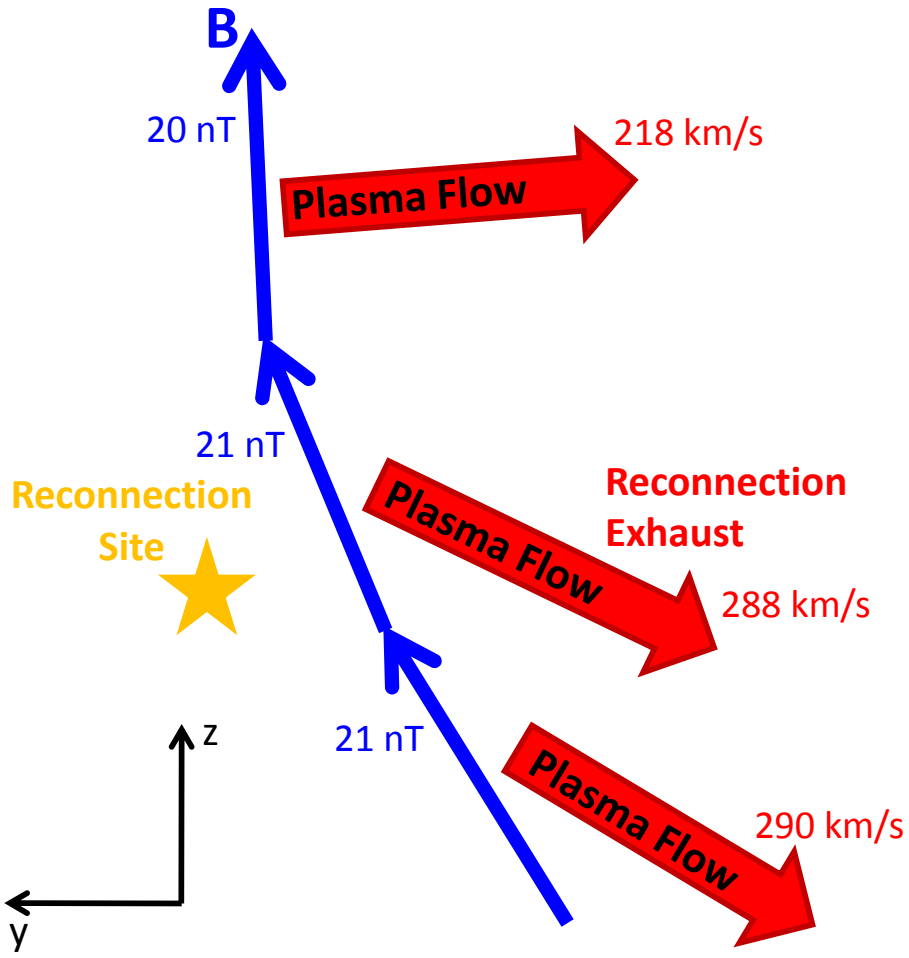

Figure 5.3: A two-dimensional schematic representation of the approximate geometry of Current Sheet 1 when magnetic field and velocity are transformed to the local frame of the current sheet. A kinked magnetic field line is observed. However, the plasma inflows expected at the boundaries of the current sheet are not observed. The speed of the outflowing plasma observed within the current sheet is comparable with the local Alfvén speed in the outflow region.

a deHoffmann-Teller frame (as described in § 2.4.4). This is a frame in which the electric field tends to zero, with the result that the magnetic structure appears stationary since there is no $E \times B$ drift of the field line, so V_f is zero by definition. A comparison of the deHoffmann-Teller velocity in CS1 ($\mathbf{V}_{HT}$ = (-488, -222, 80) km s^{-1}) with the plasma velocity in the current sheet rest frame ($\mathbf{V}$ = (-488, -220, 80) km s^{-1}), shown in Figure 5.4, reveals that they are very similar. The best approximation for the deHoffmann-Teller frame is obtained when the magnetic field is perpendicular to the solar wind flow. This is the case for CS1.

In reconnection events, the velocity of the plasma relative to the deHoffmann-Teller velocity ($V - V_{HT}$) is typically proportional to the Alfvén velocity, V_A. In

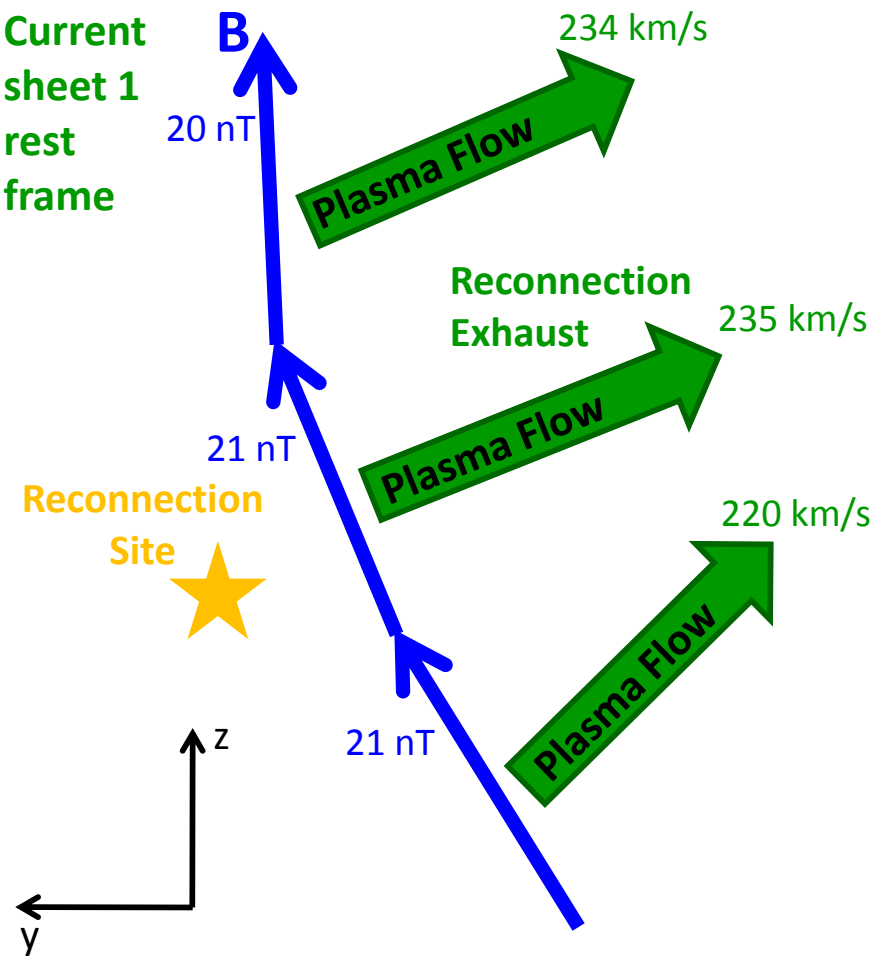

Figure 5.4: A two-dimensional schematic of the approximate geometry of Current Sheet 1 when velocity is transformed again, this time to the rest frame of the current sheet. The expected plasma inflows at the current sheet boundaries are not observed in this frame, either.

magnetopause reconnection events, the coefficient of proportionality is often in the range $\pm(0.8$ - $1.0)$. Such proportionality is interpreted as an indication that the magnetopause has the structure of a large-amplitude Alfvén wave or rotational discontinuity. Figure 5.5 shows some evidence of correlation between $V - V_{HT}$ and V_A in the y-direction, with a coefficient of proportionality of (1.25 ± 0.2) calculated between these two variables.

A second discontinuity is observed between 21:02:10 UT and 21:03:15 UT, and is herein referred to as Current Sheet 2 (CS2). The magnetic field and velocity data have been transformed to the frame of the current sheet determined from the normal to the plane of the current sheet, as before. Figure 5.6 shows evidence that the current sheet is bifurcated in B_z. However, clear changes in the bulk flow

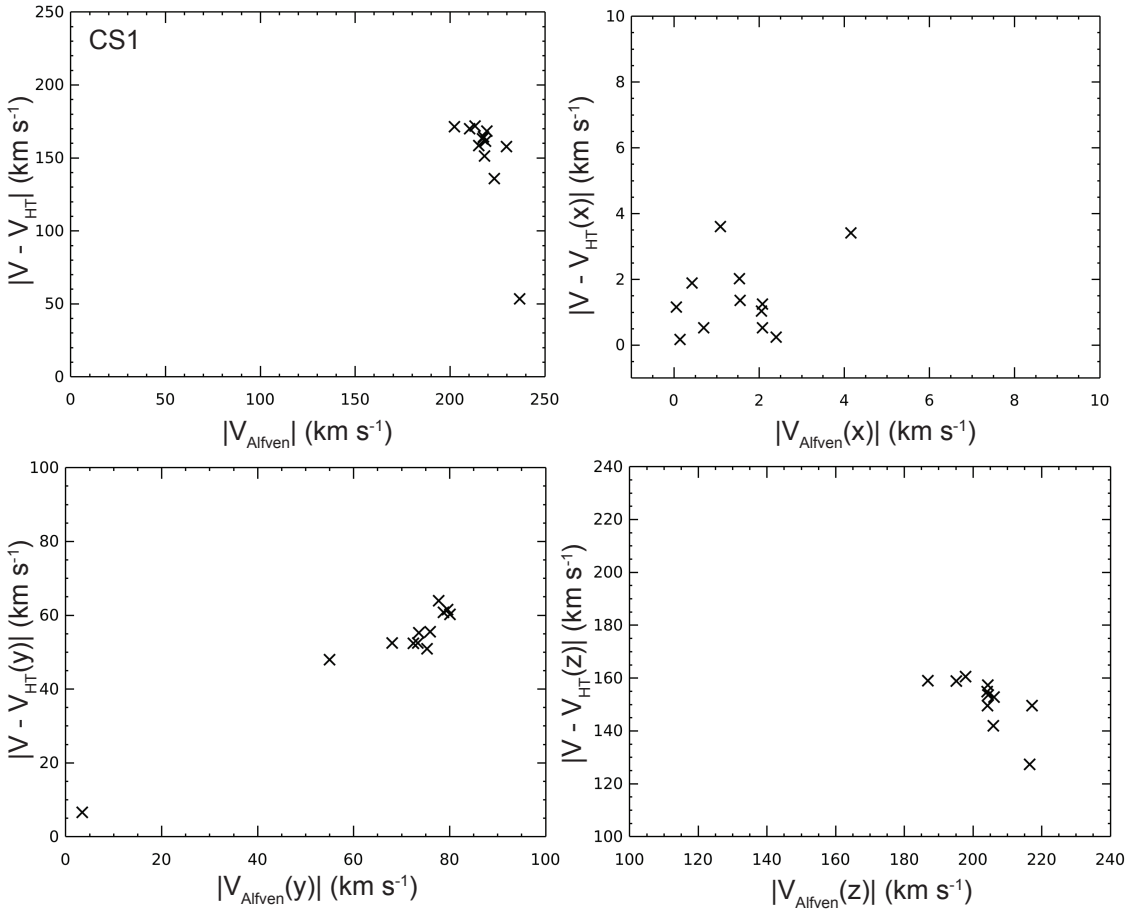

Figure 5.5: The Walén relation is used to examine the extent to which the plasma flow speed in the deHoffmann-Teller frame agrees with the Alfvén speed in a current sheet. There is some evidence of proportionality between $V - V_{HT}$ and V_A in the y-direction.

speed are not evident. From the duration of the observations and the speed of the structure, we estimate its width along the spacecraft trajectory is $\sim 3 \times 10^4$ km.

Figure 5.7 shows a two-dimensional schematic of the geometry of CS2 in the local frame of the structure in the local y-z plane, illustrating that a kinked magnetic field line is observed across CS2. The shear in the magnetic field across this region is 47°. We make the same assumptions as for CS1 and Figure 5.8 shows the plasma flow velocities in the rest frame of CS2, approximated by considering only the plasma velocity flowing perpendicular to the magnetic field within the current sheet. The plasma flows within CS2 are not consistent with the expected direction of flows with respect to the magnetic field within a reconnection exhaust; there is neither convincing observations of plasma inflows at the boundaries of the current sheet or plasma outflows within the current sheet. As in the case of CS1, the Current Sheet 2 velocities are also transformed to the deHoffmann-Teller frame. We find that the deHoffmann-Teller velocity ($\mathbf{V}_{HT}$ = (504, -262, -79) km s^{-1}) differs significantly in direction from to the plasma velocity in the approximate rest frame of the current sheet ($\mathbf{V}$ = (501, -28, 59) km s^{-1}). The magnitude is also significantly larger (274

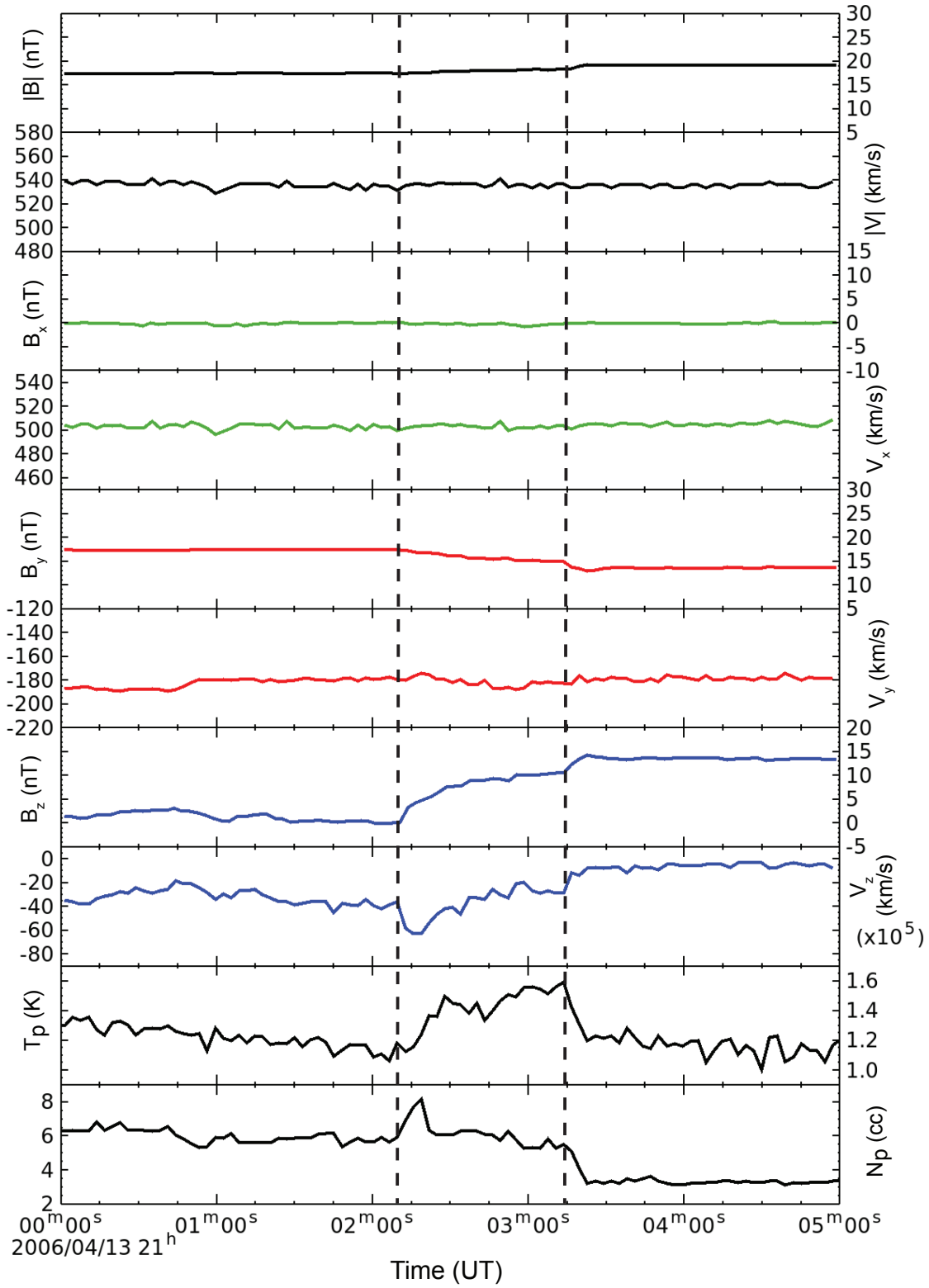

Figure 5.6: Plasma and magnetic field observations in the local frame of CS2 from the WIND spacecraft. The leading and trailing boundaries of the current sheet lie at 21:02:10 UT and 21:03:15 UT, respectively and are highlighted by vertical, dashed lines. There is some evidence in B_z that the current sheet is bifurcated. Both proton temperature and density are elevated within the current sheet.

km s^{-1}) than the outflow speed in the rest frame (65 km s^{-1}), and is comparable with the Alfvén speed in this region (225 km s $^{-1}$). This analysis of CS2 suggest

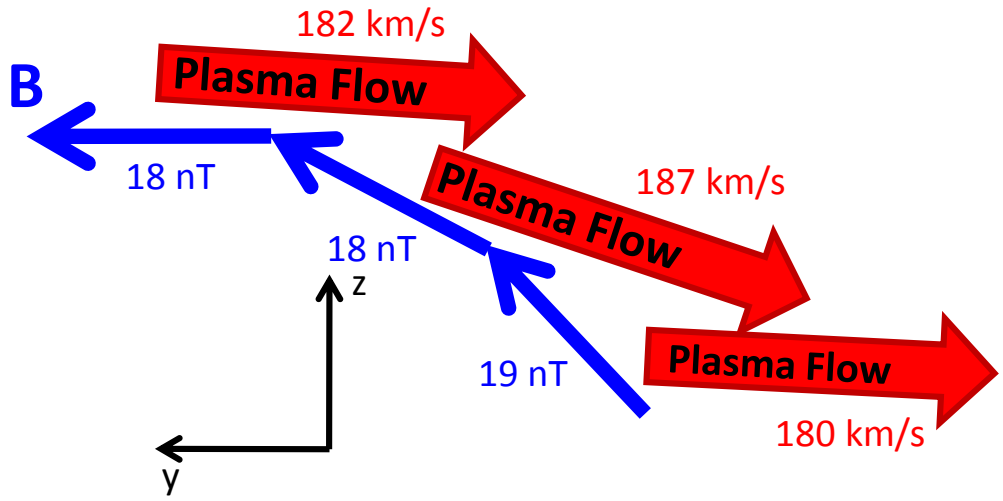

Figure 5.7: A two-dimensional schematic representation of the approximate geometry of Current Sheet 2 when magnetic field and velocity are transformed to the local frame of the current sheet. The observed plasma flows are not consistent with the expected magnitude or direction of reconnection exhaust outflows.

that magnetic reconnection is not proceeding in this region when it is observed by the WIND spacecraft.

We infer from observations of the magnetic field and velocity that quasi-stationary reconnection may occur in the region of Current Sheet 1. In the case of current sheet 2, the directions of plasma flows relative to the magnetic field in this region indicate that reconnection is unlikely to be proceeding in this region when it is observed by the Wind spacecraft.

5.2.2 Multiple Flux Ropes Within the Magnetic Cloud?

The research undertaken in this section and § 5.2.3 on solar wind interaction with ICMEs has been undertaken as part of a collaborative effort with Pascal Démoulin of Observatoire de Paris, France. Here, we employ the use of theoretical modelling to better understand the causes of magnetic cloud substructure.

There are two kinds of theoretical simulations of CMEs. The first are analytical time-dependent MHD models, which provide insights into the physical mechanisms, but cannot reproduce the detailed morphology of the observations. The second are numerical time-dependent MHD simulations, which should be able to reproduce the

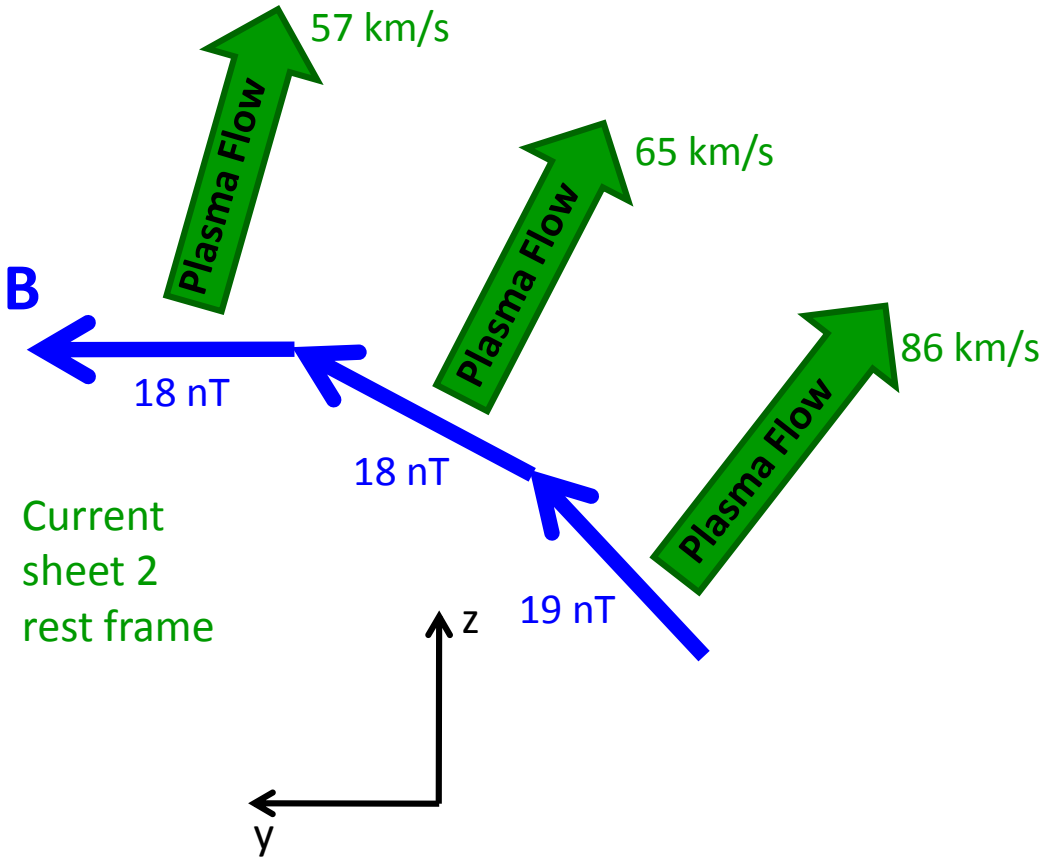

Figure 5.8: A two-dimensional schematic representation of the approximate geometry of Current Sheet 2 when velocity is transformed again, this time to the rest frame of the current sheet. The results of this transformation further confirm our assumption that reconnection is not proceeding in CS2 when this region is observed by the WIND spacecraft.

observations if sufficiently accurate initial conditions and boundary conditions are known (Aschwanden, 2009).

We investigate whether the observed substructure signatures in the magnetic field can be reproduced using numerical simulations by considering a scenario in which the 13 April 2006 magnetic cloud is composed of two consecutive flux ropes with the same sign of helicity, contained within a flux bundle.

The superposition of the magnetic fields of the flux ropes in this way is purely a numerical process. In this type of model, the physics of the interaction, such as the compression of the field or magnetic reconnection, is not considered.

A Gold & Hoyle flux rope is described by the following set of equations:

For a flux rope centred at (0, 0):

$$A(x,y) = \frac{-Log(1+r^2)}{2} \tag{5.1}$$

where A is the axial component of the vector potential of the magnetic field.

$$B_r = -\frac{1}{r}\frac{\partial A}{\partial \theta} = 0; B_\theta = \frac{\partial A}{\partial r}; B_z = e^{2A} \tag{5.2}$$

In cartesian coordinates:

$$B_x(x,y) = \frac{+rSin\theta}{(1+r^2)} \tag{5.3}$$

$$B_y(x,y) = \frac{-rCos\theta}{(1+r^2)} \tag{5.4}$$

$$B_z(x,y) = \frac{+1}{(1+r^2)} \tag{5.5}$$

where $\theta = ArcTan(x,y)$ and $r = \sqrt{x^2+y^2}$.

A simple numerical model of two consecutive flux ropes is simulated by bringing together two Gold & Hoyle force-free fields. We show that the modified fields are both no longer force-free:

Consider two force-free flux ropes 1 and 2, in which $J_1 \times B_1 = 0$ and $J_2 \times B_2 = 0$. Therefore, $J_1 = \alpha_1 B_1$ and $J_2 = \alpha_2 B_2$ with α_1 and α_2 being constant along each field line of the respective fields, 1 and 2.

If B_1 and B_2 are combined to give B (i.e. $B = B_1 + B_2$), then:

$$(J_1 + J_2) \times (B_1 + B_2) = J_1 \times B_2 + J_2 \times B_1 = (\alpha_1 - \alpha_2) B_1 \times B_2 \tag{5.6}$$

This is equal to zero if B_1 is parallel to B_2 everywhere or if $\alpha_1 = \alpha_2$, but in general the superposition of two force-free flux ropes results in a single non-force-free flux rope.

Figure 5.9 shows that when $d_x = 0$, where d_x describes the separation between the centres of the two flux ropes, a single flux rope is described and the model yields the typical bipolar signature expected of a magnetic cloud (*blue trace*). When $d_x = 4$, the flux ropes are well separated and a reversal of the gradient of the B_y

component is produced (*black trace*). However, with this model the interval of the B_y gradient reversal is comparable to the size of the entire flux rope and the multiple reversals present in the observations of B_y are not reproduced. Here, y describes the distance between the observing spacecraft and the flux rope axis during its trajectory through the flux rope. As y increases, the distance between the spacecraft and the flux rope axis increases. Figure 5.10 shows that the value of y does not significantly influence the results for B_y and B_z obtained with the model. Although, as expected B_x becomes more significant further from the flux rope axis.

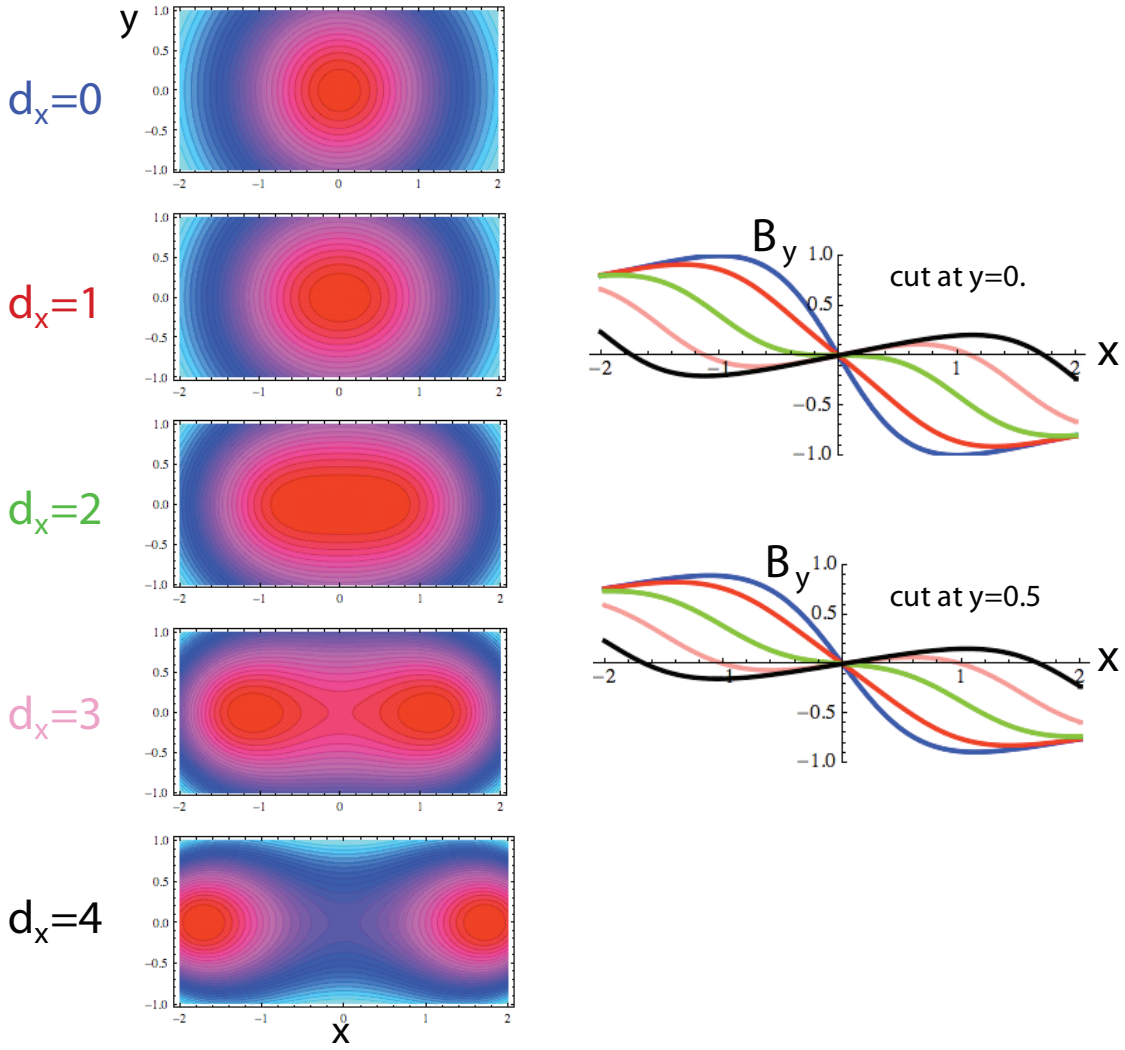

Figure 5.9: A simple numerical model of two consecutive flux ropes is simulated by bringing together two Gold & Hoyle force-free fields. When $d_x = 0$, where d_x describes the separation between the centres of the two flux ropes, a single flux rope is described and the model yields the typical bipolar signature expected of a magnetic cloud (*blue trace*). When $d_x = 4$, the flux ropes are well separated and a reversal of the gradient of the B_y component is produced within the larger-scale bipolar signature (*black trace*). The distance between the spacecraft and the flux rope axis during its trajectory through the flux rope is described by y.

Figure 5.11 shows the B_x, B_y and B_z components of the magnetic field obtained by the model when the field strength of the right-hand flux rope is decreased by half, i.e. $B_1 = 1.0$ and $B_2 = 0.5$. We find that this model is also unable to sufficiently

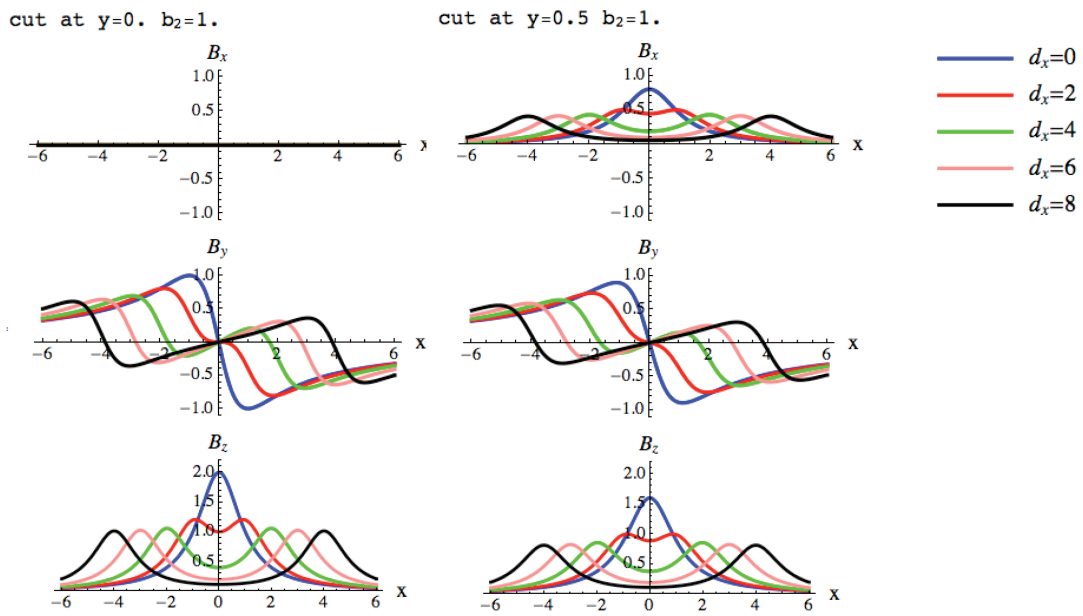

Figure 5.10: The B_x, B_y and B_z components of the magnetic field obtained from the numerical simulations of two consecutive Gold & Hoyle flux ropes when $y = 0$ and $y = 0.5$, for varying degrees of separation between the flux ropes, described by d_x. The value of y does not significantly influence the results of B_y and B_z obtained by the model. As expected, B_x becomes more significant as the distance from the flux rope axis increases (i.e. y increases).

reproduce the observed magnetic field signatures in the substructure region.

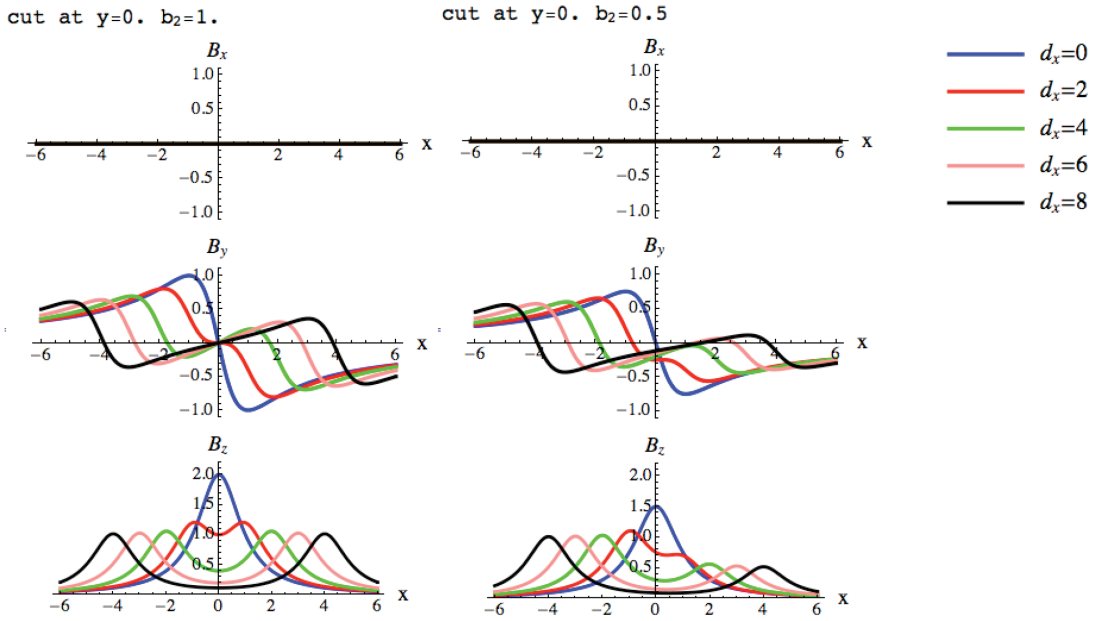

Figure 5.11: The B_x, B_y and B_z components of the magnetic field obtained from the numerical simulations of two consecutive Gold & Hoyle flux ropes when $y = 0$ and the strength of the right-hand flux rope is decreased by half, i.e. $B_1 = 1.0$ and $B_2 = 0.5$, and for varying degrees of separation between the flux ropes, described by d_x. The model is unable to reproduce the magnetic field signatures observed in the substructure region.

Alternatively, this scenario can also be modelled using two Lundquist force-

free fields. A linear force-free Lundquist field is described by the following set of equations:

For a flux rope centred at (0, 0):

$$A(x, y) = \frac{J_0(\alpha r)}{\alpha} \tag{5.7}$$

$$B_r = -\frac{1}{r}\frac{\partial A}{\partial \theta} = 0; B_\theta = \frac{\partial A}{\partial r}; B_z = \alpha A \tag{5.8}$$

In cartesian coordinates:

$$B_x(x, y) = +J_1(\alpha r) Sin\theta \tag{5.9}$$

$$B_y(x, y) = -J_1(\alpha r) Cos\theta \tag{5.10}$$

$$B_z(x, y) = +J_0(\alpha r) \tag{5.11}$$

where $\theta = ArcTan(x, y)$ and $r = \sqrt{x^2 + y^2}$. When $J_0(\alpha) = 0, \alpha = 2.405$.

In this case, the superposition of two linear Lundquist force-free flux ropes results in a flux rope which remains force-free. Here, we are combining two solutions for which the value of α is the same, therefore the resulting flux rope can also be described by a linear force-free field.

Here, we consider only the case of the superposition of two Lundquist force-free flux ropes in which the resulting flux rope remains force-free.

Figure 5.12 shows that the linear force-free field exhibits significant oscillations evident in the B_y and B_z components of the magnetic field when the two flux ropes are both close together ($d_x = 0$) and well-separated ($d_x = 3$). Here, $y = 0$ and there is no signal in the B_x component, as expected. We find that this model is also unable to reproduce the $B_{y,cloud}$ reversals observed in the substructure region.

5.2.3 A Perturbed Magnetic Cloud? Spatial Oscillations of the Magnetic Field

We now investigate whether the observed substructure signatures in the magnetic field can be reproduced by considering a scenario in which the 13 April 2006 magnetic

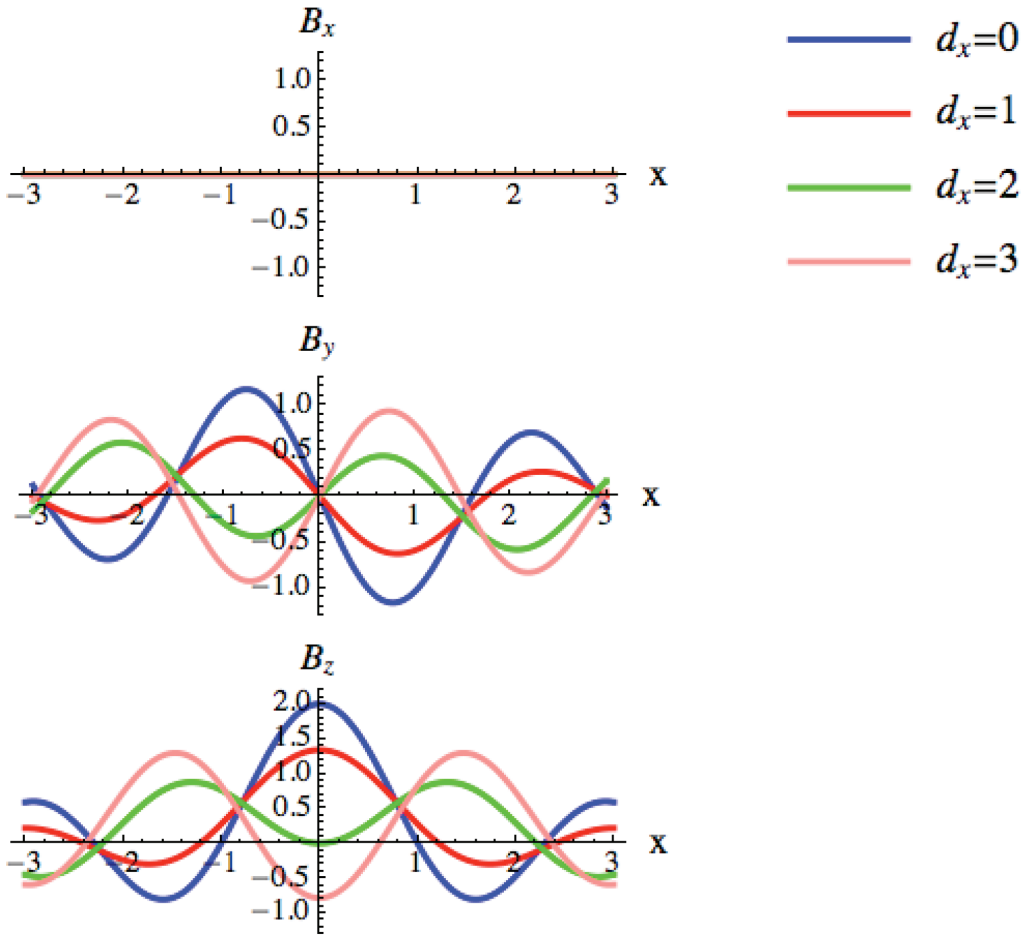

Figure 5.12: The B_x, B_y and B_z components of the magnetic field obtained from the numerical simulations of two consecutive Lundquist flux ropes when $y = 0$, for varying separation between the flux ropes, described by d_x. Oscillations are evident in the B_y and B_z components of the magnetic field, but this model is unable to reproduce the magnetic field signatures observed in the substructure region.

cloud is perturbed by spatial oscillations.

By assuming that $\nabla \cdot \mathbf{B} = 0$ and B_z is a function of A, when spatial oscillations are introduced in a Gold & Hoyle field, the flux rope can be described by the following set of equations:

$$A(r,\theta) = \frac{-(1 + eSin[n\theta + \phi])Log[1 + r^2]}{2} \tag{5.12}$$

In cartesian coordinates:

$$B_x(x,y) = \frac{+(1 + eSin[n\theta + \phi])rSin[\theta]}{(1 + r^2)} + \frac{enCos[n\theta + \phi]Cos[\theta]Log[1 + r^2]}{2r} \tag{5.13}$$

$$B_y(x,y) = \frac{-(1+eSin[n\theta+\phi])rCos[\theta]}{(1+r^2)} + \frac{enCos[n\theta+\phi]Sin[\theta]Log[1+r^2]}{2r} \quad (5.14)$$

$$B_z(x,y) = e^{2A} = (1+r^2)^{-(1+eSin[n\theta+\phi])} + \frac{enCos[n\theta+\phi]Sin[\theta]Log[1+r^2]}{2r} \quad (5.15)$$

where $\theta = ArcTan(x,y)$ and $r = \sqrt{(x^2+y^2)}$.

The oscillating perturbation is described by amplitude, e, spatial frequency, n, and phase, ϕ. As before, y corresponds to the distance between the spacecraft and the flux rope axis. The value selected affects the spatial extent of the perturbations, which broaden as y increases (i.e. the impact parameter becomes larger).

When $e = 0$, a classical Gold & Hoyle field is described. When a perturbation is introduced into the Gold & Hoyle field ($e > 0$), then the magnetic field of the structure is no longer force-free.

Figure 5.13 shows the effect of the perturbation when $n = 7$, $e = 0.2$ and $y = 0.2$. The phase, ϕ determines the location of the oscillations along the x-axis. This scenario produces multiple reversals of the gradient of the B_y component of the magnetic field towards the centre of the flux rope and most closely reproduces the $B_{y,cloud}$ observations of the 13 April 2006 magnetic cloud.

However, Figure 5.14 shows that this model is unable to reproduce the observed signatures of the substructure in the B_x and B_z components of the magnetic field.

In the linear force-free case, spatial oscillations are introduced in a Lundquist field by adding a higher mode solution, in which a "wavy" pattern in θ is expected. The flux rope can be described by the following set of equations:

$$A(r,\theta) = A(x,y) = \frac{(J_0[\alpha r] + eJ_n[\alpha r]Sin[n\theta+\phi])}{\alpha} \quad (5.16)$$

$$B_x(x,y) = +J_1[\alpha r] - eJ_{n-1}[\alpha r]Sin[n\theta+\phi])Sin[\theta] - \frac{en}{\alpha r}J_n[\alpha r]Cos[(n+1)\theta+\phi] \quad (5.17)$$

$$B_y(x,y) = +J_1[\alpha r] - eJ_{n-1}[\alpha r]Sin[n\theta+\phi])Cos[\theta] - \frac{en}{\alpha r}J_n[\alpha r]Sin[(n+1)\theta+\phi] \quad (5.18)$$

$$B_z(x,y) = J_0[\alpha r] + eJ_n[\alpha r]Sin[n\theta+\phi] \quad (5.19)$$

where $\theta = ArcTan(x,y)$ and $r = \sqrt{(x^2+y^2)}$.

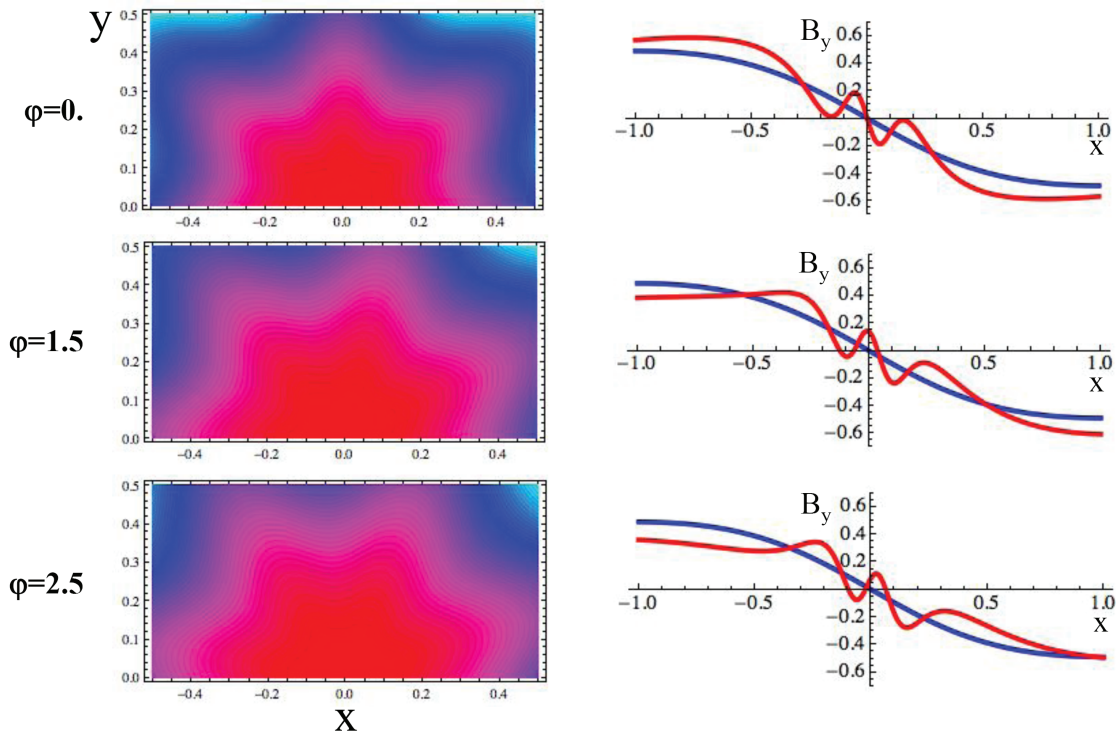

Figure 5.13: Numerical simulations of when a Gold & Hoyle flux rope is perturbed by spatial oscillations show that a similar signature to that observed in $B_{y,cloud}$ can be reproduced when $n = 7$, $e = 0.2$ and $y = 0.2$. The phase, ϕ determines the location of the oscillations along the x-axis.

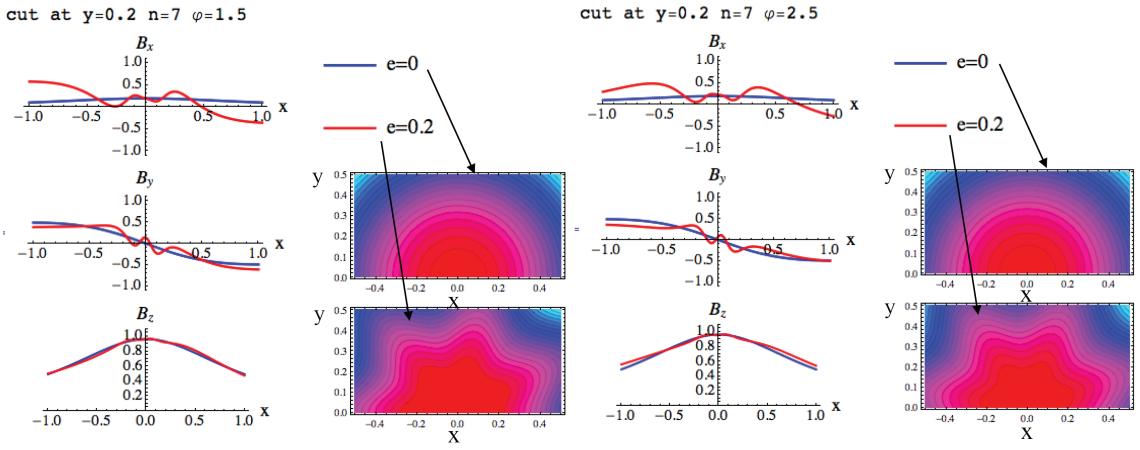

Figure 5.14: The B_x, B_y and B_z components of the magnetic field obtained from the numerical simulations of a perturbed Gold & Hoyle flux rope when $n = 7$ and $y = 0.2$, for $\phi = 1.5$ (*left*) and $\phi = 2.5$ (*right*). This model is unable to reproduce the B_x and B_z magnetic field signatures observed in the substructure region.

As before, the oscillating perturbation is described by amplitude, e, spatial frequency, n, and phase, ϕ. When $e = 0$, a classical Lundquist field is described, and the field remains force-free for all values of e.

Figure 5.15 shows that forcing spatial oscillations in the Lundquist model results in perturbations that are mostly present at the exterior of the flux rope, whilst the core remains undisturbed. Figure 5.16 illustrates that this model is unable to reproduce the observed reversals in the gradient of $B_{y,cloud}$, or the observed substructure signatures in the remaining magnetic field components. Instead, the magnetic field deviates little from the signatures expected in an unperturbed linear force-free field.

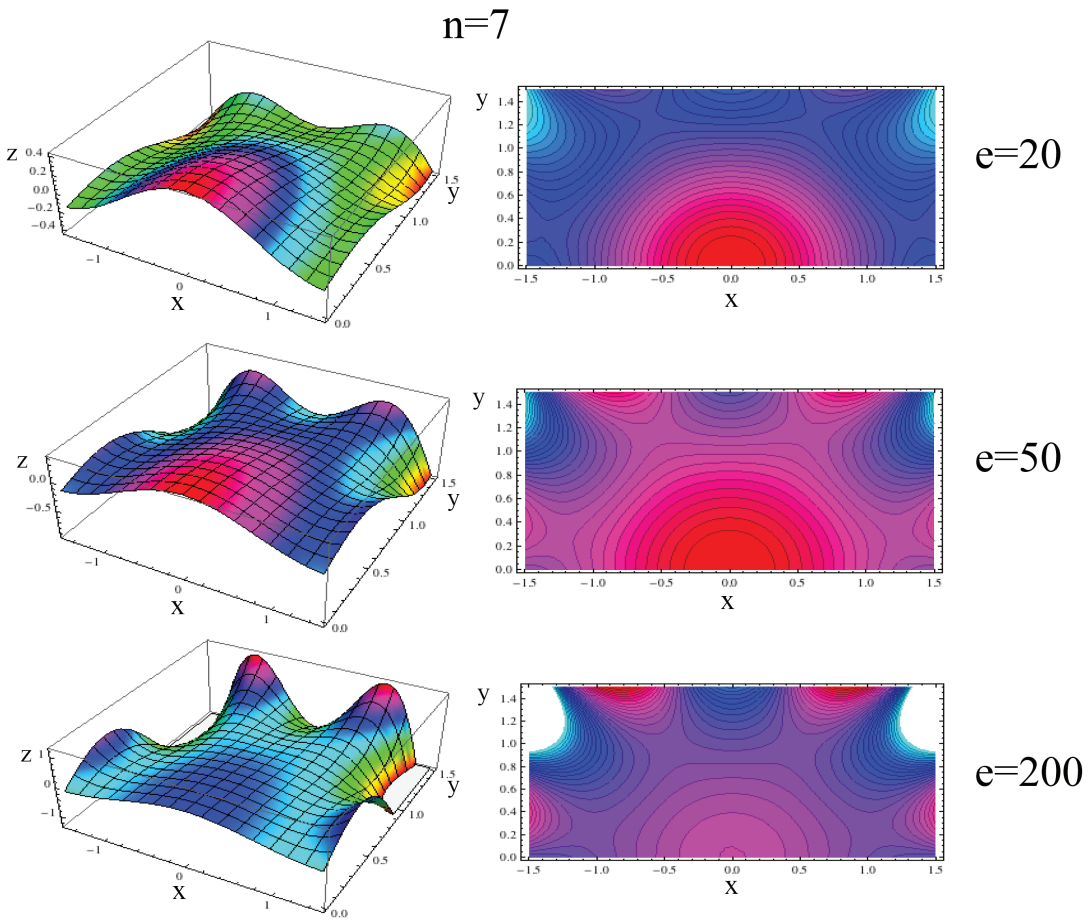

Figure 5.15: Numerical simulations of spatial oscillations in a Lundquist flux rope show that the perturbation is mostly present at the exterior of the flux rope, whilst the core remains undisturbed.

We show that neither the Gold & Hoyle or Lundquist models of perturbed flux ropes is able to sufficiently reproduce the observed substructure signatures in the B_z component of the magnetic field, which represents the axial magnetic field of the flux rope. Large-scale, cylindrical flux rope models indicate that a peak in the axial magnetic field component is expected towards the centre of a flux rope, and this is also what we find in the Gold & Hoyle and Lundquist models of a perturbed flux rope. However, a sudden and significant decrease in $B_{z,cloud}$ is observed towards the centre of the 13 April 2006 magnetic cloud, and neither model is able to reproduce this signature.

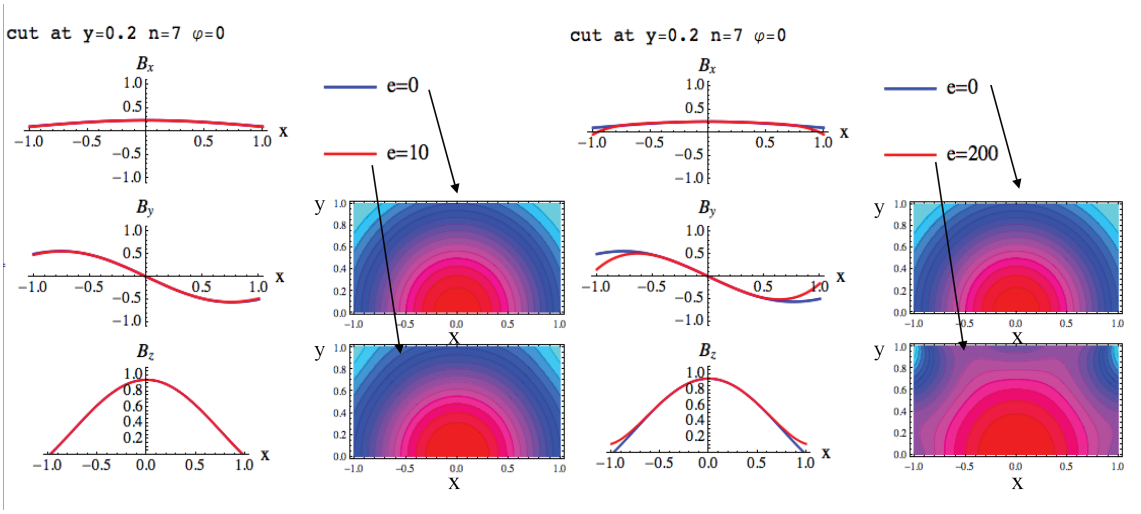

Figure 5.16: The B_x, B_y and B_z components of the magnetic field obtained from the numerical simulations of a perturbed Lundquist flux rope when $n = 7$ and $y = 0.2$ and $\phi = 0$, for $e = 0$, 10 and 200. This model is unable to reproduce the observed the observed reversals in the gradient of $B_{y,cloud}$, or the observed substructure signatures in the remaining magnetic field components. Instead, the magnetic field deviates little from the signatures expected in an unperturbed linear force-free field.

5.2.4 MHD Waves and the Magnetic Cloud

We now investigate whether MHD waves propagating at the boundaries of a flux rope can produce the magnetic field signatures observed in the substructure region of the 13 April 2006 magnetic cloud.

The condition for onset of the Kelvin-Helmholtz instability and wave growth at a boundary is given by:

$$[\underline{k} \cdot (V_1 - V_2)]^2 > \frac{n_1 + n_2}{\mu_0 m_p n_1 n_2} \left[(\underline{k} \cdot B_1)^2 + (\underline{k} \cdot B_2)^2 \right] \tag{5.20}$$

where v is plasma flow velocity, n is plasma number density, B is the magnetic field vector, m_p is proton mass, k is the wave vector and the subscripts refer to the two regions either side of the boundary.

The 13 April 2006 magnetic cloud drives a weak fast forward shock ahead of it, behind which is a region of shocked, compressed solar wind plasma and magnetic field that precedes the arrival of the magnetic cloud. In observations of the magnetic field from the WIND spacecraft, the boundary between the sheath and the magnetic cloud is observed at 15:46 UT on 13 April 2006. A time interval of several minutes is selected within both the preceding solar wind sheath region (Region 1: 15:34 - 15:44 UT) and in the magnetic cloud (Region 2: 15:48 - 15:58 UT) over which average

values for the magnetic field, plasma velocity and proton density are found. Using these values we consider whether the Kelvin-Helmholtz instability is likely to be invoked at this boundary, using the conditions described above, and find that the conditions for wave growth are not satisfied in any direction at the leading boundary of the magnetic cloud.

We also consider if the Kelvin-Helmholtz instability is invoked at the rear boundary between the magnetic cloud and the solar wind. Identification of the rear boundary is more complex than for the leading boundary of the cloud, as previously discussed in § 3.1.3 and § 3.2.2.2. However, we select the boundary at 02:05 UT on 14 April 2006, determined during the analysis of the cloud undertaken in § 3.2.2.2. A time interval of several minutes is selected within both the magnetic cloud (Region 1: 01:52 - 02:02 UT) and in the ambient solar wind following the ejecta (Region 2: 02:06 - 02:16 UT), over which average values for the magnetic field, plasma velocity and proton density are found. Using these values we consider whether the Kelvin-Helmholtz instability is likely to be invoked at this boundary, and find that the conditions for wave growth are not satisfied in any direction at the rear boundary of the magnetic cloud either.

Magnetic tension forces act to stabilise the boundary to the growth of the Kelvin-Helmholtz instability. In the case examined here, the flow shears at both the leading and trailing boundaries of the magnetic cloud are very small ($\approx 1^{\circ}$), and are insufficient to overcome the stabilising effect of these magnetic tension forces.

5.3 Discussion

Within the substructure region of the 13 April 2006 magnetic cloud two discontinuities, CS1 and CS2, were identified (see Chapter 4). The geometry of CS1, approximated from *in situ* magnetic field and velocity observations, implies the presence of a reconnection exhaust region resulting from quasi-stationary reconnection occurring south-east of the observing spacecraft. This is unlikely to also be the case in CS2, in which plasma flow velocity relative to the magnetic field does not imply the presence of a reconnection exhaust in this region.

The estimated width of the reconnection exhaust in CS1 is 2×10^4 km, and while this is smaller than the average width ($\sim 2.5 \times 10^5$ km) discussed in the literature (Gosling *et al.*, 2005a), it is consistent with later studies (Gosling *et al.*, 2007a) that show that many exhausts in the solar wind have local widths $< 4 \times 10^4$ km (corresponding to exhaust crossing times of < 100 s). Some correlation between

small exhaust widths and small shear angles has also been shown by Gosling *et al.* (2007a). This is consistent with observations of CS1, in which the shear angle of the magnetic field across the current sheet is only 31°. It is possible that the kinked field line has "opened out" by the time it is observed by the WIND spacecraft, resulting in the small magnetic field shear angle observed. However, in a study of magnetic reconnection in the solar wind at small shear angles, Gosling *et al.* (2007a) found that 70 % of the exhausts observed in March 2006 were associated with field shear angles < 90 °, and it may simply be the case that the field lines in CS1 reconnect despite the small shear angle between them.

Plasma inflows are typically observed at the boundaries of a reconnection exhaust, but these are not observed in the case of CS1. One possible explanation for the lack of observed inflows is errors in the determination of the velocity introduced during transformation of the reference frame of the structure. To better understand the geometry of the current sheet, we made several field transformations. However, the large component of velocity in the solar wind flow direction means that minor errors in the determination of each frame of reference can potentially result in significant errors in the determination of the velocity in the current sheet.

Although we have found some evidence consistent with magnetic reconnection taking place within the substructure region of the 13 April 2006 magnetic cloud, it is improbable that this is the cause of the substructure within the cloud. The magnetic configuration of a force-free magnetic flux rope is not favourable for the onset of magnetic reconnection, and so some process must distort the magnetic cloud from this ideal configuration before the conditions for the onset of magnetic reconnection are satisfied. Therefore, we propose that the magnetic reconnection proceeding within the 13 April 2006 magnetic cloud is a consequence, rather than the cause, of its unusual magnetic topology.

We have employed the use of numerical simulations to investigate the possibility that the substructure observed in the 13 April 2006 magnetic cloud is the result of the interaction between two consecutive flux ropes. In the case of two similar Gold & Hoyle flux ropes, the superposition of which results in a non-force-free field, we show that By undergoes a reversal on the scale of the entire flux rope and that multiple reversals of this magnetic field component are not produced. Similarly, in the case of two similar Lundquist flux ropes, which remain force-free, significant oscillations of the B_y and B_z components of the magnetic field are observed. Neither model is able to sufficiently reproduce the magnetic field signatures observed within the substructure region of the cloud.

If the 13 April 2006 magnetic cloud was comprised of more than one flux rope,

then the observed substructure signatures in $B_{y,cloud}$ imply that these two flux ropes are similar and have the same sign of helicity. This means that the currents flowing in each flux rope will be similarly directed, resulting in a force of repulsion between them. In order to maintain this configuration, there must be a significant amount of surrounding field and this has not been incorporated in either of the multiple flux rope models presented here. However, it seems unlikely that the 13 April 2006 magnetic cloud is comprised of more than one flux rope, since the observations suggest they would have to be remarkably similar. If the observed substructure does arise from multiple flux ropes, it is perhaps more likely that they will resemble a single flux rope with a bifurcated core, as a result of their interaction as they propagate into interplanetary space. Further investigation of this scenario involves studying the physics of the interaction between two flux ropes, for which MHD simulations are required (Lugaz *et al.*, 2005; Xiong *et al.*, 2007; Xiong, 2009).

Numerical simulations have also been utilised to model a scenario in which a magnetic cloud becomes perturbed, not unlike the "warping" scenario proposed by (Dasso *et al.*, 2006), in which they suggested that a flux rope may become distorted as a result of interactions with the ambient solar wind. In the case of the Gold & Hoyle flux rope, the model is able to adequately reproduce the multiple reversals of the B_y gradient observed towards the centre of the 13 April 2006 magnetic cloud. However, we show that neither the Gold & Hoyle or Lundquist models of perturbed flux ropes are able to sufficiently reproduce the observed substructure signatures in the B_z component of the magnetic field, which represents the axial magnetic field of the flux rope. A sudden and significant decrease in $B_{z,cloud}$ is observed towards the centre of the 13 April 2006 magnetic cloud, but B_z produced by both perturbed flux rope models resembles the peak predicted by large-scale, cylindrical flux rope models.

A comparison of the isocontours of these two models reveals that in the Gold & Hoyle case, in which the resulting flux rope becomes non-force-free, the perturbations are important at both the core and boundaries of the flux rope, while in the Lundquist case in which the resulting flux rope remains force-free, the perturbations are only significant at the flux rope boundaries and the core remains intact. It is the non-force-free nature of the modified Gold & Hoyle field that permits the perturbation to become so important in the core of the flux rope, since in the force-free case the magnetic tension is very efficient at damping inside the magnetic cloud core any perturbation set at the flux rope boundary. Here, we have derived the non-force-free perturbation for only the Gold & Hoyle field, but this should also be possible for the Lundquist case. Our results suggest that the substructure observed towards the centre of the 13 April 2006 magnetic cloud, and other similar events, is a strongly non-force-free perturbation.

Ultra-low frequency (ULF) waves in the inner magnetosphere are known to occur as a result of surface waves (Southwood, 1974; Chen, 1974; Kivelson and Southwood, 1986). Similarly, although the observed substructure in the 13 April 2006 magnetic cloud arises towards the centre of the flux rope, we suggest that it might be possible for MHD waves propagating on the flanks of the flux rope to also distort the topology of the flux rope core. In this study, we investigate whether the Kelvin-Helmholtz instability could provide an explanation for the observed substructure, but conclude that the instability is not invoked at either the leading or trailing edges of the cloud.

There have been several observed instances of ICMEs interacting with the ionised plasma and dust tails of comets, evident in both observations of the comet tail and the magnetic field and plasma observations of the ICME (Jones and Brandt, 2004; Russell *et al.*, 2009). Russell *et al.* (2009) reported the presence of a strong current sheet within the much-studied 15 December 2006 ICME, and suggested a possible link between its formation and the passage of the ICME through the extended dust trail of comet C/2006 P1 (McNaught). If this assumption is correct, they suggest that charged dust can produce twists in the interplanetary magnetic field that can persist over large distances of an AU, or more. A brief study of the trajectories of comets in and around the time that the 13 April 2006 magnetic cloud was propagating from the Sun to the Earth has revealed no candidate dust trails with which this ICME was likely to interact. This, together with the fact that the plasma and magnetic field observations of substructure within the 13 April 2006 magnetic cloud do not appear similar to the observations of other known comet dust interaction events leads us to conclude that a comet interaction is not the cause of the substructure in the 13 April 2006 magnetic cloud.

5.4 Summary and Conclusions

We discuss and evaluate several possible causes of the magnetic cloud substructure discussed in Chapter 4. The *in situ* plasma and magnetic field observations of these structures suggest that reconnection may have occurred on field lines threading structures within the substructure region at some time in the past. We cannot be sure, however, that reconnection was ongoing at the time the exhaust was encountered; nor can we tell how long ago the exhaust occurred or how long reconnection persisted at the reconnection site. While magnetic reconnection proceeds within the magnetic cloud, it is improbable that this is the cause of its unusual topology.

We suggest also that it is unlikely that the observed substructure occurs as a result of the interaction of multiple flux ropes, since the observations suggest that

the flux ropes would have to be very similar and it is improbable for this to be the case. Numerical simulations have shown that "warping" of the magnetic cloud is able to reproduce the observed multiple reversals in the azimuthal magnetic field gradient, but does not sufficiently reproduce the axial magnetic field observations. However, these results strongly imply that the magnetic structure of the 13 April 2006 magnetic cloud must be non-force-free.

In addition, we show that the substructure does not appear to be caused by Kelvin-Helmholtz waves propagating at the boundaries of the flux rope and it is unlikely that the formation of current sheets within the substructure region is a result of the interaction of the ICME with a cometary dust trail.

We conclude that the specific cause of the substructure observed within the 13 April 2006 magnetic cloud, and other similar events, still remains somewhat of a mystery.

Chapter 6

Conclusions and Future Work

6.1 Conclusions

This thesis has discussed work on the relationship between coronal mass ejections (CMEs) and their associated interplanetary counterparts, with particular emphasis on the structure and evolution of a subset of interplanetary CMEs (ICMEs), termed magnetic clouds, as they expand into the heliosphere. This work has demonstrated the importance of combining remote sensing observations of the Sun and *in situ* observations in interplanetary space, in order to construct the "bigger picture" and improve our understanding of all aspects of these large-scale phenomena. In particular, the magnetic topology of magnetic clouds has been studied, with a view to better understanding the internal structure observed in a subset of these ejecta.

A comprehensive review of the current understanding of CMEs, from what triggers their initiation, to their eruption on the Sun and subsequent expansion into the heliosphere is described. Included is a detailed review of all of the known observational signatures of CMEs and ICMEs reported in the literature to date, from both remote sensing and *in situ* instrumentation.

In Chapter 3, we discussed the process of associating magnetic clouds with their solar origins. Detailed study of the *in situ* observations of a magnetic cloud observed near Earth on 13 April 2006, and corresponding remote sensing observations of the Sun, revealed that the ejecta originated from an unusually small solar source. The link between the eruption of the associated CME in a small, spotless, northern hemisphere active region and this magnetic cloud is supported by a number of pieces of evidence. The location of the CME eruption slightly north-east of disk centre means that it is likely to be a halo, or partial halo, CME and is in approximate

agreement with the spacecraft trajectory through the western "leg" of the cloud. This study was the first of its kind to associate a magnetic cloud with its solar source by considering the surrounding solar wind conditions. We also found unique agreement between the helicity signs of the active region and the cloud, while a comparison of the magnetic fluxes within the magnetic cloud and the active region is favourable. Combining observations of a magnetic cloud from both interplanetary space and on the Sun can tell us more about how and why a CME erupted. We conclude that in the case of the 13 April 2006 magnetic cloud, it is most likely that either a flux rope is formed during the eruption, or reconnection proceeds underneath a pre-existing flux rope as it erupts.

In Chapter 4 the internal substructure observed towards the centre of a subset of magnetic clouds was investigated. While substructure is primarily identified by multiple reversals of the azimuthal magnetic gradient towards the centre of a magnetic cloud, associated changes in the behaviour of the plasma in this region are also observed. The 13 April 2006 magnetic cloud is one such event in which substructure is clearly observed. Within this particular event, we noted that two thin current sheets were present within the substructure region and showed that they bounded the region in which the observations deviated most significantly from those typically expected in magnetic clouds. We conclude from a comparison of the properties of several magnetic clouds that exhibit this unusual magnetic topology that these clouds have lower non-dimensional expansion rates than non-overtaken clouds, and that the majority of these clouds are followed by high-speed solar wind streams.

Chapter 5 focuses on the possible causes of magnetic cloud substructure. We both discussed and evaluated several possible explanations for the unusual topology observed in the 13 April 2006 magnetic cloud including, magnetic reconnection, the presence of multiple flux ropes, perturbation of a flux rope by an external influence and the propagation of MHD waves on the magnetic cloud boundaries. We showed that whilst it is possible that magnetic reconnection is proceeding within the cloud, it is improbable that this is the cause, rather than just an effect, of its unusual topology. Similarly, we found that interaction between multiple ICMEs, the onset of the Kelvin-Helmholtz instability and interaction with an extended cometary dust trail were unable to fully explain the observed substructure signatures. We conclude that while numerical simulations of a perturbed flux rope were not able to sufficiently reproduce all of the observed magnetic field signatures in the substructure region, this scenario yields the most promising results and implies that the magnetic structure of the 13 April 2006 magnetic cloud is strongly non-force-free.

6.2 Future Work

The next steps for the work on CMEs and their associated interplanetary counterparts is to more closely investigate CME initiation in unusual solar sources, like small active regions and X-ray bright points, from which well-established magnetic clouds are observed in interplanetary space. Observations of these regions have previously been limited by the spatial and temporal resolution of the solar instrumentation onboard the SOHO and TRACE spacecraft. However, the Atmospheric Imaging Assembly (AIA) onboard the Solar Dynamics Observatory (SDO), launched in 2010, provides full disk observations of the Sun in 10 different wavelengths, 6 of which are in EUV, at a vastly improved spatial resolution and with a cadence of only 10 seconds. These observations, together with additional measurements from the Helioseismic and Magnetic Imager (HMI), which measures the photospheric magnetic field with a spatial resolution of 1", will no doubt revolutionise the study of CMEs from small solar sources, allowing the pre-cursors of CMEs in these regions and the morphological changes in the corona during the eruptions themselves to be examined in unprecedented detail.

Our understanding of the causes of the unusual magnetic topology observed in a subset of magnetic clouds can be improved by determining when, during the evolution of a magnetic cloud, substructure becomes established. From the remote sensing and *in situ* observations of the 13 April 2006 magnetic cloud, it is not clear when substructure develops - in the low corona during CME initiation or eruption, or during the CMEs propagation in interplanetary space? Identifying similar events in more recent *in situ* magnetic field and plasma data would enable us to take advantage of the advanced capabilities of the solar instruments onboard SDO to more closely investigate the solar origins of such events. Similarly, a comparison of the solar source regions of such events may prove fruitful, since we will be able to identify any notable similarities in the morphology of the these regions, pre-, during and/or post-eruption.

Solar Orbiter represents the next generation of inner heliospheric spacecraft, with the ability to undertake both remote sensing of the Sun and *in situ* measurement of the inner heliospheric plasma and magnetic field environment. A significant contribution to the understanding of the evolution of ICMEs in the heliosphere is anticipated from this mission, which is set to revolutionise current ideas on solar-heliospheric connections.

In conclusion, this thesis contributes new scientific research on interplanetary coronal mass ejections (ICMEs) and solar-heliospheric connections. The complexities of linking an ICME with its associated CME and solar source region are demon-

strated, while a better understanding of the intricacies of the internal structure of magnetic clouds and the external influences on their large-scale evolution has been developed as a result of these studies. The work contained in this thesis has implications for developing our understanding of the evolution of ICMEs as they propagate into the heliosphere.

References

Allen Gary, G.: Plasma beta above a solar active region: Rethinking the paradigm, *Sol. Phys.*, **203**, 71–86, doi:10.1023/A:1012722021820, 2001.

Amari, T., Luciani, J. F., Aly, J. J., Mikic, Z., and Linker, J.: Coronal mass ejection: Initiation, magnetic helicity, and flux ropes. I. Boundary motion-driven evolution, *Astrophys. J.*, **585**, 1073–1086, doi:10.1086/345501, 2003.

Andrews, M. D.: A search for CMEs associated with big flares, *Sol. Phys.*, **218**, 261–279, doi:10.1023/B:SOLA.0000013039.69550.bf, 2003.

Antiochos, S. K.: The magnetic topology of erupting structures, *Astrophys. J.*, **502**, L181–L184, doi:10.1086/311507, 1998.

Antiochos, S. K., DeVore, C. R., and Klimchuk, J. A.: A model for solar coronal mass ejections, *Astrophys. J.*, **510**, 485–493, doi:10.1086/306563, 1999.

Aschwanden, M.: Coronal Mass Ejections (CMEs), Springer Berlin Heidelberg New York, 2009.

Aschwanden, M. J.: Particle acceleration and kinematics in solar flares - A synthesis of recent observations and theoretical concepts (Invited review), *Space Sci. Rev.*, **101**, 1–227, doi:10.1023/A:1019712124366, 2002.

Attrill, G. D. R.: Low coronal signatures of coronal mass ejections: Coronal "waves" and dimmings, Ph.D. thesis, University College London, 2008b.

Attrill, G. D. R., Nakwacki, M. S., Harra, L. K., van Driel-Gesztelyi, L., Mandrini, C. H., Dasso, S., and Wang, J.: Using the evolution of coronal dimming regions to probe the global magnetic field topology. "Unidentical Twins": A new interpretation of the 12th May 1997 event, *Sol. Phys.*, **238**, 117–139, doi:10.1007/s11207-006-0167-5, 2006.

Attrill, G. D. R., Harra, L. K., van Driel-Gesztelyi, L., and Démoulin, P.: Coronal "wave": Magnetic footprint of a coronal mass ejection?, *Astrophys. J.*, **656**, L101–104, doi:10.1086/512854, 2007.

Attrill, G. D. R., van Driel-Gesztelyi, L., Démoulin, P., Zhukov, A. N., Steed, K., Harra, L. K., Mandrini, C. H., and Linker, J.: The recovery of CME-related dimmings and the ICME's enduring magnetic connection to the Sun, *Sol. Phys.*, **252**, 349, 2008a.

Aulanier, G., Srivastava, N., and Martin, S. F.: Model prediction for an observed filament, *Astrophys. J.*, **543**, 447, doi:10.1086/317095, 2000.

Aulanier, G., Démoulin, P., and Grappin, R.: Equilibrium and observational properties of line-tied twisted flux tubes, *Astron. Astrophys.*, **430**, 1067–1087, doi:10.1051/0004-6361:20041519, 2005.

Babcock, H. W.: The topology of the sun's magnetic field and the 22-year cycle, *Astrophys. J.*, **133**, 572, 1961.

Baker, D., van Driel-Gesztelyi, L., and Attrill, G. D. R.: Evidence for interchange reconnection between a coronal hole and an adjacent emerging flux region, *Astron. Nach.*, **328**, 773–776, doi:10.1002/asna.200710787, 2007.

Bame, S. J., Asbridge, J. R., Feldman, W. C., Fenimore, E. E., and Gosling, J. T.: Solar wind heavy ions from flare-heated coronal plasma, *Sol. Phys.*, **62**, 179–201, doi:10.1007/BF00150143, 1979.

Berger, M. A.: Rigorous new limits on magnetic helicity dissipation in the solar corona, *Geophys. and Astrophys. Fluid Dynamics*, **30**, 79–104, doi:10.1080/03091928408210078, 1984.

Berger, T. E. and Lites, B. W.: Weak-field magnetogram calibration using advanced stokes polarimeter flux density maps - ii. soho/mdi full-disk model calibration, *Sol. Phys.*, **213**, 213–229, doi:10.1023/A:1023953716633, 2003.

Biesecker, D. A., Myers, D. C., Thompson, B. J., Hammer, D. M., and Vourlidas, A.: Solar phenomena associated with "EIT waves", *Astrophys. J.*, **569**, 1009–1015, doi:10.1086/339402, 2002.

Biskamp, D.: in Energy conservation and particle acceleration in the solar corona, vol. 612 of *Proc. of CESRA workshop, Ringberg, Germany*, p. 109, Springer, Berlin, 2003.

Borrini, G., Gosling, J. T., Bame, S. J., and Feldman, W. C.: Helium abundance enhancements in the solar wind, *J. Geophys. Res.*, **87**, 7370, doi:10.1029/JA087iA09p07370, 1982a.

Borrini, G., Gosling, J. T., Bame, S. J., and Feldman, W. C.: An analysis of shock wave disturbances observed at 1 AU from 1971 through 1978, *J. Geophys. Res.*, **87**, 4365–4373, 1982b.

Bothmer, V. and Rust, D. M.: The field configuration of magnetic clouds and the solar cycle, in Coronal mass ejections: Causes and consequences, vol. 99 of *Geophys. Monogr. Ser.*, pp. 139–146, AGU, Washington D. C., 1997.

Bothmer, V. and Schwenn, R.: Magnetic structures at sector boundaries in the inner heliosphere, in Solar Wind Seven, Proceedings of the 3rd COSPAR Colloquium, pp. 151–154, Goslar, Germany, 1992.

Bothmer, V. and Schwenn, R.: Eruptive prominences as sources of magnetic clouds in the solar wind, *Space Sci. Rev.*, **70**, 215–220, doi:10.1007/BF00777872, 1994.

Bothmer, V. and Schwenn, R.: The interplanetary and solar causes of major geomagnetic storms, *J. Geomagn. Geoelectr.*, **47**, 1127–1132, 1995.

Bothmer, V. and Schwenn, R.: The structure and origin of magnetic clouds in the solar wind, *Ann. Geophys.*, **16**, 1–24, 1998.

Bravo, S., Blanco-Cano, X., and Lopez, C.: Characteristics of interplanetary magnetic clouds in relation to their solar association, *J. Geophys. Res.*, **104**, 581–592, 1999.

Brueckner, G. E., Koomen, M. J., and Tousey, R.: *Sol. Phys.*, **24**, 254, 1972.

Brueckner, G. E., Howard, R. A., Koomen, M. J., Korendyke, C. M., Michels, D. J., Moses, J. D., Socker, D. G., Dere, K. P., Lamy, P. L., Llebaria, A., Bout, M. V., Schwenn, R., Simnett, G. M., Bedford, D. K., and Eyles, C. J.: The Large Angle Spectroscopic Coronagraph (LASCO), *Sol. Phys.*, **162**, 357–402, doi:10.1007/BF00733434, 1995.

Buergi, A. and Geiss, J.: Helium and minor ions in the corona and solar wind: Dynamics and charge states, *Sol. Phys.*, **103**, 347–383, doi:10.1007/BF00147835, 1986.

Burkepile, J. K., Hundhausen, A. J., Stanger, A. L., Cyr, O. C. S., and Seiden, J. A.: Role of projection effects on solar coronal mass ejection properties: 1. A study of CMEs associated with limb activity, *J. Geophys. Res.*, **109**, A03 101, doi:10.1029/2003JA010149, 2004.

Burlaga, L., Fitzenreiter, R., Lepping, R., Ogilvie, K., Szabo, A., Lazarus, A., Steinberg, J., Gloeckler, G., Howard, R., Michels, D., Farrugia, C., Lin, R. P., and Larson, D. E.: A magnetic cloud containing prominence material: January 1997, *J. Geophys. Res.*, **103**, 277–285, doi:10.1029/97JA02768, 1998.

Burlaga, L. F.: Magnetic clouds and force-free fields with constant alpha, *J. Geophys. Res.*, **93**, 7217–7224, doi:10.1029/JA093iA07p07217, 1988.

Burlaga, L. F.: Magnetic clouds, Springer-Verlag, Berlin, Heidelberg, 1991.

Burlaga, L. F.: Interplanetary magnetohydrodynamics, Oxford Univ. Press, New York, 1995.

Burlaga, L. F., Sittler, E., Mariani, F., and Schwenn, R.: Magnetic loop behind an interplanetary shock: Voyager, Helios and IMP 8 observations, *J. Geophys. Res*, **86**, 6673–6684, doi:10.1029/JA086iA08p06673, 1981.

Burlaga, L. F., Klein, L., Sheeley, N. R., Michels, D. J., Howard, R. A., Koomen, M. J., Schwenn, R., and Rosenbauer, H.: A magnetic cloud and a coronal mass ejection, *Geophys. Res. Lett.*, **9**, 1317–1320, doi:10.1029/GL009i012p01317, 1982.

Burlaga, L. F., Behannon, K. W., and Klein, L. W.: Compound streams, magnetic clouds and geomagnetic storms, *J. Geophys. Res.*, **92**, 5725–5734, doi:10.1029/JA092iA06p05725, 1987.

Burlaga, L. F., Plunkett, S. P., and Cyr, O. C. S.: Successive CMEs and complex ejecta, *J. Geophys. Res.*, **107**, 1266, doi:10.1029/2001JA000255, 2002.

Cane, H. V.: The large-scale structure of flare-associated interplanetary shocks, *J. Geophys. Res*, **93**, 1–6, doi:10.1029/JA093iA01p00001, 1988.

Cane, H. V.: Coronal mass ejections and Forbush decreases, *Space Sci. Rev.*, **93**, 55–77, doi:10.1023/A:1026532125747, 2000.

Cane, H. V. and Richardson, I. G.: What caused the large geomagnetic storm of November 1978?, *J. Geophys. Res.*, **102**, 17 445–17 449, doi:10.1029/97JA01420, 1997.

Cane, H. V. and Richardson, I. G.: Interplanetary coronal mass ejections in the near-earth solar wind during 1996-2002, *J. Geophys. Res.*, **108**, 1156–, doi:10.1029/2002JA009817, 2003a.

Cane, H. V. and Richardson, I. G.: Reply to comment on "Coronal mass ejections, interplanetary ejecta and geomagnetic storms" by Gopalswamy et al., *Geophys. Res. Lett.*, **30**, 2233, doi:10.1029/2003GL017685, 2003b.

Cane, H. V., Kahler, S. W., and Sheeley, N. R.: Interplanetary shocks preceded by solar filament eruptions, *J. Geophys. Res.*, **91**, 13 321–13 329, doi:10.1029/JA091iA12p13321, 1986.

Cane, H. V., Sheeley, N. R., and Howard, R. A.: Energetic interplanetary shocks, radio emission and coronal mass ejections, *J. Geophys. Res.*, **92**, 9869–9874, doi:10.1029/JA092iA09p09869, 1987.

Cane, H. V., Richardson, I. G., and Harvey, K.: Filament disappearances and associated shocks of May 1979, *J. Geophys. Res.*, **96**, 19 525–19 528, doi:10.1029/91JA01979, 1991.

Canfield, R. C., Hudson, H. S., and Mckenzie, D. E.: Sigmoidal morphology and eruptive solar activity, *Geophys. Res. Lett.*, **26**, 627–630, doi:10.1029/1999GL900105, 1999.

Cargill, P. J. and Harra, L.: The Solar-Comet Interactions, in Handbook of the Solar-Terrestrial Environment, edited by Y. Kamide and A. Chian, pp. 118–132, Springer Berlin Heidelberg, doi:10.1007/978-3-540-46315-3-20, 2007.

Cargill, P. J. and Schmidt, J. M.: Modelling interplanetary CMEs using magnetohydrodynamic simulations, *Ann. Geophys.*, **20**, 879–890, 2002.

Carmichael, H.: A process for flares, in AAS/NASA symposium on the physics of solar flares, p. 451, NASA, Washington, D. C., 1964.

Carrington, R. C.: Description of a singular appearance seen in the Sun on September 1, 1859, *Monthly notices of the RAS*, **20**, 13–15, 1859.

Chae, J.: Observational determination of the rate of magnetic helicity transport through the solar surface via the horizontal motion of field line footpoints, *Astrophys. J.*, **560**, L95–L98, doi:10.1086/324173, 2001.

Chapman, S.: Notes on the solar corona and the terrestrial atmosphere, *Smithsonian Contrib. Astrophys.*, **2**, 1–11, 1957.

Charbonneau, P., Christensen-Dalsgaard, J., Henning, R., Larsen, R. M., Schou, J., Thompson, M. J., and Tomczyk, S.: Helioseismic constraints on the structure of the solar tachocline, *Astrophys. J.*, **527**, 445–460, doi:10.1086/308050, 1999.

Chen, J.: Effects of toroidal forces in current loops embedded in a background plasma, *Astrophys. J.*, **338**, 453–470, 1989.

Chen, J.: Theory of prominence eruption and propagation: Interplanetary consequences, *J. Geophys. Res.*, **101**, 27 499–27 519, doi:10.1029/96JA02644, 1996.

Chen, J.: Evidence of an erupting magnetic flux rope: LASCO coronal mass ejection of 1997 April 13, *Astrophys. J.*, **409**, L191, doi:10.1086/311029, 1997.

Chen, J. L. S.: Growth of the boundary layer on a spherical gas bubble, *J. Appl. Mech.*, **873**, 873, doi:10.1115/1.3423475, 1974.

Chen, P. F. and Shibata, K.: An emerging flux trigger mechanism for coronal mass ejections, *Astrophys. J.*, **545**, 524, doi:10.1086/317803, 2000.

Cheng, C. C., Karpen, J. T., and Doschek, G. A.: Numerical simulations of loops heated to solar flare temperatures III. Asymmetrical heating, *Astrophys. J.*, **286**, 787–803, doi:10.1086/162655, 1984.

Chou, Y. P. and Charbonneau, P.: A numerical study of the pre-ejection, magnetically-sheared corona as a free boundary problem, *Sol. Phys.*, **166**, 333–369, doi:10.1007/BF00149403, 1996.

Cliver, E. W., Feynman, J., and Garrett, H. B.: An estimate of the maximum speed of the solar wind, 1938-1989, *J. Geophys. Res.*, **95**, 17 103–17 112, doi:10.1029/JA095iA10p17103, 1990.

Cocconi, G., Greisen, K., Morrison, P., Gold, T., and Hayakawa, S.: The cosmic ray flare effect, *Il Nuovo Cimento*, **8**, 161–168, doi:10.1007/BF02962516, 1958.

Cranmer, S. R., Kohl, J. L., and Noci, G.: UVCS/SOHO: The first two years, *Space Sci. Rev.*, **85**, 341–248, doi:10.1023/A:1005175106042, 1998.

Cremades, H. and Bothmer, V.: Geometrical properties of coronal mass ejections, in IAU Symposium, vol. 226 of *IAU Symposium*, pp. 48–54, doi:10.1017/S174392130500013X, 2005.

Crooker, N. U.: Solar and heliospheric distrubances, *J. Atmos. Sol. Phys.*, **62**, 1071–1085, doi:10.1016/S1364-6826(00)00098-5, 2000.

Crooker, N. U. and Horbury, T. S.: Solar imprint on ICMEs, their magnetic connectivity and helisospheric evolution, *Space Sci. Rev.*, **123**, 93–109, doi:10.1007/s11214-006-9014-0, 2006.

Crooker, N. U., Gosling, J. T., Smith, E. J., and Russell, C. T.: A bubblelike coronal mass ejection in the solar wind, in Physics of magnetic flux ropes, edited by C. T. Russell, E. R. Priest, and L. C. Lees, vol. 58 of *Geophys. Monogr. Ser.*, pp. 365–371, AGU, Washington D.C., 1990.

Crooker, N. U., Gosling, J. T., and Kahler, S. W.: Reducing heliospheric magnetic flux from coronal mass ejections without disconnection, *J. Geophys. Res.*, **107**, 3, doi:10.1029/2001JA000236, 2002.

Crooker, N. U., Larson, D. E., Kahler, S. W., Lamassa, S. M., and Spence, H. E.: Suprathermal electron isotropy in high-beta solar wind and its role in heat flux dropouts, *Geophys. Res. Lett.*, **30**, 1619, doi:10.1029/2003GL017036, 2003.

Crooker, N. U., Forsyth, R., Rees, A., Gosling, J. T., and Kahler, S. W.: Counterstreaming electrons in magnetic clouds near 5 au, *J. Geophys. Res.*, **109**, A06 110, doi:10.1029/2004JA010426, 2004.

Dal Lago, A., Schwenn, R., and Gonzalez, W. D.: Relation between the radial speed and the expansion speed of coronal mass ejections, *Adv. Space Res.*, **32**, 2637–2640, doi:10.1016/j.asr.2003.03.012, 2003.

Dasso, S.: Magnetic helicity content in solar wind flux ropes, in IAU Symposium, edited by N. Gopalswamy and D. F. Webb, vol. 257 of *IAU Symposium*, pp. 379–389, doi:10.1017/S1743921309029603, 2009.

Dasso, S., Mandrini, C. H., Démoulin, P., and Farrugia, C. J.: Magnetic helicity analysis of an interplanetary twisted flux rope, *J. Geophys. Res.*, **108**, 1362, doi:10.1029/2003JA009942, 2003.

Dasso, S., Mandrini, C. H., Démoulin, P., Luoni, M. L., and Gulisano, A. M.: Large scale MHD properties of interplanetary magnetic clouds, *Adv. Space Res.*, **35**, 711–724, doi:10.1016/j.asr.2005.02.096, 2005.

Dasso, S., Mandrini, C. H., Démoulin, P., and Luoni, M. L.: A new model-independent method to compute magnetic helicity in magnetic clouds, *Astron. Astrophys.*, **455**, 349–359, doi:10.1051/0004-6361:20064806, 2006.

Dasso, S., Nakwacki, M. S., Démoulin, P., and Mandrini, C. H.: Progressive transformation of a flux rope to an ICME, *Sol. Phys.*, **244**, 115–137, doi:10.1007/s11207-007-9034-2, 2007.

Dasso, S., Mandrini, C. H., Schmieder, B., Cremades, H., Cid, C., Cerrato, Y., Saiz, E., Démoulin, P., Zhukov, A. N., Rodriguez, L., Aran, A., Menvielle, M., and Poedts, S.: Linking two consecutive nonmerging magnetic clouds with their solar sources, *J. Geophys. Res.*, **114**, A02 109, doi:10.1029/2008JA013102, 2009.

Davis, M. S., Phan, T. D., Gosling, J. T., and Skoug, R. M.: Detection of oppositely directed reconnection jets in a solar wind current sheet, *Geophys. Res. Lett.*, **33**, L19 102, doi:10.1029/2006GL026735, 2006.

De Hoffmann, F. and Teller, E.: Magneto-Hydrodynamic Shocks, *Phys. Rev.*, **80**, 692–703, 1950.

Delaboudinière, J. P., Artzner, G. E., Brunaud, J., Gabriel, A. H., Hochedez, J. F., Millier, F., Song, X. Y., Au, B., Dere, K. P., Howard, R. A., Kreplin, R., Michels, R. J., Moses, J. D., Defise, J. M., Jamar, C., Rochus, R., Chauvineau, J. P., Marioge, J. P., Catura, R. C., Lemen, J. R., Shing, L., Stern, R. A., Gurman, J. B., Neupert, W. M., Maucherat, A., Clette, F., Cugnon, P., and van Dessel, E. L.: EIT: extreme-ultraviolet imaging telescope for the SOHO mission, *Sol. Phys.*, **162**, 291–312, doi:10.1007/BF00733432, 1995.

Delannée, C.: Another view of the EIT wave phenomenon, *Astrophys. J.*, **545**, 512–523, doi:10.1086/317777, 2000.

Démoulin, P.: A review of the quantitative links between CMEs and magnetic clouds, *Ann. Geophys.*, **26**, 3113–3125, 2008.

Démoulin, P. and Dasso, S.: Causes and consequences of magnetic cloud expansion, *Astron. Astrophys.*, **498**, 551–566, doi:10.1051/0004-6361/200810971, 2009.

Démoulin, P., Hénoux, J. C., Priest, E. R., and Mandrini, C. H.: Quasi-separatrix layers in solar flares I. Method, *Astron. Astrophys.*, **308**, 643–655, 1996.

Démoulin, P., Nakwacki, M. S., Dasso, S., and Mandrini, C. H.: Expected *in situ* velocities from a hierarchical model for expanding interplanetary coronal mass ejections, *Sol. Phys.*, **250**, 347–374, doi:10.1007/s11207-008-9221-9, 2008.

Domingo, V., Fleck, B., and Poland, A. I.: The SOHO mission: An overview, *Sol. Phys.*, **162**, 1–37, doi:10.1007/BF00733425, 1995.

Drazin, P. G. and Reid, W. H.: Hydromagnetic instability, Cambridge University Press, 1985.

Dryer, M.: Coronal transient phenomena, *Space Sci. Rev.*, **33**, 233, doi:10.1007/BF00213256, 1982.

Dungey, J. W.: Electrodynamics of the outer atmosphere, in Proceedings of the ionosphere conference, p. 225, The Physical Society of London, 1955.

Fainberg, J., Osherovich, V. A., Stone, R. G., MacDowell, R. J., and Balogh, A.: Ulysses observations of electron and proton components in a magnetic cloud and related wave activity, in Solar Wind Eight, edited by J. T. Gosling, S. R. Habbal, W. S. Kurth, and M. Neugebauer, vol. 382, pp. 554–557, AIP. Conf. Proc., Woodbury, New York, doi:10.1063/1.51513, 1996.

Falconer, D. A., Moore, R. L., and Gary, G. A.: Correlation of the coronal mass ejection productivity of solar active regions with measures of their global nonpotentiality from vector magnetograms: Baseline results, *Astrophys. J.*, **569**, 1016–1025, doi:10.1086/339161, 2002.

Farrugia, C. J.: A reconnection layer associated with a magnetic cloud, *Adv. Space Res.*, **28**, 759–764, doi:10.1016/S0273-1177(01)00529-4, 2001.

Farrugia, C. J., Osherovich, V. A., and Burlaga, L. F.: Magnetic flux rope versus the spheromak as models for interplanetary magnetic clouds, *J. Geophys. Res.*, **100**, 12 293–12 306, doi:10.1029/95JA00272, 1995.

Fenimore, E. E.: Solar wind flows associated with hot heavy ions, *Astrophys. J.*, **235**, 245–257, doi:10.1086/157628, 1980.

Fenrich, F. R. and Luhmann, J. G.: Geomagnetic response to magnetic clouds of different polarity, *Geophys. Res. Lett.*, **25**, 2999–3002, doi:10.1029/98GL51180, 1998.

Ferraro, V. C. A. and Plumpton, C.: An introduction to magneto-fluid mechanics, Oxford University Press, New York, 1966.

Fisk, L. A.: Motion of the footpoints of heliospheric magnetic field lines at the sun: Implications for recurrent energetic particle events at high heliographic latitudes, *J. Geophys. Res.*, **101**, 15 547–15 553, doi:10.1029/96JA01005, 1996.

Forbes, T. G.: Solar flare models, Institute of Physics Publishing, Grove's Dictionaries, Inc., New York, 2001.

Forbes, T. G. and Isenberg, P. A.: A catastrophe mechanism for coronal mass ejections, *Astrophys. J.*, **373**, 294–307, doi:10.1086/170051, 1991.

Forbes, T. G. and Priest, E. R.: Photospheric magnetic field evolution and eruptive flares, *Astrophys. J.*, **446**, 377–389, doi:10.1086/175797, 1995.

Forbes, T. G., Linker, J. A., Chen, J., Cid, C., Kóta, J., Lee, M. A., Mann, G., Mikić, Z., Potgieter, M. S., Schmidt, J. M., Siscoe, G. L., Vainio, R., Antiochos, S. K., and Riley, P.: CME theory and models, *Space Sci. Rev.*, **123**, 251–302, doi:10.1007/s11214-006-9019-8, 2006.

Forbush, F. E.: On the effects in cosmic-ray intensity observed during the recent magnetic storm, *Phys. Rev.*, **51**, 1108–1109, doi:10.1103/PhysRev.51.1108.3, 1937.

Forsyth, R. J., Bothmer, V., Cid, C., Crooker, N. U., Horbury, T. S., Kecskemety, K., Klecker, B., Linker, J. A., Odstrcil, D., Reiner, M. J., Richardson, I. G., Rodriguez-Pacheco, J., Schmidt, J. M., and Wimmer-Schweingruber, R. F.: ICMEs in the inner heliosphere: Origin, evolution and propagation effects, *Space Sci. Rev.*, **123**, 383–416, doi:10.1007/s11214-006-9022-0, 2006.

Foukal, P. V.: Solar astrophysics, Wiley VCH, 2004.

Foullon, C., Owen, C. J., Dasso, S., Green, L. M., Dandouras, I., Elliott, H. A., Fazakerley, A. N., Bogdanova, Y. V., and Crooker, N. U.: Multispacecraft study of the 21 January 2005 ICME, *Sol. Phys.*, **244**, 139–165, doi:10.1007/s11207-007-0355-y, 2005.

Galvin, A. B.: Minor ion composition in cme-related solar wind, in Coronal Mass Ejections, vol. 99 of *Geophys. Monogr. Ser.*, pp. 253–260, AGU, Washington D. C., 1997.

Geiss, J., Hirt, P., and Leutwyler, H.: On acceleration and motion of ions in corona and solar wind, *Sol. Phys.*, **12**, 458–483, doi:10.1007/BF00148028, 1970.

Geiss, J., Gloeckler, G., and von Steiger, R.: Origin of the solar wind from composition data, *Space Sci. Rev.*, **72**, 49–60, doi:10.1007/BF00768753, 1995.

Gibson, S. E., Fan, Y., Mandrini, C., Fisher, G., and Démoulin, P.: Observational consequences of a magnetic flux rope emerging into the corona, *Astrophys. J.*, **617**, 600–613, doi:10.1086/425294, 2004.

Gloeckler, G., Fisk, L. A., Hefti, S., Schwadron, N. A., Zurbuchen, T. H., and Ipavich, F. M.: Unusual composition of the solar wind in the 2-3 May 1998 CME observed with SWICS on ACE, *Geophys. Res. Lett.*, **26**, 157–160, doi:10.1029/1998GL900166, 1999.

Gold, T.: Plasma and magnetic fields in the solar system, *J. Geophys. Res.*, **64**, 1665–1674, 1959.

Goldstein, H.: On the field configuration in magnetic clouds, in Solar Wind Five, vol. 2280, pp. 731–733, 1983.

Goldstein, R., Neugebauer, M., and Clay, D.: A statistical study of coronal mass ejection plasma flows, *J. Geophys. Res.*, **103**, 4761, 1998.

Gonzalez, W. D. and Tsurutani, B. T.: Criteria of interplanetary parameters causing intense magnetic storms (Dst <-100 nT), *Planet. and Space Sci.*, **35**, 1101–1109, doi:10.1016/0032-0633(87)90015-8, 1987.

Gopalswamy, N., Kundu, M. R., Hanaoka, Y., Enome, S., Lemen, J. R., and Akioka, M.: Yohkoh/SXT observations of a coronal mass ejection near the solar surface, *New. Astron.*, **1**, 207–213, doi:10.1016/S1384-1076(96)00016-4, 1996.

Gopalswamy, N., Lara, A., Lepping, R. P., Kaiser, M. L., Berdichevsky, D., and Cyr, O. C. S.: Interplanetary acceleration of coronal mass ejections, *Geophys. Res. Lett.*, **27**, 145–148, doi:10.1029/1999GL003639, 2000a.

Gopalswamy, N., Yashiro, S., Kaiser, M. L., Howard, R. A., and Bougeret, J. L.: Radio signatures of coronal mass ejection interaction: Coronal mass ejection cannibalism?, *Astrophys. J.*, **548**, L91–L94, doi:10.1086/318939, 2001a.

Gopalswamy, N., Lara, A., Yashiro, S., Kaiser, M. L., and Howard, R. A.: Predicting the 1-au arrival times of coronal mass ejections, *J. Geophys. Res.*, **106**, 29 207–29 217, doi:10.1029/2001JA000177, 2001b.

Gopalswamy, N., Lara, A., Yashiro, S., and Howard, R. A.: Coronal mass ejections and solar polarity reversal, *Astrophys. J.*, **598**, L63, doi:10.1086/380430, 2003.

Gopalswamy, N., Yashiro, S., Krucker, S., Stenborg, G., and Howard, R. A.: Intensity variation of large solar energetic particle events associated with coronal mass ejections, *J. Geophys. Res.*, **109**, A12 105, doi:10.1029/2004JA010602, 2004.

Gopalswamy, N., Yashiro, S., Liu, Y., Michalek, G., Vourlidas, A., and et al., M. L. K.: Coronal mass ejections and other extreme characteristics of the 2003 October - November solar eruptions, *J. Geophys. Res.*, **110**, A09S15, doi:10.1029/2004JA010958, 2005a.

Gopalswamy, N., Fleck, B., and Gurman, J. B.: in Bringing space benefits to the Asia region, IAA, Bangalore: Astronautical Society of India, 2005b.

Gopalswamy, N., Yashiro, S., Akiyama, S., Makela, P., Xie, H., Kaiser, M. L., Howard, R. A., and Bougeret, J. L.: Coronal mass ejections, type II radio bursts, and solar energetic particle events in the SOHO era, *Ann. Geophys.*, **26**, 1–15, 2008.

Gopalswamy, N., Thompson, W. T., Davila, J. M., Kaiser, M. L., Yashiro, S., Makela, P., Michalek, G., Bougeret, J. L., and Howard, R. A.: Relation between type II bursts and CMEs inferred from STEREO observations, *Sol. Phys.*, **259**, 227–254, doi:10.1007/s11207-009-9382-1, 2009.

Gosling, J., McComas, D., Phillips, J., and Bame, S.: Geomagnetic activity associated with earth passage of interplanetary shock disturbances and coronal mass ejections, *J. Geophys. Res.*, **96**, 7831–7839, doi:10.1029/91JA00316, 1991.

Gosling, J. T.: Coronal mass ejections and magnetic flux ropes in interplanetary space, in Physics of magnetic flux ropes, edited by C. T. Russell, E. R. Priest, and L. C. Lees, vol. 58 of *Geophys. Monogr. Ser.*, pp. 343–364, AGU, Washington D.C., 1990.

Gosling, J. T.: Corotating and transient solar wind flows in three dimensions, *Annu. Rev. Astron. Astrophys.*, **34**, 35–73, doi:10.1146/annurev.astro.34.1.35, 1996.

Gosling, J. T. and Riley, P.: The acceleration of slow coronal mass ejections in the high-speed solar wind, *Geophys. Res. Lett.*, **23**, 2867, doi:10.1029/96GL02843, 1996.

Gosling, J. T., Pizzo, V., and Bame, S. J.: Anomalously low proton temperatures in the solar wind following interplanetary shock waves - Evidence for magnetic bottles?, *J. Geophys. Res.*, **78**, 2001–2009, doi:10.1029/JA078i013p02001, 1973.

Gosling, J. T., Hundhausen, A. J., and Bame, J. T.: Solar wind stream evolution at large heliocentric distances: Experimental demonstration and the test of a model, *J. Geophys. Res.*, **81**, 2111–2122, 1976.

Gosling, J. T., Asbridge, J. R., Bame, S. J., Feldman, W. C., and Zwickl, R. D.: Observations of large fluxes of he^+ in the solar wind following an interplanetary shock, *J. Geophys. Res.*, **85**, 3431–3434, doi:10.1029/JA085iA07p03431, 1980.

Gosling, J. T., Asbridge, J. R., and Bame, S. J.: Evidence for quasi-stationary reconnection at the dayside magnetopause, *J. Geophys. Res.*, **87**, 2147–2158, 1982.

Gosling, J. T., Baker, D. N., Bame, S. J., Feldman, W. C., Zwickl, R. D., and Smith, E. J.: Bidirectional solar wind electron heat flux events, *J. Geophys. Res.*, **92**, 8519–8535, doi:10.1029/JA092iA08p08519, 1987.

Gosling, J. T., Thomsen, M. F., Bame, S. J., Elphic, R. C., and Russell, C. T.: Plasma flow reversals at the dayside magnetopause and the origin of asymmetric polar cap convection, *J. Geophys. Res.*, **95**, 8073–8084, 1990a.

Gosling, J. T., Thomsen, M. F., Bame, S. J., Elphic, R. C., and Russell, C. T.: Observations of reconnection of interplanetary and lobe magnetic field lines at the high-latitude magnetopause, *J. Geophys. Res.*, **96**, 14 097, doi:10.1029/91JA01139, 1991a.

Gosling, J. T., Bame, S. J., Feldman, W. C., McComas, D. J., Phillips, J. L., and Goldstein, B. E.: Counterstreaming suprathermal electron events upstream of corotating shocks in the solar wind beyond *sim* 2 Au: Ulysses, *Geophys. Res. Lett.*, **20**, 2335–2338, doi:10.1029/93GL02489, 1993.

Gosling, J. T., Bame, S. J., McComas, D. J., Phillips, J. L., Scime, E. E., Pizzo, V. J., Goldstein, B. E., and Balogh, A.: A forward-reverse shock pair in the solar wind driven by over-expansion of a coronal mass ejection: Ulysses observations, *Geophys. Res. Lett.*, **21**, 237–240, doi:10.1029/94GL00001, 1994.

Gosling, J. T., Birn, J., and Hesse, M.: Three-dimensional magnetic reconnection and the magnetic topology of coronal mass ejection events, *Geophys. Res. Lett.*, **22**, 869–872, doi:10.1029/95GL00270, 1995a.

Gosling, J. T., Bame, S. J., McComas, D. J., Phillips, J. L., Balogh, A., and Strong, K. T.: Coronal mass ejections at high heliographic latitudes: Ulysses, *Space Sci. Rev.*, **72**, 133–136, doi:10.1007/BF00768769, 1995b.

Gosling, J. T., Skoug, R. M., and Feldman, W. C.: Solar wind electron halo depletions at 90° pitch angle, *Geophys. Res. Lett.*, **28**, 4155–4158, doi:10.1029/2001GL013758, 2001.

Gosling, J. T., Skoug, R. M., McComas, D. J., and Smith, C. W.: Direct evidence for magnetic reconnection in the solar wind near 1 au, *J. Geophys. Res.*, **110**, A01 107, doi:10.1029/2004JA010809, 2005a.

Gosling, J. T., Skoug, R. M., McComas, D. J., and Smith, C. W.: Magnetic disconnection from the sun: Observations of a reconnection exhaust in the solar wind at the heliospheric current sheet, *Geophys. Res. Lett.*, **32**, L05 105, doi:10.1029/2005GL022406, 2005b.

Gosling, J. T., Skoug, R. M., Haggerty, D. K., and McComas, D. J.: Absence of energetic particle effects associated with magnetic reconnection exhausts in the solar wind, *Geophys. Res. Lett.*, **32**, L14 113, doi:10.1029/2005GL023357, 2005c.

Gosling, J. T., Eriksson, S., Skoug, R. M., McComas, D. J., and Forsyth, R. J.: Petschek-type reconnection exhausts in the solar wind well beyond 1 au: Ulysses, *Astrophys. J.*, **644**, 613–621, 2006.

Gosling, J. T., Eriksson, S., McComas, D. J., Phan, T. D., and Skoug, R. M.: Multiple magnetic reconnection sites associated with a coronal mass ejection in the solar wind, *J. Geophys. Res.*, **112**, A08 106, doi:10.1029/2007JA012418, 2007a.

Gosling, J. T., Eriksson, S., Phan, T. D., Larson, D. E., Skoug, R. M., and McComas, D. J.: Direct evidence for prolonged magnetic reconnection at a continuous x-line within the heliospheric current sheet, *Geophys. Res. Lett.*, **34**, L06 102, doi:10.1029/2006GL029033, 2007b.

Green, L. M., Kliem, B., To(e)ro(e)k, T., van Driel-Gesztelyi, L., and Attrill, G. D. R.: Transient coronal sigmoids and rotating erupting flux ropes, *Sol. Phys.*, **246**, 365–391, doi:10.1007/s11207-007-9061-z, 2007.

Gulisano, A. M., Dasso, S., Mandrini, C. H., and Démoulin, P.: Magnetic clouds: A statistical study of magnetic helicity, *J. Atmos. Sol. Terr. Phys.*, **67**, 1761–1766, doi:10.1016/j.jastp.2005.02.026, 2005.

Gulisano, A. M., Dasso, S., Mandrini, C. H., and Démoulin, P.: Estimation of the bias of the minimum variance technique in the determination of magnetic clouds global quantities and orientation, *Adv. Space Res.*, **40**, 1881–1890, doi:10.1016/j.asr.2007.09.001, 2007.

Gulisano, A. M., Démoulin, P., Dasso, S., Ruiz, M. E., and Marsch, E.: Global and local expansion of magnetic clouds in the inner heliosphere, *Astron. Astrophys.*, **509**, A39, doi:10.1051/0004-6361/200912375, 2010.

Guo, W. P. and Wu, S. T.: A magnetohydrodynamic description of coronal helmet streamers containing a cavity, *Astrophys. J.*, **494**, 419, doi:10.1086/305196, 1998.

Hale, G. E.: Sun-spots as magnets and the periodic reversal of their polarity, *Nature*, **113**, 105–112, doi:10.1038/113105a0, 1924.

Hale, G. E., Ellerman, F., Nicholson, S. B., and Joy, A. H.: The magnetic polarity of sun-spots, *Astrophys. J.*, **49**, 153–178, 1919.

Hanaoka, Y., Kurokawa, H., Enome, S., Nakajima, H., Shibasaki, K., Nishio, M., Takano, T., Torii, C., Sekiguchi, H., Kawashima, S., Bushimata, T., Shinohara, N., Irimajiri, Y., Koshiishi, H., Shiomi, Y., Nakai, Y., Funakoshi, Y., Kitai, R.,

Ishiura, K., and Kimura, G.: Simultaneous observations of a prominence eruption followed by a coronal arcade formation in radio, soft x-rays and hα, *Publ. Astron. Soc. Japan*, **46**, 205–216, 1994.

Handy, B. N., Acton, L. W., Kankelborg, C. C., Wolfson, C. J., Akin, D. J., Bruner, M. E., Caravalho, R., Catura, R. C., Chevalier, R., Duncan, D. W., Edwards, C. G., Feinstein, C. N., Freeland, S. L., Friedlaender, F. M., Hoffmann, C. H., Hurlburt, N. E., Jurcevich, B. K., Katz, N. L., Kelly, G. A., Lemen, J. R., Levay, M., Lindgren, R. W., Mathur, D. P., Meyer, S. B., Morrison, S. J., Morrison, M. D., Nightingale, R. W., Pope, T. P., Rehse, R. A., Schrijver, C. J., Shine, R. A., Shing, L., Strong, K. T., Tarbell, T. D., Title, A. M., Torgerson, D. D., Golub, L., Bookbinder, J. A., Caldwell, D., Cheimets, P. N., Davis, W. N., Deluca, E. E., McCullen, R. A., Warren, H. P., Amato, D., Fisher, R., Maldonado, H., and Parkinson, C.: The Transition Region and Coronal Explorer, *Sol. Phys.*, **187**, 229–260, doi:10.1023/A:1005166902804, 1999.

Harra, L. K. and Sterling, A. C.: Material outflows from coronal intensity "dimming regions" during coronal mass ejection onset, *Astrophys. J.*, **561**, L215–L218, doi:10.1086/324767, 2001.

Harra, L. K., Crooker, N. U., Mandrini, C. H., van Driel-Gesztelyi, L., Dasso, S., Wang, J., Elliott, H., Attrill, G., Jackson, B. V., and Bisi, M. M.: How does large flaring activity from the same active region produce oppositely directed magnetic clouds?, *Sol. Phys.*, **244**, 95–114, doi:10.1007/s11207-007-9002-x, 2007.

Harrison, R. A.: Solar coronal mass ejections and flares, *Astron. Astrophys.*, **162**, 283–291, 1986.

Harrison, R. A., Bryans, P., Simnett, G. M., and Lyons, M.: Coronal dimming and the coronal mass ejection onset, *Astron. Astrophys.*, **400**, 1071–1083, doi:10.1051/0004-6361:20030088, 2003.

Harten, R. and Clark, K.: The design features of the GGS wind and polar spacecraft, *Space Sci. Rev.*, **71**, 23–40, doi:10.1007/BF00751324, 1995.

Henke, T., Woch, J., Schwenn, R., Mall, U., Gloeckler, G., von Steiger, R., Forsyth, R. J., and Balogh, J.: Ionization state and magnetic topology of coronal mass ejections, *J. Geophys. Res.*, **106**, 10 597–10 613, doi:10.1029/2000JA900176, 2001.

Hesse, M. and Birn, J.: Plasmoid evolution in an extended magnetotail, *J. Geophys. Res.*, **96**, 5683–5696, doi:10.1029/90JA02503, 1991.

Hidalgo, M. A.: A study of the expansion and distortion of the cross-section of magnetic clouds in the interplanetary medium, *J. Geophys. Res.*, **108**, 1320, doi:10.1029/2002JA009818, 2003.

Hidalgo, M. A., Cid, C., Medina, J., and Vinas, A. F.: A new model for the topology of magnetic clouds in the solar wind, *Sol. Phys.*, **194**, 165–174, doi:10.1023/A:1005206107017, 2000.

Hirayama, T.: Theoretical model of flares and prominences I. Evaporating flare model, *Sol. Phys.*, **34**, 323–388, doi:10.1007/BF00153671, 1974.

Hirose, S., Uchida, Y., Uemura, S., Yamaguchi, T., and Cable, S. B.: A quadruple magnetic source model for arcade flares and x-ray arcade formations outside active regions. II. Dark filament eruption and the associated arcade flare, *Astrophys. J.*, **551**, 586, doi:10.1086/320084, 2001.

Hirshberg, J. and Colburn, D. S.: Interplanetary field and geomagnetic variations - a unifield view, *Planet. Space Sci.*, **17**, 1183, doi:10.1016/0032-0633(69)90010-5, 1969.

Hirshberg, J., Alksne, A., Colburn, D. S., Bame, S. J., and Hundhausen, A. J.: Observations of a solar flare induced interplanetary shock and helium-enriched driver gas, *J. Geophys. Res.*, **75**, 1–15, doi:10.1029/JA075i001p00001, 1970.

Hirshberg, J., Bame, S. J., and Robbins, D. E.: Solar flares and solar wind helium enrichments: July 1965-July 1967, *Sol. Phys.*, **23**, 467–486, doi:10.1007/BF00148109, 1972.

Ho, G. C., Hamilton, D. C., Gloeckler, G., and Bochsler, P.: Enhanced solar wind $^3he^{2+}$ associated with coronal mass ejections, *Geophys. Res. Lett.*, **27**, 309–312, doi:10.1029/1999GL003660, 2000.

Hood, A. W., Galsgaard, K., and Parnell, C. E.: Magnetic reconnection throughout the solar atmosphere, in SOLMAG 2002. Proceedings of the magnetic coupling of the solar atmosphere euroconference and IAU colloquium 188, ESA SP-505, pp. 285–291, 2002.

Howard, R. A., Michels, D. J., N. R., J. S., and Koomen, M. J.: The observation of a coronal transient directed at earth, *Astrophys. J.*, **263**, L101–L104, 1982.

Howard, R. A., Sheeley, N. R., Michels, D. J., and Koomen, M. J.: Coronal mass ejections - 1979-1981, *J. Geophys. Res.*, **90**, 8173–8191, 1985.

Hoyng, P., Duijveman, A., Machado, M. E., Rust, D. M., Svestka, Z., Boelee, A., de Jager, C., Frost, K. T., Lafleur, H., Simnett, G. M., van Beek, H. F., and Woodgate, B. E.: Origin and location of the hard X-ray emission in a two-ribbon flare, *Astrophys. J.*, **246**, L155, 1981.

Hu, Q. and Sonnerup, B. U. O.: Reconstruction of magnetic clouds in the solar wind: Orientations and configurations, *J. Geophys. Res.*, **107**, 1142, doi:10.1029/2001JA000293, 2002.

Hu, Q., Smith, C. W., Ness, N. F., and Skoug, R. M.: Double flux-rope magnetic cloud in the solar wind at 1 au, *Geophys. Res. Lett.*, **30**, 1385, doi:10.1029/2002GL016653, 2003.

Hudson, H. S., Acton, L. W., and Friedland, S. L.: A long duration solar flare with mass ejection and global consequences, *Astrophys. J.*, **470**, 629–635, doi:10.1086/177894, 1996.

Hudson, H. S., Khan, J. I., Lemen, J. R., Nitta, N. V., and Uchida, Y.: Soft x-ray observation of a large-scale coronal wave and its exciter, *Sol. Phys.*, **212**, 121–149, 2003.

Hundhausen, A., Burkepile, J., and Cyr, O. S.: Speeds of coronal mass ejections: SMM observations from 1980 and 1984-1989, *J. Geophys. Res.*, **99**, 6543–6552, doi:10.1029/93JA03586, 1994.

Hundhausen, A. J.: The origin and propagation of coronal mass ejections, in Sixth international solar wind conference, pp. 181–214, 1987.

Hundhausen, A. J.: Sizes and locations of coronal mass ejections: SMM observations from 1980 and 1984-1989, *J. Geophys. Res.*, **98**, 13 177–13 200, doi:10.1029/93JA00157, 1993.

Hundhausen, A. J.: in The many faces of the Sun. A summary of the results from NASA's Solar Maximum, p. 143, Springer, Berlin, 1999.

Hundhausen, A. J., Gilbert, H. E., and Bame, S. J.: The state of ionization of oxygen in the solar wind, *Astrophys. J.*, **152**, L3, doi:10.1086/180165, 1968.

Hundhausen, A. J., Sawyer, C. B., House, L., Illing, R., and Wagner, W.: Coronal mass ejections observed during the solar maximum mission: Latitude distribution and rate of occurrence, *J. Geophys. Res.*, **89**, 2639–2646, doi:10.1029/JA089iA05p02639, 1984.

Huttunen, K. E. J., Schwenn, R., Bothmer, V., and Koskinen, H. E. J.: Properties and geoeffectiveness of magnetic clouds in the rising, maximum and early declining phases of solar cycle 23, *Ann. Geophys.*, **23**, 625–641, 2005.

Ipavich, F. M., Galvin, A. B., Gloeckler, G., Hovestadt, D., Bame, S. J., Klecker, B., Scholer, M., Fisk, L. A., and Fan, C. Y.: Solar wind Fe and CNO measurements in high-speed flows, *J. Geophys. Res.*, **91**, 4133–4141, doi:10.1029/JA091iA04p04133, 1986.

Isenberg, P. A., Forbes, T. G., and Démoulin, P.: Catastrophic evolution of a force-free flux rope: A model for eruptive flares, *Astrophys. J.*, **417**, 368, doi:10.1086/173319, 1993.

Ivanov, K. G. and Kharshiladze, A. F.: Interplanetary hydromagnetic clouds as flare-generated spheromaks, *Sol. Phys.*, **98**, 379–386, doi:10.1007/BF00152467, 1985.

Ivanov, K. G., Kharshiladze, A. F., Eroshenko, E. G., and Styazhkin, V. A.: Configuration, structure and dynamics of magnetic clouds from solar flares in light of measurements on board Vega 1 and Vega 2 in January-February 1986, *Sol. Phys.*, **120**, 407–419, doi:10.1007/BF00159888, 1989.

Janoo, L., Farrugia, C. J., Torbert, R. B., Quinn, J. M., Szabo, A., Lepping, R. P., Ogilvie, K. W., Lin, R. R., Larson, D., Scudder, J. D., Osherovich, V. A., and Steinberg, J. T.: Field and flow perturbations in the October 18-19 1995, magnetic cloud, *J. Geophys. Res.*, **103**, 17 249, doi:10.1029/97JA03173, 1998.

Jian, L., Russell, C. T., Luhmann, J. G., and Skoug, R. M.: Properties of interplanetary coronal mass ejections at one AU during 1995-2004, *Sol. Phys.*, **239**, 393–436, doi:10.1007/s11207-006-0133-2, 2006.

Jing, J., Yurchyshyn, V. B., Yang, G., and Wang, H.: On the relation between filament eruptions, flares and coronal mass ejections, *Astrophys. J.*, **614**, 1054–1062, doi:10.1086/423781, 2004.

Jones, G. H. and Brandt, J. C.: The interaction of comet 153P/Ikeya-Zhang with interplanetary coronal mass ejections: Identification of fast ICME signatures, *Geophys. Res. Lett.*, **31**, L20 805, doi:10.1029/2004GL021166, 2004.

Jones, G. H., Rees, A., Balogh, A., and Forsyth, R. J.: The draping of heliospheric magnetic fields upstream of coronal mass ejecta, *Geophys. Res. Lett.*, **29**, 1520, doi:10.1029/2001GL014110, 2002.

Jurac, S., Kasper, J. C., Richardson, J. D., and Lazarus, A. J.: Geomagnetic disturbances and their relationship to interplanetary shock parameters, *Geophys. Res. Lett.*, **29**, 1463, doi:10.1029/2001GL014034, 2002.

Kahler, S. W., Crooker, N. W., and Gosling, J. T.: A magnetic polarity and chirality analysis of ISEE 3 interplanetary magnetic clouds, *J. Geophys. Res.*, **104**, 9911–9918, doi:10.1029/1999JA900040, 1999.

Kamide, Y. and Maltsev, Y.: Geomagnetic storms, in Handbook of the Solar-Terrestrial Environment, edited by Y. Kamide and A. Chian, pp. 355–374, Springer Berlin Heidelberg, doi:10.1007/978-3-540-46315-3-20, 2007.

Kane, S. R.: Spatial structure of high energy photon sources in solar flares, *Sol. Phys.*, **86**, 355–365, 1983.

Khan, J. I. and Hudson, H. S.: Homologous sudden disappearances of transequatorial interconnecting loops in the solar corona, *Geophys. Res. Lett.*, **27**, 1083–1086, doi:10.1029/1999GL010730, 2000.

Khrabrov, A. V. and Sonnerup, B. U. O.: DeHoffmann-Teller analysis, in Analysis methods for multi-spacecraft data, pp. 221–248, International Space Science Institute (ISSI), 1998.

Kivelson, M. and Southwood, D. J.: Coupling of global magnetospheric mhd eigenmodes to field line resonances, *J. Geophys. Res.*, **91**, 4345–4351, 1986.

Klein, L. W. and Burlaga, L. F.: Interplanetary magnetic clouds at 1 AU, *J. Geophys. Res.*, **87**, 613–624, doi:10.1029/JA087iA02p00613, 1982.

Kliem, B., Mackinnon, A., Trottet, G., and Bastian, T.: Recent progress in understanding energy conversion and particle acceleration in the solar corona, *Lecture Notes in Physics*, **612**, 263–293, 2003.

Klimchuk, J. A.: Shear-induced inflation of coronal magnetic fields, *Astrophys. J.*, **354**, 745–754, doi:10.1086/168731, 1990.

Klimchuk, J. A.: Theory of coronal mass ejections, *Geophys. Monogr.*, **125**, 143–157, 2001.

Kopp, G., Lawrence, G., and Rottman, G.: The total irradiance monitor (TIM): Science results, *Sol. Phys.*, **20**, 129–139, doi:10.1007/s11207-005-7433-9, 2005.

Kopp, R. A. and Holzer, T. H.: Dynamics of coronal hole regions, *Sol. Phys.*, **49**, 43–56, doi:10.1007/BF00221484, 1976a.

Kopp, R. A. and Pneuman, G. W.: Magnetic reconnection in the corona and the loop prominence phenomenon, *Sol. Phys.*, **50**, 85–98, doi:10.1007/BF00206193, 1976.

Kosugi, T. and Somov, B. M.: Magnetic reconnection and particle acceleration in solar flares, in Observational plasma astrophysics: Five years of Yohkoh and beyond, In proceedings of the Yohkoh fifth anniversary symposium, pp. 297–306, 1998.

Krall, J., Chen, J., and Santoro, R.: Drive mechanisms of erupting solar magnetic flux ropes, *Astrophys. J.*, **539**, 964, doi:10.1086/309256, 2000.

Laming, J. M. and Feldman, U.: The solar helium abundance in the outer corona determined from observations with SUMER/SOHO, *Astrophys. J.*, **546**, 552–558, doi:10.1086/318238, 2001.

Leighton, R. B.: A magneto-kinetic model of the solar cycle, *Astrophys. J.*, **156**, 1, 1969.

Lengyel-Frey, D., Stone, R. G., and Bougeret, J. L.: Fundamental and harmonic emission in interplanetary type II radio bursts, *Astron. Astrophys.*, **151**, 215–221, 1985.

Lepping, R. P., Jones, J. A., and Burlaga, L. F.: Magnetic field structure of interplanetary magnetic clouds at 1 AU, *J. Geophys. Res.*, **95**, 11 957–11 965, doi:10.1029/JA095iA08p11957, 1990.

Lepping, R. P., Acuna, M. H., Burlaga, L. F., Farrell, W. M., Slavin, J. A., Schatten, K. H., Mariani, F., Ness, N. F., Neubauer, F. M., Whang, Y. C., Byrnes, J. B., Kennon, R. S., Panetta, P. V., Scheifele, J., and Worley, E. M.: The WIND magnetic field investigation, *Space Sci. Rev.*, **71**, 207–229, doi:10.1007/BF00751330, 1995.

Lepping, R. P., Burlaga, L. F., Szabo, A., Ogilvie, K. W., Mish, W. H., Vassiliadis, D., Lazarus, A. J., Steinberg, J. T., Farrugia, C. J., Janoo, L., and Mariani, F.: The Wind magnetic cloud and events of October 18 - 20 1995: Interplanetary properties and as triggers for geomagnetic activity, *J. Geophys. Res.*, **102**, 14 049–14 063, doi:10.1029/97JA00272, 1997.

Lepping, R. P., Berdichevsky, D. B., Szabo, A., Arqueros, C., and Lazarus, A. J.: Profile of an average magnetic cloud at 1 AU for the quiet solar phase: Wind observations, *Sol. Phys.*, **212**, 425–444, doi:10.1023/A:1022938903870, 2003.

Lepri, S. T. and Zurbuchen, T. H.: Iron charge state distributions as an indicator of hot ICMEs: Possible sources and temporal and spatial variations during solar maximum, *J. Geophys. Res.*, **109**, A01 112, doi:10.1029/2003JA009954, 2004.

Lepri, S. T., Zurbuchen, T. H., Fisk, L. A., Richardson, I. G., Cane, H. V., and Gloeckler, G.: Iron charge distribution as an identifier of interplanetary coronal mass ejections, *J. Geophys. Res.*, **106**, 29 231–29 238, doi:10.1029/2001JA000014, 2001.

Lin, J., Forbes, T. G., Isenberg, P. A., and Démoulin, P.: The effect of curvature on flux-rope models of coronal mass ejections, *Astrophys. J.*, **504**, 1006–1019, doi:10.1086/306108, 1998.

Lin, N., Kellogg, P. J., Goetz, K. A., Monson, S. J., and MacDowall, R. J.: Plasma waves in coronal mass ejections: Ulysses observations, vol. 471 of *Solar Wind Nine, Proceedings of the ninth international solar wind conference*, pp. 673–676, AIP Conf. Proc., 1999.

Lin, R. P., Anderson, K. A., Ashford, S., Carlson, C., Curtis, D., Ergun, R., Larson, D., McFadden, J., McCarthy, M., Parks, G. K., Rème, H., Bosqued, J. M., Coutelier, J., Cotin, F., d'Uston, C., Wenzel, K. P., Sanderson, T. R., Henrion, J., and Ronnet, J. C.: A three-dimensional plasma and energetic particle investigation for the Wind spacecraft, *Space Sci. Rev.*, **71**, 125–153, doi:10.1007/BF00751328, 1995.

Lindsay, G. M., Luhmann, J. G., Russell, C. T., and Gazis, P. R.: On the sources of interplanetary shocks at 0.72 AU, *J. Geophys. Res.*, **99**, 11–17, doi:10.1029/93JA02666, 1994.

Lindsay, G. M., Luhmann, J. G., Russell, C. T., and Gosling, J. T.: Relationships between coronal mass ejection speeds from coronagraph images and interplanetary characteristics of associated interplanetary coronal mass ejections, *J. Geophys. Res.*, **104**, 12 515–12 523, doi:10.1029/1999JA900051, 1999.

Liu, Y.: The speed of halo coronal mass ejections and properties of associated active regions, *Adv. Space Res.*, **39**, 1767–1772, doi:10.1016/j.asr.2007.03.043, 2007.

Lopez, R. E.: Solar cycle invariance in solar wind proton temperature relationships, *J. Geophys. Res.*, **92**, 11 189–11 194, doi:10.1029/JA092iA10p11189, 1987.

López Fuentes, M. C., Démoulin, P., Mandrini, C. H., and van Driel-Gesztelyi, L.: The counterkink rotation of a non-Hale active region, *Astrophys. J.*, **544**, 540–549, doi:10.1086/317180, 2000.

Low, B. C.: Solar activity and the corona, *Sol. Phys.*, **167**, 217–265, doi:10.1007/BF00146338, 1996.

Low, B. C.: Coronal mass ejections, flares and prominences, vol. 171 of *Solar Wind Nine, Proceedings of the ninth international solar wind* , pp. 109–114, AIP Conf. Proc., doi:10.1063/1.58788, 1999.

Low, B. C. and Smith, D. F.: The free energies of partially open coronal magnetic fields, *Astrophys. J.*, **410**, 412–425, doi:10.1086/172758, 1993.

Lugaz, N., Manchester, W. B., and Gombosi, T. I.: Numerical simulation of the interaction of two coronal mass ejections from Sun to Earth, *Astrophys. J.*, **634**, 651, doi:10.1086/491782, 2005.

Lundquist, S.: Magnetostatic fields, *Ark. Fys.*, p. 2361, 1950.

Lynch, B. J., Zurbuchen, T. H., Fisk, L. A., and Antiochos, S. K.: Internal structure of magnetic clouds: Plasma and composition, *J. Geophys. Res.*, **108**, 1239–1253, doi:10.1029/2002JA009591, 2003.

Magara, T., Mineshige, S., Yokoyama, T., and Shibata, K.: Numerical simulation of magnetic reconnection in eruptive flares, *Astrophys. J.*, **466**, 1054–1066, doi:10.1086/177575, 1996.

Malitson, H. H., Fainberg, J., and Stone, R. G.: Observation of a type II solar radio burst to 37 $R_\odot$, *Astrophys. Lett.*, **14**, 111–114, 1973.

Manchester, W. B. and Zurbuchen, T. H.: Are high latitude forward-reverse shock pairs driven by CME overexpansion?, *J. Geophys. Res.*, **111**, A05 101, doi:10.1029/2005JA011461, 2006.

Mandrini, C. H., Pohjolainen, S., Dasso, S., Green, L. M., Démoulin, P., van Driel-Gesztelyi, L., Copperwheat, C., and Foley, C.: Interplanetary flux rope ejected from an X-ray bright point - The smallest magnetic cloud source-region ever observed, *Astron. Astrophys.*, **434**, 725–740, doi:10.1051/0004-6361:20041079, 2005.

Mandrini, C. H., Nakwacki, M. S., Attrill, G., van Driel-Gesztelyi, L., Démoulin, P., Dasso, S., and Elliott, H.: Are CME-related dimmings always a simple signature of interplanetary magnetic cloud footpoints?, *Sol. Phys.*, **244**, 25–43, doi:10.1007/s11207-007-9020-8, 2007.

Marsden, R. G., Sanderson, T. R., Tranquille, C., Wenzel, K.-P., and Smith, E. J.: ISEE 3 observations of low-energy proton bidirectional events and their relation to isolated interplanetary magnetic structures, *J. Geophys. Res*, **92**, 11 009–11 019, doi:10.1029/JA092iA10p11009, 1987.

Martin, S. F.: Mass motions associated with solar flares, *Sol. Phys.*, **121**, 215–238, 1989.

Martin, S. F.: Signs of helicity in solar prominences and related features, *Adv. in Space Res.*, **32**, 1883–1893, doi:10.1016/S0273-1177(03)90622-3, 2003.

Martinez Oliveros, J. C., Couvidat, S., Schou, J., Krucker, S., Lindsey, C., Hudson, H. S., and Scherrer, P.: Imaging spectroscopy of a white-light solar flare, *Sol. Phys.*, **269**, 269–281, doi:10.1007/s11207-010-9696-z, 2011.

Marubashi, K.: Interplanetary magnetic flux ropes and solar filaments, in Coronal Mass Ejections, edited by N. Crooker, J. Jocelyn, and J. Feynman, vol. 99 of *Geophys. Monogr. Ser.*, pp. 147–156, AGU, Washington D.C., 1997.

Marubashi, K.: Physics of interplanetary flux ropes: Toward prediction of geomagnetic storms, *Adv. Space Res.*, **26**, 55–66, doi:10.1016/S0273-1177(99)01026-1, 2000.

McComas, D. J., Gosling, J. T., Bame, S. J., Smith, E. J., and Cane, H. V.: A test of magnetic field draping induced b_z perturbations ahead of fast coronal mass ejecta, *J. Geophys. Res.*, **94**, 1465–1471, doi:10.1029/JA094iA02p01465, 1989.

McComas, D. J., Bame, S. J., Barker, P., Feldman, W. C., Phillips, J. L., Riley, P., and Griffee, J. W.: Solar Wind Electron Proton Alpha Monitor (SWEPAM) for the Advanced Composition Explorer, *Space Sci. Rev.*, **86**, 563–612, doi:10.1023/A:1005040232597, 1998.

McKenzie, D. E.: Signatures of reconnection in eruptive flares, in Multi-wavelength observations of coronal structure and dynamics, Yohkoh 10th anniversay meeting, vol. 13 of *COSPAR Colloquia series*, pp. 155–164, doi:10.1016/S0964-2749(02)80041-5, 2002.

Mitchell, D. G., Roelof, E. C., and Bame, S. J.: Solar wind iron abundance variations at speed > 600 km s^{-1}, 1972-1976, *J. Geophys. Res.*, **88**, 9059–9068, doi:10.1029/JA088iA11p09059, 1983.

Montgomery, M. D., Asbridge, J. R., Bame, S. J., and Feldman, W. C.: Solar wind electron temperature depressions following some interplanetary shock waves: Evidence for magnetic merging?, *J. Geophys. Res.*, **79**, 3103–3110, doi:10.1029/JA079i022p03103, 1974.

Moon, Y. J., Choe, G. S., and et al., H. W.: A statistical study of two classes of coronal mass ejections, *Astrophys. J.*, **581**, 694–702, doi:10.1086/344088, 2002.

Moore, R. L., LaRosa, T. N., and Orwig, L. E.: The wall of reconnection-driven magnetohydrodynamic turbulence in a large solar flare, *Astrophys. J.*, **438**, 985–996, doi:10.1086/175140, 1995.

Morrison, P.: Solar-connected variations of the cosmic rays, *Phys. Rev.*, **95**, 641, 1954.

Moses, D., Clette, F., Delaboudiniére, J. P., Artzner, G. E., Bougnet, M., Brunaud, J., Carabetian, C., Gabriel, A. H., Hochedez, J. F., Millier, F., Song, X. Y., Au, B., Dere, K. P., Howard, R. A., Kreplin, R., Michels, D. J., Defise, J. M., Jamar, C., Rochus, P., Chauvineau, J. P., Marioge, J. P., Catura, R. C., Lemen, J. R., Shing, L., Stern, R. A., Gurman, J. B., Neupert, W. M., Newmark, J., Thompson, B., Maucherat, A., Portier-Fozzani, F., Berghmans, D., Cugnon, P., Dessel, E. L. V., and Gabryl, J. R.: EIT observations of the extreme ultraviolet Sun, *Sol. Phys.*, **175**, 571–599, doi:10.1023/A:1004902913117, 1997.

Mouradian, Z., Soru-Escaut, I., and Pojoga, S.: On the two classes of filament-prominence disappearance and their relation to coronal mass ejections, *Sol. Phys.*, **158**, 269–281, doi:10.1007/BF00795663, 1995.

Mulligan, T. and Russell, C. T.: Multispacecraft modelling of the flux rope structure of interplanetary coronal mass ejections: Cylindrically symmetric versus nonsymmetric topologies, *J. Geophys. Res.*, **106**, 10 581–10 596, doi:10.1029/2000JA900170, 2001.

Mulligan, T., Russell, C. T., and Gosling, J. T.: On interplanetary coronal mass ejection identification at 1 AU, in Solar Wind Nine, edited by S. R. Habbal, R. Esser, H. J. V., and P. A. Isenberg, vol. 471, pp. 693–696, AIP Conf. Proc., Woodbury, New York, 1999.

Nakagawa, T., Nishida, A., and Saito, T.: Planar magnetic structures in the solar wind, *J. Geophys. Res.*, **94**, 11 761–11 775, doi:10.1029/JA094iA09p11761, 1989.

Nakagawa, Y., Raadu, M. A., Billings, D. E., and McNamara, D.: On the topology of filaments and chromospheric fibrils near sunspots, *Sol. Phys.*, **19**, 72–85, doi:10.1007/BF00148825, 1971.

Neugebauer, M.: Observations of solar-wind helium, *Fundam. Cosmic Phys.*, **7**, 131–199, 1981.

Neugebauer, M., Goldstein, R., and Goldstein, B. E.: Features observed in the trailing regions of interplanetary clouds from coronal mass ejections, *J. Geophys. Res.*, **102**, 19 743–19 751, doi:10.1029/97JA01651, 1997.

Neugebauer, M., Steinberg, J. T., Tokar, R. L., Barraclough, B. L., Dors, E. E., Wiens, R. C., Gingerich, G. E., Luckey, D., and Whiteaker, D. B.: Genesis onboard determination of the solar wind flow regime, *Space Sci. Rev.*, **105**, 661–679, doi:10.1023/A:1024478129261, 2003.

Neupert, W. M.: Comparison of solar x-ray line emission with microwave emission during flares, *Astrophys. J.*, **153**, L59, 1968.

Odstrcil, D. and Pizzo, V. J.: Three-dimensional propagation of coronal mass ejections (cmes) in a structured solar wind flow 1. cme launched within the streamer belt, *J. Geophys. Res.*, **104**, 483–492, doi:10.1029/1998JA900019, 1999a.

Odstrcil, D. and Pizzo, V. J.: Three-dimensional propagation of coronal mass ejections (CMEs) in a structured solar wind flow 2. CME launched adjacent to the streamer belt, *J. Geophys. Res.*, **104**, 493–503, doi:10.1029/1998JA900038, 1999b.

Odstrcil, D., Vandas, M., Pizzo, V. J., and Macneice, P.: Numerical simulation of interacting magnetic flux ropes, in Solar Wind Ten: Proceedings of the tenth solar wind conference, p. 669, 2003.

Odstrcil, D., Riley, P., and Zhao, X. P.: Numerical simulation of the 12 May 1997 interplanetary CME event, *J. Geophys. Res.*, **109**, A02 116, doi:10.1029/2003JA010135, 2004.

Osherovich, V., Farrugia, C., Burlaga, L., Lepping, R., Fainberg, J., and Stone, R.: Polytropic relationship in interplanetary magnetic clouds, *J. Geophys. Res.*, **98**, 15 331–15 342, doi:10.1029/93JA01012, 1993.

Osherovich, V. A., Fainberg, J., and Stone, R. G.: Multi-tube model for interplanetary magnetic clouds, *Geophys. Res. Lett.*, **26**, 401–404, doi:10.1029/1998GL900306, 1999.

Owens, M. J.: The formation of large-scale current sheets within magnetic clouds, *Sol. Phys.*, **260**, 207–217, doi:10.1007/s11207-009-9442-6, 2009.

Palmer, I. D., Allum, F. R., and Singer, S.: Bidirectional anisotropies in solar cosmic ray events: Evidence for magnetic bottles, *J. Geophys. Res.*, **83**, 75–90, doi:10.1029/JA083iA01p00075, 1978.

Parker, E. N.: Sweet's mechanism for merging magnetic fields in conducting fluids, *J. Geophys. Res.*, **62**, 509–520, doi:10.1029/JZ062i004p00509, 1957.

Parker, E. N.: Dynamic instability in an anisotropic ionized gas of low density, *Phys. Rev.*, **109**, 1874–1876, doi:10.1103/PhysRev.109.1874, 1958.

Parker, E. N.: Sudden expansion of the corona following a large solar flare and the attendant magnetic field and cosmic-ray effects, *Astrophys. J.*, **133**, 1014, doi:10.1086/147105, 1961.

Parker, E. N.: The solar-flare phenomena and the theory of reconnection and annihilation of magnetic fields, *Astrophys. J. Supp.*, **8**, 177–211, doi:10.1086/190087, 1963.

Parker, E. N.: Solar wind, in Handbook of the solar-terrestrial environment, pp. 95–116, Springer-Verlag, Berlin Heidelberg, doi:10.1007/11367758-4, 2007.

Paschmann, G., Sonnerup, B. U. O., and Papamastorakis, I.: Plasma acceleration at the earth's magnetopause: evidence for reconnection, *Nature*, **282**, 243–246, 1979.

Paschmann, G., Papamastorakis, I., and Baumjohann, W.: The magnetopause for large magnetic shear: AMPTE/IRM observations, *J. Geophys. Res.*, **91**, 11 099–11 115, doi:10.1029/JA091iA10p11099, 1986.

Petschek, H. E.: The physics of solar flares, in AAS-NASA Symposium (NASA SP-50), p. 425, (Greenbelt, MD: NASA), 1964.

Pevtsov, A. A. and Balasubramaniam, K. S.: Helicity patterns on the Sun, *Adv. in Space Res.*, **32**, 1867–1874, doi:10.1016/S0273-1177(03)90620-X, 2003.

Pevtsov, A. A., Canfield, R. C., and McClymont, A. M.: On the subphotospheric origin of coronal electric currents, *Astrophys. J.*, **481**, 973–977, doi:10.1086/304065, 1997.

Phan, T. D., Paschmann, G., and Sonnerup, B. U. O.: Low-latitude dayside magnetopause and boundary layer for high magnetic shear 2. Occurrence of magnetic reconnection, *J. Geophys. Res.*, **101**, 7817–7828, doi:10.1029/95JA03751, 1996.

Phan, T. D., Kistler, L. M., Klecker, B., Haerendel, G., Paschmann, G., Sonnerup, B. U. O., Baumjohann, W., Bavassano-Cattaneo, M. B., Carlson, C. W., DiLellis, A. M., Fornacon, K. H., Frank, L. A., Fujimoto, M., Georgescu, E., Kokubun, S., Moebius, E., Mukai, T., Oieroset, M., Paterson, W. R., and Reme, H.: Extended magnetic reconnection at the earth's magnetopause from detection of bi-directional jets, *J. Geophys. Res.*, **404**, 848–850, doi:10.1038/35009050, 2000.

Phan, T. D., Gosling, J. T., Davis, M. S., Skoug, R. M., Oeieroset, M., Lin, R. P., Lepping, R. P., McComas, D. J., Smith, C. W., Reme, H., and Balogh, A.: A magnetic reconnection X-line extending more than 390 Earth radii in the solar wind, *Nature*, **439**, 175–178, doi:10.1038/nature04393, 2006.

Phillips, J. L., Bame, S. J., Gosling, J. T., McComas, D. J., Goldstein, B. E., Smith, E. J., Balogh, A., and Forsyth, R. J.: Ulysses plasma observations of coronal mass ejections near 2.5 AU, *Geophys. Res. Lett.*, **19**, 1239–1242, doi:10.1029/92GL00529, 1992.

Phillips, K. J. H., Feldman, U., and Landi, E.: Ultraviolet and X-ray spectroscopy of the solar atmosphere, Cambridge University Press, doi:10.1017/CBO9780511585968, 2008.

Pick, M., Forbes, T. G., Mann, G., Cane, H. V., Chen, J., Ciaravella, A., Cremades, H., Howard, R. A., Hudson, H. S., Klassen, A., Klein, K. L., Lee, M. A., Linker, J. A., Maia, D., Mikic, Z., Raymond, J. C., Reiner, M. J., .Simnett, G. M., Srivastava, N., Tripathi, D., Vainio, R., Vourlidas, A., Zhang, J., Zurbuchen, T. H., Sheeley, N. R., and Marqué, C.: Multi-wavelength observations of CMEs and associated phenomena, *Space Sci. Rev.*, **123**, 341–382, doi:10.1007/s11214-006-9021-1, 2006.

Pilipp, W. G., Miggenrieder, H., Mu(e)hlha(e)user, K., Rosenbauer, H., Schwenn, R., and Neubauer, F. M.: Variations of electron distribution functions in the solar wind, *J. Geophys. Res.*, **92**, 1103–1118, doi:10.1029/JA092iA02p01103, 1987.

Plunkett, S. P., Thompson, B. J., Howard, R. A., Michels, D. J., Cyr, O. C. S., Tappin, S. J., Schwenn, R., and Lamy, P. L.: LASCO observations of an Earth-directed coronal mass ejection on May 12, 1997, *Geophys. Res. Lett*, **25**, 2477–2480, doi:10.1029/98GL50307, 1998.

Pohjolainen, S., Maia, D., Pick, M., Vilmer, N., Khan, J. I., Otruba, W., Warmuth, A., Benz, A., Alissandrakis, C., and Thompson, B. J.: On-the-disk development of the halo coronal mass ejection 1998 May 2, *Astrophys. J.*, **556**, 421–431, doi:10.1086/321577, 2001.

Priest, E., Titov, V. S., Vekestein, G. E., and Rickard, G. J.: Steady linear X-point magnetic reconnection, *J. Geophys. Res.*, **99**, 21 467–21 480, doi:10.1029/94JA01412, 1994.

Priest, E. R.: Solar magneto-hydrodynamics, D. Reidel Pub. Co., Dordrecht, Holland, 1982.

Pudovkin, M. I., Zaitseva, S. A., and Benevslenska, E. E.: The structure and parameters of flare streams, *J. Geophys. Res.*, **84**, 6649–6652, doi:10.1029/JA084iA11p06649, 1979.

Qiu, J., Hu, Q., Howard, T. A., and Yurchyshyn, V. B.: On the magnetic flux budget in low-corona magnetic reconnection and interplanetary coronal mass ejections, *Astrophys. J.*, **659**, 758–772, doi:10.1086/512060, 2007.

Reiner, M. J., Kaiser, M. L., and Bougeret, J. L.: On the deceleration of cmes in the corona and interplanetary medium deduced from radio and white-light observations, in Solar Wind Ten, vol. 679 of *AIP Conference Proceedings*, pp. 152–155, Melville, NY, doi:10.1063/1.1618564, 2003.

Richardson, I. G.: Using energetic particles to probe the magnetic topology of ejecta, in Coronal Mass Ejections, vol. 99 of *Geophys. Mongr. Ser.*, pp. 189–196, AGU, Washinton D. C., 1997.

Richardson, I. G. and Cane, H. V.: Signatures of shock drivers in the solar wind and their dependence on the solar source location, *J. Geophys. Res.*, **98**, 15 295–15 304, doi:10.1029/93JA01466, 1993.

Richardson, I. G. and Cane, H. V.: Regions of abnormally low proton temperature in the solar wind (1965-1991) and their association with ejecta, *J. Geophys. Res.*, **100**, 23 397–23 412, doi:10.1029/95JA02684, 1995.

Richardson, I. G. and Cane, H. V.: Identification of interplanetary coronal mass ejections at 1 AU using multiple solar wind plasma composition anomalies, *J. Geophys. Res.*, **109**, A09 104, doi:10.1029/2004JA010598, 2004.

Richardson, I. G. and Cane, H. V.: The fraction of interplanetary coronal mass ejections that are magnetic clouds: Evidence for a solar cycle variation, *Geophys. Res. Lett.*, **31**, L18 804, doi:10.1029/2004GL020958, 2004b.

Richardson, I. G., Berdichevsky, D., Desch, M. D., and Farrugia, C. J.: Solar-cycle variation of low density solar wind during more than three solar cycles, *Geophys. Res. Lett.*, **27**, 3761–3764, 2000.

Richardson, I. G., Cliver, E. W., and Cane, H. V.: Sources of geomagnetic storms for solar minimum and maximum conditions during 1972-2000, *Geophys. Res. Lett.*, **28**, 2569–2572, doi:10.1029/2001GL013052, 2001.

Richardson, I. G., Cane, H. V., Lepri, S. T., Zurbuchen, T. H., and Gosling, J. T.: Spatial relationship of signatures of interplanetary coronal mass ejections, in Solar Wind Ten, edited by M. Velli, R. Bruno, and F. Malara, vol. 679, pp. 681–684, doi:10.1063/1.1618686, 2003.

Riley, P., Gosling, J. T., and Pizzo, V. J.: A two-dimensional simulation of the radial and latitudinal evolution of a solar wind disturbance driven by a fast, high-pressure coronal mass ejection, *J. Geophys. Res.*, **102**, 14 677–14 686, doi:10.1029/97JA01131, 1997.

Riley, P., Gosling, J. T., McComas, D. J., and Forsyth, R. J.: Properties and radial trends of coronal mass ejecta and their associated shocks observed by Ulysses in the ecliptic plane, *J. Geophys. Res.*, **105**, 12 617–12 626, doi:10.1029/1999JA000169, 2000.

Rodriguez, L., Woch, J., Krupp, N., Franz, M., von Steiger, R., Forsyth, R. J., Reisenfeld, D. B., and Glassmeier, K. H.: A statistical study of oxygen freezing-in temperature and energetic particles inside magnetic clouds observed by ulysses, *J. Geophys. Res.*, **109**, A01 108, doi:10.1029/2003JA010156, 2004.

Romashets, E. P. and Ivanov, K. G.: The shape of a magnetic cloud in the solar wind, *Geomag. Aeron.*, **31**, 583–586, 1991.

Russell, C. T. and Shinde, A. A.: ICME identification from solar wind ion measurements, *Sol. Phys.*, **216**, 285–294, doi:10.1023/A:1026108101883, 2003.

Russell, C. T., Jian, L. K., and Luhmann, J. G.: An unusual current sheet in an ICME: Possible association with C/2006 P1 (McNaught), *Geophys. Res. Lett.*, **36**, L7105, doi:10.1029/2009GL037615, 2009.

Rust, D. M.: Coronal disturbances and their terrestrial effects, *Space Sci. Rev.*, **34**, 21–36, doi:10.1007/BF00221193, 1983.

Rust, D. M.: A new paradigm for solar filament eruptions, *J. Geophys. Res.*, **106**, 25 075–25 088, doi:10.1029/2000JA004016, 2001.

Rust, D. M. and Martin, S. E.: Solar active region evolution: Comparing models with observations, in ASP Conf. Ser., vol. 68, p. 337, 1994.

Ruzmaikin, A., Martin, S., and Hu, Q.: Signs of magnetic helicity in interplanetary coronal mass ejections and associated prominences: Case study, *J. Geophys. Res.*, **108**, 1096, doi:10.1029/2002JA009588, 2003.

Scherrer, P. H., Bogart, R. S., Bush, R. I., Hoeksema, J. T., Kosovichev, A. G., Schou, J., Rosenberg, W., Springer, L., Tarbell, T. D., Title, A., Wolfson, C. J., Zayer, I., and the MDI engineering team: The Solar Oscillations Investigation - Michelson Doppler Imager, *Sol. Phys.*, **162**, 129–188, doi:10.1007/BF00733429, 1995.

Schindler, K. and Hornig, G.: Magnetic reconnection, Institute of Physics Publishing, Grove's Dictionaries, Inc., New York, 2001.

Schmidt, J. M. and Cargill, P. J.: Magnetic cloud evolution in a two-speed solar wind, *J. Geophys. Res.*, **106**, 8283–8289, 2001.

Schmidt, J. M. and Cargill, P. J.: A numerical study of two interacting coronal mass ejections, *Ann. Geophys.*, **22**, 2245–2254, 2004.

Schwenn, R.: Relationship of coronal transients to interplanetary shocks: 3D aspects, *Space Sci. Rev.*, **44**, 139–168, doi:10.1007/BF00227230, 1986.

Schwenn, R.: Large scale structure of the interplanetary medium, in Physics of the inner heliosphere 1, pp. 99–181, Springer-Verlag, Berlin, Heidelberg, New York, 1990.

Schwenn, R.: Mass ejections from the sun and their interplanetary counterparts, in Solar Wind Eight, vol. 382, pp. 426–429, AIP Conf. Proc., doi:10.1063/1.51425, 1996.

Schwenn, R., Rosenbauer, H., and Muhlhauser, K.-H.: Singly-ionized helium in the driver gas of an interplanetary shock wave, *Geophys. Res. Lett.*, **7**, 201–204, doi:10.1029/GL007i003p00201, 1980.

Schwenn, R., Lago, A. D., Huttunen, E., and Gonzalez, W. D.: The association of coronal mass ejections with their effects near the earth, *Ann. Geophys.*, **23**, 1033–1059, 2005.

Schwenn, R., Raymond, J. C., Alexander, D., Ciaravella, A., Gopalswamy, N., Howard, R., Hudson, H., Kaufmann, P., Klassen, A., Maia, D., Munoz-Martinez, G., Pick, M., Reiner, M., Srivastava, N., Tripathi, D., Vourlidas, A., Wang, Y. M., and Zhang, J.: Coronal observations of CMEs, *Space Sci. Rev.*, **123**, 127–176, doi:10.1007/s11214-006-9016-y, 2006.

Sheeley, N. R., Bohlin, J. D., Brueckner, G. E., Purnell, J. D., Scherrer, V. E., Tousey, R., Smith, J. B., Speich, D. M., Tandberg-Hanssen, E., and Wilson, R. M.: Coronal changes associated with a disappearing filament, *Sol. Phys.*, **45**, 377–392, doi:10.1007/BF00158457, 1975.

Sheeley, N. R., Howard, R. A., Koomen, M. J., and Michels, D. J.: Associations between coronal mass ejections and soft X-ray events, *Astrophys. J.*, **272**, 349–354, doi:10.1086/161298, 1983.

Shibata, K.: Coronal dynamics and flares: New results from Yohkoh SXT, vol. 5 of *Proceedings of 2nd SOLTIP Symposium, STEP GBRSC News (SOLTIP)*, pp. 85–96, 1995.

Shibata, K.: New observational facts about solar flares from Yohkoh studies - Evidence of magnetic reconnection and a unified model of flares, *Adv. Space. Res.*, **17**, 9–18, doi:10.1016/0273-1177(95)00534-L, 1996.

Shibata, K.: Evidence of magnetic reconnection in solar flares and a unified model of flares, *Astrophys. Space. Sci.*, **264**, 129–144, 1999.

Shodhan, S., Crooker, N., Kahler, S., Fitzenreiter, R., Larson, D., Lepping, R., Siscoe, G., and Gosling, J.: Counterstreaming electrons in magnetic clouds, *J. Geophys. Res.*, **105**, 27 261–27 268, doi:10.1029/2000JA000060, 2000.

Silva, A. V. R., Wang, H., Gary, D. E., Nitta, N., and Zirin, H.: Imaging the chromospheric evaporation of the 1994 June 30 solar flare, *Astrophys. J.*, **481**, 978, 1997.

Siscoe, G. and Schwenn, R.: CME disturbance forecasting, *Space Sci. Rev.*, **123**, 453–470, doi:10.1007/s11214-006-9024-y, 2006.

Siscoe, G. L. and Suey, R. W.: Significance criteria for variance matrix applications, *J. Geophys. Res.*, **77**, 1321–1322, doi:10.1029/JA077i007p01321, 1972.

Sittler Jr., E. C. and Burlaga, L. F.: Electron temperatures within magnetic clouds between 2 and 4 AU: Voyager 2 observations, *J. Geophys. Res.*, **103**, 17 447–17 454, doi:10.1029/98JA01289, 1998.

Smith, C. W., L'Heureux, J., Ness, N. F., na, M. H. A., Burlaga, L. F., and Scheifele, J.: The ACE Magnetic Fields Experiment, *Space Sci. Rev.*, **86**, 613–632, doi:10.1023/A:1005092216668, 1998.

Smith, E. J., Tsurutani, B. T., and Rosenberg, R. L.: Observations of the interplanetary sector structure up to heliographic latitudes of 16°: Pioneer 11, *J. Geophys. Res.*, **83**, 717–724, doi:10.1029/JA083iA02p00717, 1978.

Smith, S. F. and Harvey, K. L.: Observational effects of flare-associated waves, in Physics of the Solar Corona, edited by C. J. Macris, p. 156, 1971.

Sonnerup, B. U. and Cahill, J. L.: Magnetosphere structure and attitude from Explorer 12 observations, *J. Geophys. Res.*, **72**, 171–183, doi:10.1029/JZ072i001p00171, 1967.

Sonnerup, B. U. O.: Magnetopause reconnection rate (relating to electric and magnetic field configurations), *J. Geophys. Res.*, **79**, 1546–1549, 1974.

Sonnerup, B. U. O. and Scheible, M.: Minimum and maximum variance analysis, International Space Science Institute (ISSI), 1998.

Sonnerup, B. U. O., Paschmann, G., Papamastorakis, I., Sckopke, N., Haerendel, G., Bame, S. J., Asbridge, J. R., Gosling, J. T., and Russell, C. T.: Evidence for magnetic field reconnection at the earth's magnetopause, *J. Geophys. Res.*, **86**, 10 049–10 067, 1981.

Southwood, D. J.: Some features of field line resonances in the magnetosphere, *Planetary and Space Sci.*, **483**, 483–491, doi:10.1016/0032-0633(74)90078-6, 1974.

Spiegel, E. A. and Zahn, J. P.: The solar tachocline, *Astron. Astrophys.*, **126**, 106–114, 1992.

St. Cyr, O. C., Burkepile, J. T., Hundhausen, A. J., and Lecinski, A. R.: A comparison of ground-based and spacecraft observations of coronal mass ejections from 1980-1989, *J. Geophys. Res.*, **104**, 12 493–12 506, doi:10.1029/1999JA900045, 1999.

St. Cyr, O. C., Howard, R. A., Sheeley, N. R., Plunkett, S. P., Michels, D. J., Paswaters, S. E., Koomen, M. J., Simnett, G. M., Thompson, B. J., Gurman, J. B., Schwenn, R., Webb, D. F., Hildner, E., and Lamy, P. L.: Properties of coronal mass ejections: SOHO LASCO observations from January 1996 to June 1998, *J. Geophys. Res.*, **105**, 18 169–18 185, doi:10.1029/1999JA000381, 2000.

Steed, K., Owen, C. J., Harra, L. K., Green, L. M., Dasso, S., A. P. Walsh, P. D., and van Driel-Gesztelyi, L.: Locating the solar source of 13 April 2006 magnetic cloud, *Ann. Geophy.*, **26**, 3159–3168, 2008.

Steed, K., Owen, C. J., Démoulin, P., and Dasso, S.: Investigating the observational signatures of magnetic cloud substructure, *J. Geophys. Res.*, **116**, A01 106, 2011.

Sterling, A. C. and Hudson, H. S.: Yohkoh SXT observations of X-ray "dimming" associated with a coronal mass ejection, *Astrophys. J. Lett.*, **491**, L55, doi:10.1086/311043, 1997.

Stone, E. C., Frandsen, A. M., Mewaldt, R. A., Christian, E. R., Margolies, D., Ormes, J. F., and Snow, F.: The Advanced Composition Explorer, *Space Sci. Rev.*, **86**, 1–22, doi:10.1023/A:1005082526237, 1998.

Sturrock, P. A.: Model of the high-energy phase of solar flares (Theoretical model for high energy phase of solar flares including radio bursts, proton acceleration and plasma cloud ejection), *Nature*, **211**, 695–697, doi:10.1038/211695a0, 1966.

Sturrock, P. A.: A model of solar flares, in Structure and development of solar active regions, edited by K. O. Kiepenheuer, IAU Symposium, 35, p. 471, 1968.

Sui, L., Holman, G. D., and Dennis, B. R.: Enigma of a flare involving multiple-loop interactions: Emergins, colliding loops or magnetic breakout?, *Astrophys. J.*, **646**, 605–614, 2006.

Svestka, Z.: in Solar Flares, vol. 8 of *Geophysics and Astrophysics Monographs*, Reidel, Dordrecht, Netherlands; Boston; USA, 1976.

Svestka, Z.: Varieties of coronal mass ejections and their relation to flares, *Space Sci. Rev.*, **95**, 135–146, doi:10.1023/A:1005225208925, 2001.

Sweet, P. A.: The neutral point theory of solar flares, in Electromagnetic phenomena in cosmical physics, pp. 123–134, 1958.

Szabo, A., Lepping, R. P., Merka, J., Smith, C. W., and Skoug, R. M.: The evolution of interplanetary shocks driven by magnetic clouds, in Solar Encounter, Proceedings of the First Solar Orbiter Workshop, edited by B. Battrick and H. Sawaya-Lacoste, pp. 383–387, 2001.

Thompson, B. J., Plunkett, S. P., Gurman, J. B., Newmark, J. S., Cyr, O. C. S., and Michels, D. J.: SOHO/EIT observations of an Earth-directed coronal mass ejection on May 12, 1997, vol. 25, pp. 2465–2468, doi:10.1029/98GL50429, 1998.

Thompson, B. J., Cliver, E. W., Nitta, N., Delannée, C., and Delaboudinière, J. P.: Coronal dimmings and energetic cmes in april-may 1998, *Geophys. Res. Lett.*, **27**, 1431–1434, doi:10.1029/1999GL003668, 2000.

Titov, V. S. and Démoulin, P.: Basic topology of twisted magnetic configurations in solar flares, *Astron. Astrophys.*, **351**, 707–720, 1999.

Toeroek, T. and Kliem, B.: Numerical simulations of fast and slow coronal mass ejections, *Astron. Nach.*, **328**, 743–746, doi:10.1002/asna.200710795, 1997.

Toeroek, T. and Kliem, B.: The evolution of twisting coronal magnetic field flux tubes, *Astron. Astrophys.*, **406**, 1043–1059, doi:10.1051/0004-6361:20030692, 2003.

Toeroek, T. and Kliem, B.: Confined and ejective eruptions of kink-unstable flux ropes, *Astrophys. J. Lett.*, **630**, L97–L100, doi:10.1086/462412, 2005.

Totten, T. L., Freeman, J. W., and Arya, S.: An empirical determination of the polytropic index for the free-streaming solar wind using Helios 1 data, *J. Geophys. Res.*, **100**, 13–17, doi:10.1029/94JA02420, 1995.

Tripathi, D., Bothmer, V., and Cremades, H.: The basic characteristics of EUV post-eruptive arcades and their role as tracers of coronal mass ejection source regions, *Astron. Astrophys.*, **422**, 337–349, doi:10.1051/0004-6361:20035815, 2004.

Tsuneta, S.: Structure and dynamics of magnetic reconnection in a solar flare, *Astrophys. J.*, **456**, 840–849, doi:10.1086/176701, 1996.

Tsuneta, S.: Interacting active regions in the solar corona, *Astrophys. J.*, **456**, L63–, 1996b.

Tsuneta, S.: Moving plasmoid and formation of the neutral sheet in a solar flare, *Astrophys. J.*, **483**, 507–514, doi:10.1086/304236, 1997a.

Tsuneta, S. and Lemen, J. R.: Dynamics of the solar corona observed with the Yohkoh soft X-ray telescope, 1993.

Tsuneta, S., Hara, H., Shimizu, T., Acton, L. W., Strong, K. T., Hudson, H. S., and Ogawara, Y.: Observations of a solar flare at the limb with the YOHKOH soft X-ray telescope, *Publ. Astron. Soc. Japan*, **44**, L63–L69, 1992.

Tsuneta, S., Masuda, S., Kosugi, T., and Sato, J.: Hot and superhot plasmas above an impulsive flare loop, *Astrophys. J.*, **478**, 787, 1997b.

Tsurutani, B. T. and Gonzalez, W. D.: The interplanetary causes of magnetic storms: A review, in Magnetic clouds, vol. 98 of *Geophys. Monogr. Ser.*, pp. 77–89, 1997.

Tsurutani, B. T., Smith, E. J., Gonzalez, W. D., Tang, F., and Ajasofu, S. I.: Origin of interplanetary southward magnetic fields responsible for major magnetic storms near solar maximum(1978-1979), *J. Geophys. Res.*, **93**, 8519–8531, 1988.

Tsurutani, B. T., Kamide, Y., Arballo, J. K., Gonzalez, W. D., and Lepping, R. P.: Interplanetary causes of great and superintense magnetic storms, *Phys. Chem. Earth (C)*, **24**, 101–105, doi:10.1016/S1464-1917(98)00015-4, 1999.

Uberoi, C.: Space plasmas, in Handbook of the Solar-Terrestrial Environment, edited by Y. Kamide and A. Chian, pp. 250–278, Springer Berlin Heidelberg, doi:10.1007/978-3-540-46315-3-20, 2007.

Uchida, Y.: in Solar flares, A monograph from SKYLAB solar workshop II, p. 67 and 110, Colorado Associated University Press, Boulder, Colorado, 1980.

Uchida, Y., Hirose, S., Cable, S., Uemura, K., Fujisaki, K., Torii, M., and Morita, S.: MHD simulation of dark filament eruption in the quadrupole source model, in New perspectives on solar prominences, vol. 150 of *Proc. IAU Colloquium 167*, p. 384, Astronomical Society of the Pacific Conference Series, San Francisco, 1998a.

Uchida, Y., Hirose, S., and et al., S. M.: Observations of flares and active regions from Yohkoh, and magnetodynamic models explaining them, *Astrophys. Space Sci.*, **264**, 145–169, doi:10.1023/A:1002469301152, 1998b.

Ugai, M.: Basic physical mechanism of fast reconnection evolution in space plasmas, *Space Sci. Rev.*, **95**, 601–611, doi:10.1023/A:1005205222921, 2001.

Van Ballegooijen, A. A. and Martens, P. C. H.: Formation and eruption of solar prominences, *Astrophys. J.*, **343**, 971–984, doi:10.1086/167766, 1989.

Van Tend, W. and Kuperus, M.: The development of coronal electric current systems in active regions and their relation to filaments and flares, *Sol. Phys.*, **59**, 115, doi:10.1007/BF00154935, 1978.

Vandas, M., Fischer, S., Pelant, P., and Geranios, A.: *Magnetic clouds - Comparison between spacecraft measurements and theoretical force-free solutions*, pp. 671–674.

Vandas, M., Fischer, S., and Geranios, A.: Spherical and cylindrical models of magnetized plasma clouds and their comparison with spacecraft data, *Planet. Space Sci.*, **39**, 1147–1154, doi:10.1016/0032-0633(91)90166-8, 1991.

Vandas, M., Fischer, S., Pelant, P., and Geranios, A.: Spheroidal models of magnetic clouds and their comparison with spacecraft measurements, *J. Geophys. Res.*, **98**, 11 467–11 475, doi:10.1029/93JA00055, 1993.

Vasquez, B. J., Farrugia, C., Markovskii, S., Hollweg, J., Richardson, I., Ogilvie, K., Lepping, R., Lin, R., and Larson, D.: Nature of fluctuations on directional discontinuities inside a solar ejection: Wind and IMP 8 observations, *J. Geophys. Res.*, **106**, 29 283–29 298, doi:10.1029/2001JA000142, 2001.

Walsh, A. P.: New perspectives on magnetotail dynamic processes from combined Cluster and Doublestar observations, Ph.D. thesis, University College London, 2009.

Wang, C., Du, D., and Richardson, J. D.: Characteristics of the interplanetary coronal mass ejections in the heliosphere between 0.3 and 5.4 AU, *J. Geophys. Res.*, **99**, 4201–4220, doi:10.1029/2005JA011198, 2005.

Wang, Y. M., Wang, S., and Ye, P. Z.: Multiple magnetic clouds in interplanetary space, *Sol. Phys.*, **211**, 333–344, doi:10.1023/A:1022404425398, 2002.

Warren, H. P., Bookbinder, J. A., Forbes, T. G., Goluv, L., H. S, H., Reeves, K., and Warshall, A.: Trace and yohkoh observations of high-temperature plasma in a two-ribbon limb flare, *Astrophys. J.*, **527**, L121–L124, 1999.

Watari, S., Watanabe, T., and Marubashi, K.: Soft X-ray solar activities associated with interplanetary magnetic flux ropes, *Sol. Phys.*, **202**, 363–384, doi:10.1023/A:1012202703510, 2001.

Webb, D., Jackson, B., Hick, P., Schwenn, R., Bothmer, V., and Reames, D.: Comparison of CMEs, magnetic clouds, and bidirectionally streaming proton events in the heliosphere using helios data, *Adv. Space Res.*, **13**, 71–74, doi:10.1016/0273-1177(93)90459-O, 1993.

Webb, D. F. and Hundhausen, A. J.: Activity associated with the solar origin of coronal mass ejections, *Sol. Phys.*, **108**, 383–401, doi:10.1007/BF00214170, 1987.

Webb, D. F. and Jackson, B. V.: The identification and characteristics of solar mass ejections observed in the heliosphere by Helios 2 photometers, *J. Geophys. Res.*, **95**, 20 641–20 661, doi:10.1029/JA095iA12p20641, 1990.

Webb, D. F., Kahler, S. W., McIntosh, P. S., and Klimchuk, J. A.: Large-scale structures and multiple neutral lines associated with coronal mass ejections, *J. Geophys. Res.*, **102**, 24 161–24 174, doi:10.1029/97JA01867, 1997.

Webb, D. F., Lepping, R. P., Burlaga, L. F., DeForest, C. E., Larson, D. E., Martin, S. F., Plunkett, S. P., and Rust, D. M.: The origin and development of the May 1997 magnetic cloud, *J. Geophys. Res.*, **105**, 27 251–27 259, doi:10.1029/2000JA000021, 2000.

Wei, F., Liu, R., Fan, Q., and Feng, X.: Identification of the magnetic cloud boundary layers, *J. Geophys. Res.*, **108(A6)**, 1263, 2003.

Wimmer-Schweingruber, R. F., Bochsler, P., and Wurz, P.: Isotopes in the solar wind: New results from ACE, SOHO and WIND, in Solar Wind Nine, AIP Conf. Proc., pp. 147–152, AIP Press, Woodbury, N. Y.

Wimmer-Schweingruber, R. F., Crooker, N. U., Balogh, A., Bothmer, V., Forsyth, R. J., Gazis, P., Gosling, J. T., Horbury, T., Kilchenmann, A., Richardson, I. G., Richardson, J. D., Riley, P., Rodriguez, L., von Steiger, R., Wurz, P., and Zurbuchen, T. H.: Understanding interplanetary coronal mass ejection signatures, *Space Sci. Rev.*, **123**, 177–216, doi:10.1007/s11214-006-9017-x, 2006.

Wolfson, R. and Dlamini, B.: Cross-field currents: An energy source for coronal mass ejections?, *Astrophys. J.*, **483**, 961, doi:10.1086/304263, 1997.

Wu, C. C.: The MHD intermediate shock interaction with an intermediate wave: Are intermediate shocks physical?, *J. Geophys. Res.*, **93**, 3969–3982, doi:10.1029/JA093iA05p03969, 1988.

Wu, C. C. and Hada, T.: On rotational discontinuities in both two-fluid and hybrid models, *J. Geophys. Res.*, **96**, 3755–3767, doi:10.1029/90JA02567, 1991.

Wu, C. C. and Lepping, R. P.: Comparison of the characteristics of magnetic clouds and magnetic cloud-like structures for the events of 1995-2003, *Sol. Phys.*, **242**, 159–165, doi:10.1007/s11207-007-0323-6, 2007.

Wu, C. C., Lepping, R. P., and Gopalswamy, N.: Variations of magnetic clouds and CMEs with solar activity, in Solar variability as an input to the Earth's environment, International Solar Cycle Studies (ISCS) Symposium 23, pp. 429–432, 2003.

Wu, S. T.: Numerical simulation of magnetohydrodynamic shock propagation in the corona, *Space Sci. Rev.*, **32**, 115–129, doi:10.1007/BF00225180, 1982.

Wurz, P., Ipavich, F. M., Galvin, A. B., Bochsler, P., Aellig, M. R., Kallenbach, R., Hovestadt, D., Grunwaldt, H., Hilchenbach, M., Axford, W. I., Balsiger, H., Burgi, A., Coplan, M. A., Geiss, J., Gliem, F., Gloeckler, G., Hefti, S., Hsieh, K. C., Klecker, B., Lee, M. A., Managadze, G. G., Marsch, E., Mobius, E., Neugebauer, M., Reiche, K. U., Scholer, M., Verigin, M. I., and Wilken, B.: Elemental composition of the january 6, 1997, cme, *Geophys. Res. Lett.*, **25**, 2557–2560, doi:10.1029/98GL50478, 1998.

Xiong, M.: Magnetohydrodynamic simulation of the interaction between two interplanetary magnetic clouds and its consequent geoeffectiveness: 2. Oblique collision, *J. Geophys. Res.*, **114**, A11 101, doi:10.1029/2009JA014079, 2009.

Xiong, M., Zheng, H., Wang, Y., and Wang, S.: Magnetohydrodynamic simulation of the interaction between interplanetary strong shock and magnetic cloud and its consequent geoeffectiveness, *J. Geophys. Res.*, **111**, A08 105, doi:10.1029/2005JA011593, 2006.

Xiong, M., Zheng, H., and Wang, S.: Magnetohydrodynamic simulation of the interaction between two interplanetary magnetic clouds and its consequent geoeffectiveness: 2. oblique collision, *J. Geophys. Res.*, **112**, A11 103, 2007.

Yang, G. and Wang, H.: 2002.

Yashiro, S., Gopalswamy, N., Michalek, G., Cyr, O. C. S., Plunkett, S. P., and et al., N. B. R.: A catalog of white light coronal mass ejections observed by the SOHO spacecraft, *J. Geophys. Res.*, **109**, A07 105, doi:10.1029/2003JA010282, 2004.

Yurchyshyn, V. B.: Evidence of a flux-rope model for coronal mass ejections based on observations of the limb prominence eruption on 2002 january 4, *Astrophys. J.*, **576**, 493–496, doi:10.1086/341628, 2002.

Yurchyshyn, V. B., Wang, H., Goode, P. R., and Deng, Y.: Orientation of the magnetic fields in interplanetary flux ropes and solar filaments, *Astrophys. J.*, **563**, 381–388, doi:10.1086/323778, 2001.

Yurchyshyn, V. B., Hu, Q., and Abramenko, V.: Structure of magnetic fields in NOAA active regions 0486 and 0501 and in the associated interplanetary ejecta, *Space Weather*, **3**, S08C02, doi:10.1029/2004SW000124, 2005.

Zhang, G. and Burlaga, L. F.: Magnetic clouds, geomagnetic disturbances, and cosmic ray decreases, *J. Geophys. Res.*, **93**, 2511–2518, doi:10.1029/JA093iA04p02511, 1988.

Zhang, J.: in Coronal and stellar mass ejections, Proc. IAU Symp. 226, pp. 65–70, Cambridge Univ. Press, Cambridge, UK, 2005.

Zhang, J., Dere, K. P., Howard, R. A., Kundu, M. R., and White, S. M.: On the temporal relationship between coronal mass ejections and flares, *Astrophys. J.*, **559**, 452–462, doi:10.1086/322405, 2001.

Zhang, J., Dere, K. P., Howard, R. A., and Bothmer, V.: Identification of solar sources of major geomagnetic storms between 1996 and 2002, *Astrophys. J.*, **582**, 520–533, doi:10.1086/344611, 2003.

Zhang, J., Dere, K. P., Howard, R. A., and Vourlidas, A.: A study of the kinematic evolution of coronal mass ejections, *Astrophys. J.*, **604**, 420–432, doi:10.1086/381725, 2004.

Zhao, X.: Interaction of fast steady flow with slow transient flow: A new cause of shock pair and interplanetary b_z event, *J. Geophys. Res.*, **97**, 15 051–15 055, doi:10.1029/92JA01535, 1992.

Zhao, X. P. and Hoeksema, J. T.: Central axial field direction in magnetic clouds and its relation to southward interplanetary magnetic field events and dependence on disappearing solar filaments, *J. Geophys. Res.*, **103**, 2077–2083, doi:10.1029/97JA03234, 1998.

Zhao, X. P., Plunkett, S. P., and Liu, W.: Determination of geometrical and kinematical properties of halo corona mass ejections using the cone model, *J. Geophys. Res.*, **107**, 1223, doi:10.1029/2001JA009143, 2002.

Zhukov, A. N. and Veselovsky, I. S.: Global coronal mass ejections, *Astrophys. J. Lett.*, **664**, 131–134, doi:10.1086/520928, 2007.

Zurbuchen, T., Fisk, L. A., Lepri, S. T., and von Steiger, R.: Temperature anisotropies of heavy solar wind ions from ulysses-swics, in Solar Wind Ten, AIP Conf. Proc., p. 604, Mellville, N. Y., 2003.

Zurbuchen, T. H. and Richardson, I. G.: In-situ solar wind and magnetic field signatures of interplanetary coronal mass ejections, *Space Sci. Rev.*, **123**, 31–43, doi:10.1007/s11214-006-9010-4, 2006.

Zwickl, R. D., Asbridge, J. R., Bame, S. J., Feldman, W. C., Gosling, J. T., and Smith, E. J.: Plasma properties of driver gas following interplanetary shocks observed by ISEE-3, in Solar Wind Five, edited by M. Neugebauer, vol. 2280, pp. 711–717, NASA Conf. Proc., NASA, Washington D. C., 1983.